
An MCNP simulation study of an oil well logging
benchmarking tool and a test enclosure

by

MARIA ISABEL PINILLA

B.S., Kansas State University, 2014

AN ABSTRACT OF A DISSERTATION

submitted in partial fulfillment of the requirements for the degree

DOCTOR OF PHILOSOPHY

Department of Mechanical and Nuclear Engineering
Carl R. Ice College of Engineering

KANSAS STATE UNIVERSITY
Manhattan, Kansas

2019

Abstract

The research contained within outlines a series of simulation studies conducted to design an oil well logging tool and a testing enclosure that will be used to benchmark a Monte Carlo Library Least Squares (MCLLS) code, currently under development at North Carolina State University. Computer simulations were conducted to aid in the design of the benchmarking tool, as well as a test enclosure to be used as an infinite medium where measurements were to take place. An initial tool configuration was modeled in MCNP6[®] to perform simulations while varying design parameters to learn about the behavior of the tool. Shielding and effectively infinite medium studies were conducted in order to optimize the tool geometry and experiment design. A deuterium-tritium (D-T) generator, which produces up to 1.6×10^8 neutrons per second, will be used as a source to replace the Am-Be and cesium-137 sources typically found in well logging tools. Helium-3 and NaI(Tl) detectors will be used to measure the γ -ray and neutron spectra when different materials such as water, sand, and limestone surround the tool. The MCLLS code being developed could lead to new computer algorithms that take advantage of inelastic-scatter γ -rays generated by high-energy neutrons in the surrounding material to determine the composition of the formation.

An MCNP simulation study of an oil well logging
benchmarking tool and a test enclosure

by

MARIA ISABEL PINILLA

B.S., Kansas State University, 2014

A DISSERTATION

submitted in partial fulfillment of the requirements for the degree

DOCTOR OF PHILOSOPHY

Department of Mechanical and Nuclear Engineering
Carl R. Ice College of Engineering

KANSAS STATE UNIVERSITY
Manhattan, Kansas

2019

Approved by:

Major Professor
William L. Dunn

Copyright

MARIA ISABEL PINILLA

2019

Abstract

The research contained within outlines a series of simulation studies conducted to design an oil well logging tool and a testing enclosure that will be used to benchmark a Monte Carlo Library Least Squares (MCLLS) code, currently under development at North Carolina State University. Computer simulations were conducted to aid in the design of the benchmarking tool, as well as a test enclosure to be used as an infinite medium where measurements were to take place. An initial tool configuration was modeled in MCNP6[®] to perform simulations while varying design parameters to learn about the behavior of the tool. Shielding and effectively infinite medium studies were conducted in order to optimize the tool geometry and experiment design. A deuterium-tritium (D-T) generator, which produces up to 1.6×10^8 neutrons per second, will be used as a source to replace the Am-Be and cesium-137 sources typically found in well logging tools. Helium-3 and NaI(Tl) detectors will be used to measure the γ -ray and neutron spectra when different materials such as water, sand, and limestone surround the tool. The MCLLS code being developed could lead to new computer algorithms that take advantage of inelastic-scatter γ -rays generated by high-energy neutrons in the surrounding material to determine the composition of the formation.

Table of Contents

List of Figures	x
List of Tables	xiii
Acknowledgements	xiv
Dedication	xv
1 Introduction	1
1.1 Motivation	2
1.2 Objectives	4
1.3 Methods	4
2 Overview of Nuclear Oil Well Logging	6
2.1 Gamma-Ray Logging	7
2.1.1 Passive Measurement	8
2.1.2 Active Interrogation	9
2.2 Neutron Porosity Logging	9
2.3 Carbon/Oxygen Logging	10
2.4 Radioactive Sources Used in Nuclear Well Logging	11
2.5 Previous Efforts in Oil Well Logging Source Replacement	12
3 Modeling and Simulation Methods	15
3.1 Monte Carlo Methods	15
3.1.1 Origins and History	16

3.1.2	Modern Capabilities	17
3.1.3	Deterministic vs. Monte Carlo Methods	17
3.2	MCNP [®]	18
3.2.1	MCNP [®] Structure	19
3.2.2	Geometry	19
3.2.3	Physics	20
3.2.4	Tallies Used	22
3.2.5	Special Tally Treatment Cards	24
3.2.6	Output	26
3.2.7	Error Estimation	27
3.2.8	Variance Reduction Techniques	27
4	Design of an Oil Well Logging Benchmarking Tool	31
4.1	Tool Configuration	32
4.2	Tool Components	32
4.2.1	Neutron Source	33
4.2.2	Detectors	35
4.3	Source Shielding Studies	36
4.3.1	Shielding Effectiveness	36
4.3.2	Shielding Effect on Porosity Sensitivity	38
4.4	Detector Spacing Studies	40
4.4.1	Spacing Between Near and Far Sets of Detectors	41
4.4.2	Effect of Near to Far Detector Spacing on Porosity	42
5	Design of Test Enclosure	44
5.1	Effectively Infinite Medium Radius	45
5.2	Source Depth	47
5.3	Height and Width of Enclosure	49

5.4	Laboratory Facility Overview	51
5.5	Engineering Controls and Interlocks	53
5.6	Shielding Design	54
5.7	Dosimetry Calculations	56
5.8	Shielding Design Verification	59
6	AmBe Experiments and Simulations	61
6.1	Source Characterization	62
6.1.1	ACER Experiment	62
6.1.2	MCNP Simulation of ACER Experiment	64
6.1.3	Source Strength Analysis	68
6.1.4	Source Strength Comparison	72
6.2	AmBe Water Experiment in Test Enclosure	75
6.3	MCNP Simulation of AmBe Water Experiment	77
6.3.1	MCNP Geometry	78
6.3.2	^3He Detectors	79
6.3.3	NaI(Tl) Detectors	79
6.4	NaI(Tl) Activation	81
6.4.1	Theory	81
6.4.2	MCNP Procedure	82
6.5	MCNP Simulation of AmBe Water Experiment with NaI(Tl) Activation . . .	85
7	DT Experiments and Simulations	87
7.1	Gamma Ray Database	88
7.2	DT Experiments in Test Enclosure	89
7.2.1	Tool Configuration	89
7.2.2	Measurement System	91
7.2.3	Materials	91

7.2.4	Experimental Procedure	92
7.2.5	Sample Experimental Results - Water	92
7.3	MCNP Simulation of DT Experiments	96
7.3.1	Material Definitions	97
7.3.2	Simulation Physics	98
7.4	Simulation Results vs Experimental Measurements	99
7.4.1	Water	100
7.4.2	Limestone	103
7.4.3	Wet Limestone	106
7.4.4	Dry Sand	108
7.4.5	Wet Sand	110
7.4.6	Summary	112
8	Conclusion	114
8.1	Summary	114
8.1.1	Tool Design	115
8.1.2	Testing Enclosure Design	115
8.1.3	Experimental Results vs. MCNP Simulations	116
8.2	Objectives	117
8.3	Contribution to Research Efforts	117
8.4	Future Work	118
	Bibliography	120
A	Gamma Ray Database	125

List of Figures

4.1	Oil well logging benchmarking tool geometry	32
4.2	AmBe, D-D, and D-T neutron energy spectra	33
4.3	X-ray image of ^3He detector	35
4.4	Approximate tool geometry used in shielding studies	36
4.5	Near NaI(Tl) detector responses for limestone (<i>left</i>) and water (<i>right</i>)	37
4.6	Near ^3He detector responses for limestone (<i>left</i>) and water (<i>right</i>)	38
4.7	Tool geometry used in detector spacing studies	40
4.8	Far detector responses for different spacing between detector sets	41
4.9	Far detector responses for different spacing between detector sets	42
4.10	Near to Far ^3He detector response ratio vs. limestone porosity	43
4.11	Near to Far ^3He detector response ratio vs. sandstone porosity	43
5.1	Section of barrel geometry	46
5.2	Near ^3He detector response (normalized) vs. barrel radius	46
5.3	Far NaI(Tl) detector response vs. source depth	48
5.4	Far ^3He detector response vs. source depth	48
5.5	New test enclosure geometry	49
5.6	Detector response vs. height and width of test enclosure	50
5.7	Detector response vs. height and width of test enclosure	50
5.8	CNEC area of operations and surrounding areas.	52
5.9	King Hall Annex floor plan and CNEC area of operations.	52
5.10	King Hall Annex: Room 101 (operator room)	53
5.11	King Hall Annex: Safety features	54

5.12	Final test enclosure design	55
5.13	Removable shielding cap for borehole pipe	56
5.14	King Hall Annex, room 207, shielding configuration and expected ambient dose rates	57
6.1	ACER experiment geometry, top-view (not to scale).	63
6.2	ACER experimental detector responses.	63
6.3	NaI(Tl) simulated responses for ACER experiment.	65
6.4	CeBr ₃ simulated responses for ACER experiment (No GEB).	65
6.5	ACER AmBe experiment, 4.44 MeV peak analysis of CeBr ₃ measurement.	66
6.6	ACER AmBe Experiment, CeBr ₃ MCNP Simulation with GEB.	67
6.7	ACER AmBe Experiment, 4.44 MeV peak analysis of NaI(Tl) measurement.	69
6.8	ACER AmBe Experiment, NaI(Tl) MCNP simulation peak analysis.	69
6.9	ACER AmBe Experiment, 4.44 MeV peak analysis of CeBr ₃ measurement.	71
6.10	ACER AmBe Experiment, CeBr ₃ MCNP simulation peak analysis.	71
6.11	ACER experimental vs simulated NaI detector response.	74
6.12	ACER experimental vs simulated CeBr ₃ detector response.	74
6.13	AmBe water experiment, ³ He background subtracted sensor response.	76
6.14	AmBe water experiment, NaI(Tl) background subtracted sensor response.	76
6.15	NaI(Tl) post-background measurements in 10 minute intervals.	77
6.16	³ He MCNP simulation versus experimental measurements.	80
6.17	Preliminary MCNP simulation versus experimental measurements.	80
6.18	Energy-dependent F4 neutron tally in near NaI(Tl) detector.	82
6.19	ENDF/B (n,γ) cross sections for ²³ Na and ¹²⁷ I	83
6.20	MCNP pulse height tally (F8) for NaI(Tl) with a distributed beta source.	84
6.21	MCNP NaI(Tl) water simulation with AmBe source vs. experimental results.	86
6.22	MCNP NaI(Tl) simulation with activation added versus experimental results.	86

7.1	BF ₃ water measurement with DT source.	94
7.2	³ He water measurement with DT source.	94
7.3	NaI(Tl) water measurement with DT source.	95
7.4	MCNP BF ₃ water simulation with DT source vs. experimental results	100
7.5	MCNP ³ He water simulation with DT source vs. experimental results	102
7.6	MCNP NaI(Tl) water simulation with DT source vs. experimental results . .	102
7.7	MCNP BF ₃ dry limestone simulation with DT source vs. experimental results	103
7.8	MCNP ³ He dry limestone simulation with DT source vs. experimental results	104
7.9	MCNP NaI(Tl) dry limestone simulation with DT source vs. experimental results	105
7.10	MCNP BF ₃ wet limestone simulation with DT source vs. experimental results	106
7.11	MCNP ³ He wet limestone simulation with DT source vs. experimental results	107
7.12	MCNP NaI(Tl) wet limestone simulation with DT source vs. experimental results	107
7.13	MCNP BF ₃ dry sand simulation with DT source vs. experimental results . .	108
7.14	MCNP ³ He dry sand simulation with DT source vs. experimental results . .	109
7.15	MCNP NaI(Tl) dry sand simulation with DT source vs. experimental results	109
7.16	MCNP BF ₃ wet sand simulation with DT source vs. experimental results . .	111
7.17	MCNP ³ He wet sand simulation with DT source vs. experimental results . .	111
7.18	MCNP NaI(Tl) wet sand simulation with DT source vs. experimental results	112

List of Tables

1.1	Characteristics of radionuclide sources often used in oil well logging tools.	3
2.1	Some naturally occurring background γ -rays [1]	8
2.2	Inelastic scatter γ -rays commonly used in carbon/oxygen logging	11
4.1	Neutron flux at near and far ^3He detector locations and calculated migration lengths	39
5.1	Hallway ambient dose rates for different thicknesses of borated polyethylene	55
5.2	Ambient Dose Rates [ICRP74H*(10mm)], Water-Filled Testing Enclosure	58
5.3	Ambient Dose Rates [ICRP74H*(10mm)], Air-Filled Testing Enclosure	58
5.4	Survey meter readings while operating with the DT generator on	60
6.1	ACER AmBe experiment, CeBr_3 Gaussian fit peak data	66
6.2	ACER AmBe experiment, $\text{NaI}(\text{Tl})$ Gaussian fit peak data.	70
6.3	ACER AmBe experiment, CeBr_3 Gaussian fit peak data.	72
6.4	ACER AmBe experiment, $\text{NaI}(\text{Tl})$ and CeBr_3 Gaussian fit peak data.	73
7.1	Spectral features of $\text{NaI}(\text{Tl})$ response due to 14.1 MeV neutrons.	96
7.2	Material composition for limestone, density = 2.610 g/cm ³ [2]	97
7.3	Material composition for sand, density = 1.70 g/cm ³ [2]	98
7.4	Estimated DT source strength.	100
7.5	Spectral features of $\text{NaI}(\text{Tl})$ response due to 14.1 MeV neutrons in limestone.	105
7.6	Spectral features of $\text{NaI}(\text{Tl})$ response due to 14.1 MeV neutrons in sand.	110

Acknowledgments

I would like to express my sincerest gratitude to my advisor, Dr. William Dunn, for giving me the opportunity to be a part of his research team. I have learned so much from you and thoroughly enjoyed working on this research project. Thank you for encouraging me to face my fears and work on my weaknesses.

Thank you to my committee, Dr. J. Ken Shultis, Dr. Walter McNeil, Dr. Kristan Corwin, and Dr. William Dunn for making your time available and serving as both mentors and role models. I am honored to have had the chance to learn from you. Thanks to my colleagues, Long Vo and Aaron Hellinger for being good friends and teammates.

And finally, I want to thank my family and friends for supporting me. Your patience and kindness has made my work possible.

Dedication

This work is dedicated to my mom, Sandra.

Thank you for encouraging my passions. Thank you for your incredible sacrifice and hard work. And thank you for always being a source of inspiration, strength, and good humor. I hope to make you proud.

Chapter 1

Introduction

This work addresses the replacement of radioisotope sources by machine sources in oil well logging tools. Kansas State University (KSU) is a member of the Consortium for Nonproliferation Enabling Capabilities (CNEC), a project funded by the National Nuclear Security Agency (NNSA), and is the lead institution for the thrust area concerned with replacement of dangerous radiological sources (RDRS). A research effort has been undertaken by KSU, North Carolina State University (NCSU), and Georgia Institute of Technology (GaTech). A Monte Carlo-Library Least Squares (MCLLS) code is being developed at NCSU to improve elemental analysis of rock formations using the full spectrum of γ rays generated by high-energy neutrons from deuterium-tritium (D-T) sources. An improved computational algorithm may encourage the oil industry to phase out dangerous long-lived radioisotopes in favor of safer machine sources.

KSU has been tasked with developing a benchmarking oil well logging tool, designing and constructing a laboratory facility to test the tool, and providing high fidelity experimental measurements. The experimental data collected at KSU will be used to test and further develop the MCLLS code capabilities. With computing capabilities increasing exponentially throughout the years, this new computer algorithm attempts to extract much more information about the subsurface environment from down-hole measurements utilizing the full γ -ray spectrum.

1.1 Motivation

Concerns over national security have greatly increased following the terrorist attacks on September 11, 2001. As a result, the United States Congress requested the study of other technologies that could be used for nefarious purposes, including those involving radioactive materials. A committee on radiation source use and replacement was formed by the National Research Council of the National Academy of Sciences to make recommendations. The committee's findings, which can be found in a report published in 2008 [3], outlined several industries where improvements can be made to safeguard from future accidents and attacks involving the dispersal of nuclear material.

The oil well logging industry is one of several that were thoroughly studied in order to make recommendations. Chapter 9 of the Radiation Source and Replacement report was solely dedicated to the evaluation of radiation sources used in oil well logging due to their availability, dispersability, persistence, and potential to cause harm. Unlike radioisotopes used in medical and federal facilities, the radioactive sources routinely used in oil well logging are often found in unsecured and remote locations. Occasionally a source will fall down the well and never be retrieved [4], causing concern for underground water wells and other environmental effects. When these radioisotopes are stolen or unaccounted for, they pose a potential national security risk, such as the intentional dispersal of radioactive material through the use of dirty bombs.

The two major radioisotopes that were recommended for replacement studies in the oil well logging industry are ^{137}Cs and ^{241}Am .

- ^{137}Cs :
 - Emits 0.662 MeV γ rays and has a half life of 30.17 years
 - Sources are often in the form of Cs-Cl, which is soluble in water
 - Cesium formate is a slightly alkaline salt that is sometimes used in the oil well logging industry as a drilling fluid
 - Poses a health risk, whether internal or external to the human body

- ^{241}Am
 - Decays by α emission and has a half life of 432.2 y
 - Often used in conjunction with ^9Be (Am-Be) to produce neutrons
 - If ^{241}Am is ingested, the α particles emitted can alter the DNA structure of cells
 - If released into the environment, americium can cause harm to plants and animals over a long period of time due to its long half life

Some characteristics of these two radionuclides are summarized in the table below.

Table 1.1: Characteristics of radionuclide sources often used in oil well logging tools.

Radionuclide	Half Life	Decay Particles and Energies (MeV)	US Inventory (Ci)
$^{241}\text{AmBe}$	432.2 y	α : 5.64; γ : 0.060	6,482
^{137}Cs	30.17 y	β : 0.518 max, 1.18 max; γ : 0.662	2,800,000

As part of the Atoms for Peace Program, started in the 1960s, the Atomic Energy Commission (AEC) used to provide radionuclides for commercial, medical, and research applications. The Department of Energy (DOE) replaced the AEC in 1990 and its Isotope Program centralized efforts for radionuclide distribution. Even though the DOE Isotope Program still produces ^{252}Cf , over the years it has stopped producing and supplying ^{137}Cs and ^{241}Am . Currently, REVISS, an Anglo-Russian consortium, is the only supplier of ^{137}Cs and ^{241}Am . As a result, the price of oil well logging sources has aggressively increased and the time to fulfill an order can take a couple of years, calling into question future availability of these isotopes [3].

1.2 Objectives

The objective of this research is to design an oil well logging tool and a laboratory testing facility to collect experimental measurements. The oil well logging tool is to be designed after well-known tool configurations. The tool design must be simple, yet capable of testing different radioactive sources for the purpose of studying the replacement of dangerous radioactive sources in oil well logging. The laboratory space should mimic a borehole environment, must accommodate the designed tool, and must be well characterized. Proper shielding for the laboratory space must also be designed to protect workers and the public, according to regulations set by the Nuclear Regulatory Commission (NRC)[5]. A Monte Carlo model of the experimental set up should be also be developed to reasonably agree with measurements.

1.3 Methods

In order to provide validation for the MCLLS code, Kansas State University has been tasked with with designing and constructing an oil well logging tool and a testing facility. MCNP6[®] was used extensively in the design of both the tool and the testing facility. The facility has been used to take measurements in a highly controlled environment. These experimental measurements have been compared to MCNP6[®] and MCLLS code predictions to effectively benchmark the approach.

A simple oil well logging tool was modeled in MCNP6[®] to study a variety of design parameters and understand the behavior of the tool. The tool carries on-board a D-T neutron generator in place of a radioisotope source, two neutron detectors, and two γ -ray detectors. The initial design incorporated ^3He and NaI(Tl) detectors to measure the neutron and γ -ray signal. A later design replaced one ^3He detector with a BF_3 detector. Shielding studies were conducted to determine the effect of different shielding materials on the tool's performance and its sensitivity to porosity. Distances from the source to the detectors and the spacing between the detectors were varied in MCNP6[®] simulations to optimize the

design while minimizing the size of the tool.

MCNP6[®] also was used to design a test facility where experimental measurements have been taken using the tool designed. A test enclosure was modeled and simulated to achieve an effectively infinite medium that mimics a borehole environment. To mimic a borehole, an aluminum pipe was suspended horizontally in the middle of the enclosure, which is where the tool will be placed to take measurements. Ambient dose rate simulation studies were conducted for the test enclosure and the laboratory space to design the proper shielding configuration. The final configuration conforms to the NRC standards (10 CFR Part 20) to protect operators, technicians, and the public from receiving high doses of radiation while a neutron source is operating[5].

The enclosure was filled with water, sand, and limestone to acquire their signature responses. These experimental measurements were compared to MCNP6[®] simulations to benchmark the tool and testing facility. The data collected using the tool in the test enclosure provides much needed validation for the MCNP6[®] and MCLLS code. An overarching goal of the research collaboration is to show that replacing radioisotopes with machine sources can provide comparable information about the formation through the use of new computer algorithms, such as the MCLLS code.

Chapter 2

Overview of Nuclear Oil Well Logging

Oil well logging comprises a wide array of techniques used to survey or log the properties of rock formations surrounding a borehole, with the particular goal to determine the location of sediments rich in natural gas or oil. A typical well logging tool, sometimes referred to as a sonde, consists of a cylindrical housing containing a set of one or more sensors [6]. Tool lengths can range up to 100 ft. depending on how many sensors are connected in succession [7]. The tool housing is typically less than 4 in. wide to allow it to fit inside boreholes, which can be as narrow as 6 in. in diameter [7].

There are two main methods used to generate well logs: wireline (WL) and logging while drilling (LWD) [8]. Wireline logging is achieved by lowering a sonde, made up of a variety of sensors, into a pre-dilled borehole [9]. Measurements are recorded while the sonde is raised from the bottom of the borehole to the surface. Data from wireline measurements is recorded as a function of depth and can be transferred in real-time to the surface or saved on a memory card and retrieved once the sonde returns to the surface [10].

Logging while drilling was introduced in the 1970s and became widely available in the 1980s. This new technique incorporated the measurement sensors into the drilling tool; therefore, data can be recorded and transmitted to the surface in real-time as the borehole is being drilled [10]. While detailed measurements are stored on a memory card on-board the tool, lower sample rate measurements are sent to the surface using mud pulse telemetry

(MPT) [7]. In MPT, valves are used to control the flow of drilling fluid. Pressure pulses travel up to the surface where information can be retrieved in binary; ones and zeros [7]. Logging while drilling is a slow process that exposes the sensors on-board to extreme shock and vibrations, thus greatly reducing the lifetime of the tool [9]. However, a major advantage is the ability to receive real-time information about the formation, which allows the operators to correct and optimize the borehole trajectory as the tool is drilling.

Although well logging has been around since the 1920s, it was not until the 1940s that radiation-based well logging techniques began to emerge [10]. In the following decades these techniques grew in popularity and became widely accepted by industry. The research being presented deals solely with radiation-based well logging techniques; therefore, only nuclear logging methods will be discussed. The following chapter contains background information on well logging and an overview of common radiation-based logging techniques.

2.1 Gamma-Ray Logging

A typical nuclear logging tool consists of an optional radioactive source and one or more radiation detectors. Nuclear well logging tools without a source, sometimes referred to as passive or natural γ -ray logging, measure the natural background radiation of the formation [1]. However, a gamma-ray and/or neutron source can be used on-board the tool to actively interrogate the surrounding medium. In active interrogation the source particles interact with the sediment, generating scattered and secondary radiation which can be detected and measured to infer characteristics about the surrounding rock.

Gamma-ray logging was the earliest form of radiation-based well logging. Gamma-ray interactions with matter provide information that can be used to determine the density and composition of rock formations. Although passive γ -ray logging does not use a source, typical γ -ray sources used in active interrogation techniques include cobalt-60 and cesium-137 [10]. Gamma-ray logging is often used in conjunction with other logging techniques to determine possible oil-rich formations.

2.1.1 Passive Measurement

The simplest of all radiation-based logging tools consists of a sonde with one or more radiation detectors [11]. Passive or natural γ -ray logging is accomplished by measuring the natural background radiation of a well as a function of depth. Uranium, thorium, and potassium are three radionuclides commonly found in the earth’s crust [1]. Each of these elements have unique decay chains that produce secondary radiation; i.e. α particles, β particles, γ -rays, and/or radioactive daughter isotopes. For example, the two most abundant uranium isotopes are ^{235}U and ^{238}U , which decay by α -emission to a radioactive thorium isotope—which undergoes its own decay chain [10].

Table 2.1: Some naturally occurring background γ -rays [1]

Element	γ -ray energy (MeV)
^{238}U	1.76
^{232}Th	2.62
^{40}K	1.46

In passive γ -ray logging, there are two main measurement methods. The first one involves recording the background radiation count rate as a function of well-depth. Increases in count rate suggest the location of rock formations with higher levels of radioactivity, such as shale [9]. In general, salt (NaCl), evaporites, and coals have low radiation levels compared to shale and potash (KCl) [10]. The second method involves collecting full γ -ray spectra, which can be used to determine not only the presence of specific isotopes but also their quantity using inverse analysis techniques. However, this method often yields poor counting statistics due to low background radiation levels, short data collection time, and detector efficiency limits [9]. Therefore, count rate measurements are most often preferred for passive logging methods.

2.1.2 Active Interrogation

In active γ -ray logging, a γ -ray source on-board a sonde interacts with the surrounding rock formation and the scattered radiation is measured by one or more detectors. Gamma-gamma density measurements usually involve a cesium-137 source which produces 662 keV γ -rays [10]. The γ -rays interact with the rock formation surrounding the borehole and a set of detectors are able to measure the scattered radiation from the source at two different locations along the axis of the tool. The γ -ray signal can be used to infer knowledge about the electron density as well as the photoelectric cross section of the surrounding material [9]. Using these two sets of data, one can estimate the density of the formation along the depth of the well.

Capture and prompt γ -ray spectroscopy utilizes a fast neutron source to generate high-energy inelastic scatter and neutron capture γ -rays in the formation [9]. The γ -ray signal is collected using high quality detectors with spectroscopic capabilities. Measured spectra can then be used to calculate the relative and absolute concentrations of elements present in the formation. Additional information can be obtained by utilizing a pulsed neutron source, such as a D-T or a D-D generator. For example, the measurement system can synchronize the neutron pulses and record time stamps with every detection event. Using the time stamps, γ -ray spectra can be derived from a measurement for different time windows. By measuring γ -rays between pulses, the inelastic-scatter and capture γ -ray signals can be isolated and used to improve elemental analysis accuracy [10].

2.2 Neutron Porosity Logging

Porosity generally refers to the ratio of the volume of the pores to the total or bulk volume of a material in a formation [10]. As such, it is unitless, although this fraction often is multiplied by 100 and expressed in porosity units (pu), whose values range from 0 to 100. Porosity is highly dependent on the grain size of the material and each pore is assumed to be filled with water, air, or hydrocarbons. Generally, in neutron porosity logging, a neutron

source interacts with the rock formation where the neutrons are absorbed and scattered by the medium. One or more neutron detectors in the logging tool, spaced at different distances from the source, record the count rate observed at each location [12].

In neutron porosity logging, water-filled porosity refers to the fraction of fresh water, by volume, in the rock formation [10] and air-filled porosity refers to the volume fraction of free air in the medium. When it is known that only water is present, as in some of the cases considered here, neutron porosity logging attempts to determine the amount of hydrogen in the medium. Because hydrogen has a high neutron scattering and absorption cross section, higher concentrations of hydrogen will scatter and absorb more neutrons in a shorter distance. Based on neutron transport theory, Hearst [10] showed that the average distance the neutrons travel in the formation, or average neutron migration length, is proportional to the ratio of the count rates at two distances from the source, see section 4.3.2 for more details. A shorter average migration length is indicative of high hydrogen content in the medium, and therefore a higher likelihood of oil, water, or natural gas being present.

2.3 Carbon/Oxygen Logging

Similar to capture and prompt γ -ray spectroscopy logging, carbon/oxygen logging uses a pulsed neutron source to generate inelastic-scatter and capture γ -rays in the formation [9; 13; 14]. Detectors with spectroscopic capabilities are used to measure the γ -ray spectra generated during two time-windows, one within a few microseconds of the pulse and another while the source is turned off [10]. The spectra collected during each time-window correspond to the γ -rays generated via inelastic scattering and neutron capture, respectively. The capture spectrum is generally subtracted from the inelastic-scattering spectrum to determine the amount of carbon, oxygen, calcium, and silicon present in the formation [10]. Then the ratio of carbon to oxygen, and calcium to silicon, is calculated to determine whether the presence of carbon is due to mineral formations, such as calcium carbonate, or hydrocarbons.

Table 2.2: Inelastic scatter γ -rays commonly used in carbon/oxygen logging

Element	γ -ray energy (MeV)
^{12}C	4.44
^{16}O	6.13
^{28}Si	1.78
^{40}Ca	3.74

Table 2.2 shows the energy of inelastic-scatter γ -rays for elements which are of specific interest to the carbon/oxygen logging technique. However, the energy measured is often lower than the energy of emission because the capture and inelastic-scatter γ -rays must travel back through the medium before being registered in the detectors. For this reason, it is common practice to analyze spectra using wide energy windows around the values specified in Table 2.2 instead of analyzing detailed energy peaks [10].

2.4 Radioactive Sources Used in Nuclear Well Logging

In active interrogation methods, the logging tool often houses a radioisotope as a source that emits radiation which interacts with the surrounding medium. Some of the radiation will scatter and be absorbed within the medium and some will scatter until it makes its way back to a detector on-board the tool. Common sources used in these techniques include americium-beryllium ($^{241}\text{AmBe}$), ^{252}Cf , and ^{137}Cs .

AmBe produces a spectrum of neutrons with a maximum energy of 11 MeV and average energy of 4 MeV. The source also produces a 4.44 MeV γ -ray coincident with a neutron emission 56% of the time [15–17]. ^{137}Cs emits 662 keV gamma-rays. $^{241}\text{AmBe}$, ^{252}Cf , and ^{137}Cs pose serious health, safety, and national security risks; therefore current research focuses on finding alternatives to these radioisotopes.

New sources being studied for use in oil well logging include accelerator based neutron sources. One such source is a D-T-generator, which produces 14.1 MeV neutrons from the fusion of deuterium (stable) and tritium (radioactive). D-T generators are particle accelerators that contain deuterium gas and a tritium target in a fully sealed containment.

The D-T generator heats up the deuterium gas and creates a plasma that is then focused at a tritium target on a metal disk. The fusion generates monoenergetic 14.1 MeV neutrons emitted isotropically. A D-T generator can easily produce more than 10^8 neutrons per second. The generator is operated from a computer interface that allows the voltage and the current of the accelerator to be adjusted. By changing these values, one is able to adjust the neutron output rate of the generator.

Another such source is a D-D generator, where deuterium atoms are fused together to generate a spectrum of neutrons with an average energy of 2.5 MeV. The neutron spectrum from a D-D generator is much closer to that of an AmBe source. However, DD reactions are less efficient and the generator output is typically two orders of magnitude lower than that of a similarly sized D-T generator. D-D generators are incredibly safe because deuterium is a neutral gas (non-radioactive) that only produces neutrons when the machine is turned on.

These new accelerator based neutron sources are inherently safer than radioactive sources because the emission of radiation can be turned on and off and negligible radioactive material can be extracted from them. Other advantages of using machine sources include the facts that the neutron intensity can be adjusted and fast electronics can take advantage of the pulsed nature of neutron production.

2.5 Previous Efforts in Oil Well Logging Source Replacement

In this section, I would like to point the reader to published articles that go over recent developments in the oil well logging industry. In order to fully understand the context of our current research efforts, it is important to have an idea of the previous efforts of other researchers. Replacement of dangerous radionuclides in the oil well logging industry has been a hot topic over the past decade. Many researchers and scientists have published work studying the current state of oil well logging, needs in the industry, and the future of the technology.

A. Nikitin (2010) [9] wrote an overview of current oil well logging techniques, as well as current and future challenges of the industry. He laid out the specific hardware specifications needed to operate in the hostile environment of a borehole and described new technologies that may upgrade current hardware. He concludes that the challenges faced by the oil well logging industry can be improved upon by introducing new gamma-ray and neutron detection technologies. While Nikitin (2010) mainly focuses on the need for better detection technology, recent research efforts indicate that by replacing the current radioactive sources with a neutron generator and utilizing better Monte Carlo-based techniques, the challenges of older detection technology can be overcome.

Also in 2010, C.R. Peeples [4] published an article on replacing AmBe sources in oil well logging. In the article, the author explored possible alternatives to AmBe using Monte Carlo simulations. Peeples used neutron diffusion theory to calculate porosity sensitivity of an oil well logging tool using AmBe and DT generator sources in simulations. He concluded that a D-T neutron generator had potential to replace AmBe. The article ultimately recommended further study into the replacement of AmBe with D-T and DD neutron generators.

Following previous research published by Peeples, A.X. Chen (2012) [18] studies the replacement of AmBe with both D-T and D-D neutron generators using Monte Carlo simulations. The article described the MCNP model used to simulate a simple oil well logging tool. The research focused on determining the sensitivity to porosity of all three sources (AmBe, D-T, and D-D) using MCNP[®]. In his conclusion he discussed the viability of replacing AmBe with machine neutron sources. He states that D-D neutron sources show greater sensitivity to porosity, however more research is needed to develop smaller D-D generators with higher neutron output for it to be a viable replacement to AmBe.

In 2013, C.M. Frankle [19] used MCNP6[®] to compare oil well logging tool responses using AmBe, D-D, D-T, filtered D-T, and T-T (tritium-tritium) sources. He used various techniques to compute porosity and carbon/oxygen ratio responses using unconventional machine sources to compare to typical well logging tool responses from an AmBe source. He determined that TT and D-T sources were possible replacements for AmBe. He also suggested that modification of the D-T spectrum for oil well logging purposes is not viable.

It is important to note that previous research and conclusions have been produced only through simulations. However, the CNEC collaboration is going a step further to actually build an oil well logging benchmarking tool and a test facility, and is collecting data to make better recommendations on the replacement of dangerous radioisotopes in oil well logging. The strongest feature of this research collaboration is the combination of simulation, measurement, and new algorithms such as the MCLLS code.

Chapter 3

Modeling and Simulation Methods

Monte Carlo modeling is an incredibly powerful set of techniques widely used in science and engineering. In nuclear engineering, it is often used to simulate radiation particle transport through matter. With computer capabilities exponentially increasing over the last few decades, Monte Carlo methods have become a very accessible and effective tool for modeling applications.

3.1 Monte Carlo Methods

Monte Carlo methods have a long history throughout various fields in science, engineering, statistics, business, and even politics. The wide array of techniques that fall under the umbrella of Monte Carlo methods serve a variety of purposes in our modern world. The roots of Monte Carlo methods lie in the laws of statistics and probabilities, giving this type of mathematics an incredibly flexible set of tools to tackle all kinds of problems, such as simulating radiation particle transport, predicting political polls, and assessing risk for insurance companies.

3.1.1 Origins and History

Although probability is often associated with gambling, probability studies can be used to simulate radiation transport and calculate approximate detector response functions. Monte Carlo methods can be described as a group of numerical methods that can be used to solve complex mathematical problems. Monte Carlo is incredibly flexible and can also be used as a form of quadrature to estimate definite integrals. In this context, Monte Carlo can be defined as a statistical sampling method that uses the sample mean to estimate the population mean of a random variable. In this case, a random variable refers to any measured quantity that has an inherent distribution or uncertainty about an average value.

Monte Carlo is based upon the law of large numbers and is often associated with Buffon's needle-dropping problem [20]. In 1689 Jacob Bernoulli produced his law of large numbers, which showed that probabilities are in fact precise quantities and not just abstract concepts [21]. Then, in the 1700s, Comte de Buffon experimented with Bernoulli's law of large numbers in his needle dropping experiments, which later became a popular pastime among intellectuals [22]. The Buffon needle dropping practice is an early form of analog Monte Carlo, where needles of length L are dropped on a plane of parallel lines a distance D apart. For cases where $L \leq D$, Comte de Buffon calculated the probability (P_{cut}) that a needle would land intersecting one of the lines as twice the needle length (L) divided by π times the spacing between the parallel lines (D), as seen in Equation 3.1 [20].

$$P_{cut} = \frac{2L}{\pi D} \quad (3.1)$$

$$\pi = \frac{2L}{P_{cut} D} \quad (3.2)$$

Nearly a decade after Comte de Buffon published his findings, Pierre-Simone de Laplace showed that the value of π could be calculated using the ratio of the number of needles that landed intersecting a line to the total number of needles dropped [20]. This relationship is easy to see from Equation 3.2, where P_{cut} becomes a random variable that can be sampled a number of times by dropping needles and counting the number of successes over the number of trials. By increasing the number of times P_{cut} is sampled, its uncertainty and therefore the uncertainty of π decreases.

3.1.2 Modern Capabilities

The Buffon needle problem is an illustration of the use of random sampling to estimate a desired quantity, which is at the heart of Monte Carlo methods. In a similar fashion, random sampling can be used to simulate and transport radiation particles based on their probability of interaction and on other processes. In order to obtain a result with reasonable confidence bounds, many Monte Carlo calculations have to be made for any one problem; sometimes on the order of millions or billions of calculations. As computer capabilities have increased, Monte Carlo methods have become increasingly common in many fields [23]. In the context of this research, Monte Carlo techniques are the building blocks of the code package used to conduct the radiation simulation studies presented in the following chapters.

3.1.3 Deterministic vs. Monte Carlo Methods

The strength of Monte Carlo methods lies in its ability to solve very complex, multidimensional problems through the use of repeated random sampling. Random numbers are generated to sample pre-determined probability functions that represent all types of behaviors in a system. Sampling from a probability distribution function yields a random variable or sample. By repeating the sampling process and calculating the sample mean we can infer the behavior of the population mean. This technique can be used to solve complex integrals and serves as a form of quadrature, capable of solving multi-variable equations that could not be solved deterministically.

Mathematically, Monte Carlo techniques are no more complicated than algebraic equations. A complex multi-variable integral can be broken down into the probability density functions of each variable and easily computed by sampling said probabilities using random variables. While one alone cannot usually calculate these probabilities in significant enough quantities to obtain an average value with a low statistical error by hand, current computer capabilities allow for thousands of these calculations per second. It is the state of our computational power that allows Monte Carlo techniques to be so useful.

3.2 MCNP[®]

The Monte Carlo N-Particle transport code (MCNP[®]) was developed at Los Alamos National Laboratory (LANL). The software package has been supported and improved by the laboratory since the 1950s [24]. The code package originally utilized Monte Carlo methods to analyze the radiation transport of neutral particles, such as photons and neutrons. At the same time at LANL, almost in parallel, a separate Monte Carlo code package was developed to simulate charged particles, such as ions and nucleons, called MCNPX[®] [24]. After the release of MCNP5[®], the two software packages (MCNP5[®] and MCNPX[®]) were merged and later released as MCNP6[®]. In its current form, MCNP6.1[®] has been expanded to include over 34 different types of particles and more than 2,000 heavy ions at nearly all energies [24].

The use of MCNP6.1[®] to simulate neutron and γ -ray sources in a laboratory facility to determine various detector responses and ambient dose rates for an oil well logging benchmarking tool is described in the following chapters. Only the MCNP[®] features relevant to this research will be discussed.

3.2.1 MCNP[®] Structure

MCNP[®] takes in a user-defined text file to define a three-dimensional geometry, one or more radioactive sources with their corresponding locations, and the type of tally or result desired. The code transports and follows each source particle as it travels through and interacts with materials within the problem geometry. As each particle history is tracked, a thorough record of its location, energy, and direction of travel is kept. Various types of tallies are used to estimate the radiation field at user specified locations. Special tally treatment cards can be used to convert certain tallies to approximate detector response functions or ambient dose rates. Once a simulation is finished, the input code, statistical checks, flags, warnings, and tally results are written to an output text file.

3.2.2 Geometry

MCNP uses the right-handed Cartesian coordinate system to define a space; the origin of the coordinate system is specified by the user. Surfaces within the space are defined by equations in the x , y , z coordinate system. MCNP provides predetermined equations for various commonly used planes and surfaces that can be called upon by the user using simple variable names and parameters. One or more planes in the 3D space form a surface. MCNP simplifies this step by providing combinations of planes that make up commonly used surfaces; i.e. a circular plane and two intersecting right-angle planes make up a cylindrical surface.

Surfaces divide space into positive and negative regions, where a point's coordinates may be positive or negative in relation to the surface plane depending on its orientation. Surfaces are connected by intersection, union and/or complement operators to form cells. That is to say, a cell is defined by the points located in a 3D region bounded by intersecting surfaces.

Materials are assigned to a cell by providing the density and the atomic composition of the material, either by weight fraction or atomic fraction. The Nuclide Identification Number (ZAID) is used to identify different elements and isotopes and is used to call upon the proper material cross sections when an interaction occurs within the material.

3.2.3 Physics

Monte Carlo methods are at the core of the MCNP6[®] code. These techniques are used to simulate radiation transport using random sampling and ray-physics algorithms. In MCNP6[®], the problem geometry, source definition, and tally specifications are set by the user. Then, source particles are generated and the code transports each source particle through through the materials in 3D space, and creates appropriate tallies, such as the average number of particles that pass through a surface or are absorbed in a particular cell.

Random Numbers

Probabilistic quantities, such as the interaction rates of radiation particles, have inherent distributions based on the material of interaction, the energy of the particle, and the type of interaction. These distributions are called probability distribution functions (PDFs). In Monte Carlo, random numbers are used to sample from such PDFs the outcomes of particle interactions.

For example, as a particle travels through a cell, a random number is used to determine whether the particle will interact within the cell or pass right through. If the particle interacts, a second random number is used to determine whether the particle is scattered or absorbed. If the particle is scattered, a new random number is used to determine the length of the scattered particle's path within the same cell or whether it crosses the surface or boundary into another cell.

Nuclear Data Files (ENDF)

A core component in the simulation of radioactive particles is the set of Evaluated Nuclear Data Files (ENDF). ENDF refers to a file format in which the empirical probabilities of nuclear reactions are compiled. The ENDF files serve as the standard from which nuclear interaction probabilities are sampled in Monte Carlo simulations. These nuclear interaction probability standards are imperative in simulating the transport of radiation particles through matter.

There are several nuclear data organizations throughout the world, the most prominent being the Network of Nuclear Reaction Data Centers (NRDC) which operates under the International Atomic Energy Agency (IAEA). In the United States and Canada, the major group is the Cross Section Evaluation Working Group (CSEWG), which is a collaboration among universities, industry, and national laboratories. The CSEWG produces the U.S. Evaluated Nuclear Data File ENDF/B, which is used in MCNP to run simulations.

Nuclear data files contain the probabilities that any one particle will interact in various ways with any nucleus. These interactions include particle capture, scatter, inelastic collision, absorption, fission, and many others. The ENDF files provide energy-dependent cross-sections for the previously listed interactions. During a radiation transport simulation, the ENDF file is used as a library from which cross-section probabilities are sampled to determine the interaction a particle may undergo when it interacts with an atom.

Radiation Transport

In a typical radiation transport simulation, a particle is initiated using the parameters predetermined by the user. Its angular distribution is sampled to determine in which direction the particle moves. The particle's interaction coefficient is then sampled to determine how far it travels along the trajectory direction. Ray physics is used to transport the particle to its new location. As the particle travels through a medium, a random number generator is implemented to determine what interaction, if any, the particle undergoes. Each time the particle moves, MCNP uses the ENDF nuclear data libraries to look up the particle's interaction cross sections and uses the random number generator to choose an interaction to determine if the particle history is terminated (absorbed in the medium) or it moves again. Hundreds of thousands, even millions of particles are simulated in this way to obtain the average behavior of the system.

3.2.4 Tallies Used

As mentioned before, in MCNP6[®], the user can define a region in space, such that, if a particle enters or interacts in that region, its properties are recorded or tallied. As in other Monte Carlo methods, the final score of the tally is the average of all simulated particles. There are various different types of scoring mechanisms, some record average particle flux on a surface or a cell (F4 tally), some record average flux at a point (F5 tally), some record energy deposition in a region (F6 tally), and some record the pulse height distribution in a cell (F8 tally). The MCNP code provides different tally types to accommodate many types of scoring that may be desired by the user. The main tallies used within this research are briefly described below.

Flux/Fluence Tallies

The F4 tally corresponds to fluence averaged over a cell and is expressed in units of particles/cm². The F4 tally is a track length estimator in a volumetric region. To estimate the average fluence of a particle in a cell, the path length (s_i) of the i^{th} particle traveling through the cell is summed over all histories and divided by the number of particles simulated (N) and the volume of the cell (V). For non-analog, or biased simulations, the weight W_i of the particle is multiplied times it's path length (s_i) inside the cell to keep the simulation fair (see eq. 3.3). However, this is a simplistic explanation of the tally that does not account for scattering within the tally volume, a more detailed account can be found in [20].

$$\bar{\Phi}_V = \frac{1}{NV} \sum_{i=1}^N W_i s_i \quad (3.3)$$

In the context of this research, F4 neutron tallies were used to determine the average energy-dependent neutron flux through the NaI(Tl) detectors. The F4 neutron tallies in the NaI(Tl) crystals were used in conjunction with energy-dependent neutron cross-section files to calculate the reaction rate of the activation of each crystal through neutron capture. More details on this technique are found in section 6.4.

To estimate the flux at a point detector, a different method of scoring must be used. The F5 tally estimates particle flux at a point or ring detector in units of particles $\text{cm}^{-2} \text{s}^{-1}$. Because the tally region is defined as a point in space instead of a cell, the F5 tally uses a next-event estimator to calculate the average flux.

The next-event estimator calculates the probability that a particle will reach the point detector without interacting along the path. This technique uses deterministic calculations to speed up the Monte Carlo simulation. Because a point detector has no volume or a volume that approaches zero, scoring particles that reach such a small region renders the previous method ineffective. Therefore, as a particle is transported through the problem geometry, the probability that it will reach the point detector without a collision is estimated. Each time a particle interacts, the next-event generator estimates the tally contribution from that particle; since a particle may undergo many collisions and interactions before it is terminated, a single particle can make many contributions to the final tally.

In this project, the F5 tally was used to estimate the neutron and photon flux at various locations inside the laboratory space with the DT generator on. The simulation was conducted with various shielding configurations. The F5 tally results were converted to dose rates to design the proper shielding and protect both workers and the public from excessive radiation exposure.

Energy Deposition Tally

The energy deposition averaged over a cell tally, F6, is in units of MeV/g. This type of tally is a track length flux estimator (F4 tally) multiplied by an energy-dependent heating function, $H(E)$. For an F6 neutron tally, the heating function is given by equation 3.4, i.e. the neutron incident energy (E), minus a summation of the probability of neutron interaction $p(i)$ at the incident energy multiplied by the average exiting neutron energy ($\bar{E}_{i,out}$) minus the Q-value (Q_i) of the reaction plus the average exiting gamma energy for that reaction ($\bar{E}_{i,\gamma}$).

$$H(E) = E - \sum_i p_i(E) [\bar{E}_{i,out}(E) - Q_i + \bar{E}_{i,\gamma}(E)] \quad (3.4)$$

$$H(E) = E - \sum_{i=1}^3 p_i(E) [\bar{E}_{i,out}(E)] \quad (3.5)$$

For gamma rays, the heating function is the incident energy (E), minus the sum of the probabilities of each reaction (i) times the average exiting gamma ray energy for each reaction (see eq. 3.5). The three types of reactions used for $i = 1, 2,$ and 3 are: incoherent (Compton) scattering, pair production, and photoelectric absorption.

Pulse-Height Tally

The pulse-height (F8) tally generates the energy distribution of pulses created in a detector. This type of tally is akin to a physical detector and can be used in conjunction with the Gaussian Energy Broadening special tally treatment card to simulate real-life detector responses. In an F8 tally, the result is a histogram, in which each energy bin corresponds to the total energy deposited in a detector by each physical particle. Most other tallies record the energy of the particle being scored.

The F8 tally is incredibly useful when modeling a real-world experiment. In this research, the F8 tally was used to model the detector responses from NaI(Tl) detectors in an oil well logging benchmarking tool using both an AmBe and a DT neutron generator source. These detector response simulations were used to validate the MCNP code results with experimental results.

3.2.5 Special Tally Treatment Cards

MCNP[®] simulates detector responses by applying special treatments to specific tally cards. The most common special tally treatment is the Gaussian Energy Broadening (GEB) card, which applies a statistical Gaussian broadening to events recorded in the tally to better match experimental results. The Pulse Height Light Output (PHL) special tally treatment card is often used to calculate ambient dose rate or detector responses from scintillators. These two special tally treatment cards are more carefully described below.

Gaussian Energy Broadening

For a radiation particle of a particular energy, a real-life radiation detector records its energy as a Poisson distribution, commonly simplified as a Gaussian function. This spread is due to noise in the detector, the detector's inherent imperfect collection efficiency, and variation in the amount of charge carriers for any one event [25]. Therefore, to simulate the pulse height spectrum from a detector, an F8 tally must be modified by a virtual Gaussian spreading function [24].

When an event is recorded in a tally, the energy of the particle is broadened by sampling from a Gaussian function, see equation 3.6; where E is the broadened energy, E_0 is the unbroadened energy of the tally, C is a normalization constant, and A is the Gaussian width [24]. We can obtain the Gaussian width, A , using the full width half maximum (FWHM) of a peak using equation 3.7.

$$f(E) = Ce^{-\left(\frac{E-E_0}{A}\right)^2} \quad (3.6)$$

$$A = \frac{FWHM}{2\sqrt{\ln 2}} \quad (3.7)$$

$$FWHM = a + b\sqrt{E + cE^2} \quad (3.8)$$

In MCNP[®], the detector-dependent parameters for a GEB function, a , b , and c , can be obtained by fitting equation 3.8 to experimental spectra from a specific detector [26]. An example of this procedure for a stilbene scintillation detector is given by Kim in 2015 [27]. For a 3 in. by 3 in. cylindrical NaI(Tl) crystal (the type of detector used for this research) the GEB parameters are: $a = -0.00789$, $b = 0.06769$, and $c = 0.21159$ [28; 29]. Although GEB is a great approximation for most detectors, it is not a perfect solution for non-linear crystals.

Pulse-Height with Anticoincidence

In order to model ^3He detectors, the pulse-height with anticoincidence (PHL) special tally treatment was used. The PHL card allows an F8 pulse-height tally to be based on energy or light deposition in multiple regions. Therefore, to model a ^3He tube, the energy deposition from protons and tritons are tallied inside the detector's active region, separately. Then, an F8 (pulse-height) tally is used with the PHL special tally treatment to convert the energy deposition from protons and tritons (F6 tallies) into a pulse-height spectrum.

Other

Various other tally treatment cards can be very useful to obtain output tally results in a desired way. The energy (E) special tally treatment breaks up a tally into energy bins from user-defined parameters, such as: minimum energy, maximum energy, and desired number of bins. This card is especially useful when dividing pulse height (F8) histograms into specific energy bins. The E card is also useful when the user wants to obtain energy-dependent flux.

The FM card can be used to multiply a tally by a scalar quantity such as source strength or time. The dose energy (DE) or dose function (DF) special tally treatment cards are useful when converting a tally to a dose rate. The E, FM, DE, and DF cards were used throughout this research to obtain simulation tally results in the desired format for pulse-height and dose comparisons with real life measurements.

3.2.6 Output

The MCNP code interprets the user-defined input file to determine the problem geometry, source energy and location, and physics parameters to begin a simulation. Once the simulation begins, MCNP initiates an output file, which includes a copy of the input file, any flags or warnings the code encounters, and initial statistics about the simulation. When all particle histories finish running, MCNP runs statistical checks for each tally. Then, MCNP writes the final tally results with their corresponding relative errors to the output file. The user defines the way that each tally result is presented in the output file through the use of

special tally treatment cards. For example, the user can define the energy range and number of energy bins printed for a specific tally in the output file. The statistical checks for each tally give the user a level of confidence in the result depending on how many checks the tally has passed.

3.2.7 Error Estimation

Each MCNP tally output includes the estimated relative error for each bin and/or the total tally. The estimated relative error is calculated by dividing standard deviation of the mean divided by the estimated mean of all contributions for each bin or total tally. The estimated relative error provides a confidence interval about the estimated quantity, whether it is an energy bin or a total tally score. An estimated relative error less than 5% is a good indication that the tally is reliable; a relative error between 5% and 10% indicates that the true result is within an order of magnitude, but a relative error larger than 10% is not too reliable and the simulation should be run with a larger number of particle histories.

3.2.8 Variance Reduction Techniques

There are various techniques in MCNP to reduce the variance in the tallies and improve computation time. The beauty of Monte Carlo is that any simulation can be biased to improve the outcome. However, variance reduction techniques must be used with great care to not bias the simulation unfairly, thus generating erroneous results. For this reason, each particle has a weight related to it which can be modified to account for any bias in a simulation.

For any simulation, the number of histories or particles simulated is a major contributor in the variance or relative error of the results. Typically, the more particle histories are simulated, the better the average behavior of the system can be determined, and the lower the variance. Some variance reduction techniques are aimed at speeding up the simulation in order to be able to run more particle histories in the same amount of time. Other techniques artificially bias the simulation to give more weight or importance to particles that contribute to the desired tallies. A few of these common techniques are described below.

Energy Cutoffs

In an MCNP simulation, source particles are initiated and transported through a system until the particle is absorbed or the particle history is terminated. As a particle moves through a medium it loses energy. A user can specify an energy cutoff for any type of particle, such that once the energy of a particle of that type is below the cutoff or threshold, the particle history is terminated and a new history is started. In many cases, particles below a certain energy can be ignored due to negligible contributions to the overall simulation result. By terminating these particle histories before the particles are absorbed, many calculations can be eliminated, thus speeding up the simulation.

Cell Importances

For each cell in an MCNP geometry, an importance value can be designated for each particle type. A default importance value of 1 is assigned to all particles being simulated in all cells. However, sometimes there are regions in a simulation that one can safely ignore and set those cell importances to zero. The particle importance is taken into account as a weighing factor in the calculation of the average particle behavior for a tally.

For example, typically, a large surface surrounding the system being studied is modeled to create the problem boundary. Particles that move past the problem boundary will no longer affect the system, therefore importances in the region outside the problem boundary can be set to zero. In this case, once a particle moves past the problem boundary it is terminated and the simulation moves onto the next particle. This system of particle importances in relation to cells is used in other variance reduction techniques and can be very useful in simplifying and speeding up a simulation.

Weight Windows and Weight Windows Generator

The weight windows and weight window generator were added to the MCNP code in the early 1980's [30]. Although Booth and Hendricks wrote the original paper on weight window generators, many researchers have significantly improved and enhanced its capability over the years. As a graduate student, Booth looked at how particle random walks behaved using MCNP's PTRAC option. PTRAC is a keyword in MCNP that lets the program know that the user wants a detailed output of every particle's event history.

Booth noticed that some particles had very large weight and others had very small weight. He concluded that computationally it was not very efficient to follow particles at extreme weights, either too large or too small. For particles with very small weights, a roulette algorithm was implemented to either kill the particle or change its weight to an acceptable range. For particles with large weights, the particle was split into the smallest integer that would allow the resulting particles to have weights within an acceptable range. The range of acceptable weights is what Booth called the "weight window" [30].

The weight windows generator is a tool provided by MCNP that allows the user to specify a tally region to be optimized for variance reduction. Weight windows works by running a short simulation after which MCNP suggests weights to be applied to each cell in a geometry. These weights bias the simulation to give more importance to cells that contribute more to the desired tally. That is to say, particles that travel in the direction of the tally region give a greater contribution to the final tally, thus reducing the tally variance. The weight windows tool is used iteratively to generate the optimum cell importances for a desired tally.

Geometry Splitting and Russian Roulette

Russian roulette and geometry splitting work in conjunction to reduce tally variance by killing particles that are not likely to contribute to a desired tally, and multiplying particles that will. This technique was useful in shielding calculations, where the user manually divided the problem geometry into smaller cells and assigned cell importance parameters using physical intuition. The user would then run several simulations to corroborate or adjust cell importances to enhance the simulation.

As particles travel through a large absorbing medium, many of them will be absorbed and not contribute to the tally total. This slows down the simulation and the small pool of particles that reach the tally region contribute to a higher variance. To improve such simulation, the user can divide the geometry into smaller cells, called geometry splitting. Then, each region can be set to multiply or kill particle histories depending on the location of the desired tally. This method is called Russian Roulette and splitting.

Russian roulette can be used to kill the particles traveling away from the tally region and splitting to multiply those traveling towards the tally. Such biased simulation is kept fair by decreasing the weight of particles that were multiplied. This increases the population of particles near the tally region and decreases the population of particles not likely to contribute to the tally.

Chapter 4

Design of an Oil Well Logging Benchmarking Tool

The work contained in this chapter describes simulation studies conducted to design an oil well logging benchmarking tool. The purpose of the tool is to generate experimental measurements in a highly controlled environment, that can be used to benchmark a Monte Carlo-Library Least Squares (MCLLS) code being developed at North Carolina University. MCLLS will utilize Monte Carlo methods to generate libraries of characteristic signals for common rock formations at various levels of porosity. The generated libraries will be compared against real-time measurements using least-squares analysis until a positive match is found.

The tool was designed for the specific purpose of benchmarking the Monte Carlo-Library Least Squares code previously mentioned. The design was optimized for ease of modeling as well as a high level of flexibility; each component can be easily replaced with another for direct comparison. The aim was to make the tool very simple by modeling it after well-known tool configurations used in a variety of oil well logging techniques [31].

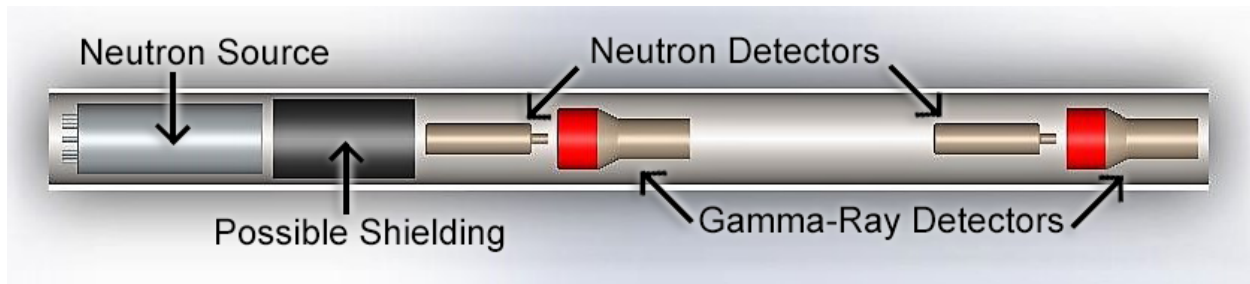


Figure 4.1: Oil well logging benchmarking tool geometry

4.1 Tool Configuration

The chosen tool configuration incorporates a machine neutron source and two sets of γ -ray and neutron detectors as shown in Fig. 4.1. The detectors are placed at various distances from the source; they will be referred to as near and far detectors based on their location in reference to the source. ^3He and $\text{NaI}(\text{Tl})$ detectors were chosen to measure the neutron flux and γ -ray spectrum, respectively. The initial tool design can be used to obtain data used in many γ -ray and neutron logging techniques; such as γ -ray density, capture and elastic-scatter γ -ray spectroscopy, compensated porosity, and carbon/oxygen logging.

The following studies were conducted to learn about typical detector responses in oil well logging applications and to investigate the effects of several design parameters on the tool response. Different types of shielding were simulated between the source and detectors to determine their effect on tool sensitivity. The spacing between the source and near detector and the spacing between the two sets of detectors were varied and simulated to observe their effects.

4.2 Tool Components

Before beginning to model the tool it was important to carefully consider and choose each component. The first step was to determine what type of source the tool would use to replace AmBe . Two major sources were considered, a Deuterium-Tritium (D-T) generator and a

Deuterium-Deuterium (D-D) generator. Then, two sets of detectors were chosen, one set was used measure the neutron response and another to measure the γ -ray response generated by the neutron source in the surrounding sediment. The detectors chosen are typically used in industry and can be easily simulated using a radiation transport code such as MCNP[®].

4.2.1 Neutron Source

In active-interrogation well logging techniques, radiation from one or more radioactive sources interacts with the surrounding medium while sensors measure the resulting spectra to determine the density, porosity, carbon to oxygen ratio, and/or composition of the medium. AmBe is commonly used in oil well logging applications due to its high neutron yield, long half-life, compact size, and robustness against high temperatures and strong vibrations. As Americium-241 decays, it emits alpha particles which interact with Beryllium-9 and produce neutrons with a broad energy range (Eq. 4.1). The resulting AmBe neutron spectrum has an average neutron energy of ~ 4 MeV and a maximum energy of ~ 10 MeV, as shown in Fig. 4.2.

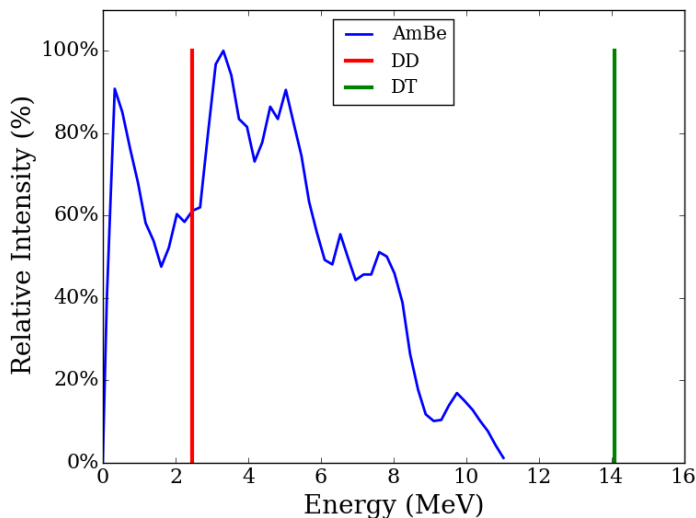
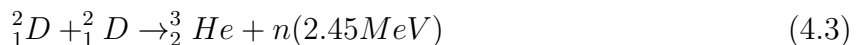
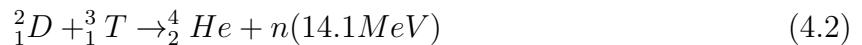


Figure 4.2: AmBe, D-D, and D-T neutron energy spectra

This research attempts to demonstrate the viability of using machine neutron sources to replace dangerous radioisotope sources used in the oil well logging industry. These radioisotope sources can often be found in unsecured and remote locations, which creates a risk of being improperly disposed of, dumped in the environment, or being stolen and used in dirty bombs. The two main candidates being studied to replace AmBe are D-T and D-D neutron generators. A D-T generator produces 14.1 MeV neutrons by accelerating deuterium into a tritium target, see Eq. 4.2. Similarly, a D-D generator produces 2.45 MeV neutrons by fusing deuterium atoms, see Eq. 4.3. D-T generators have a higher neutron yield compared to D-D generators. Typical D-T generators produce approximately $5-10 \times 10^7$ n/s versus $1-2 \times 10^6$ n/s for D-D generators [4]. Although D-D machine sources generate neutrons with energies comparable to those from an AmBe source, their output flux is typically too low to produce responses with good counting statistics.



A D-T neutron generator was chosen as the source for the tool because it produces a high flux of high-energy neutrons. One advantage of using a D-T generator is that high-energy neutrons are able to travel farther into the surrounding medium and provide a larger interrogation volume around the source. As high-energy neutrons slow down they generate inelastic-scatter gamma rays, which can provide extra information about the elements in the surrounding sediment. The neutron yield of a D-T generator is actually larger than a typical AmBe source used in compensated neutron logging, which generally have an activity of 10-20 Ci and produce 10^7 n/s [18].

The tool was initially designed for a D-T generator. However, simulations were conducted in parallel for both D-T and D-D neutron sources to ensure the tool would be compatible with both source types. The following studies are simulations using only a D-T neutron source due to its higher neutron energy and yield compared to a D-D neutron source. A D-T

generator has been acquired from ThermoFisher Scientific in Colorado Springs, Co. The unit is fully sealed and contains a small tritium target, which is bombarded with deuterium gas to generate 14.1 MeV neutrons with an actual yield of 1.6×10^8 n/s.

4.2.2 Detectors

Two γ -ray and two neutron detectors were chosen to go on-board the tool in order to gather information from the surrounding medium. The initial tool design uses well-characterized detectors commonly used in oil well logging [32; 33]. Proportional gas detectors were chosen, due to their robustness and legacy in the oil well logging industry, to measure the neutron response. Two ^3He detectors were obtained from LND. Each detector is 12 in. long and has a diameter of 1 in. with an active length of approximately 8 in., see Fig. 4.3. The detector nearest the source is filled to 4.0 atm of pressure, and the detector farthest from the source is filled to 2.0 atm pressure.

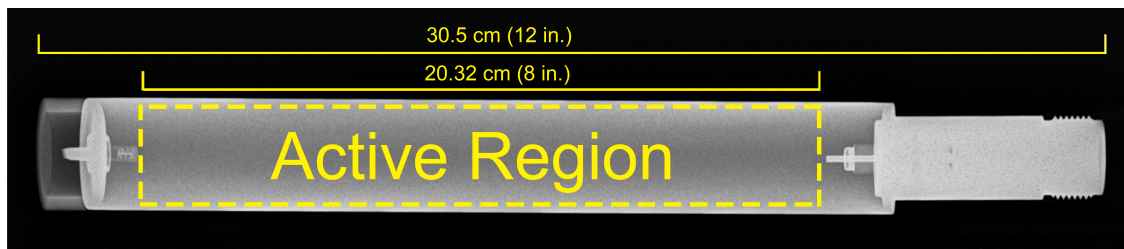


Figure 4.3: X-ray image of ^3He detector

NaI(Tl) detectors were chosen to measure the spectrum of inelastic scattered and capture gamma rays generated from the high-energy neutron source interacting with the surrounding material. Each γ -ray detector is composed of a 3x3 in. NaI(Tl) crystal, enclosed in a Lambertian surface, and coupled to a photomultiplier tube. When a radiation particle interacts within the scintillator crystal, it excites electrons which subsequently emit photons. The light collected eventually interacts with a photocathode, which produces electrons that go into the photomultiplier tube, which then amplifies the signal allowing it to be measured.

4.3 Source Shielding Studies

One aspect to consider when designing an oil well logging tool is whether or not to include shielding between the source and detectors, and what kind of material to use, if necessary. Three shielding materials of varying thicknesses were simulated between the source and nearest detector. The response of the near set of detectors was used to determine the effectiveness of each material in attenuating direct streaming along the tool. Porosity studies were conducted and the average migration length of neutrons was calculated for three different shielding materials and four different types of sediment. Geometry effects were also studied to understand the effect of the near detector distance from the source as well as the distance between the near and far sets of detectors.

4.3.1 Shielding Effectiveness

In this study, three different shielding materials at different thicknesses were simulated. For this simulation, the tool geometry shown in Fig. 4.4 was modeled in MCNP6[®]. An aluminum pipe with an inner radius of 10.16 cm (4 in.) and a wall thickness of 0.64 cm (0.25 in.) was modeled to serve as a type of borehole casing. An effectively infinite medium was filled with limestone and placed around the borehole pipe. Both the borehole pipe and the surrounding medium were modeled to be effectively infinite along one axis. The source and detectors were placed inside the borehole pipe in a co-linear fashion.

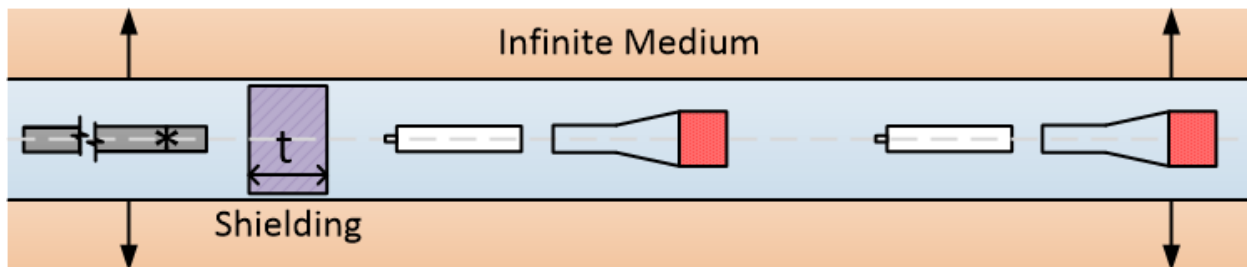


Figure 4.4: Approximate tool geometry used in shielding studies

The distance of the near ^3He , near NaI(Tl), far ^3He , and far NaI(Tl) detectors from the source were approximately 35 cm, 85 cm, 110 cm, and 160 cm, respectively. Note that detector distances were measured approximately from the location of the source to the nearest edge of the active volume of the detector. For ^3He detectors, the active region is 20.32 cm (8 in.) in length and it is located roughly in the middle of the gas chamber as seen in Fig. 4.3. However, the active volume for the NaI(Tl) detectors is the 3 in. x 3 in. crystal. A cylinder with a 10 cm radius was modeled between the source and nearest detector. The thickness of the cylinder was varied in 5 cm increments for each of the three shielding materials: boron carbide, titanium hydride, and tungsten. The normalized near NaI(Tl) detector responses for various shielding thicknesses can be seen in Fig. 4.5 (Note: error bars are too small to be seen).

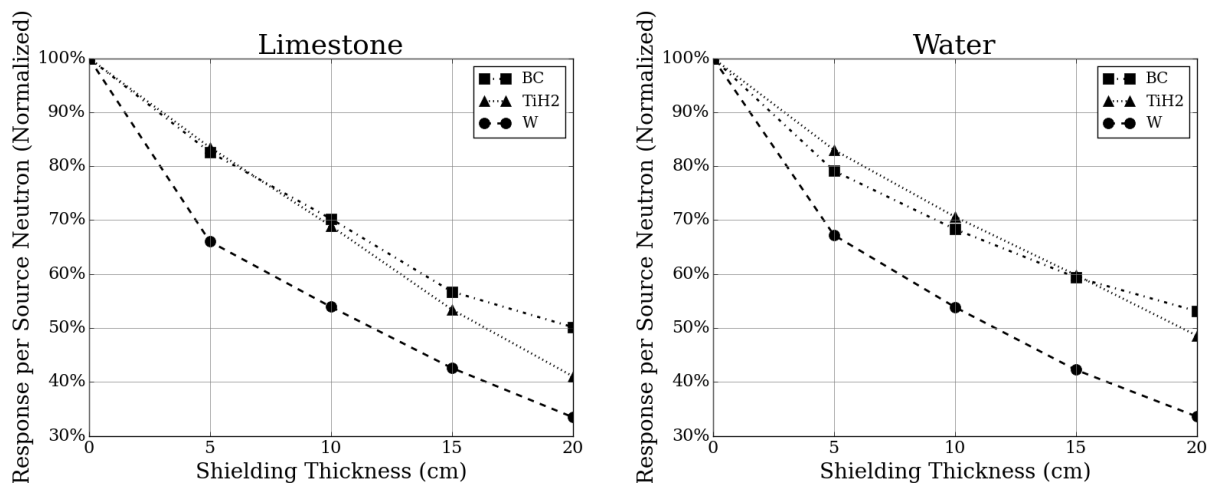


Figure 4.5: Near NaI(Tl) detector responses for limestone (*left*) and water (*right*)

As expected, tungsten performed best as a shield for γ -rays due to its high atomic number. A tungsten shield, 5 cm in thickness, reduced the γ -ray flux by 33 – 34% in both water and limestone. In contrast, the same thickness of boron carbide and titanium hydride only reduced the γ -ray response by approximately 17-20%. The near ^3He detector responses for limestone and water can be seen in Fig. 4.6. Based on simulation results, tungsten had a similar performance as titanium hydride for the neutron detectors. From Fig. 4.5 and Fig. 4.6, one can observe that the most amount of attenuation is achieved in the first 5 cm of shielding material.

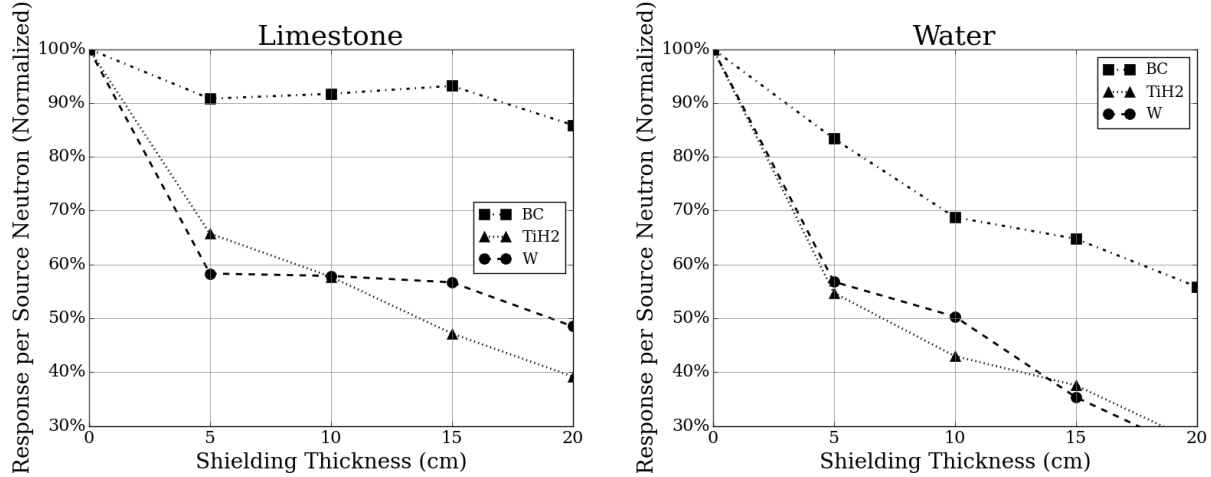


Figure 4.6: Near ³He detector responses for limestone (*left*) and water (*right*)

4.3.2 Shielding Effect on Porosity Sensitivity

To study the effect of shielding on porosity sensitivity, the tool was modeled with a 5 cm thick disc of shielding material between the source and the nearest detector. The three types of shielding materials simulated were boron carbide (BC), titanium hydride (TiH₂), and tungsten (W). The tool was placed concentrically inside an aluminum pipe with a diameter of 20.32 cm (8 in.) and a wall thickness of 0.64 cm (0.25 in.). The volume surrounding the pipe was filled with limestone, sand, water, and light Texas oil.

$$\frac{\phi_N}{\phi_F} = \frac{r_F}{r_N} \exp\left(\frac{r_f - r_n}{L_s}\right) \quad (4.4)$$

For a fast neutron source with two co-linear neutron detectors placed at distances r_N and r_F , the average neutron migration length can be calculated from the average neutron flux at each detector location (ϕ_N and ϕ_F), as seen in Eq. 4.4 [10]. For this study, the average neutron flux of each detector volume (ϕ_N , ϕ_F) was calculated using the F4 tally in MCNP6[®]. Each detector volume consists of a cylinder with a 1 in. diameter and 20.32 cm in length.. The distance from the source to the middle of each detector was 42 cm for the near detector (r_N) and 117.5 cm for the far detector (r_F). The average neutron migration length (L_s) was calculated Using Equation 4.4, the results are shown in Table 4.1, where ϕ represents flux and σ is the calculated relative error.

Table 4.1: Neutron flux at near and far ^3He detector locations and calculated migration lengths

Water	ϕ_{near}	σ	ϕ_{far}	σ	ϕ_{near}/ϕ_{far}	L_s
No Shielding	2.65E-03	1.94%	2.03E-04	7.02%	13.07	49.10
Boron Carbide	2.20E-03	2.13%	1.40E-04	8.45%	15.70	43.87
Titanium Hydride	1.65E-03	2.46%	1.32E-04	8.70%	12.52	50.50
Tungsten	1.78E-03	2.37%	1.30E-04	8.77%	13.67	47.71
Oil	ϕ_{near}	σ	ϕ_{far}	σ	ϕ_{near}/ϕ_{far}	L_s
No Shielding	2.71E-03	1.92%	2.29E-04	6.61%	11.81	52.55
Boron Carbide	2.25E-03	2.11%	1.58E-04	7.95%	14.21	46.57
Titanium Hydride	1.67E-03	2.45%	1.61E-04	7.88%	10.35	57.87
Tungsten	1.84E-03	2.33%	1.22E-04	9.05%	15.09	44.90
Sandstone	ϕ_{near}	σ	ϕ_{far}	σ	ϕ_{near}/ϕ_{far}	L_s
No Shielding	5.60E-03	1.33%	7.27E-04	3.71%	7.70	74.84
Boron Carbide	5.48E-03	1.35%	6.92E-04	3.80%	7.92	72.78
Titanium Hydride	4.64E-03	1.46%	5.88E-04	4.12%	7.90	72.99
Tungsten	4.83E-03	1.43%	6.45E-04	3.94%	7.49	76.86
Limestone	ϕ_{near}	σ	ϕ_{far}	σ	ϕ_{near}/ϕ_{far}	L_s
No Shielding	4.79E-03	1.44%	5.15E-04	4.41%	9.30	63.02
Boron Carbide	4.53E-03	1.48%	4.39E-04	4.77%	10.32	57.99
Titanium Hydride	3.87E-03	1.61%	3.62E-04	5.25%	10.68	56.52
Tungsten	4.20E-03	1.54%	4.66E-04	4.63%	9.01	64.76

A clear distinction was observed between the average migration lengths calculated for hydrogen-rich (*e.g.* water and oil) and non-hydrogen-rich sediments (*e.g.* sandstone and limestone), as seen in Table 4.1. Calculations showed that the ratio of the near to far neutron flux is highly dependent upon the transport of neutrons through the surrounding medium, not on the type of shielding material used. Therefore, using the ratio of the near to far neutron flux serves as a good indication of formation porosity.

Neither shielding material showed any improvement in the tool's sensitivity to porosity. An improvement in tool sensitivity due to the presence of shielding would show a noticeable decrease in the neutron migration length (L_s) calculated for water and oil, and an increase for limestone and sandstone, when compared to the case with no shielding. Therefore, the amount of shielding needed between the tool and the detectors will be determined based on detector dead time during measurements.

4.4 Detector Spacing Studies

MCNP6[®] simulations were conducted to investigate the effect of the distance between the near and far detector sets in the tool. A tool skeleton was modeled inside an infinite medium with varying distances between the end of the near NaI(Tl) detector and the far ³He detector; the model geometry can be seen in Fig. 4.7. The distance of the near ³He, near NaI(Tl), far ³He, and far NaI(Tl) detectors from the source were approximately 30 cm, 80 cm, 105 cm, and 155 cm, respectively, for a detector spacing of 5 cm. The distance of the far detectors was increased in 5 cm increments for each simulation. Note that detector distances were measured approximately from the location of the source to the nearest edge of the active volume of the detector. For ³He detectors, the active region is 20.32 cm (8 in) in length and it is located roughly in the middle of the gas chamber as seen in Fig. 4.3. The active volume for the NaI(Tl) detectors is the 3 in. x 3 in. crystal. No shielding was placed between the source and the nearest detector because there was no marginal improvement in tool sensitivity when shielding was introduced, as discussed in section 4.3.2. The simulation studies were conducted with the infinite medium surrounding the tool filled with limestone and water are discussed in section 4.4.1. Results for limestone with varying levels of porosity are discussed in section 4.4.2.

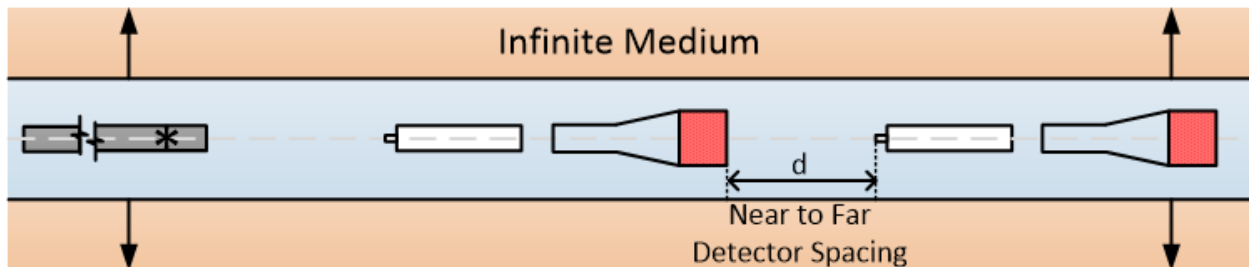


Figure 4.7: Tool geometry used in detector spacing studies

4.4.1 Spacing Between Near and Far Sets of Detectors

Detector spacing simulation studies were conducted using the geometry described in section 4.4, see Fig. 4.7. The far detector responses for ^3He in an infinite medium filled with limestone, sandstone, and water, can be seen in Fig. 4.8. From the figure, one can observe that as the far detector distance increased the detector response decreased, as is expected. However, when the detector distance was larger than 20 cm, the far ^3He detector responses for limestone and sandstone became indistinguishable.

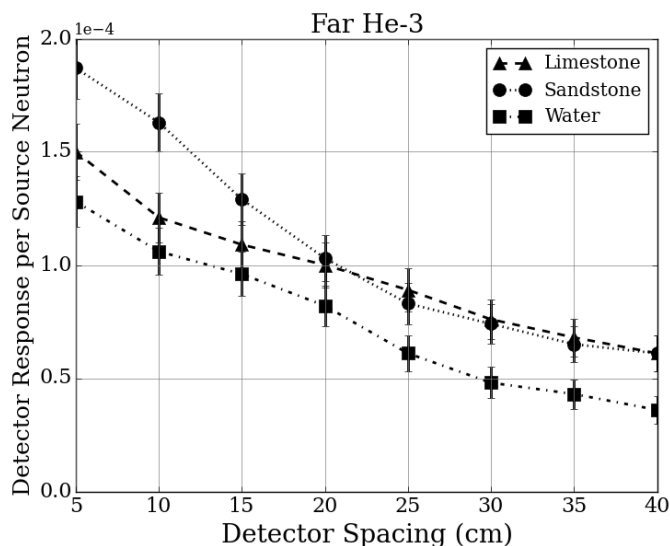


Figure 4.8: Far detector responses for different spacing between detector sets

Figure 4.9 shows the detector responses for the far NaI(Tl) detector. At 25 cm detector spacing, the near NaI(Tl) detector response was nearly same for all three materials. This study indicates that a tool with large distances between the near and far sets of detectors could be less sensitive to different materials. Ideally, a tool with the the optimal detector spacing has different responses to different materials. Therefore, based on the responses shown, smaller distances between the detectors provide better material discrimination.

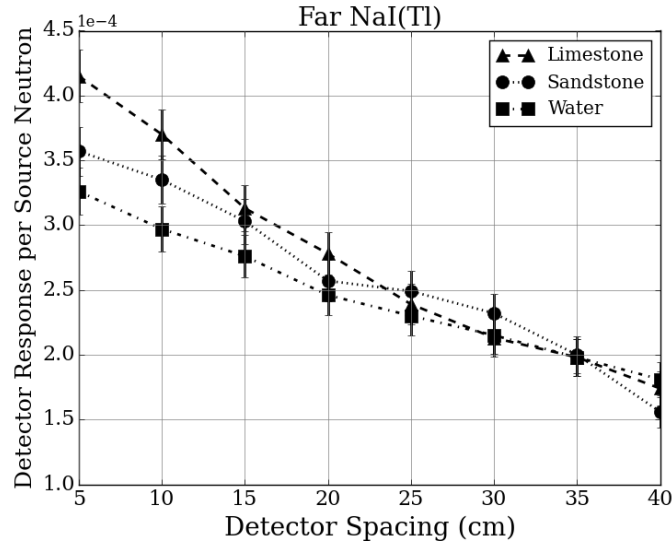


Figure 4.9: Far detector responses for different spacing between detector sets

4.4.2 Effect of Near to Far Detector Spacing on Porosity

The ratio of the near to far neutron detector responses serves as an indicator of formation porosity. A detailed description of the tool geometry simulated is included in section 4.4. The spacing between the near and far sets of detectors was varied to determine its effect on the tool’s sensitivity to porosity [34]. In this study, the detector spacing refers to the distance between the farthest edge of the near γ -ray detector to the nearest edge of the far neutron detector, see Fig. 4.7 for reference. Simulations were conducted with detector spacing distances of 10, 20, and 30 cm. The ratio of the near to far ^3He detector responses for limestone and sandstone of varying porosity can be seen in Fig. 4.10 and Fig. 4.11, respectively.

From these simulations, the tool showed greater sensitivity to changes in porosity for larger ^3He detector spacing. In contrast, as seen in section 4.4.1, the γ -ray detectors seem to have better sensitivity to density when they are placed closer together. Based on these results, and taking into consideration laboratory space limitations, the final tool design has a detector spacing of ~ 20 cm.

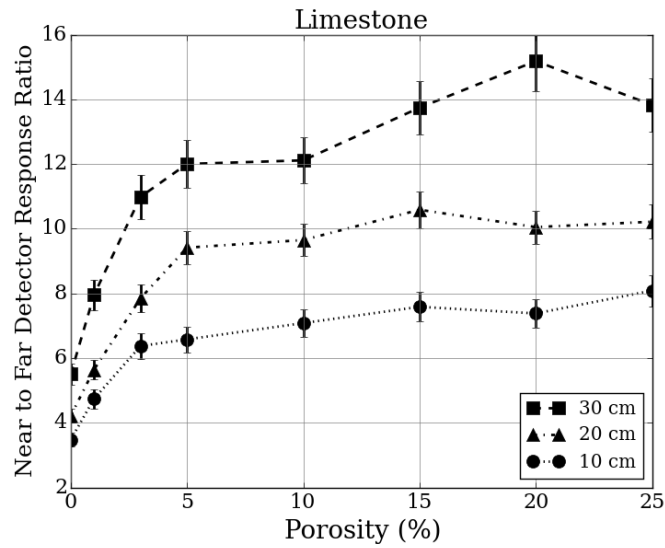


Figure 4.10: Near to Far ^3He detector response ratio vs. limestone porosity

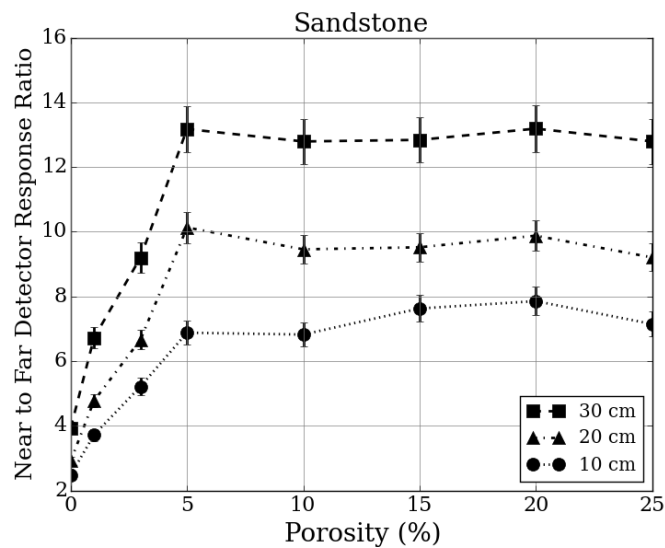


Figure 4.11: Near to Far ^3He detector response ratio vs. sandstone porosity

Chapter 5

Design of Test Enclosure

A mockup borehole environment was designed and constructed to test the oil well logging tool prototype, and to acquire signature responses from each of the materials that will be tested. The data collected were used to benchmark Monte Carlo simulations, including the MCLLS code being developed by North Carolina State University and our own Monte Carlo models. The test enclosure described in this chapter was constructed in room 107 of the King Hall Annex at Kansas State University. It consists of a box, 8 ft. long by 6.5 ft. wide by 6.7 ft. tall, surrounded by 8 in. thick concrete walls and an open top. An 8 in. aluminum tube is suspended horizontally, in the middle, to simulate a borehole. The enclosure will serve as a controlled environment in which to take measurements using the tool whose design was described in Chapter 4.

A series of simulations were conducted using MCNP6[®] to design the test enclosure. The goal of the following studies are:

1. To determine the minimum size necessary for the test enclosure to behave as an effectively infinite medium
2. To determine the appropriate depth for the test enclosure to obtain the maximum signal from the DT source
3. To design a final testing enclosure to be built in the King Hall Annex
4. To design appropriate shielding for the laboratory space
5. To verify simulated ambient dose rates with survey meter measurements

The final laboratory space will be used to take measurements of various materials using the oil well logging benchmarking tool previously described. The testing enclosure will be filled with materials such as water, sand and limestone. Following chapters will describe experimental procedures, measurement results, and compare those results to simulations.

5.1 Effectively Infinite Medium Radius

The first step in designing a test facility was to determine the minimum enclosure size that would yield an effectively infinite medium around the benchmarking tool. The geometry for these studies consists of a cylindrical barrel with a concentric aluminum pipe to simulate a borehole; a section of the geometry is shown in Fig. 5.1. The borehole pipe has an inner radius of 10 cm and a wall thickness of 0.64 cm. Both the barrel and the borehole were modeled with an effectively infinite length to simulate an infinite medium. The tool designed in Chapter 4 was placed roughly in the middle of the length of the borehole pipe (Note: Fig. 5.1 is not drawn to scale). The barrel was filled with sandstone and limestone and simulations were conducted varying the barrel radius between 30 and 200 cm. The normalized ^3He detector responses for the near detector were plotted against barrel radius, as seen in Fig. 5.2.

Figure 5.2 shows that the neutron detector response plateaus at a barrel radius of 100 cm for both sandstone and limestone. Therefore, the test enclosure should have at least a 100 cm radius, including the borehole pipe, to behave as an effectively infinite medium. The simulations completed provide valuable information on the size of the interrogated volume needed for maximum signal acquisition and minimum neutron leakage.

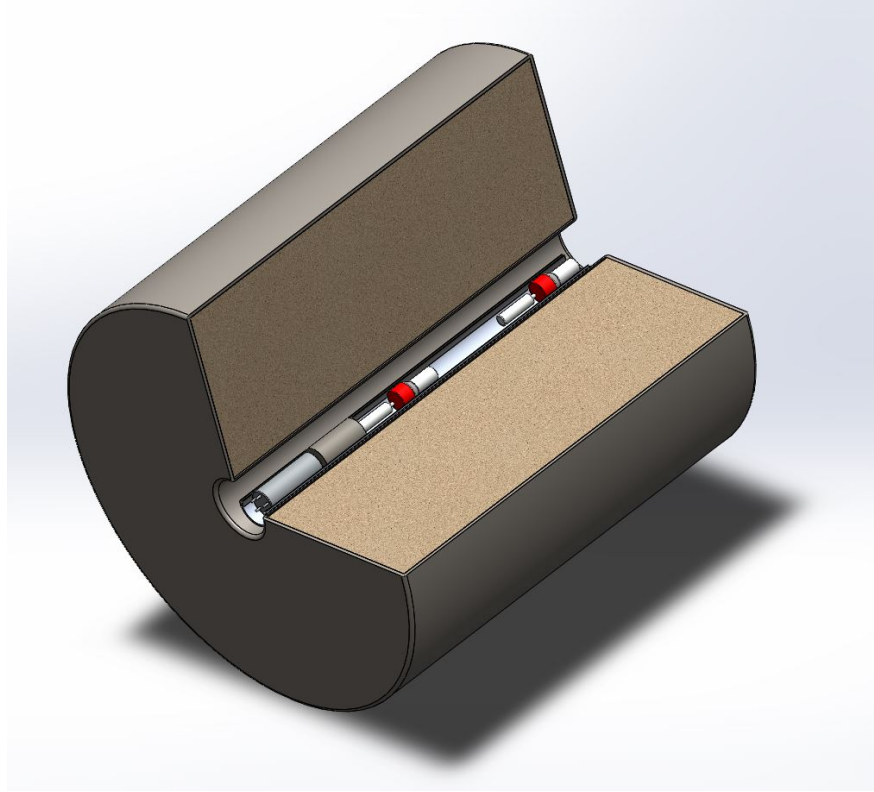


Figure 5.1: Section of barrel geometry

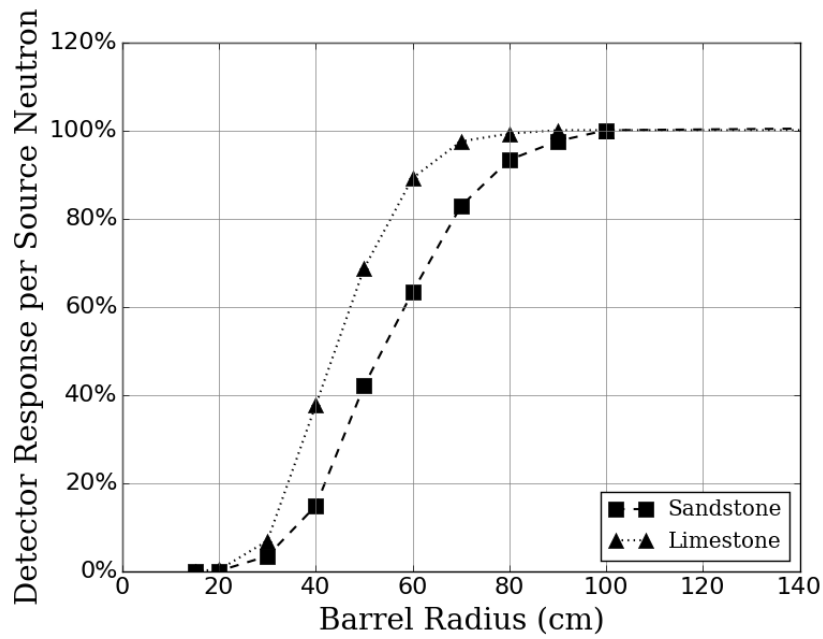


Figure 5.2: Near ^3He detector response (normalized) vs. barrel radius

5.2 Source Depth

Once the minimum radius of the enclosure was determined, the next step involved finding the minimum depth necessary for a cylindrical borehole enclosure to house the oil well logging benchmarking tool and obtain the maximum signal from each source. These studies were conducted using solely the DT source due to the resulting neutrons having a much higher energy than an AmBe source.

The DT source was initially placed at one end of a long cylinder (100 cm radius), with the sets of near and far, γ -ray and neutron detectors going into the cylinder. Simulations were performed with the source at different depths into the cylinder, starting at 0 cm (cylinder edge), and moving the source 10 cm deeper into the cylinder in subsequent simulations. Fig. 5.3 and Fig. 5.4 show the normalized detector responses for the near NaI(Tl) and ^3He detectors as a function of source depth into the enclosure. Both far detector responses saturated when the source was 50 cm inside the edge of the enclosure.

These sets of simulations helped determine the depth of the testing enclosure. A minimum source depth between 30 cm and 50 cm was added to the benchmarking tool length to determine the depth of the enclosure. This was ensure that once the tool was placed inside the enclosure, the source placement would be deep enough into the medium to obtain maximum signal. The final depth of the enclosure was chosen to be approximately 8 ft. to fully accommodate the benchmarking tool, the source depth needed, future shielding, and leave enough room in the laboratory space to maneuver the tool in and out of the enclosure.

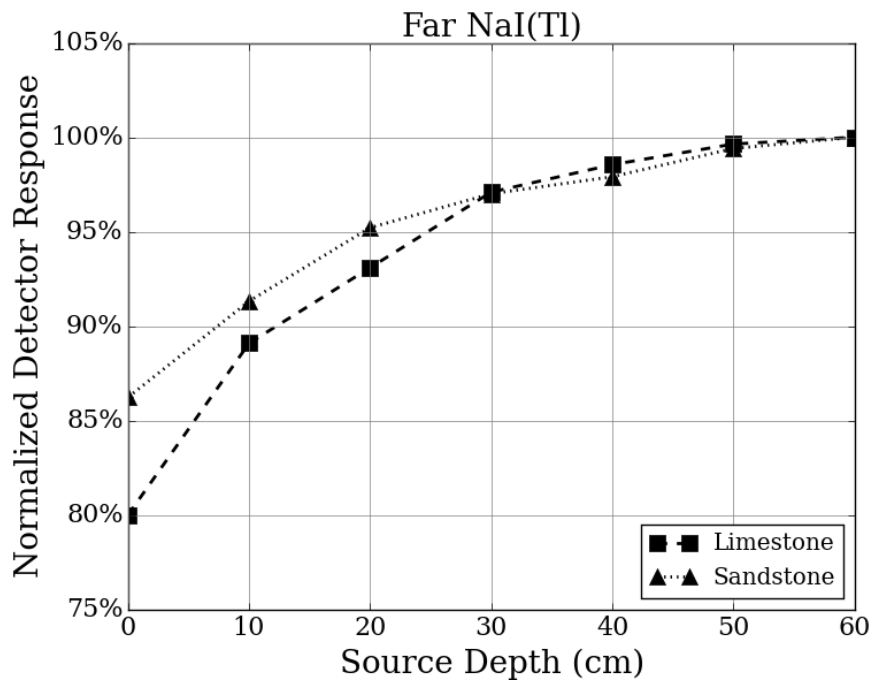


Figure 5.3: Far NaI(Tl) detector response vs. source depth

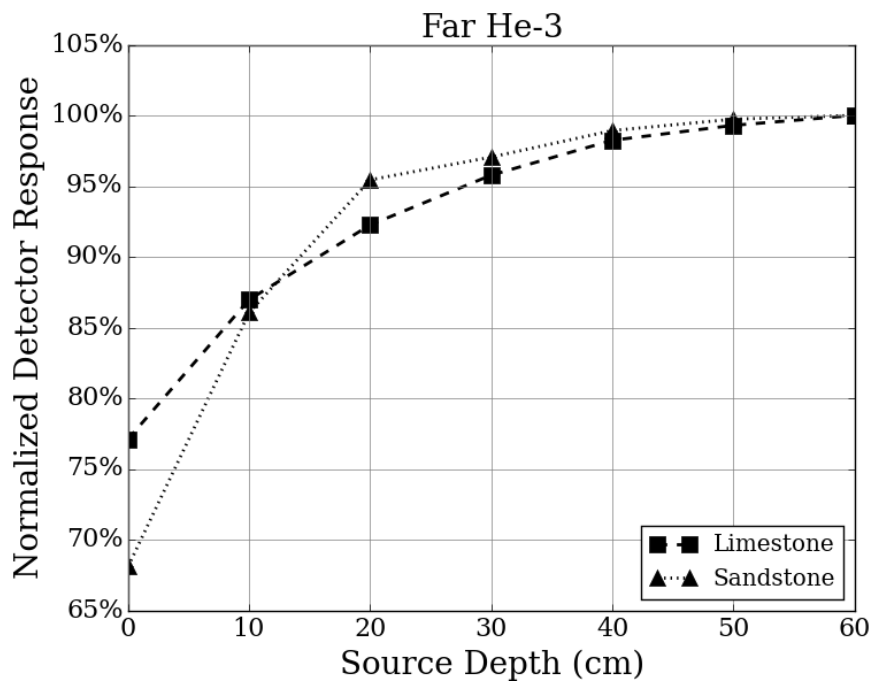


Figure 5.4: Far ^3He detector response vs. source depth

5.3 Height and Width of Enclosure

A cylindrical, barrel-like enclosure proved challenging to build due to the large amount of test material it would have to hold. Therefore, the tool was simulated inside a rectangular parallelepiped geometry to determine the appropriate height and width of an enclosure that would act as an infinite medium, and would also fit in the laboratory space that had been acquired for this project. As previously mentioned, the test enclosure was chosen to be approximately 245 cm (~8 ft.) deep based on rough estimates the final benchmarking tool dimensions, the minimum depth at which the source should be located, and extra space was added to allow for shielding. The geometry used in the MCNP6[®] simulations can be seen in Fig. 5.5.

The testing enclosure was simulated using limestone and sandstone. The width and height of the enclosure were varied between 120 and 300 cm (4-10 ft.). The flux per source particle at each detector was tallied using MCNP6[®] to get an idea of how large the enclosure needed to be to be for the detector responses to plateau, indicating an effectively infinite medium. Fig. 5.7 shows the simulated responses from the far ³He detector, which indicates that the response plateaus when the box is approximately 180 cm (6 ft.) tall and wide.

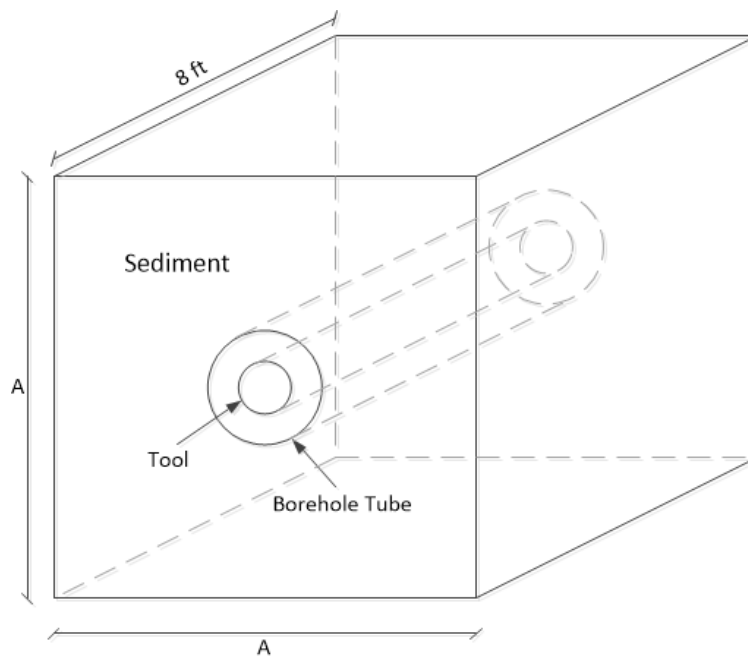


Figure 5.5: New test enclosure geometry

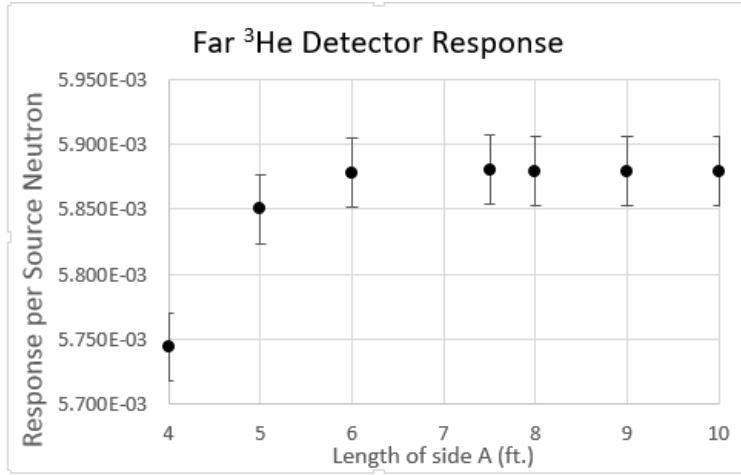


Figure 5.6: Detector response vs. height and width of test enclosure

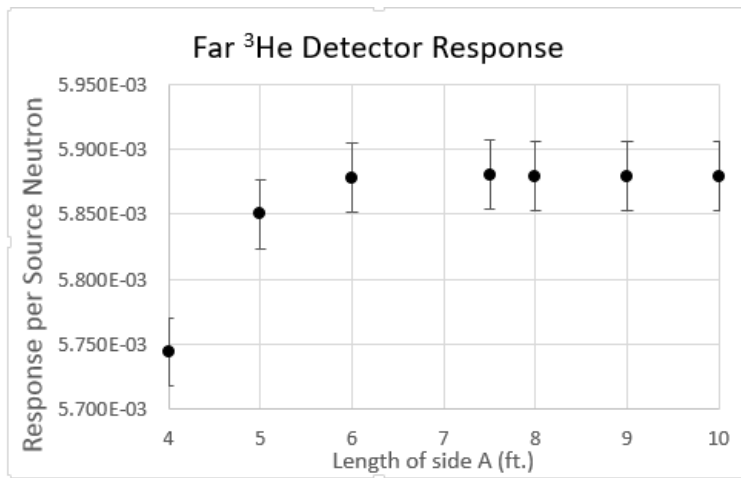


Figure 5.7: Detector response vs. height and width of test enclosure

Once the minimum dimensions required for the enclosure were determined, the design was adjusted to better fit in the laboratory space. The containment was integrated into the space by building two, 8 in. thick reinforced concrete walls against a corner of the room. The design took advantage of two of the 12 in. thick concrete walls that make up the corner of the room, which allowed ample space for the enclosure to be built.

5.4 Laboratory Facility Overview

The testing facility was constructed in a former chemical storage building called the King Hall Annex, on the Kansas State University (KSU) campus. This laboratory space was ideal for many reasons. The building is located in an area of low foot traffic and is mostly used as a storage facility. While many students take laboratory courses in King Hall, the annex building is detached and mostly surrounded by landscaping and a parking lot, therefore students do not usually walk or linger in areas surrounding the building. Being a previous chemical storage building, the structure has concrete walls that are 12 to 18 inches thick, blowout roof panels, a loading dock where materials can be delivered, an adjacent parking lot, and very restricted access. The King Hall Annex building location on the campus map is shown in Fig. 5.8.

The test enclosure was built in room 107 of the King Hall Annex, see Fig. 5.9. As mentioned, exterior areas of the building are not areas where individuals of the public linger and reflect an occupancy factor of 1/40. Outdoor egress areas, directly adjacent to the King Hall Annex building, are not high traffic areas as they provide only access to restricted points of entry to King Hall as well as the Annex building. The one exception for possible high traffic is the path-way (side-walk) at the top of Fig. 5.8 which rests at 30 feet or greater from the building.

In order to ensure the safety of everyone with access the building, room 107 was modeled in MCNP6[®] and simulations were conducted to design the necessary shielding for the room. The physical access to radiological source operational areas is depicted in Fig. 5.9. Operations are executed within the CNEC Controlled Areas where access is limited to those directly related to the project. The source location is fixed near the southwest corner of room 107 and CNEC operators occupy room 101.

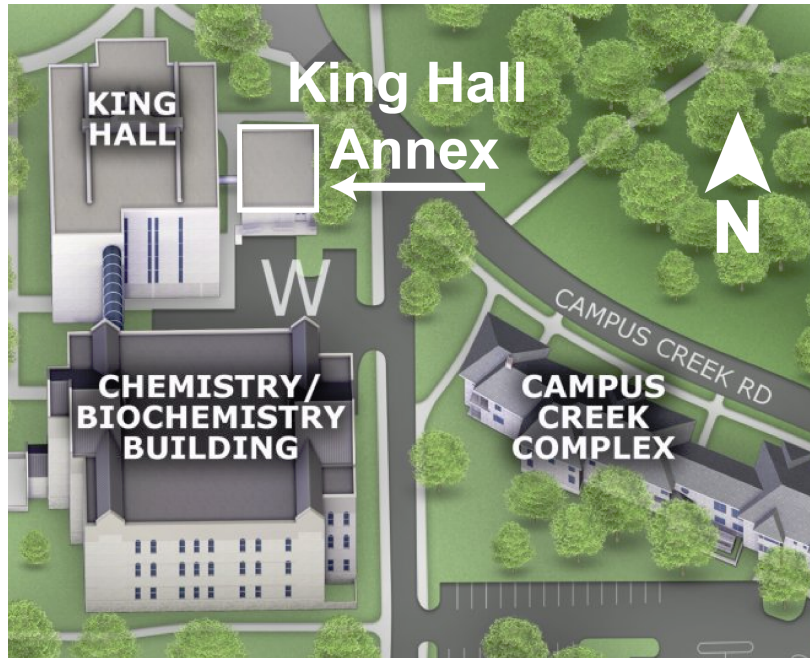


Figure 5.8: CNEC area of operations and surrounding areas.

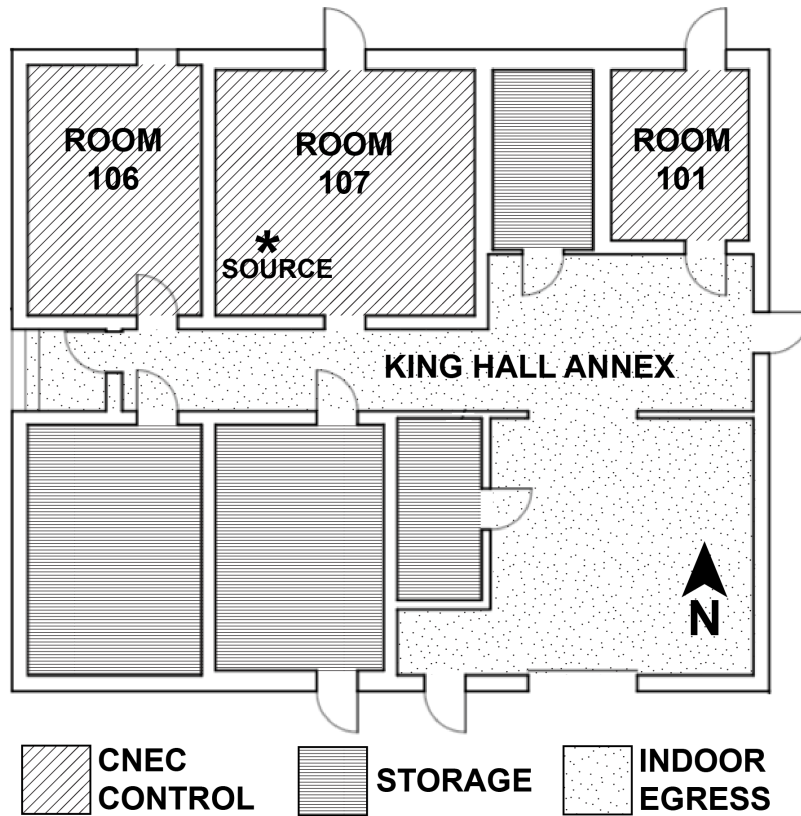


Figure 5.9: King Hall Annex floor plan and CNEC area of operations.

5.5 Engineering Controls and Interlocks

The DT generator has a computer interface that allows the operators to turn the generator on and off from a distance (Fig. 5.10). Therefore, to further reduce the dose received by the operators, all data collection and control instruments are located in room 101 of the King Hall Annex (see building layout in Fig. 5.9).

To prevent unintentional exposure while the DT neutron generator is operating, a series of interlocks and monitoring systems are employed. Interlock switches exist at the removable shielding cap (described in the next section) and every entry point to rooms 106 and 107 (see Fig. 5.11). Thus, entry into these rooms while operating will turn off the generator. Furthermore, flashing red lights indicate the operation of the machine. The neutron generator can be turned off from within the experiment room 107 by simply exiting through any door.

Operators can also turn off the machine from the control room by observation of the surveillance camera and its motion detection feature. If any of the switches fail, the machine source will be unable to start. Other safety features include intercommunication system and postings. Only when all entries/exit are secured and the removable shielding cap is installed, will the DT generator be operational.

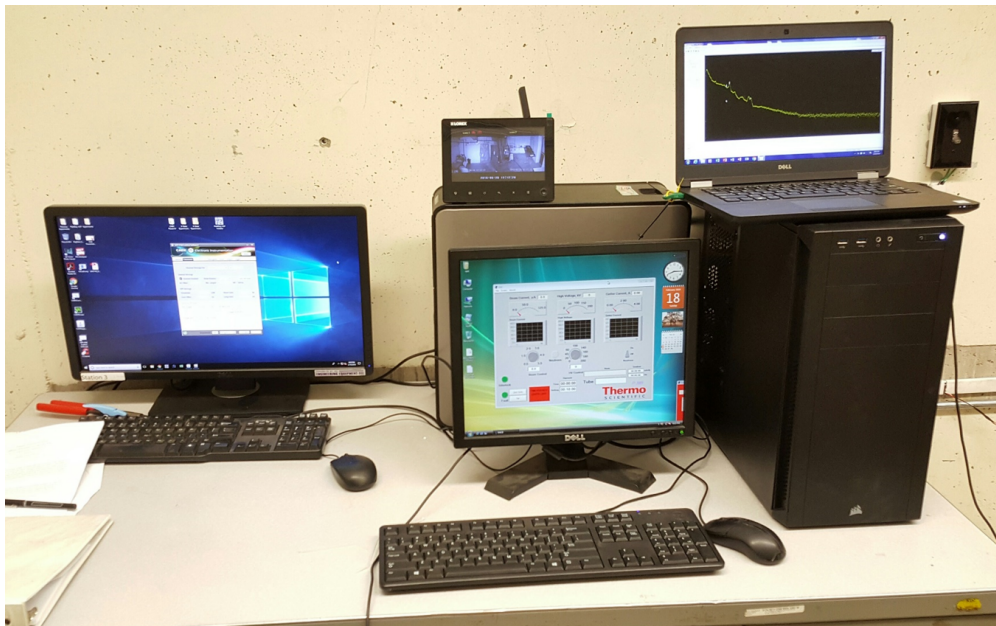


Figure 5.10: King Hall Annex: Room 101 (operator room)

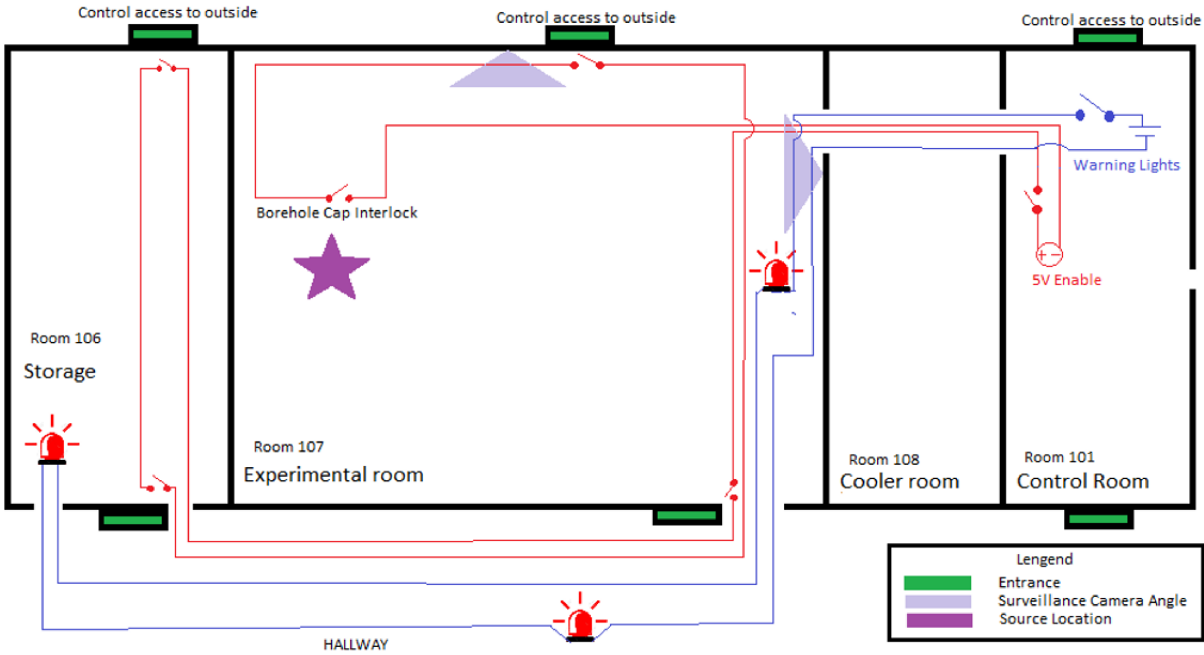


Figure 5.11: King Hall Annex: Safety features

5.6 Shielding Design

Despite the thick concrete walls of the building, care was taken to design shielding that would prevent streaming along the borehole tube, into the hallway. Simulation studies were conducted varying the thicknesses of 3 ft. wide sheets of borated polyethylene, which were placed up against the wall inside the enclosure, as seen in Fig. 5.12.

Table 5.1 shows the dose rates calculated using different thicknesses of borated polyethylene. In order to keep the dose rate below 2 mrem/hr[5], a shield of a minimum thickness of 10 in. was required. Based on simulation results, the shielding was designed as follows: Eleven 1-in. thick sheets of borated polyethylene were firmly secured to the inside of the wall. The last sheet, furthest from the wall, had a hole cut out to fit the borehole pipe (8.5 in. OD) and hold it suspended horizontally in the middle of the enclosure. The borated polyethylene sheets installed are commercially available in 1-inch thick sheets. The type used here contain 8% boron by weight. An aluminum plate was welded to the end of the borehole pipe that meets the shielding to create a tight seal and prevent water or other materials from leaking into the pipe, therefore protecting the tool during operation.

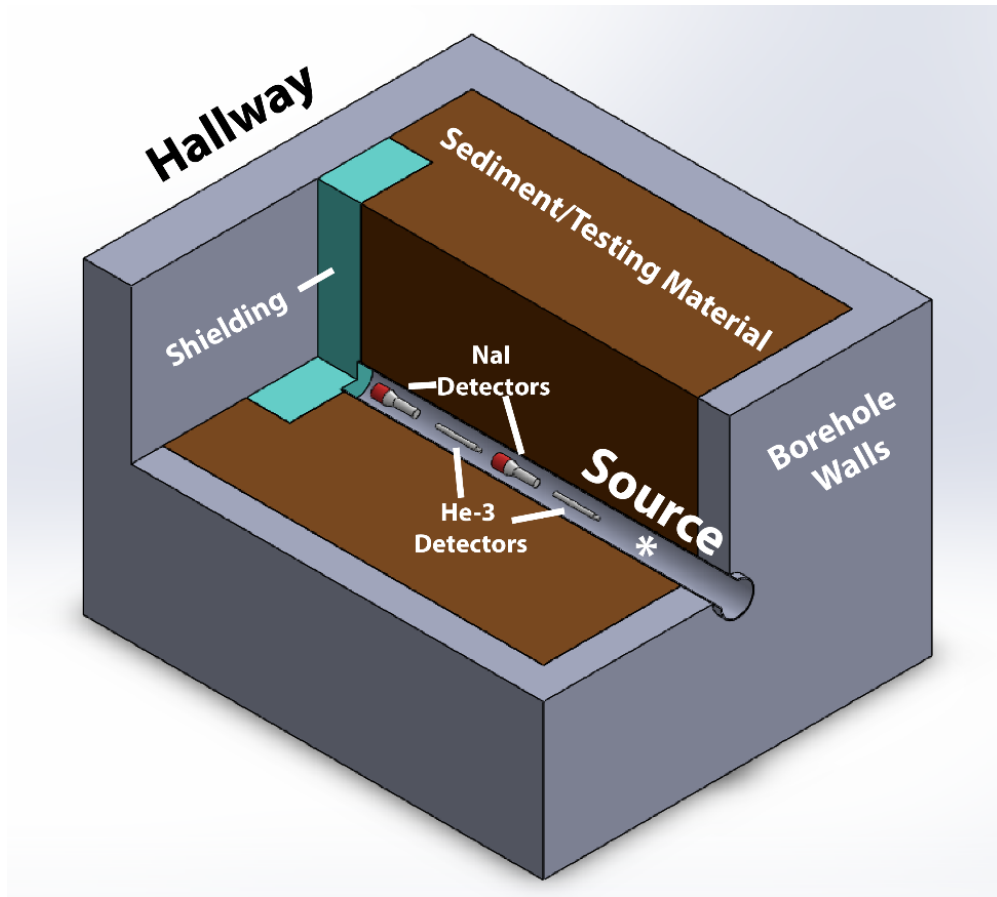


Figure 5.12: Final test enclosure design

Table 5.1: Hallway ambient dose rates for different thicknesses of borated polyethylene

Shielding Thickness (in.)	mrem/h
0	9.90 ± 0.42
1	7.98 ± 0.30
2	6.49 ± 0.26
3	5.53 ± 0.24
4	4.93 ± 0.23
5	4.18 ± 0.19
6	3.55 ± 0.18
7	3.10 ± 0.20
8	2.61 ± 0.24
9	2.41 ± 0.24
10	1.68 ± 0.12
11	1.54 ± 0.12
12	1.32 ± 0.14

As an additional safety feature, a removable shielding cap was designed to prevent streaming through the aluminum pipe into room 107. This was done to further reduce exposure to workers while troubleshooting the benchmarking tool or measurement systems. The shielding cap is made of borated polyethylene sheets in an octagonal shape around the borehole pipe, see Fig. 5.13. The cap features a channel to run wires from the tool to the measurement system as well as an interlock switch that prevents the DT neutron generator to turn on while the shielding cap is removed.



Figure 5.13: Removable shielding cap for borehole pipe

5.7 Dosimetry Calculations

Room 107 in the King Hall Annex, the testing enclosure, and final shielding design were modeled in MCNP6[®]. Simulations were conducted to estimate ambient dose rates around the room. Detectors were placed at key points along the perimeter of the room to identify the dose rate while the borehole is filled. Figure 5.14 shows the room layout as well as the location of each detector. Room 107 was modeled with the borehole enclosure filled with water to

simulate regular operation. Room 106 is primarily used for storage and has restricted access during operation. The expected ambient dose rates at each detector location, using the DT generator as the source, can be seen in Table 5.2. These simulations were conducted using the DT generator as a source because dose rates for the AmBe source are expected to be more than an order of magnitude lower.

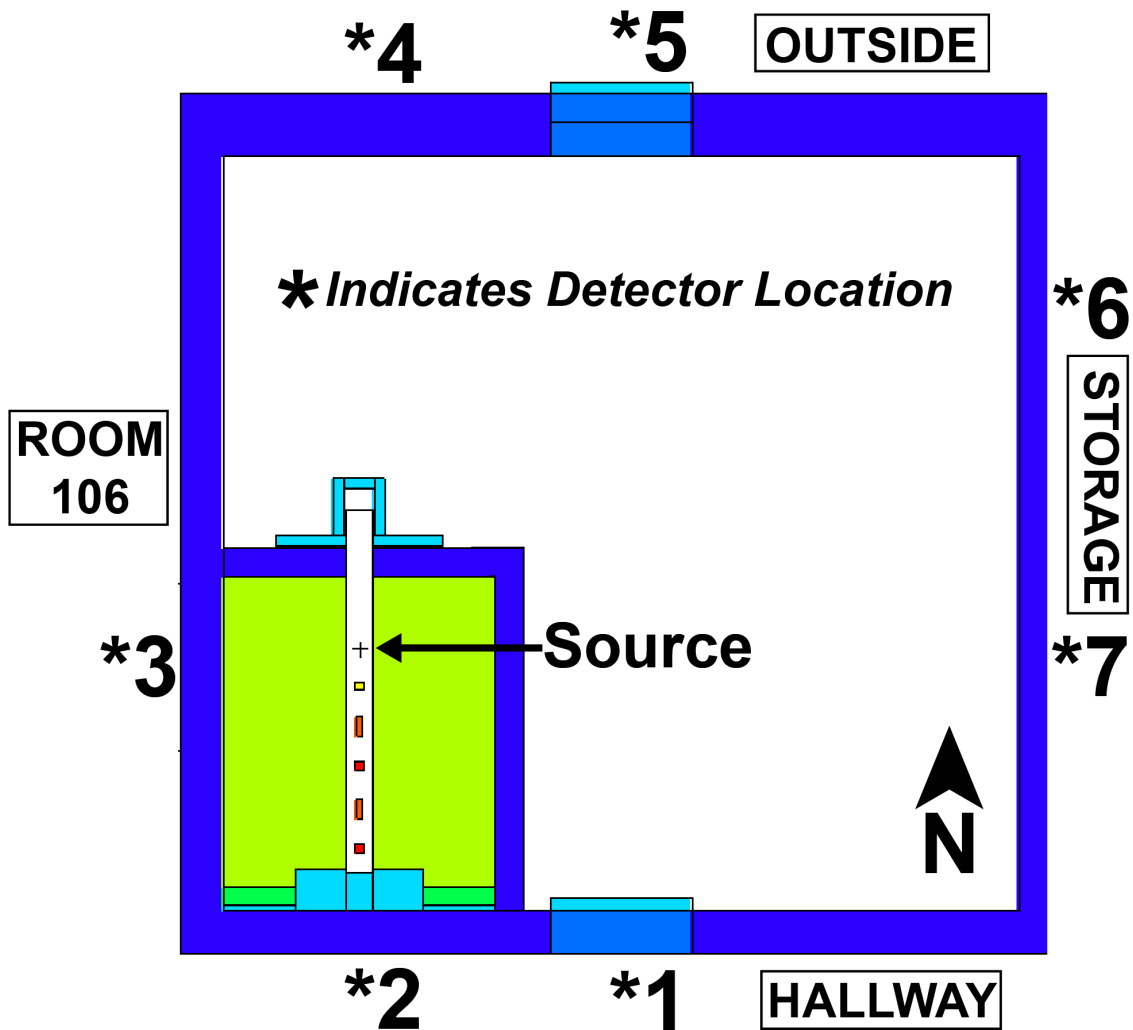


Figure 5.14: King Hall Annex, room 207, shielding configuration and expected ambient dose rates

Table 5.2: Ambient Dose Rates [ICRP74H*(10mm)], Water-Filled Testing Enclosure

Access Category	Occupancy Factor	Detector Location	Neutron Dose Rate (mrem/hr)	Photon Dose Rate (mrem/hr)
Annex Access	1/40	1	0.003 ± 16.9%	0.003 ± 2.43%
Annex Access	1/40	2	0.203 ± 12.8%	0.017 ± 3.37%
CNEC Access	Workload	3	0.052 ± 5.07%	0.032 ± 0.90%
Public Access	1/40	4	0.341 ± 4.28%	0.010 ± 3.28%
Public Access	1/40	5	0.124 ± 11.8%	0.018 ± 2.20%
CNEC Access	Workload	6	0.006 ± 19.5%	0.001 ± 13.4%
CNEC Access	Workload	7	0.003 ± 28.0%	0.001 ± 10.5%

Table 5.3: Ambient Dose Rates [ICRP74H*(10mm)], Air-Filled Testing Enclosure

Access Category	Occupancy Factor	Detector Location	Neutron Dose Rate (mrem/hr)	Photon Dose Rate (mrem/hr)
Annex Access	1/40	1	2.859 ± 0.77%	0.178 ± 0.29%
Annex Access	1/40	2	1.370 ± 3.29%	0.097 ± 2.10%
CNEC Access	Workload	3	23.15 ± 0.26%	0.590 ± 0.22%
Public Access	1/40	4	0.567 ± 3.09%	0.028 ± 1.70%
Public Access	1/40	5	1.851 ± 4.03%	0.119 ± 0.16%
CNEC Access	Workload	6	0.581 ± 5.46%	0.029 ± 2.72%
CNEC Access	Workload	7	1.037 ± 4.90%	0.043 ± 2.16%

Ambient dose rate simulations were also conducted with the test enclosure filled with air to simulate a worst-case scenario. The expected ambient dose rates at each detector location in Fig. 5.14 can be seen in table 5.3. Note that detector #3 in Fig. 5.14 is located in room 106, which is primarily used for storage and has restricted access during operation. Even in a worst-case scenario where the test enclosure is empty, estimated ambient dose rates for public areas remains well below 2 mrem/hr. The air-filled simulation indicates that in this worst case scenario, access to room 106 and the hallway should be restricted during operation.

5.8 Shielding Design Verification

The Kansas State University Department of Environmental Health and Safety performed survey meter readings throughout the King Hall Annex to ensure proper shielding during operation. Background radiation levels throughout the building were measured at <0.06 mrem/h. Dose rate readings were taken at approximately the detector locations seen in Fig. 5.14 using a Ludlum survey meter, model 2363 with a Ludlum 42-41 probe. The dose rate measurements were taken while the DT generator was operating on two separate occasions, one when the test chamber was filled with water and then filled with air (see table 5.4).

All survey meter readings with the DT generator on were below our ambient dose rate estimations, with many readings being at the background radiation level. The largest source of discrepancy between our estimated ambient dose rates and those recorded by the survey meter are at detector locations #1 and #5 (Fig. 5.14); this is because in order to be conservative, the doors themselves (not the shielding attached to them) to room 107 were modeled as voids. As a result, our simulations estimated much higher ambient dose rates at these locations. Comparing tables 5.2, 5.3, and 5.4 shows that the dose rate measurements taken validated the shielding design for the KSUMI facility.

Table 5.4: Survey meter readings while operating with the DT generator on

Access Category	Occupancy Factor	Detector Location	Water Filled Enclosure (mrem/hr)	Air Filled Enclosure (mrem/hr)
Annex Access	1/40	1	0.05	1.0
Annex Access	1/40	2	0.07	0.75
Public Access	1/40	4	0.15	0.45
Public Access	1/40	5	0.12	0.20
CNEC Access	Workload	7	0.05	0.25

Chapter 6

AmBe Experiments and Simulations

A benchmarking oil well logging tool was designed and constructed. A test enclosure was designed and built in a laboratory space to house the tool and mimic an effectively infinite medium with a borehole. The tool was used to collect detector responses from various neutron sources in the test enclosure. The laboratory space in which the test enclosure was built was fitted with proper shielding and other safety features to permit safe operation of the tool.

In this chapter two experiments using AmBe as a source will be described. The first experiment was designed to measure the gamma-ray output of AmBe to determine the source strength. The second experiment was performed using the oil well logging tool inside the test enclosure filled with water. Both experiments were modeled in MCNP. The purposes of these experimental measurements were to compare them to our simulation results and test the fidelity of our MCNP model.

6.1 Source Characterization

The AmBe source used in the following experiments was previously used in the oil well logging industry and is approximately 30 years old. In order to properly simulate the AmBe source, its current strength must be determined. Therefore, a simple experiment was performed at the ACER facility at Kansas State University.

6.1.1 ACER Experiment

The ACER facility is housed in a large building made of concrete. The facility was chosen because it has spacious areas to reduce the effect of scattering when taking measurements. The experiment at the ACER facility was designed to measure the output of the AmBe source using two different gamma-ray detectors.

The experiment was set up in a room with the AmBe source elevated 5.5 ft off the concrete floor. Two 3 in. by 3 in. gamma-ray detectors, NaI(Tl) and CeBr₃, were also placed 5.5 ft from the floor. Each detector was placed 8 ft away from the AmBe source and 6.5 ft away from each other to prevent detector cross-talk. The geometry of the experimental setup is depicted in Fig. 6.1.

A background measurement (without the source) was taken for 3 hours. A second measurement was taken with the source in place for 1 hour. The background subtracted spectra from the NaI(Tl) detector and the CeBr₃ detector can be seen in Fig. 6.2. Both detectors show a full-energy peak at 4.44 MeV, with single and double escape peaks at 3.93 MeV and 3.42 MeV, respectively. It is important to note that the CeBr₃ detector has a higher efficiency than the NaI(Tl) and therefore registered a higher number of counts. However, the CeBr₃ data were collected using a larger number of channels with smaller bin widths.

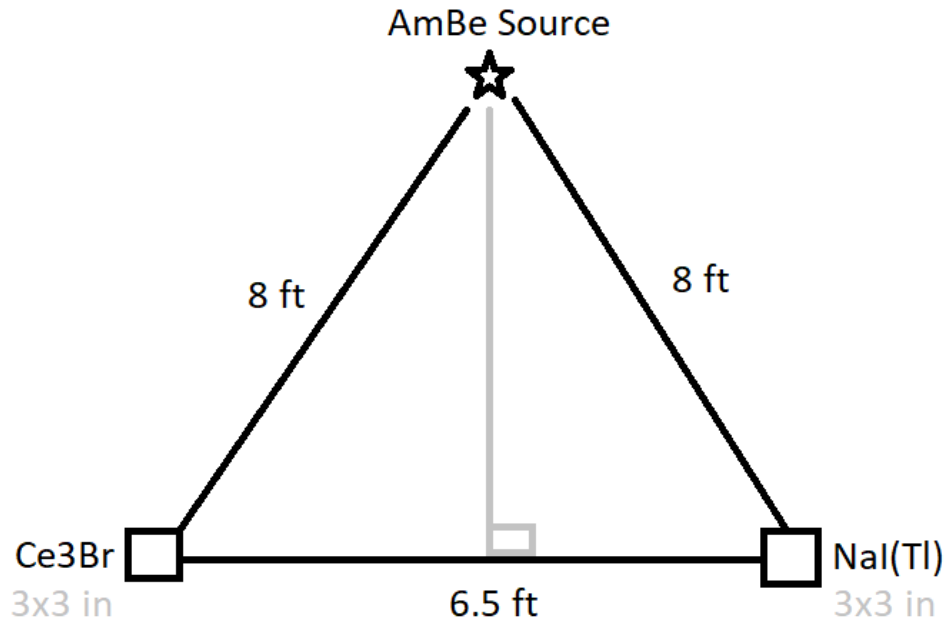


Figure 6.1: ACER experiment geometry, top-view (not to scale).

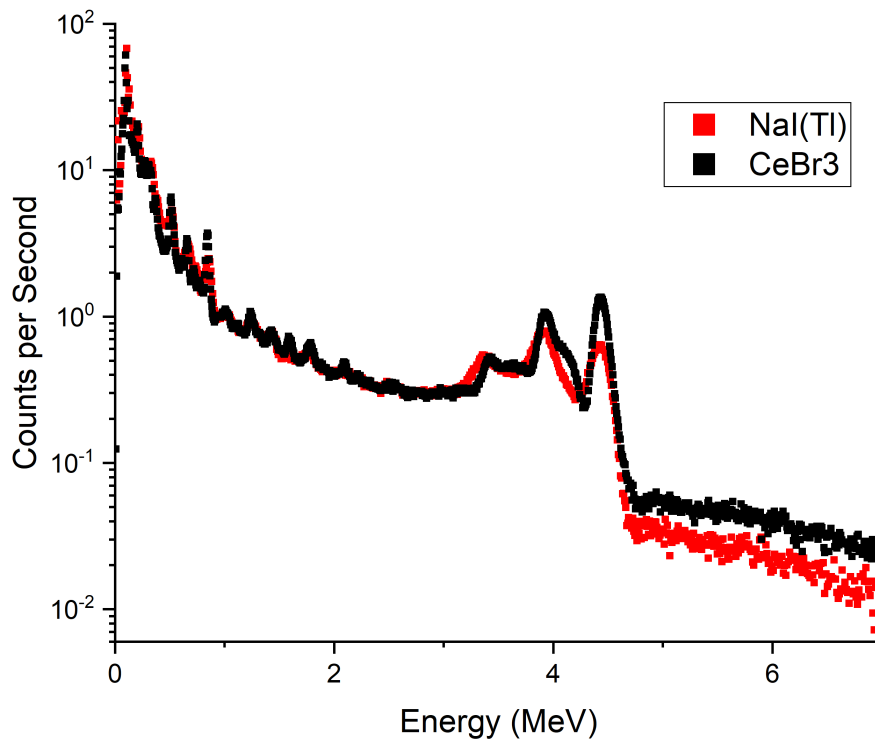


Figure 6.2: ACER experimental detector responses.

6.1.2 MCNP Simulation of ACER Experiment

The ACER experiment was simulated in MCNP. The MCNP geometry consists of a 12 in. thick semi-infinite parallelepiped filled with concrete. The source was placed 5.5 ft above the semi-infinite concrete surface. Each detector was modeled as a 3 in. by 3 in. cylinder with the appropriate material definitions for NaI(Tl) and CeBr₃. The detectors were placed at the same height as the source at the locations indicated in Fig. 6.1. Then, an F8 tally was specified for each detector region to obtain its respective simulated pulse height spectrum. The tripods, photomultiplier tubes, measurement systems, walls, source holder, and other materials present in the laboratory space were not modeled in the simulation.

We know that for each neutron emitted from the AmBe source, a 4.44 MeV gamma ray is also emitted 56% of the time [15–17]. Because an AmBe source produces both neutrons of various energies and sometimes a single gamma ray, separate simulations were conducted for each particle type. That is to say, the source was defined as an isotropic neutron source with the neutron energy distribution of AmBe in one simulation, and as an isotropic 4.44 MeV gamma ray in another. The resulting simulated pulse height spectrum for each detector is therefore the combination of the responses simulated from the neutron source and the gamma ray source, each scaled by its branching ratio.

The NaI(Tl) F8 tally was modified by the GEB special tally treatment card. The coefficients used were found empirically by Hakimabad [28], see section 3.2.5. The simulated NaI(Tl) pulse height spectrum from the neutron simulation, the gamma-ray simulation, and the resulting total spectrum is shown in Fig. 6.3. Note that the combined spectrum accounts for the 4.44 MeV gamma ray only being emitted coincident with a neutron 56% of the time.

Similarly, the CeBr₃ crystal was simulated in MCNP as a 3 in. by 3 in. cylinder. An F8 (pulse height) tally was assigned to the detector region. However, the GEB parameters for CeBr₃ are not well known. Without the GEB card, the energy peaks of the simulated detector response are not broadened (see Fig. 6.4). Therefore, direct comparison with experimental spectra was not initially possible.

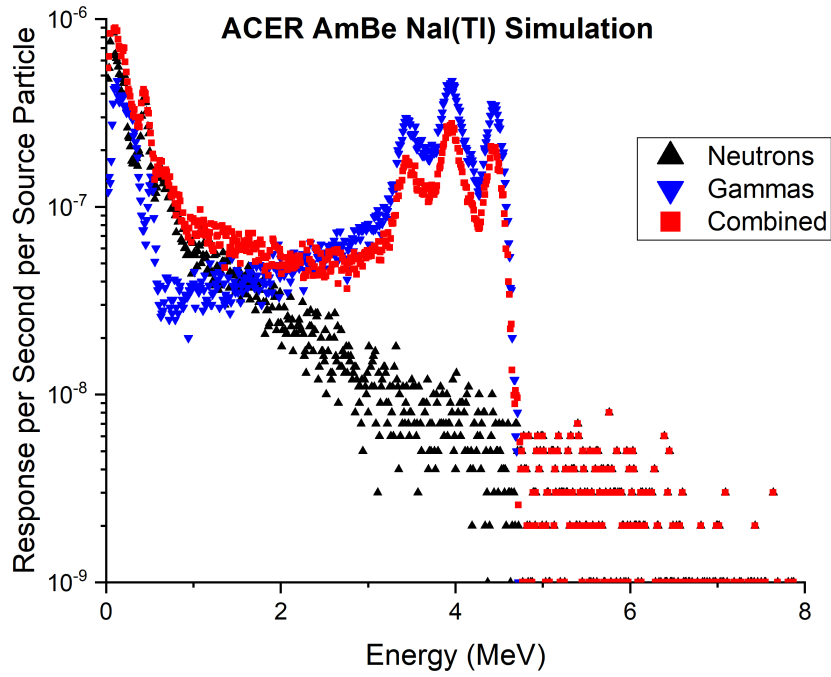


Figure 6.3: NaI(Tl) simulated responses for ACER experiment.

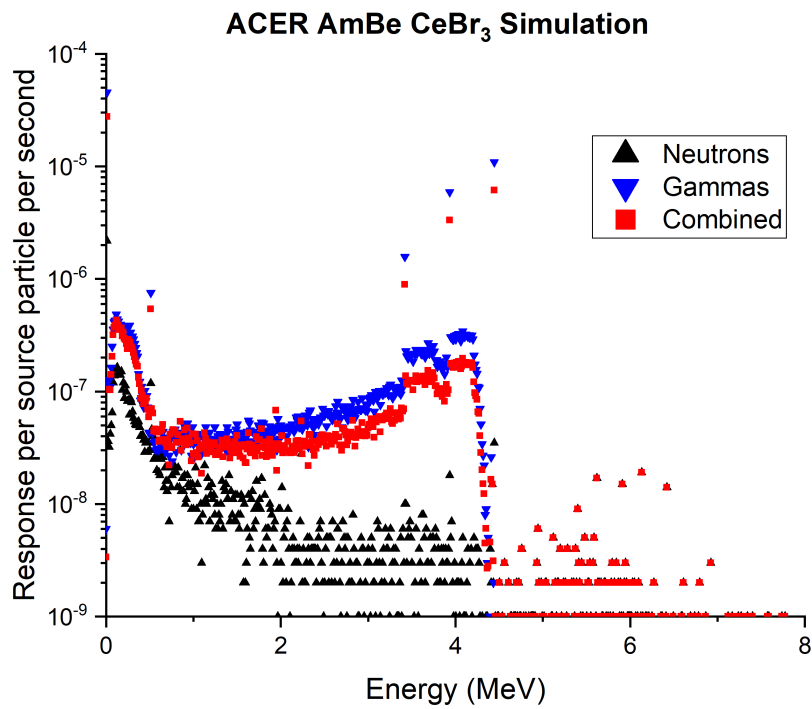


Figure 6.4: CeBr₃ simulated responses for ACER experiment (No GEB).

Here, we attempt to determine the appropriate GEB parameters for CeBr_3 . Ideally, a set of experiments using the CeBr_3 detector to measure spectra from isotopes emitting a wide range of energies would be performed to determine the GEB parameters specific to the detector. However, we try to use the experimental data collected to at least obtain approximate broadening parameters. The first step is to fit Gaussian functions to each peak in the experimental data collected with the CeBr_3 detector. Then, determine the FWHM and the centroid energy of each peak. The software Origin Student 2018 was used for its peak analysis capabilities to create fits for the convolved peaks (see Fig. 6.5).

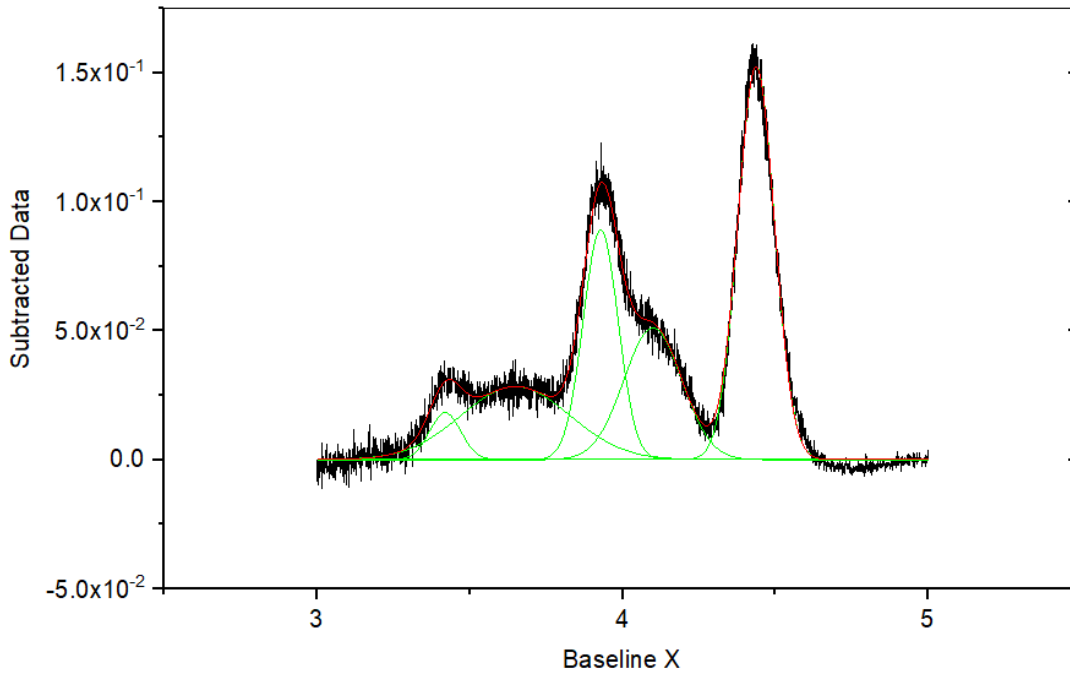


Figure 6.5: ACER AmBe experiment, 4.44 MeV peak analysis of CeBr_3 measurement.

Table 6.1: ACER AmBe experiment, CeBr_3 Gaussian fit peak data

Peak Index	Centroid Energy (MeV)	FWHM (MeV)
1	3.41990 ± 0.00176	0.12011 ± 0.00584
2	$3.92891 \pm 8.223\text{E-}4$	0.13486 ± 0.00186
3	$4.43815 \pm 2.275\text{E-}4$	$0.14098 \pm 5.516\text{E-}4$

Table 6.1 was extracted from the Gaussian fitting of the experimental CeBr_3 data. Only the 4.44 MeV energy peak, the 3.93 MeV single escape peak, and the 3.42 MeV double escape peak were considered. The two extra peaks are artificial peaks that appear due to photon scattering. The centroid energy and FWHM of each peak were used to least-squares fit the MCNP[®] GEB formula, see equation 6.1. The GEB parameters found were: $a = -0.52793$, $b = 0.44342$, and $c = -0.10979$.

$$FWHM = a + b\sqrt{E + cE^2} \quad (6.1)$$

The new parameters (a , b , and c) were added to the GEB card for the pulse height (F8) tally in the CeBr_3 detector region. A new simulation was conducted and the results can be seen in Fig. 6.6. Please note that because the data points used in the curve fitting algorithm were between 3.5 MeV and 4.5 MeV, these GEB parameters do not fully represent the GEB function for a CeBr_3 detector. However, even with limited data, the broadening parameters found significantly improved the simulation results.

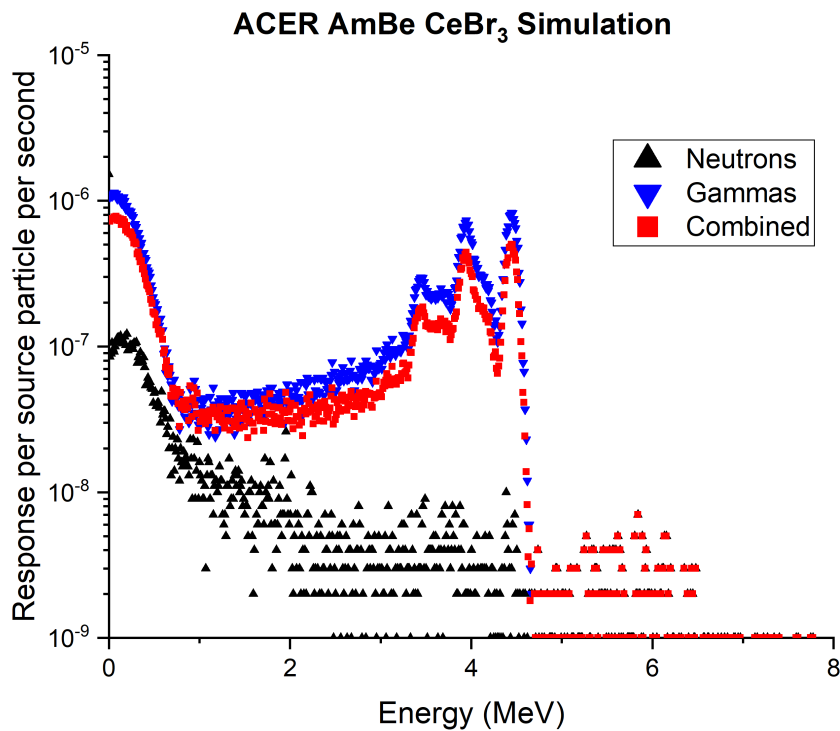


Figure 6.6: ACER AmBe Experiment, CeBr_3 MCNP Simulation with GEB.

6.1.3 Source Strength Analysis

In this section, the experimental data collected at ACER are compared to simulated data to determine the strength of the AmBe source. Analysis is performed for each detector independently. Gaussian peak fitting is used to determine the area under the 4.44 MeV, single escape, and double escape peaks in order to estimate the source strength from each detector. The results are compared and discussed.

Source Strength from NaI(Tl)

The NaI(Tl) experimental measurement and MCNP results were compared to obtain an approximate AmBe source strength. Gaussian functions were fit to the 4.44 MeV full-energy peak, the 3.93 MeV single escape peak, and the 3.42 MeV double escape peaks of both experimental and simulation data. The peak-fitting process for the NaI(Tl) detector is described below.

The Origin Pro peak-fitting analysis tool was used to obtain the following Gaussian fits. First, the set of data points that contain the peaks was selected from the NaI(Tl) experimental measurements. A linear baseline was established using the endpoints of the data and was subtracted from the spectrum. Three approximate peak locations were selected and the software fit a Gaussian function to each peak. The centroid energy, FWHM, integral of each peak, and a variety of other fitting parameters were then output onto a spreadsheet. The peak-fitting plots for the NaI(Tl) experimental data and the MCNP simulated output are seen in Fig. 6.2 and Fig. 6.8, respectively.

To obtain the AmBe source strength, we can divide the integral of each experimental peak by the integral of each simulated peak. In other words, we can divide net number of counts per second under an experimental peak by the net number of pulses per second per source particle in the corresponding simulated peak to obtain the number of particles per second that must be simulated to match experimental results.

Chi²=6.78326E-004
SS=1.70260E-001

Adj. R-Square=9.80018E-001
Degrees of Freedom=251

of Data Points=260

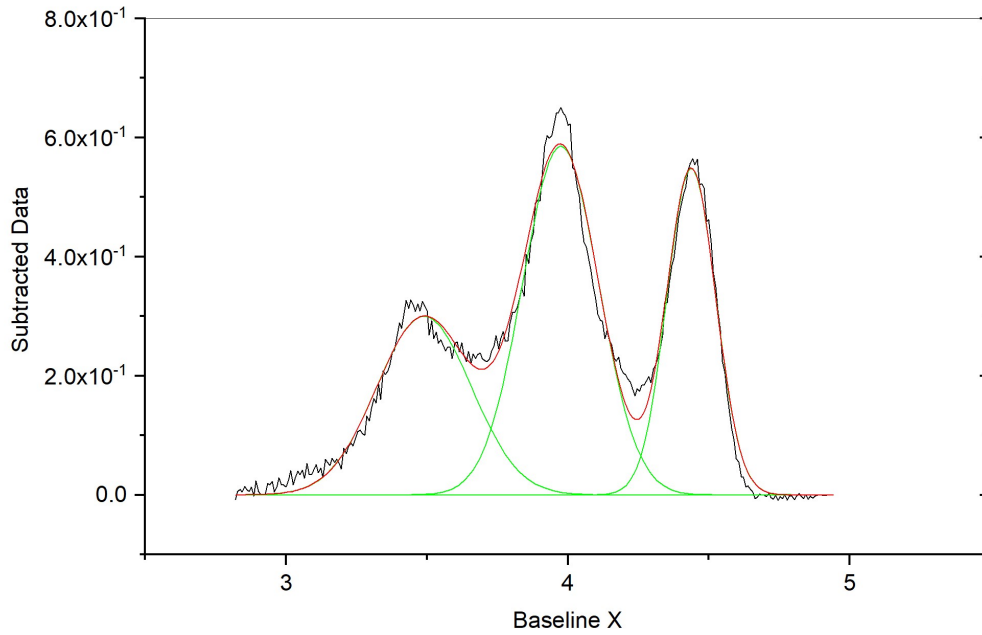


Figure 6.7: ACER AmBe Experiment, 4.44 MeV peak analysis of NaI(Tl) measurement.

Chi²=1.20568E-016
SS=2.13405E-014

Adj. R-Square=9.74925E-001
Degrees of Freedom=177

of Data Points=186

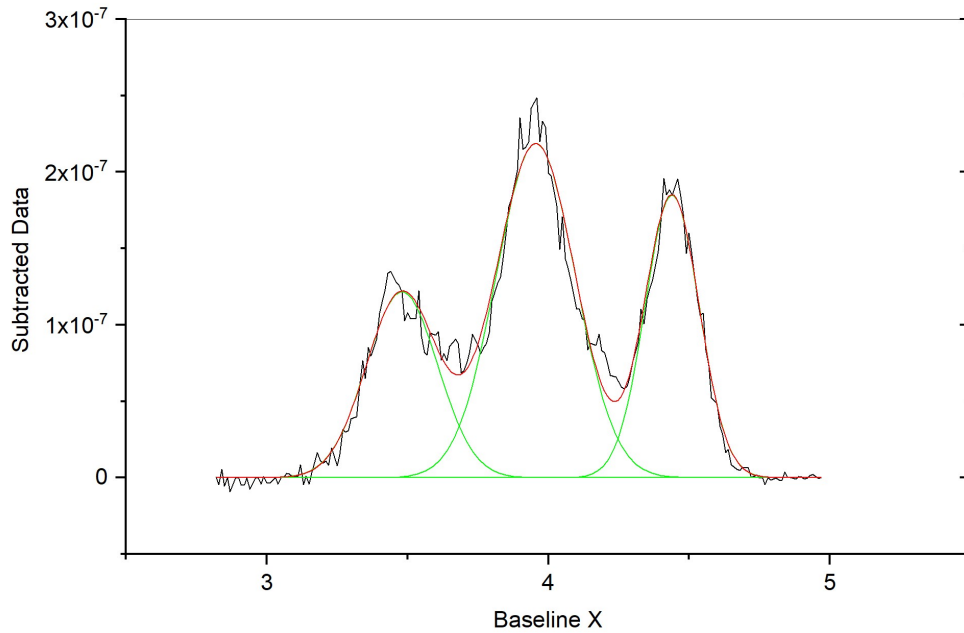


Figure 6.8: ACER AmBe Experiment, NaI(Tl) MCNP simulation peak analysis.

Table 6.2: ACER AmBe experiment, NaI(Tl) Gaussian fit peak data.

Energy (MeV)	Experimental Net Area (cps)	MCNP Net Area (cps per source n)	Source Strength (n per second)
3.42	0.12596 ± 0.00319	$3.86215\text{E-}8 \pm 1.18524\text{E-}9$	$3.26\text{E}6 \pm 5.42\%$
3.93	0.19840 ± 0.00309	$7.69932\text{E-}8 \pm 1.30446\text{E-}9$	$2.57\text{E}6 \pm 2.30\%$
4.44	0.11944 ± 0.00170	$4.46936\text{E-}8 \pm 9.06802\text{E-}10$	$2.67\text{E}6 \pm 2.48\%$

Table 6.2 summarizes the net peak areas for the experimental and simulated data sets and shows the corresponding source strength calculated from each peak. The AmBe source strength results varied between 2.6 and 3.3 million neutrons per second. However, the higher estimate had a lower number of net counts and therefore a larger uncertainty. Based on these findings, our best estimate of the source strength is approximately 2.6 million neutrons per second, plus or minus 3.4%.

Source Strength from CeBr₃

To calculate the AmBe source strength from the CeBr₃ data, the same procedure was followed as with the NaI(Tl) detector. Origin Pro was also used to fit Gaussian peaks to experimental and simulation results. The purpose of using a second set of data is to attempt to validate previous source strength calculations. However, as it will become apparent, the CeBr₃ spectrum features were more difficult to work with allowed for larger sources of error.

Using the same peak analysis tool as before, Gaussian peaks were fitted to both experimental and simulated data as seen in Fig. 6.9 and Fig. 6.10, respectively. As before, we can see two broad peaks in addition to our peaks of interest (4.44 MeV, 3.93 MeV, and 3.42 MeV).

Chi²=3.86137E-004
SS=1.15841E-001

Adj. R-Square=9.95369E-001
Degrees of Freedom=300

of Data Points=315

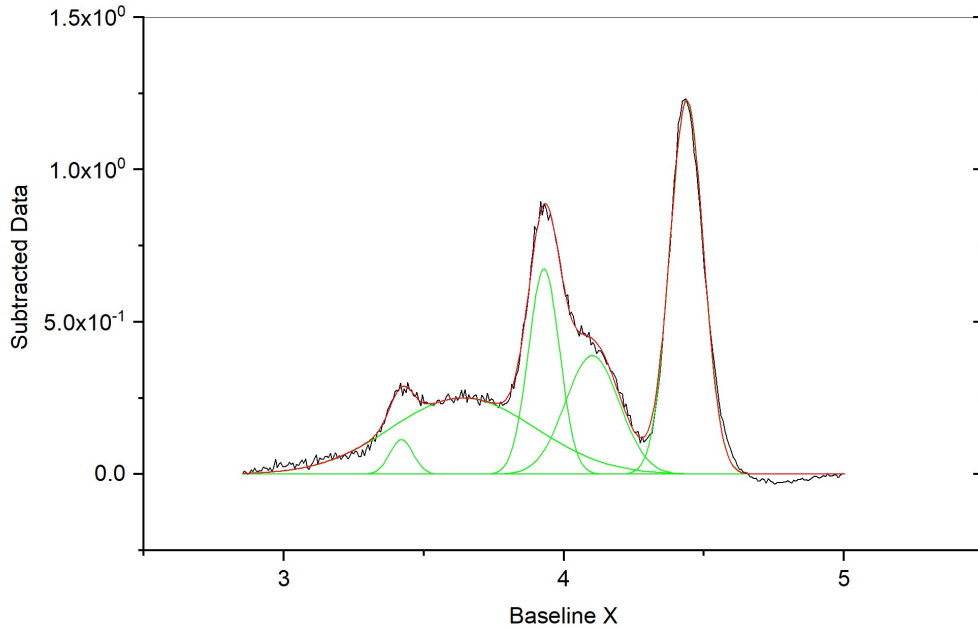


Figure 6.9: ACER AmBe Experiment, 4.44 MeV peak analysis of CeBr₃ measurement.

Chi²=4.96631E-017
SS=1.50479E-014

Adj. R-Square=9.90434E-001
Degrees of Freedom=303

of Data Points=318

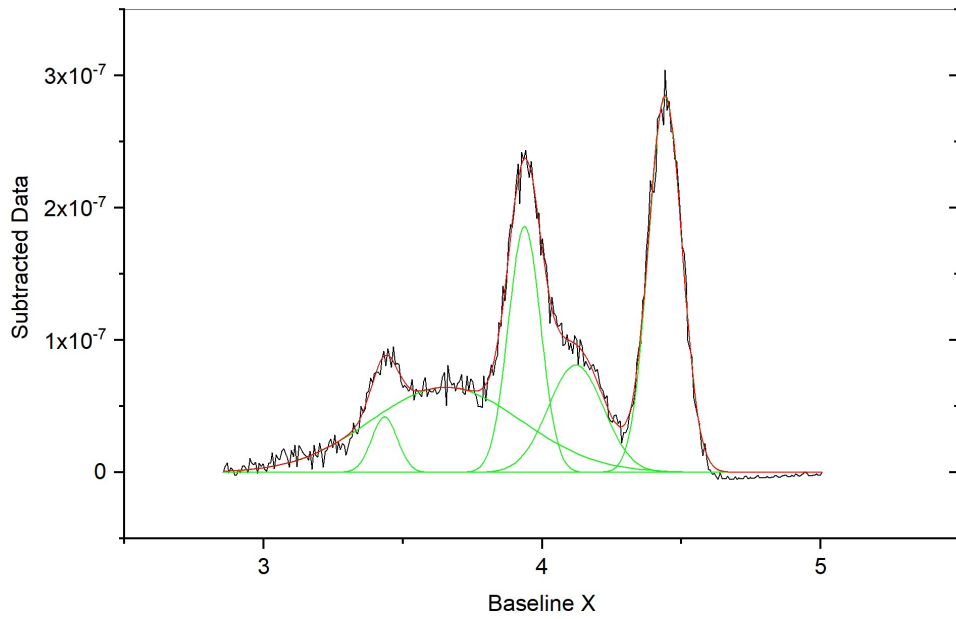


Figure 6.10: ACER AmBe Experiment, CeBr₃ MCNP simulation peak analysis.

Following the same procedure, the net area under each experimental peak was divided by the net area under each simulated peak to obtain the number of neutrons per second that AmBe emits. Table 6.3 summarizes the experimental and simulated net peak areas for the full-energy, single escape, and double escape peaks with their corresponding calculated source strengths.

Table 6.3: ACER AmBe experiment, CeBr₃ Gaussian fit peak data.

Energy (MeV)	Experimental Net Area (cps)	MCNP Net Area (cps per source n)	Source Strength (n per second)
3.42	0.01178 ± 0.00122	$4.87757\text{E-}9 \pm 5.22497\text{E-}10$	$2.41\text{e}6 \pm 14.9\%$
3.93	0.09376 ± 0.00426	$2.69585\text{E-}8 \pm 1.52393\text{E-}9$	$3.47\text{e}6 \pm 7.25\%$
4.44	0.18453 ± 0.00104	$4.28230\text{E-}8 \pm 3.99342\text{E-}10$	$4.30\text{e}6 \pm 1.09\%$

The AmBe source strength calculated from the CeBr₃ data varied between 2.4 and 4.3 million neutrons per second, which is consistent with the NaI(Tl) estimates but much less precise. Certain features of the CeBr₃ made fitting Gaussian functions to the peaks of interest more challenging. The two apparent peaks at 3.6 MeV and 4.1 MeV were actually part of the 4.44 MeV Compton continuum. Deconvolving the spectra accurately proved difficult and the results were inconsistent between the measured and simulated data sets. Therefore, only the full energy peak should be considered when calculating the true source strength because the escape peaks sit atop the Compton continuum and were not able to be properly fitted.

6.1.4 Source Strength Comparison

The AmBe source strength was calculated using measured and simulated detector responses from NaI(Tl) and CeBr₃. The results obtained from both detectors are summarized in Table 6.4. The NaI(Tl) simulation matches experimental data well; the source strength calculated from the 3.93 MeV and 4.44 MeV peaks had small uncertainties and were within each other's margin of error. Difficulties fitting the CeBr₃ peaks resulted in a large error

in the calculated source strength between the NaI(Tl) and CeBr₃ data sets. Therefore, the actual AmBe source strength is between 2.5 and 2.7 million neutrons per second with 3.4% uncertainty.

Table 6.4: ACER AmBe experiment, NaI(Tl) and CeBr₃ Gaussian fit peak data.

Energy (MeV)	Source Strength NaI(Tl) (nps)	Source Strength CeBr ₃ (nps)
3.42	3.26E6 ± 5.42%	2.41e6 ± 14.9%
3.93	2.57E6 ± 2.30%	3.47e6 ± 7.25%
4.44	2.67E6 ± 2.48%	4.30e6 ± 1.09%

As a final check, the simulated detector spectra for the ACER experiment were scaled by the estimated AmBe source strength, 2.6 million neutrons per second. The comparison between measured and simulated spectra for NaI(Tl) and for Cebr₃ can be seen in Fig. 6.11 and Fig. 6.12, respectively.

The simulated spectra for NaI(Tl) and CeBr₃ matches the 3-5 MeV region very well. However, below 3 MeV experimental measurements recorded a much higher continuum of counts than simulation. The MCNP model was modified and tested several times to attempt to correct this difference. In some simulations, extra concrete was added to the simulation in the form of walls and and a thicker floor to determine whether scattering from concrete could be the culprit. However, no meaningful differences were noticed in the simulated spectra.

Two journal articles feature AmBe measurements and simulations using NaI(Tl) detectors [16; 28]. The measured and simulated spectra from both papers have a similar spectral shape to our MCNP simulations. However, our experimental measurements register much higher counts below 3-MeV compared to the published articles. One possible cause for the discrepancy may have been the presence of radioactive material in the room where measurements were taken.

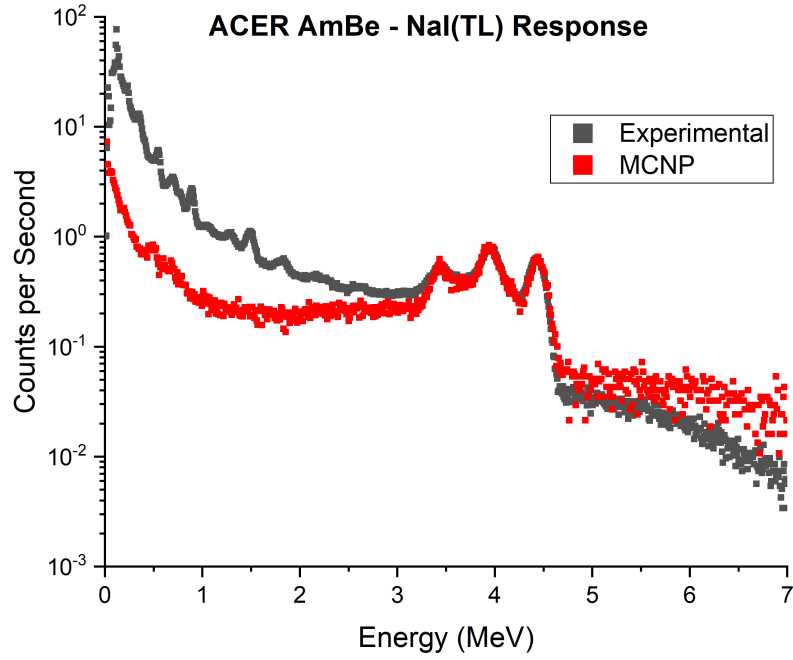


Figure 6.11: ACER experimental vs simulated NaI detector response.

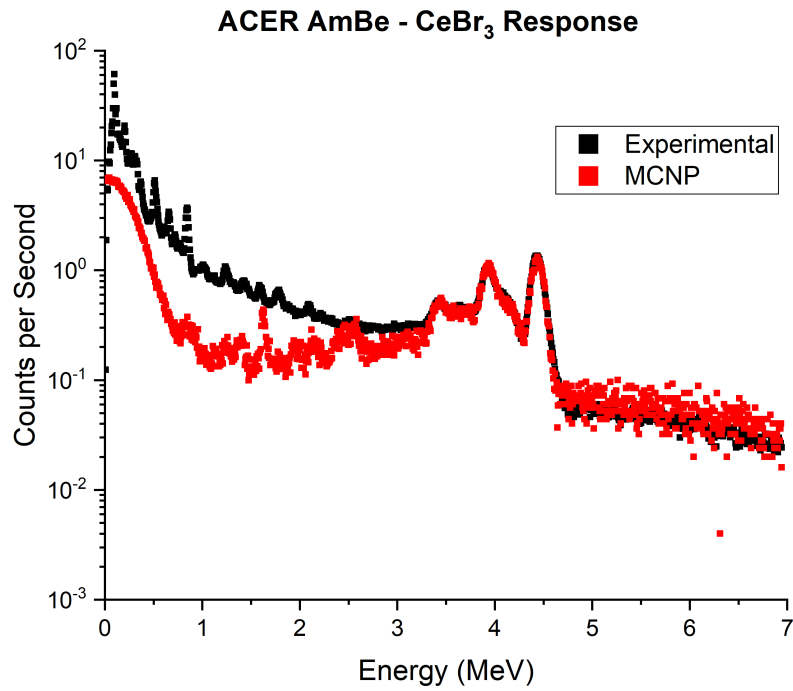


Figure 6.12: ACER experimental vs simulated CeBr₃ detector response.

6.2 AmBe Water Experiment in Test Enclosure

The first set of measurements taken in the testing facility with the benchmarking tool used the AmBe source. The test enclosure was filled with water at STP to a height of 6 ft, or approximately 2,500 gallons of water. The tool is made of 4 threaded aluminum rods that are held in place at one end by an aluminum disk. The disk marks the edge of the tool that is inserted first into the test chamber. Aluminum brackets and spacers were machined to slide onto the threaded rods to hold the detectors in place at consistent locations.

For this experiment, the prototype tool had the following configuration. The source was located 64 in. from the farthest edge of the tool. The centers of the near ^3He , near NaI(Tl), far ^3He , and far NaI(Tl) detectors were 22 in., 33 in., 46 in., and 57 in. from the source, respectively.

The prototype tool was fully inserted into the test enclosure without the source and a background measurement was taken for 3 hours. Then the source was added to the tool and re-inserted back into the enclosure. The source was approximately 40 cm from the inner edge of the test enclosure wall. An in-source measurement was taken for 1 hour. The background subtracted spectra for ^3He and NaI(Tl) detectors are shown in Fig. 6.13 and Fig. 6.14, respectively.

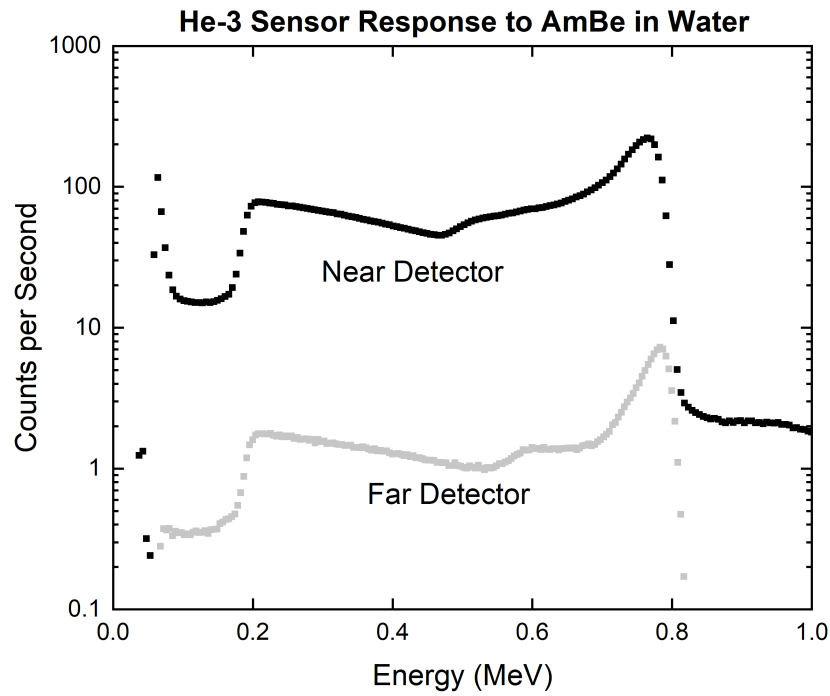


Figure 6.13: AmBe water experiment, ^3He background subtracted sensor response.

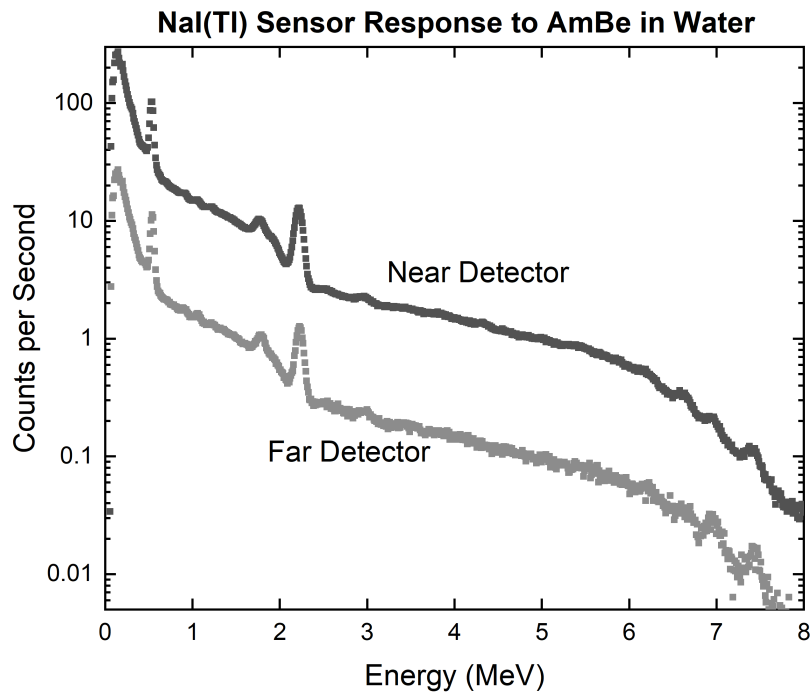


Figure 6.14: AmBe water experiment, NaI(Tl) background subtracted sensor response.

After the 1 hour measurement, the AmBe source was removed from the tool. The tool was placed back inside the enclosure and post-background measurements were taken for six consecutive 10-minute intervals, two 30-minute intervals, and one final 60-minute interval. The post-background NaI(Tl) measurements are shown in Fig. 6.15.

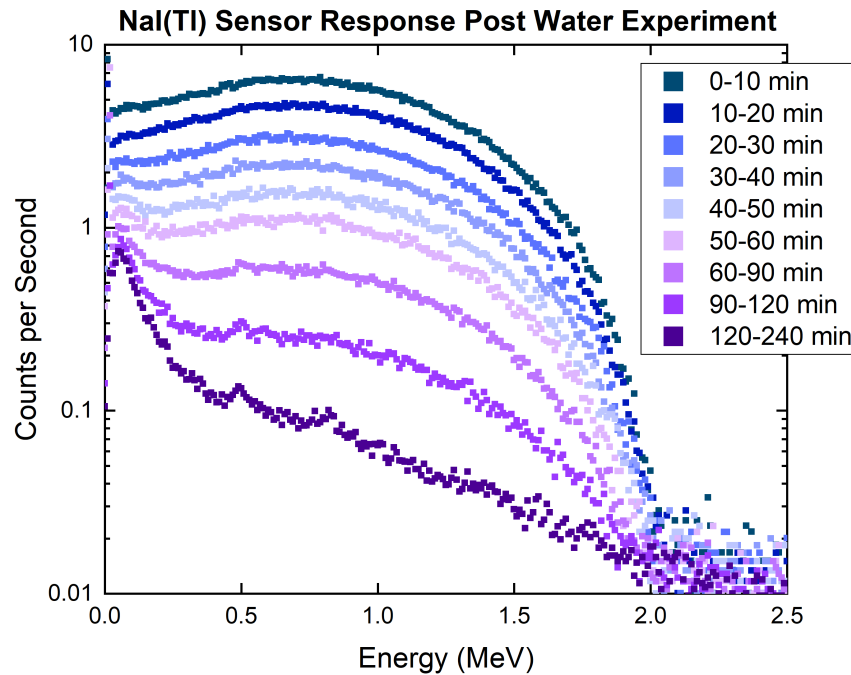


Figure 6.15: NaI(Tl) post-background measurements in 10 minute intervals.

6.3 MCNP Simulation of AmBe Water Experiment

The goal of this simulation is to compare the measured versus simulated detector responses from AmBe in the water-filled test enclosure. An MCNP model of the room, the test enclosure, and the benchmarking tool was created to simulate the experiment. Then, the simulated detector responses are compared to experimental measurements to assess the fidelity of the MCNP model and make improvements where needed.

6.3.1 MCNP6 Geometry

The MCNP6[®] geometry models room 107 of the king hall annex, with the test enclosure and benchmarking tool inside. The inside of room 107 is 18 ft deep, 19 ft wide, and 10 ft high. The west, east, and south walls are 12in. thick. The north wall is 18in. thick. The floor is 12 in. thick. The room's walls and floor are made of concrete. The south and north walls have doors that align with the middle of the room. The ceiling has blow-out panels and shielding above the test enclosure.

The test enclosure is located on the southwest corner of the room. The north and east walls of the enclosure are 8 in. thick and 7 ft tall. The inside of the test enclosure is 8 ft long and 6.5 ft wide. The pipe in the middle of the enclosure is suspended 3 ft from the floor and centered along the width of the enclosure. The pipe has an inner diameter of 8 in. with a wall thickness of 0.25 in. The shielding against the south wall of the enclosure measures 3 ft wide by 7 ft tall with a thickness of 12 in. There is a 1 in. deep hole cut out of the shielding where the end of the aluminum pipe is inserted.

The benchmarking tool detectors are modeled inside the pipe in a configuration matching the experimental setup. The middle of the detectors are 22 in. (near ³He), 33 in. (near NaI), 46 in. (far ³He), and 57 in. (far NaI) from the source location. The source was placed 64 in. from the tool edge that is inserted into the enclosure.

The door shielding is 3 ft wide, 7 ft tall, and 3 in. thick. The door to the hallway was shielded inside the room, while the outside wall was shielded outside the room. All shielding modeled is polyethylene with 8% boron content.

Similar to the ACER experiment, two simulations were run to represent the neutron and the gamma ray components of the AmBe source output separately. The neutron component was defined as an isotropic point source with an AmBe neutron distribution (see Fig. 4.2) [35]. The gamma ray component was defined as isotropic, monoenergetic, 4.44 MeV photons. The MCNP6[®] code was used to run 10^9 particle histories.

6.3.2 ^3He Detectors

The ^3He detectors were modeled as cylindrical volumes with a diameter of 2.5 cm and an active length of 20.3 cm. The near and far ^3He detectors were filled to 4 atm and 1.5 atm of pressure, respectively.

For the neutron simulation, light ion recoil and the neutron capture algorithm were turned on in the physics card to properly simulate the ^3He response. Protons, tritons, and helions were tracked inside the detector region. F6 neutron tallies were used to track the energy deposited inside the ^3He tubes by each particle. Then an F8 pulse height tally was assigned to each detector region. The F8 tallies were modified using PHL and GEB cards. The PHL card converts the energy deposited by protons, tritons, and helions into pulses with a built-in default gas gain factor for ^3He [36]. The GEB card was used to broaden the pulse height spectra to 2.5% FWHM at 764 keV. The near and far simulated ^3He detector responses were multiplied by the AmBe source strength (2.6 million neutrons per second) and are compared to experimental measurements in Fig. 6.13.

6.3.3 NaI(Tl) Detectors

The NaI(Tl) detectors were modeled as rectangular cylinders measuring 7.6 cm in diameter and 7.6 cm in length. F8 (pulse height) tallies were assigned to the detector cells to simulate the near and far NaI(Tl) responses. The GEB special tally treatment card was used to broaden both F8 tallies. Simulated NaI(Tl) responses were multiplied by the AmBe source strength (2.6 million neutrons per second). The experimental and simulated γ -ray spectra are shown in Fig. 6.17.

The MCNP6 results differ from the experimental spectra below 2 MeV. The discrepancy was suspected to be due to activation inside the NaI(Tl) crystal [29]. The effect is apparent in the post-experiment background measurements shown in Fig. 6.15. Therefore, the simulated results need to be corrected for neutron activation inside the NaI(Tl) crystals. The simulation procedure followed to account for activation is described in the next section.

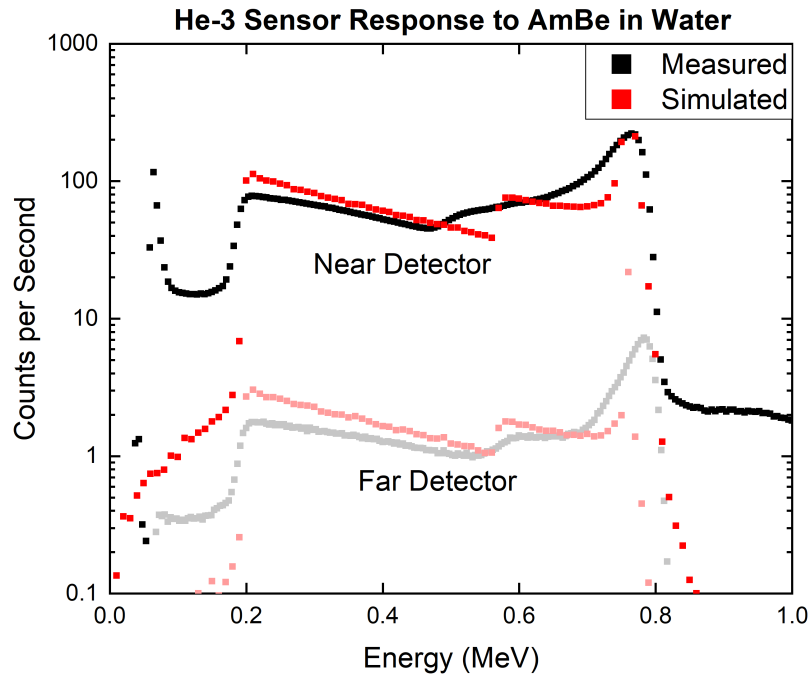


Figure 6.16: ^3He MCNP simulation versus experimental measurements.

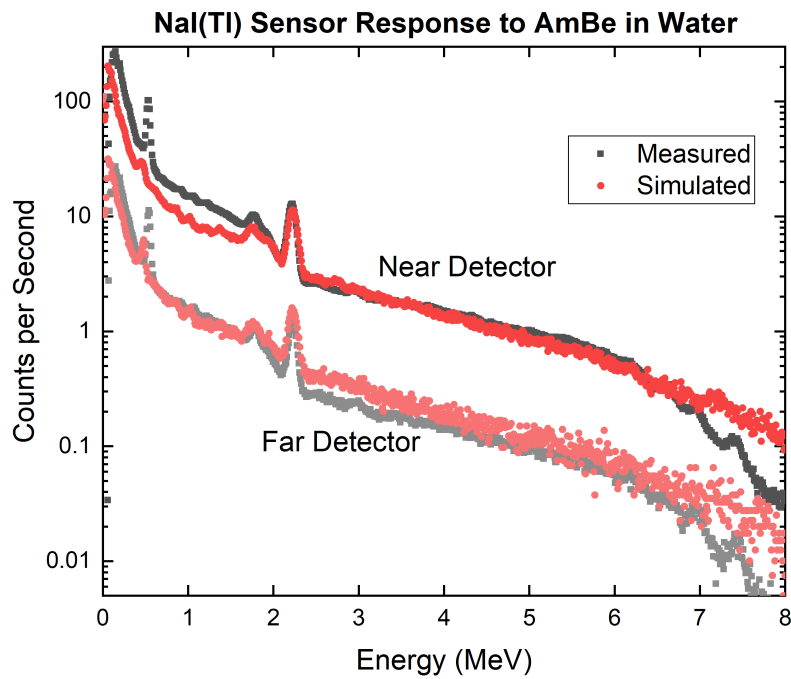


Figure 6.17: Preliminary MCNP simulation versus experimental measurements.

6.4 NaI(Tl) Activation

Due to discrepancies in the simulated versus experimental results, a closer look was taken at the interactions happening inside the NaI(Tl) detectors during measurements. As discussed before, AmBe emits neutrons with an average energy of 4 MeV and a maximum energy of 11 MeV. As source or scattered neutrons reach a NaI(Tl) detector, the ^{23}Na and ^{127}I inside the crystal are activated through reactions shown in equations 6.2 and 6.3.



The activated ^{24}Na and ^{128}I subsequently undergo beta decay with half-lives of 14.5 hours and 25 minutes, respectively [37; 38]. The prompt gamma rays and decay beta particles emitted by ^{24}Na and ^{128}I form a signal in the detector that was not modeled in the original MCNP simulation. However, the prompt gamma-ray component of a NaI(Tl) spectrum is an order of magnitude smaller than the beta decay component [29] and thus negligible. Therefore, the goal is to simulate the near and far NaI(Tl) detector response contributions resulting from neutron activation and subsequent beta decay of these isotopes.

6.4.1 Theory

Because it is not well known exactly how long the detector was exposed to the source before taking measurements, saturation activity is assumed. Therefore, for any one neutron capture reaction we assume a decay event. The neutron capture reaction rate (R) is described by Eq. 6.4, where $\Sigma(E)$ is the energy-dependent ENDF cross section for the (n,γ) reaction and $\phi(E)$ is the average energy-dependent neutron flux in each detector.

$$R = \int_0^{\infty} \Sigma(E) \cdot \phi(E) dE \quad (6.4)$$

In this case, the neutron capture reaction rate (R) represents the number of beta emissions by one isotope per second. Therefore, we can simulate a distributed beta source inside a NaI(Tl) crystal, with energies corresponding to the decay of a specific isotope, to determine the average detector response due to one decay event. The resulting pulse height spectra from the beta source can then be multiplied by the number of events happening in one second (R) to obtain the detector response from activation of an isotope at saturation activity.

6.4.2 MCNP Procedure

The full MCNP model of the facility, enclosure, and tool was used to obtain the neutron flux at the near and far NaI(Tl) detectors. An F4, flux averaged over a cell, neutron tally was assigned to the volume of each NaI(Tl) crystal. The source was modeled using the neutron energy distribution of AmBe. The simulation ran for 10^9 particles. The average energy-dependent neutron flux inside the near NaI(Tl) detector is shown in Fig. 6.18.

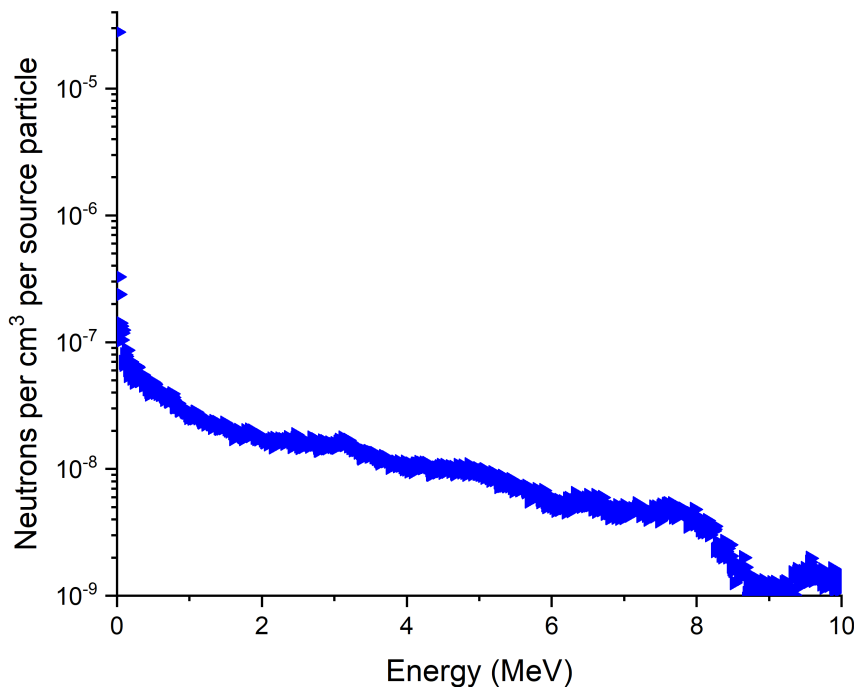


Figure 6.18: Energy-dependent F4 neutron tally in near NaI(Tl) detector.

The ENDF (n, γ) reaction cross sections for ^{23}Na and ^{127}I are shown in Fig. 6.19. The neutron activation reaction cross-sections for ^{23}Na is orders of magnitude smaller than for ^{127}I . Also, ^{24}Na has a longer half-life (14.5 hours) than ^{128}I (25 minutes). Therefore, the contribution from the activation of ^{23}Na is negligible and only the contribution from the decay of ^{128}I will be considered [39].

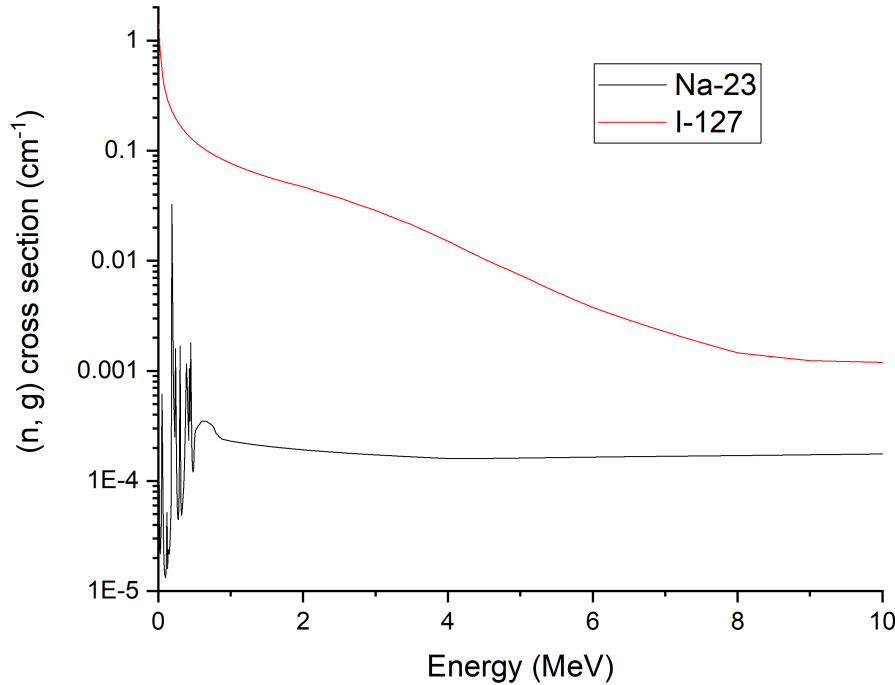


Figure 6.19: ENDF/B (n, γ) cross sections for ^{23}Na and ^{127}I

The energy-dependent neutron flux $[\phi(E)]$ from each detector was multiplied by the energy-dependent (n, γ) cross section $[\Sigma(E)]$ of ^{127}I and integrated to obtain the number of activation/decay events per source particle per second (R), see Eq. 6.4. The activation rate of the near and far NaI(Tl) detectors are 4.06×10^{-7} and 5.37×10^{-8} events per source particle per second, respectively. Because more neutrons arrive at the near NaI(Tl) detector, the rate of activation is much higher. As a quick comparison, the ^{23}Na activation rate for the near and far NaI(Tl) detectors are 9.1×10^{-11} and 1.3×10^{-11} activation/decay events per source particle per second, respectively. As stated before, the activation rate for ^{23}Na is three to four orders of magnitude lower than for ^{127}I , therefore it is ignored.

To simulate the NaI(Tl) response due to ^{128}I decay, an evenly distributed beta source was simulated inside a NaI(Tl) detector. A 7.6 cm x 7.5 cm (3 in. by 3 in.) cylindrical NaI(Tl) crystal was modeled in MCNP6[®] with a distributed beta source corresponding to the beta decay of ^{128}I [40]. The simulation ran for 10^9 particle histories. The resultant pulse height spectrum (F8 Tally) represents the NaI(Tl) detector response from betas emitted per decay of each ^{128}I isotope, see Fig. 6.20. The spectrum was then scaled by the near and far detector reaction rates (R) and the AmBe source strength to approximate the NaI(Tl) responses due to the activation of ^{127}I .

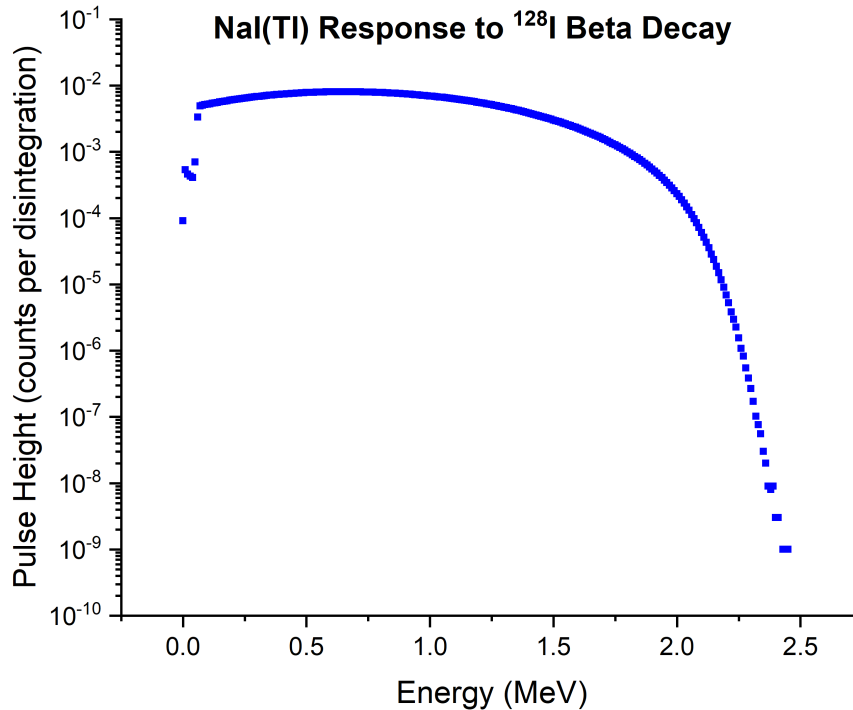


Figure 6.20: MCNP pulse height tally (F8) for NaI(Tl) with a distributed beta source.

6.5 MCNP Simulation of AmBe Water Experiment with NaI(Tl) Activation

The estimated spectra from the decay of ^{128}I was added to the previously simulated near and far detector responses. The combined spectra better matches experimental results as shown in Fig. 6.22. A close up of the previous figure shows the simulation results with and without activation added, see Fig. 6.22. Even though the activation correction improved the NaI(Tl) simulated spectra below 2 MeV, the near and far experimental data has prominent peaks at 511 keV that are not matched by simulations.

Many attempts to improve the simulation fell flat without any promising leads. First, the boron content of the shielding was exaggerated in simulations to determine whether it was originally simulated correctly. Following neutron capture, boron emits a 478 keV gamma ray that we thought may contribute to the missing peak. However, simulations with high boron content and even with extra shielding inside the test enclosure did not change the NaI(Tl) results significantly, but instead added a peak at a lower energy than the missing peak. These simulations confirmed that the shielding was modeled correctly and was not the source of the discrepancy.

Another source for the discrepancy could be that the MCNP model is simplified and things like support brackets, PMT tubes, source casing, and electronic cables are not modeled. Therefore, the MCNP model was altered by adding common materials found in PMT tubes [41; 42] right next to the NaI(Tl) crystal, as well as adding common water impurities to medium. However, after the addition of over a dozen isotopes to the geometry, the simulation results did not improve.

Two Master's theses and a report published by PNNL found a similar discrepancy between measured and simulated data [43–45]. All three reports found that while there is a prominent 511 keV peak in their experimental data, simulations done with MCNP do not have that feature. Further investigation into this issue is needed in future research.

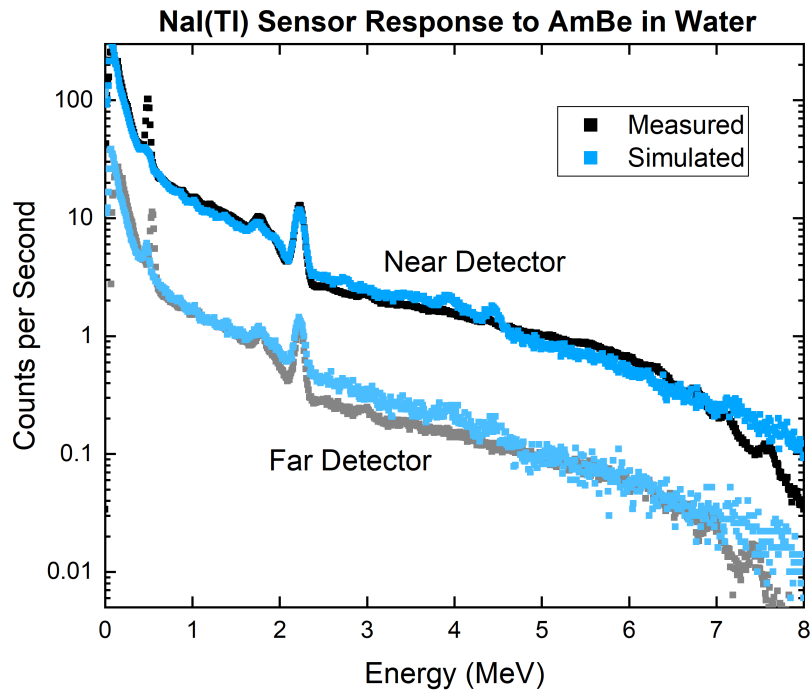


Figure 6.21: MCNP NaI(Tl) water simulation with AmBe source vs. experimental results.

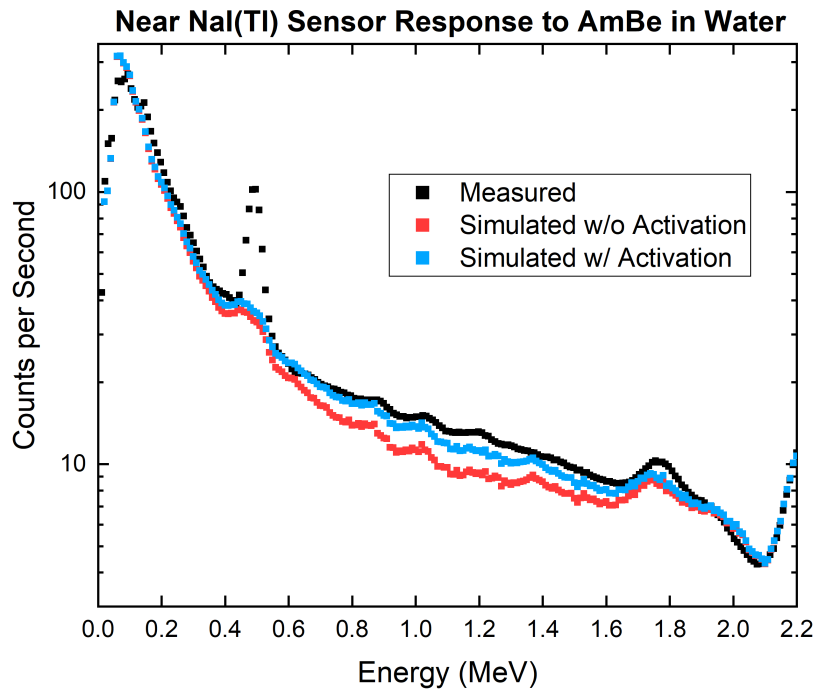


Figure 6.22: MCNP NaI(Tl) simulation with activation added versus experimental results.

Chapter 7

DT Experiments and Simulations

The following chapter describes the compilation of an inelastic and capture gamma ray database and a series of DT generator experiments with their corresponding simulations. The gamma ray database was created using MCNP simulations of 14.1 MeV neutrons, such as those emitted by the DT generator, interacting with different isotopes and recording the energy deposited by gamma rays that resulted from inelastic scatter or a neutron capture event. The database was created as a tool to determine the origins of peaks we may observe in experimental measurements.

Experiments were conducted using the benchmarking tool with a DT neutron generator inside the testing facility. The test enclosure was filled with different materials, such as: water, dry limestone, wet limestone, dry sand, and wet sand. The work to produce the MCNP simulation model was described in previous chapters. However, the model was modified to replace the AmBe source with the DT generator and update detector locations. This chapter discusses in detail how the MCNP model was updated and compares simulation results with experimental measurements.

7.1 Gamma Ray Database

Before experimental measurements were taken using the DT generator, it was decided to identify the gamma rays emitted by materials being tested when exposed to a DT neutron source. A capture and inelastic gamma ray database from 14.1 MeV neutrons was compiled using MCNP simulations. The goal of this study was to simulate individual isotopic responses to high-energy neutrons and understand the types and energies of gamma rays that will be observed.

A list of elements commonly found in oil well logging applications was compiled to determine isotopes of interest. Each isotope was simulated as an effectively infinite medium surrounding a 14.1 MeV neutron point source. An F6 photon tally was used to calculate the energy deposited within the medium from capture and inelastic gamma rays. The resulting energy deposition distribution from each element was plotted in a semi-log plot and major peaks were identified. The most prominent peaks for each element were compiled in tables sorted by element and by energy. These tables help identify the element and reaction that may cause a peak in question when studying experimental gamma-ray spectra.

The MCNP model used for these simulations consists of a sphere, 13 ft. in diameter, inside a void. The sphere was filled with one element or isotope at a time. Each isotope was assigned a density between 0.5 and 1 g/cm³. An isotropic 14.1 MeV neutron point source was placed at the center of the sphere. An F6 tally was assigned to the volume of the sphere to obtain the energy deposited by neutron capture and inelastic gamma rays in the volume. The MCNP F6 Tally results were plotted for each of the 21 isotopes simulated.

The gamma ray database, sorted tables, and a description of the simulations carried out to obtain these results can be found in [appendix A](#).

7.2 DT Experiments in Test Enclosure

After taking measurements and performing simulations using an AmBe neutron source, experiments were conducted with a DT neutron generator. The measurements collected from both AmBe and DT sources serve to improve our MCNP model and provide data to test the MCLLS code. For these sets of experiments, the test enclosure was filled with different wet and dry materials to measure neutron and gamma-ray detector responses using the DT generator. The tool configuration used, measurement systems, type of materials, and experimental procedure are discussed in this section.

7.2.1 Tool Configuration

The overall design of the tool was kept the same; a neutron source, near and far neutron detectors, and near and far gamma ray detectors. However, a few changes were made to the tool from the configuration used to take measurements with the AmBe source. A major change was the replacement of the AmBe source with a DT generator. The near ^3He detector was also replaced with a BF_3 detector. The source and sensor locations within the tool also changed as modifications were made. More details on the tool components and dimensions are provided below.

Tool Components

Two new components were added to the tool configuration for the next set of experiments; the AmBe source was replaced with a DT generator and the near ^3He detector was replaced with a BF_3 proportional counter. The new source is a DT Pulsed Neutron Generator (PNG), model B322, obtained from ThermoFischer Scientific in Colorado Springs, CO. The DT generator emits 14.1 MeV neutrons with a 1 KHz frequency and a 10% duty cycle. To be specific, the DT generator produces a pulse every microsecond and neutrons are emitted during the first 1/10 of each microsecond. The DT generator is operated using a computer interface where the beam current and voltage can be adjusted to produce a maximum output of 2×10^8 neutrons per second.

A BF_3 proportional counter, filled to 1 atm, was used as the near neutron detector. The far neutron detector was a ^3He proportional counter, filled to 2 atm. And finally, two cylindrical $\text{NaI}(\text{Tl})$ detectors were used as the near and far gamma-ray sensors. A lead shield was placed between the source holder and the nearest detector to reduce dead time in the detectors. The lead shield reduces direct streaming of radiation from the source to the detectors.

Tool Dimensions

As previously described, the tool is made of a thick aluminum disk at one end with four 8 ft long, equally spaced, threaded aluminum rods attached along its perimeter. Aluminum brackets slide onto the rails and hold each component at a specific location. The tool is inserted into the testing enclosure by sliding the end of the tool with the aluminum disk into the horizontal pipe in the middle of the enclosure. The tool is assembled by sliding the far detectors and their brackets through the rails until reaching the aluminum disk. Then the near detectors, the shielding, and lastly the source are slid into place.

The DT generator is made of an aluminum housing that contains a tritium target and a particle accelerator. Separate to the body of the DT generator is an aluminum bracket that holds the circuit board and connectors. The aluminum body is held in place by aluminum brackets that slide and lock onto the rails of the tool at a consistent location. The DT generator's aluminum housing is 40 in. long with a 2 in. diameter. The tritium target, where neutrons are emitted, is located 5.5 in. from one end of the aluminum housing. The DT generator is oriented in the tool such that the edge closest to the source faces the near detector. The lead shield between the source and the BF_3 detector is 2 in. thick and located 5 in. away from the edge of the DT generator's aluminum housing, or 10.5 in. away from the neutron source.

The BF_3 proportional counter has a pressure of 1 atm and is 12 in. long with a 1 in. diameter and is located closest to the source. The far neutron detector is a ^3He proportional counter. The ^3He is 12 in. long, has a 1.5 in. diameter, and is filled to 2 atm of pressure.

Two cylindrical, 3 in. by 3 in. NaI(Tl) detectors were used to obtain the near and far gamma-ray signals. The center of the BF₃, near NaI(Tl), ³He, and far NaI(Tl) detectors (not including connectors or PMTs) were 17 in., 35 in., 47 in., and 65 in. away from the neutron source, respectively.

7.2.2 Measurement System

A CAEN DT5730 digitizer was used to collect data from all four sensors, two gamma-ray and two neutron detectors. The digitizer records all analog waveforms of individual events in each sensor. The digitizer was set up to output the pulse height of each waveform and a corresponding timestamp for each event. A waveform generator was used to synchronize the DT generator pulses and the digitizer. The waveform generator outputs a 1 KHz digital pulse that triggers the DT generator and an analog tail-pulse that is recorded by the digitizer. The timestamp of each tail-pulse matches the beginning of each 1/10 microsecond period during which neutrons are emitted. The waveform, DT generator, and digitizer are connected to a computer where all output data are stored.

7.2.3 Materials

Five experiments were conducted using the DT neutron generator. In each experiment, the test enclosure was filled with one of the following materials: water, dry limestone, wet limestone, dry sand, and wet sand. During the water experiment, the test enclosure was filled with 2,500 gallons of water. For the dry limestone and dry sand experiments, the test enclosure was filled with limestone chips or sand to a height of 6 ft. For the wet limestone experiment, water was then added to the limestone until the moisture content reached 63%. And for the wet sand experiment, water was added to the sand until moisture content reached 15%. Although the water mixed well with the limestone, the water in the wet sand experiment all sunk to the bottom of the test enclosure, which may prove difficult to simulate accurately.

7.2.4 Experimental Procedure

The DT generator was purchased from Colorado and shipped to the laboratory facility. When the DT generator arrived, the main chamber was filled with SF₆ to 110 psig. The DT generator was tested extensively before beginning any experiments. Once the operators felt comfortable with the DT generator, an experimental procedure was determined to keep experiments consistent.

The experiments were performed as follows. The test enclosure was filled with the appropriate material for an experiment. The tool was inserted into the enclosure and the following experimental procedure began:

1. 5 minute NaI(Tl) calibration
2. 2 hour background measurement
3. Second 5 minute NaI(Tl) calibration
4. 1 hour DT ON measurement
5. Third 5 minute NaI(Tl) calibration
6. 4 hour background measurement

First, the DT generator was turned on by powering its circuit board with 200 V at 24 μ A. Using the computer interface, the DT generator was configured to operate at 40 kV and 40 μ A. Then, the neutron output was allowed to stabilize for at least 1 minute before taking measurements. Three calibrations were performed throughout the experiment to make sure no gain shift occurred over time. The procedure was repeated using different materials and was kept consistent among experiments to allow direct comparisons.

7.2.5 Sample Experimental Results - Water

The sensor responses obtained from the water experiment using the DT neutron source are shown in Figs. 7.1-7.3. All experimental measurements shown were energy calibrated, background subtracted, and normalized per unit time. Expected and unexpected spectral features are discussed next.

BF₃ - Near Neutron Detector

The BF₃ spectrum (see Fig. 7.1) features two peaks at 2.31 MeV and 2.79 MeV that correspond to the energy deposited by secondary particles produced in the gas. When ¹⁰B absorbs a neutron, an alpha particle and a recoil ⁷Li ion are ejected in opposite directions. In this type of reaction, 96% of the time the ⁷Li ion is left in an excited state instead of its ground state. When left in its ground state, both the ⁷Li ion and the alpha particle are emitted with higher kinetic energy, 1.02 MeV and 1.78 MeV, respectively. The sum of the kinetic energies of both particles accounts for the smaller peak at 2.81 MeV because this only occurs 4% of the time. On the other hand, 96% of the time when the ⁷Li ion is left in an excited state, both particles are emitted with lower kinetic energies which account for the 2.31 MeV peak in the spectrum. The wall effect is also noticeable in the spectrum. This occurs when the neutron capture event occurs near the wall of the detector and either the ⁷Li ion or the alpha particle escape the detector volume before depositing all of its kinetic energy. Therefore we can see a ⁷Li escape peak at 1.47 MeV and an alpha escape peak at 0.84 MeV.

³He - Far Neutron Detector

The ³He sensor response (see Fig. 7.2) has the expected spectral shape. There is a prominent 764 keV energy peak that results from the energy deposited by secondary particles after a neutron absorption event. As neutrons enter the detector volume, thermal neutrons are absorbed by the ³He atoms and a proton and a triton ion are emitted. The proton and triton are emitted with 573 keV and 191 keV of kinetic energy, respectively. When both particles deposit their full energy, it results in the 764-keV energy peak seen in the spectrum. Due to the wall effect, the triton escape peak at 573 keV and proton escape peak at 191 keV can also be observed in Fig. 7.2.

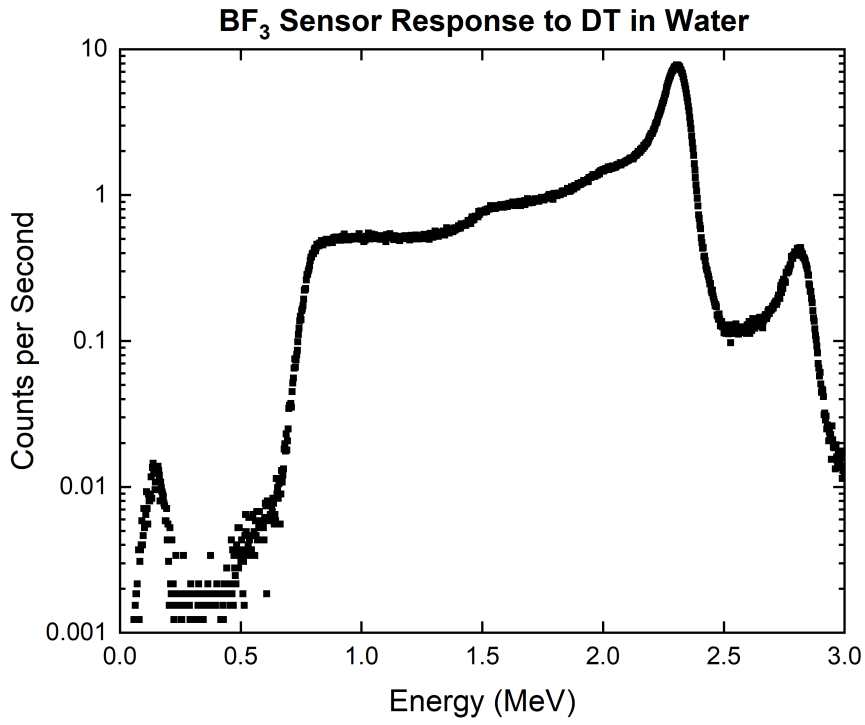


Figure 7.1: BF₃ water measurement with DT source.

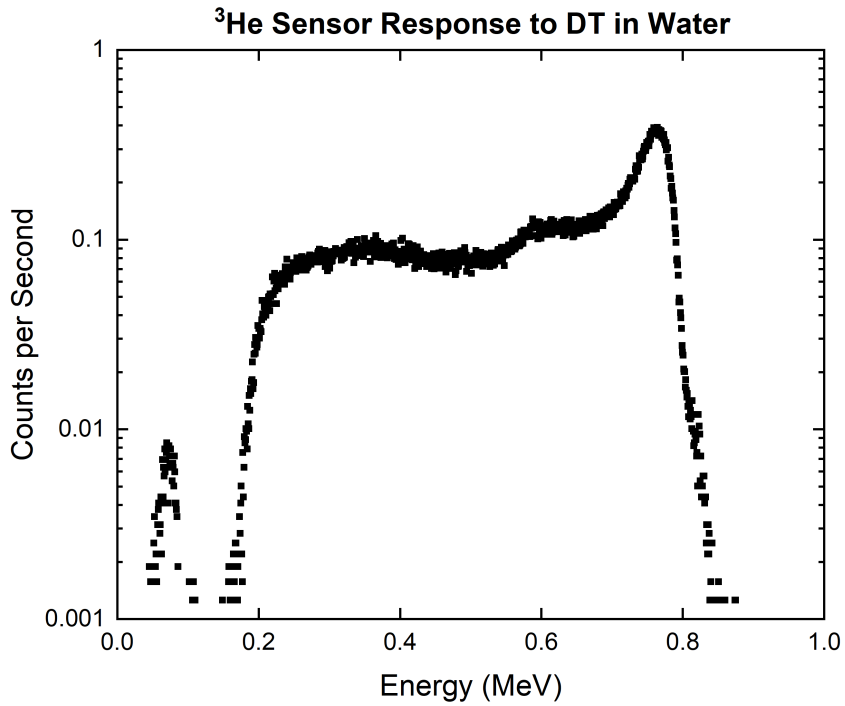


Figure 7.2: ³He water measurement with DT source.

NaI(Tl) - Near and Far Gamma-Ray Detector

The near and far NaI(Tl) detector responses, seen in Fig. 7.3, have the same spectral features with the only difference being the intensity of the signal, as expected. The near NaI(Tl) detector recorded approximately ten times more counts than the far detector. Both spectra have several energy peaks that we can identify using the Gamma Ray Database in Appendix A. The two most visible peaks are the 511 keV annihilation peak due to pair production and the 2.22 MeV hydrogen peak due to neutron capture. We can also observe several high-energy gamma-ray peaks between 5 MeV and 7 MeV that are a result of gamma rays produced due to the inelastic scatter of neutrons with boron, oxygen, and lead. A less distinguished peak (due to poor counting statistics) can be seen between 7 MeV and 8 MeV, which is likely caused by gamma rays emitted due to neutron capture in the aluminum tube surrounding the tool. The most prominent features of the spectra are at the energies seen in Table 7.1.

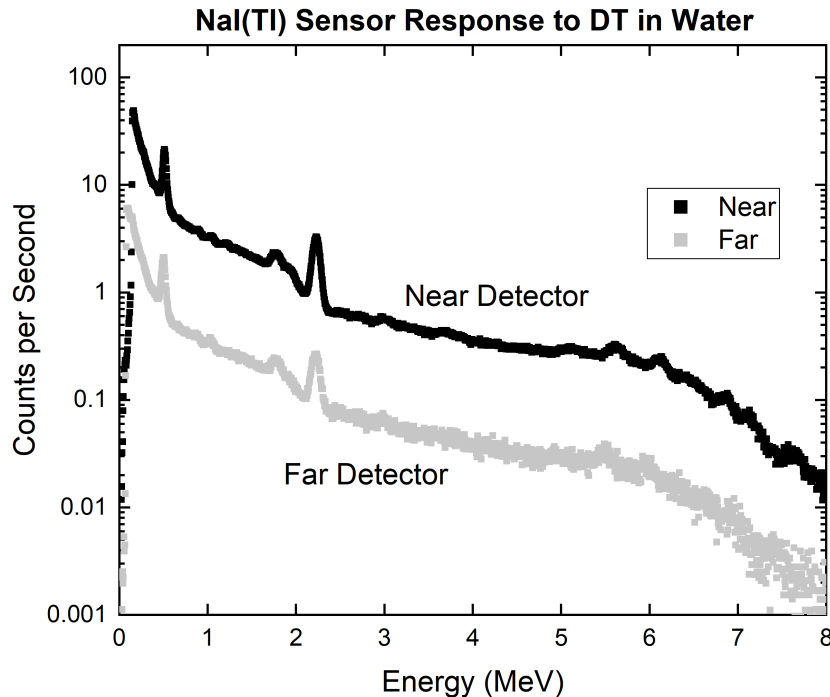


Figure 7.3: NaI(Tl) water measurement with DT source.

Table 7.1: Spectral features of NaI(Tl) response due to 14.1 MeV neutrons.

Energy	Element	Phenomenon
511 keV	-	Annihilation
1.72 MeV	Hydrogen	Single Escape Peak
2.22 MeV	Hydrogen	Neutron Capture
5.85 MeV	Boron	Inelastic Scatter
6.13 MeV	Oxygen	Inelastic Scatter
6.74 MeV	Boron, Lead	Inelastic Scatter
7.1 MeV	Oxygen	Inelastic Scatter
7.69 MeV	Aluminum	Neutron Capture
7.73 MeV	Aluminum	Neutron Capture

7.3 MCNP Simulation of DT Experiments

The MCNP model used for these sets of simulations was based on the one used for the AmBe water simulation in Chapter 6. The model was modified to fit the experimental set up used to collect the DT measurements. There were four major changes to the MCNP model:

- The AmBe source was replaced with a DT neutron source
- The near ^3He detector was replaced with a BF_3 detector
- The detectors moved slightly from their previous locations
- The MCNP physics settings were modified to simulate the BF_3 detector

The active area of the BF_3 tube was modeled as a cylinder, 8.8 in. long with a 0.5 in. diameter. The detector volume was filled with ^{10}B and ^{19}F with a density of 0.0028 g/cm^3 . The middle of the BF_3 active area was 17 in. from the source. The active area of the ^3He tube was modeled as a cylinder with a length of 8 in. and a 0.5 in. diameter. The detector was filled with 0.00025 g/cm^3 of ^3He and the middle of the volume was located 47 in. away from the source.

The near and far NaI(Tl) detectors were modeled as cylinders, 3 in. long with a 1.5 in. diameter. The middle of the near and far detectors were 35 in. and 65 in. away from

the source. For the DT simulations, the source was defined as isotropic, monoenergetic, 14.1 MeV neutrons. The source was located 64 in. from the farthest end of the tool.

7.3.1 Material Definitions

The PNNL materials compendium was used to assign material properties to the MCNP model. The limestone and sand material compositions are shown in Tables 7.2 and 7.3, respectively. Water was added to each material composition, depending on the level of moisture or porosity, to simulate the bulk materials inside the testing enclosure during measurements. For example, the experiment performed using dry limestone was simulated with a 5% moisture content because the material was slightly rained on before being loaded into the test enclosure.

Table 7.2: Material composition for limestone, density = 2.610 g/cm³ [2]

Element	ZAID	Weight Fraction	Atom Fraction
H	1001	0.000899	0.017089
C	6000	0.113782	0.181445
O	8016	0.497802	0.595930
Na	11023	0.000373	0.000310
Mg	12000	0.047860	0.037715
Al	13027	0.004254	0.003019
Si	14000	0.024419	0.016653
S	16000	0.000201	0.000120
K	19000	0.000334	0.000163
Ca	20000	0.305865	0.146173
Ti	22000	0.000361	0.000145
Fe	26000	0.003513	0.001205
Pb	82000	0.000337	0.000031

Table 7.3: Material composition for sand, density = 1.70 g/cm³ [2]

Element	ZAID	Weight Fraction	Atom Fraction
H	1001	0.007833	0.135405
C	6000	0.003360	0.004874
O	8016	0.536153	0.583890
Na	11023	0.017063	0.012932
Al	13027	0.034401	0.022215
Si	14000	0.365067	0.226483
K	19000	0.011622	0.005179
Ca	20000	0.011212	0.004874
Fe	26000	0.013289	0.004146

7.3.2 Simulation Physics

In order to simulate the ³He and Bf₃ proportional counters correctly, the MCNP physics card was set to mode N, P, H, T, A, #, where, the symbols indicate the type of particles to be transported, such as: neutrons (N), photons (P), protons (H), tritons (T), alpha particles (A), and heavy ions (#). The neutron physics card (PHYS:N) was set to turn on light ion recoil and the neutron capture algorithm (7th entry).

Energy deposition (F6) tallies were assigned to the active region of the ³He detector to record the energy deposited by protons (H) and tritons (T) in the volume. A pulse height (F8) tally with the PHL option was set to convert the energy deposited by protons and tritons into a pulse height tally with a built-in default gas gain factor for ³He. A GEB special tally treatment card with $a = 0.0$, $b = 0.0537$, and $c = 0.0$ was used on the F8 tally to broaden the spectrum.

Energy deposition (F6) tallies were also assigned to the active region of the BF₃ detector to record the energy deposited by alpha particles (A) and ⁷Li ions (#). A pulse height (F8) tally with PHL was used to convert the energy deposited by alpha and ⁷Li ions into a pulse height spectrum with a default function for the BF₃ gas gain factor. A GEB special tally treatment card was used to broaden the BF₃ pulse height (F8) tally. The GEB card parameters were: $a = 0.0$, $b = 0.09$, and $c = 0.0$. The GEB parameters used to broaden both

the BF_3 and ^3He spectra were obtained by following the procedure described in Section 3.2.5, an example of this process was described in Section 6.1.2.

7.4 Simulation Results vs Experimental Measurements

In this section, the MCNP simulated detector responses are compared directly with experimental measurements of the DT generator. Five experiments were carried out using the DT generator as a neutron source. The test enclosure was filled with a different material for each experiment. The materials tested were: water, dry limestone, wet limestone, dry sand, and wet sand. An MCNP model of the test facility, the test enclosure, and the benchmarking tool was used to generate simulated detector responses from a DT neutron source. In the model, the material inside the test chamber was modified to match each experiment. In each simulation, the pulse height (F8) tally for each detector was binned to match the corresponding experimental detector output.

The near and far NaI(Tl) simulated spectra for all materials has been corrected to account for activation by following the procedure described in Section 6.4. The source strength for each experiment was determined by finding a constant that when multiplied by simulated detector responses, matches experimental measurements.

To find the source strength, each of the measured and simulated NaI(Tl) responses had a Gaussian function fit to the 2.22 MeV hydrogen peak. The Gaussian fits were integrated to find the net number of counts under the peak and divide the net experimental counts by the net simulated counts to find the multiplication constant. The the full energy peak of the simulated and experimental neutron responses were also fit with Gaussian functions and integrated to estimate their respective multiplication constants. The multiplication factor for most detectors were within 5% of each other for each experiment and an estimated source strength could be determined (see Table 7.4).

Table 7.4: Estimated DT source strength.

Experiment	Estimated Source Strength
Water	2.0×10^6 n/s
Dry Limestone	2.8×10^6 n/s
Wet Limestone	2.0×10^6 n/s
Dry Sand	3.5×10^6 n/s
Wet Sand	3.0×10^6 n/s

7.4.1 Water

The experimental and simulated responses for the BF_3 detector, ^3He detector, and near and far $\text{NaI}(\text{Tl})$ detectors are shown in figures 7.4, 7.5, and 7.6, respectively. The simulated BF_3 detector response closely fit experimental measurements. While the fit was not perfect, the tally used to obtain the simulated response was broadened using a simple fit with only one parameter. Overall, MCNP performed well simulating the BF_3 detector. This was somewhat surprising as very little literature was found on BF_3 simulations using MCNP[®].

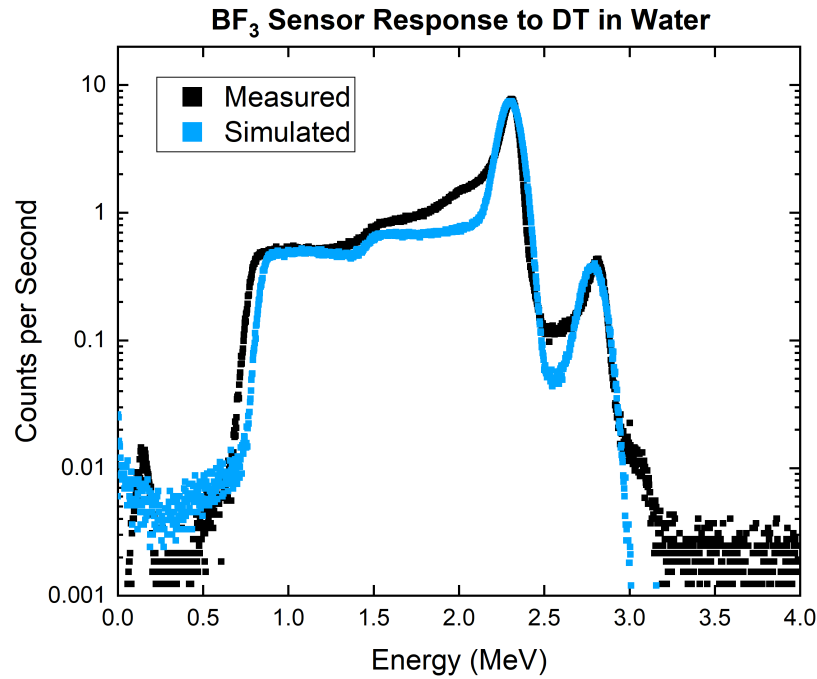


Figure 7.4: MCNP BF_3 water simulation with DT source vs. experimental results

The simulated ^3He detector response matches the 764 keV full-energy peak and the 573 keV triton escape peak. However, below 550 keV the simulated response is much higher than the measured spectrum. This feature was not apparent in the AmBe simulations, but is consistent in all DT simulations regardless of the material in the test enclosure. The source for the higher response below 550 keV is not known but it does not affect the number of counts under the full energy peak.

The simulated near and far NaI(Tl) detector responses closely match experimental measurements. All but one of the spectral features identified in Table 7.1 (Section 7.2.5) are present in the simulated responses. As seen in Fig. 7.5, the 511 keV peak present in the near and far experimental measurements are not matched by simulation. The simulated far NaI(Tl) detector response has much larger 511 keV peak that nearly matches the experimental spectrum. However, the simulated near NaI(Tl) detector response is almost completely missing the 511 keV peak. This discrepancy was also observed in the AmBe water experiment simulations (Section 6.5), and can be seen throughout the all the NaI(Tl) DT simulations. The reason for this error is not yet known. Both near and far detectors are modeled with identical dimensions, materials, densities, physics settings, and tally definitions.

The most prominent feature of the NaI(Tl) responses to water is the 2.22 MeV neutron capture gamma ray from hydrogen. Also seen in Fig. 7.6, the 1.72 MeV single escape peak is visible but slightly underestimated. In contrast, the magnitude of the hydrogen peaks in the near and the far detector are matched well by simulation.

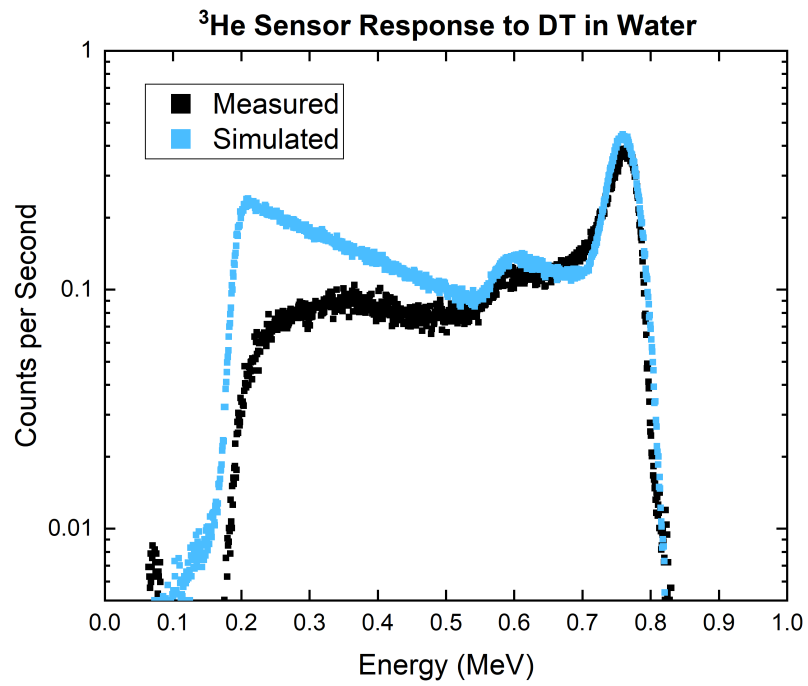


Figure 7.5: MCNP ^3He water simulation with DT source vs. experimental results

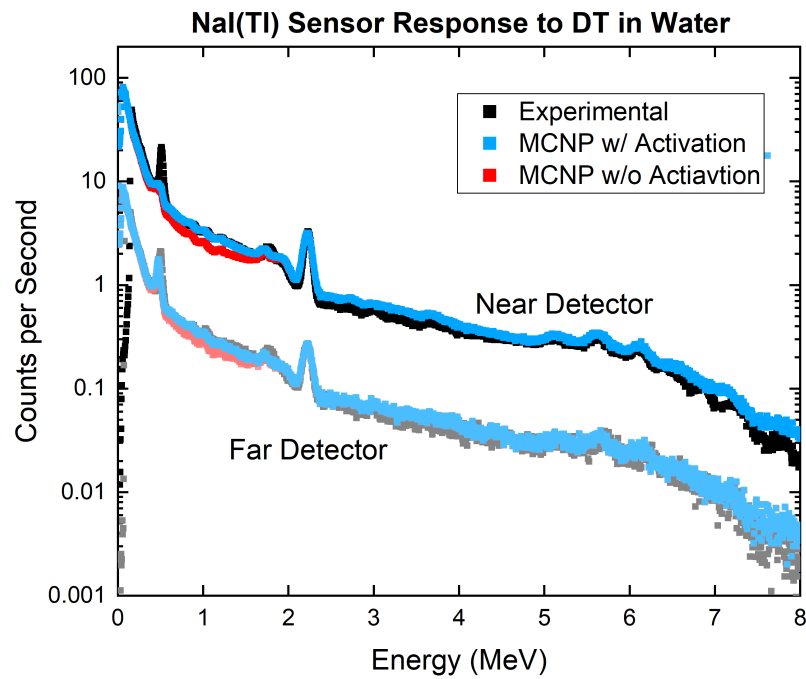


Figure 7.6: MCNP NaI(Tl) water simulation with DT source vs. experimental results

7.4.2 Limestone

The limestone acquired for the experiment was purchased and delivered to the loading dock of the King Hall Annex. Prior to loading the limestone into the test enclosure, a light rain dampened the material. The true moisture content of the material was not well known at the time of measurement. However, based on analysis performed by a colleague and several simulation trials, the 'dry' limestone experiments have approximately 5% moisture content. All simulated responses were scaled by a source strength of 2.8×10^6 neutrons per second.

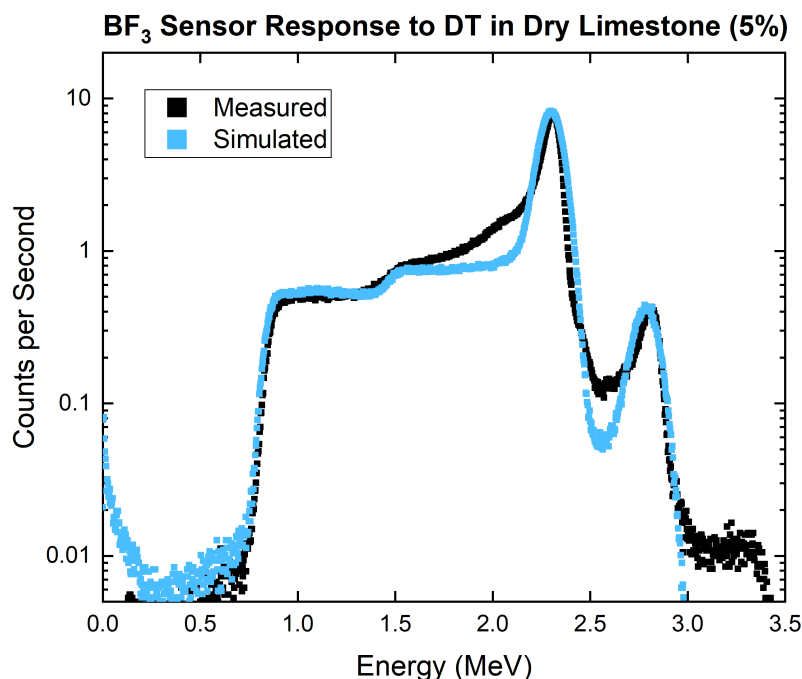


Figure 7.7: MCNP BF₃ dry limestone simulation with DT source vs. experimental results

The measured and simulated BF₃, ³He, and NaI(Tl) detector responses to a DT neutron source in a limestone medium can be seen in Figures 7.7, 7.8, and 7.9, respectively. Both neutron detector simulated responses match experimental results well. The only major discrepancy between simulation and measurements is below 550 keV in the ³He; this observation was previously discussed and will continue to appear in all ³He simulation results.

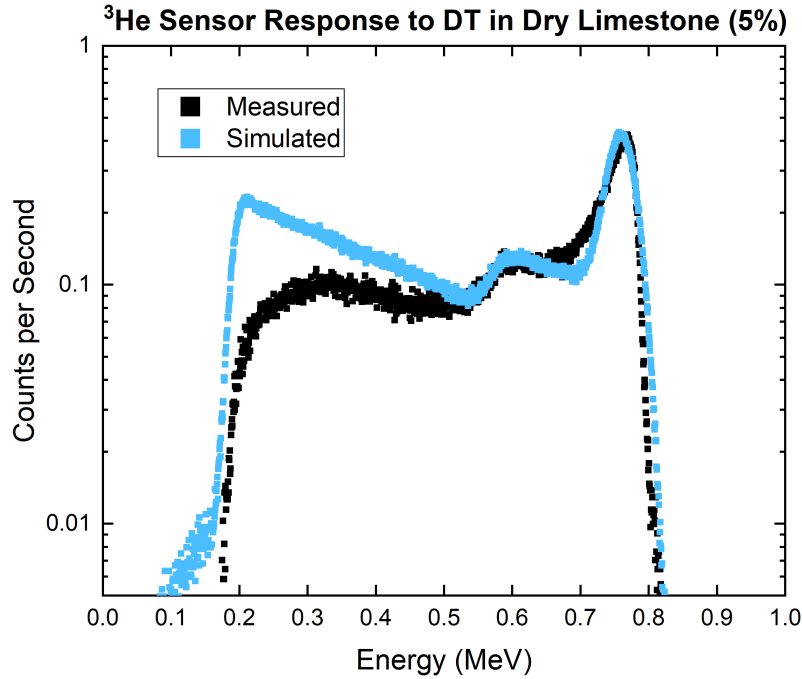


Figure 7.8: MCNP ^3He dry limestone simulation with DT source vs. experimental results

The near and far NaI(Tl) simulated versus measured responses are shown in Fig. 7.9. Both near and far detector simulations match the experimental spectra well. The 511 keV discrepancy persists. The simulation slightly underestimated the hydrogen peak in both detectors. This is likely due to simulating a lower amount of moisture than what was actually present during measurements. Previously, it was stated that due to unexpected rain, the limestone absorbed an unknown amount of water. Simulations also underestimated the hydrogen single-escape peak. This discrepancy was also observed in the water simulations but it was much less prevalent.

Signature high-energy gamma-ray peaks due to the interaction of neutrons in the limestone are visible in the NaI(Tl) spectra. These gamma rays are a result of inelastic scatter or neutron capture events. Several spectral features seen in the NaI(Tl) spectra are listed in Table 7.5. The calcium and magnesium in the limestone produce recognizable patterns and strong enough signals to visibly identify their peaks.

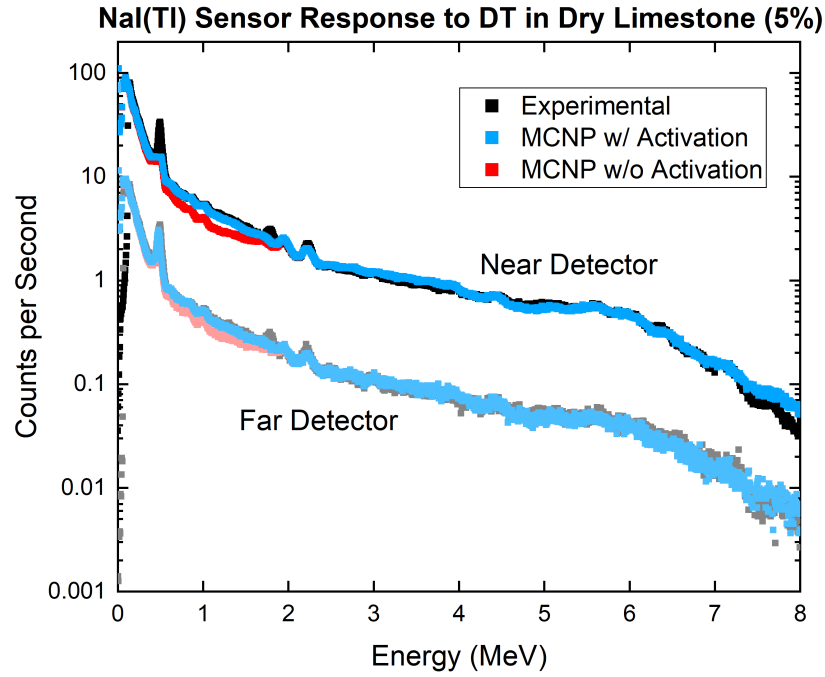


Figure 7.9: MCNP NaI(Tl) dry limestone simulation with DT source vs. experimental results

Table 7.5: Spectral features of NaI(Tl) response due to 14.1 MeV neutrons in limestone.

Energy	Element	Phenomenon
511 keV	-	Annihilation
1.72 MeV	Hydrogen	Single Escape Peak
1.78 MeV	Silicon	Inelastic Scatter
1.81 MeV	Magnesium	Neutron Capture
1.94 MeV	Calcium	Neutron Capture
2.00 MeV	Calcium	Neutron Capture
2.22 MeV	Hydrogen	Neutron Capture
3.05 MeV	Magnesium	Neutron Capture
4.42 MeV	Calcium	Neutron Capture
4.43 MeV	Oxygen	Inelastic Scatter
4.44 MeV	Calcium	Inelastic Scatter
5.52 MeV	Calcium	Inelastic Scatter
6.38 MeV	Silicon	Neutron Capture
6.42 MeV	Calcium	Inelastic/Neutron Capture
7.70 MeV	Aluminum	Neutron Capture
7.73 MeV	Aluminum	Neutron Capture

7.4.3 Wet Limestone

Once experiments were taken using limestone, the test enclosure was filled with water to saturate the material. Enough water was introduced to raise the moisture (or porosity) to 28%. The experimental procedure was followed as with previous experiments and the results are discussed next. Please note that simulated responses were multiplied by a source strength of 2.0×10^6 neutrons per second.

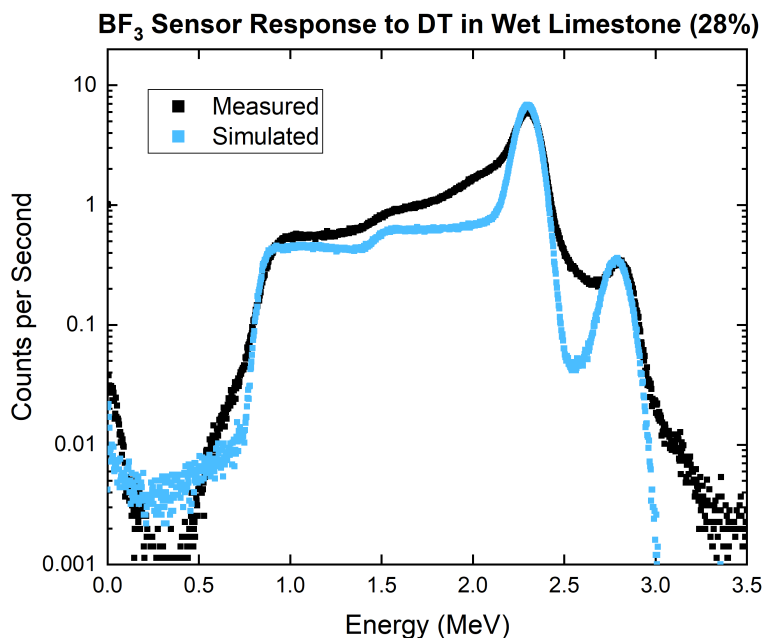


Figure 7.10: MCNP BF₃ wet limestone simulation with DT source vs. experimental results

The BF₃ detector measurement and simulated spectrum can be seen in Fig. 7.10. The measured spectrum is much more broadened when compared to the same detector response in the limestone and water experiments. The simulated spectrum uses the same GEB parameters as before and therefore does not match the measured spectrum. The ³He measured and simulated spectra are shown in Fig. 7.11. The discrepancy below 550 keV is present, as was expected from previous results. The measured spectra was also more broadened than seen in the limestone or water experiment. The near and far NaI(Tl) spectra (seen in Fig. 7.12) have the same features as the dry limestone measurements, with the exception that the 2.22 MeV hydrogen peak is much larger in the wet limestone experiment. This difference was expected due to the higher amount of hydrogen present in wet limestone.

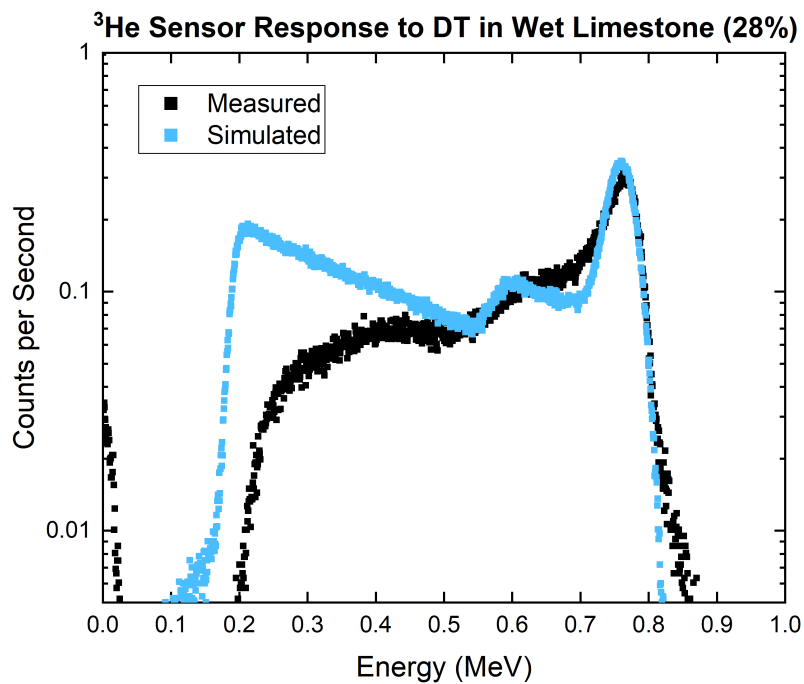


Figure 7.11: MCNP ^3He wet limestone simulation with DT source vs. experimental results

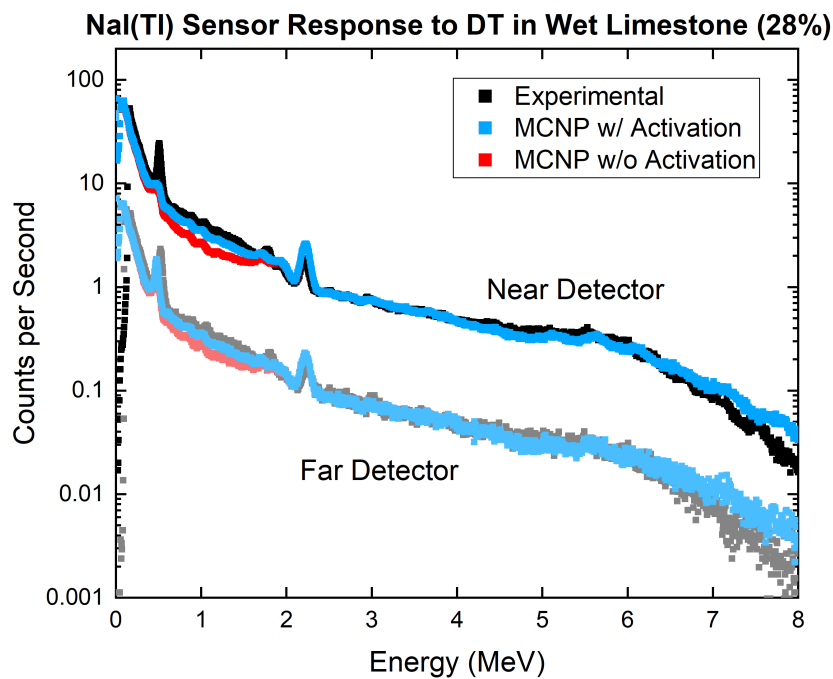


Figure 7.12: MCNP NaI(Tl) wet limestone simulation with DT source vs. experimental results

7.4.4 Dry Sand

The test enclosure was completely cleaned and emptied out at the end of the wet limestone experiments. Sand was added to the test enclosure to a height of 6 ft. No extra moisture was added to the MCNP model for the sand simulations. All simulated responses were multiplied by a 3.5×10^6 neutrons per second source strength.

Measured and simulated responses for the BF_3 detector, ^3He detector, and near and far NaI(Tl) detectors are shown in figures 7.13, 7.14, and 7.15, respectively. The simulated BF_3 and ^3He detector responses matched experimental results well. Both experimental spectra were slightly more broadened than simulation and the ^3He simulated response was overestimated below 550 keV. The near and far NaI(Tl) measurements were matched well by simulation (see Fig. 7.15). The recurring 511 keV discrepancy is still present. Curiously, simulation underestimates the hydrogen single-escape peak as observed in the dry limestone experiment. Neutron capture and inelastic scatter gamma rays from silicon are visible in the spectra in the form of small, broad peaks. Table 7.6 lists some of the more prominent peaks in the NaI(Tl) spectra.

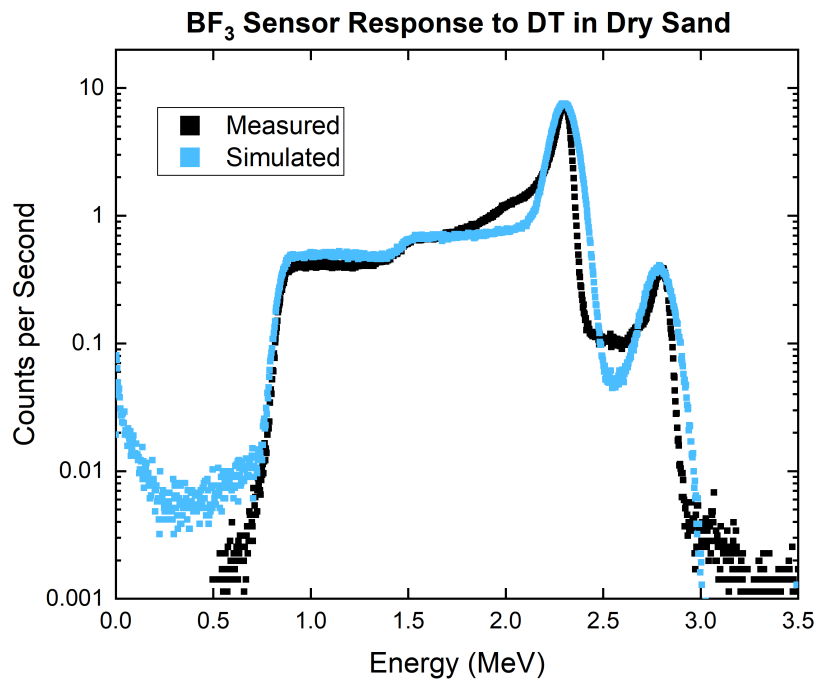


Figure 7.13: MCNP BF_3 dry sand simulation with DT source vs. experimental results

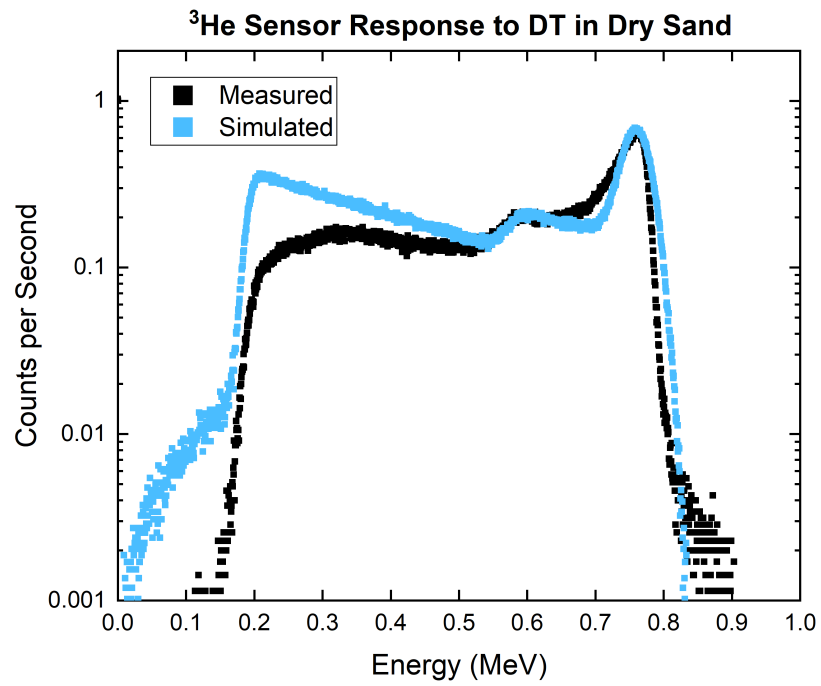


Figure 7.14: MCNP ³He dry sand simulation with DT source vs. experimental results

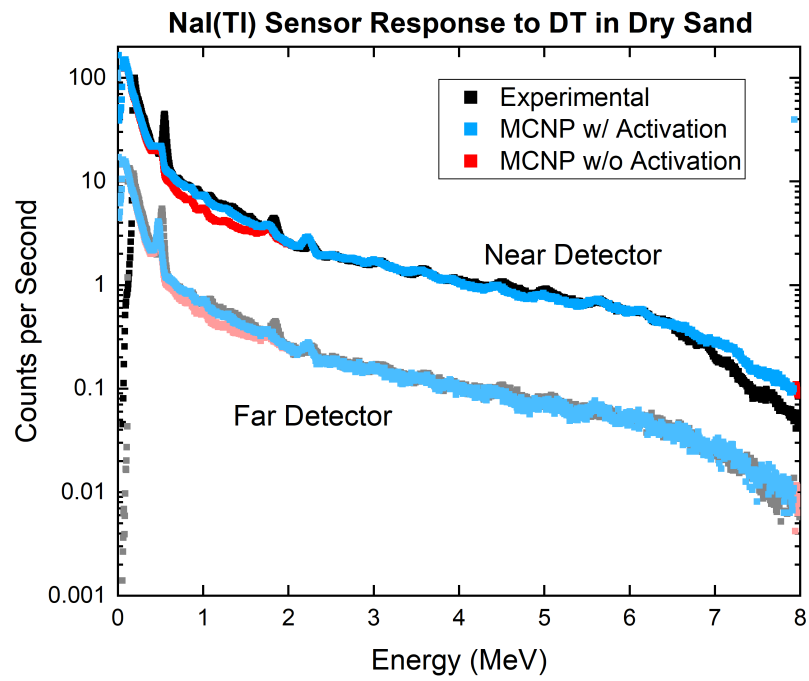


Figure 7.15: MCNP NaI(Tl) dry sand simulation with DT source vs. experimental results

Table 7.6: Spectral features of NaI(Tl) response due to 14.1 MeV neutrons in sand.

Energy	Element	Phenomenon
511 keV	-	Annihilation
3.05 MeV	Magnesium	Neutron Capture
3.54 MeV	Silicon	Neutron Capture
3.47 MeV	Aluminum	Neutron capture
4.58 MeV	Aluminum	Inelastic Scatter
4.94 MeV	Silicon	Neutron Capture
5.62 MeV	Sodium	Neutron Capture
6.23 MeV	Aluminum	Inelastic Scatter
6.38 MeV	Silicon	Neutron Capture
7.20 MeV	Silicon	Neutron Capture

7.4.5 Wet Sand

The enclosure, previously filled with sand, was filled with water until a 30% moisture (or porosity) was reached. The large majority of the water sank to the bottom of the test enclosure. As a result, the bulk material became inhomogeneous with different densities at the top and bottom of the enclosure. The MCNP model was filled with a homogeneous mixture of sand and water at an estimated average density. Due to the size of the test enclosure, the bulk material mimics an infinite medium and acts as a buffer in material density. The simulated results for all detectors were multiplied by a source strength of 3.0×10^6 neutrons per second.

The simulated and measured BF_3 , ^3He , and NaI(Tl) responses from wet limestone are shown in figures 7.16, 7.17, and 7.18. Simulated detector responses matched experimental results fairly well. Simulated responses for the neutron sensors were close to experimental measurements with the same discrepancies noticed in previous experiments. The NaI(Tl) spectra show a larger 2.2 MeV hydrogen peak when compared to the dry sand experiment. Simulated near and far NaI(Tl) responses also underestimate the 1.71 MeV single escape peak.

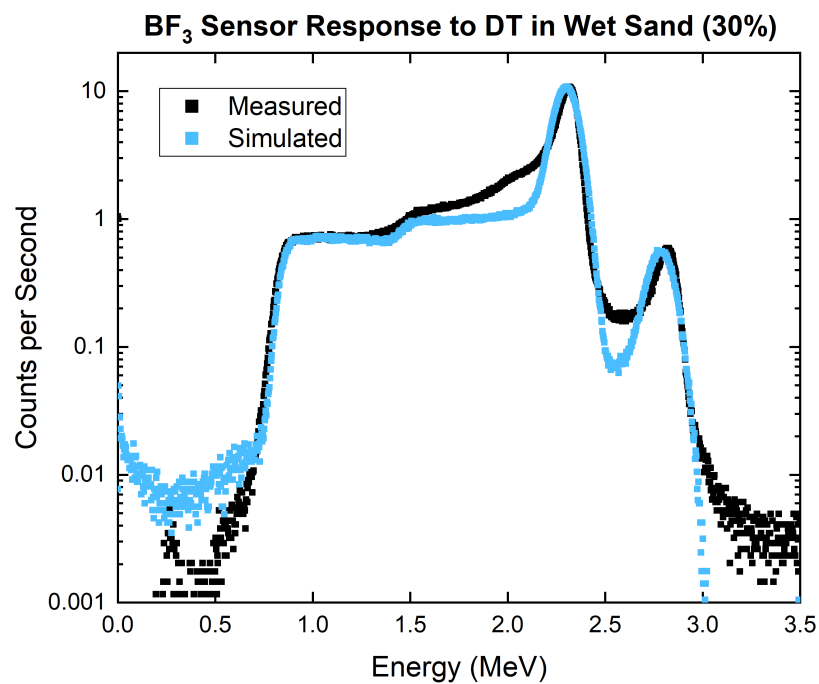


Figure 7.16: MCNP BF_3 wet sand simulation with DT source vs. experimental results

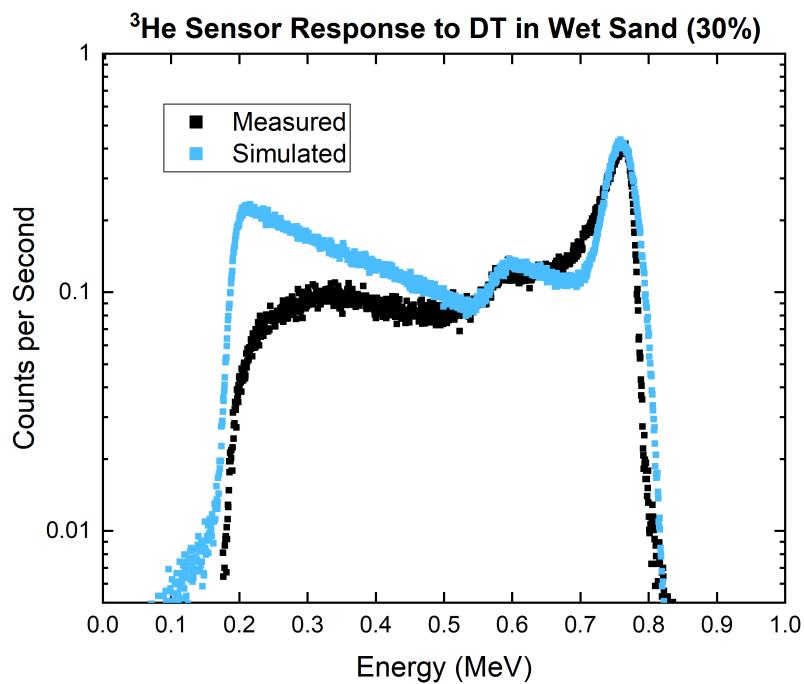


Figure 7.17: MCNP ^3He wet sand simulation with DT source vs. experimental results

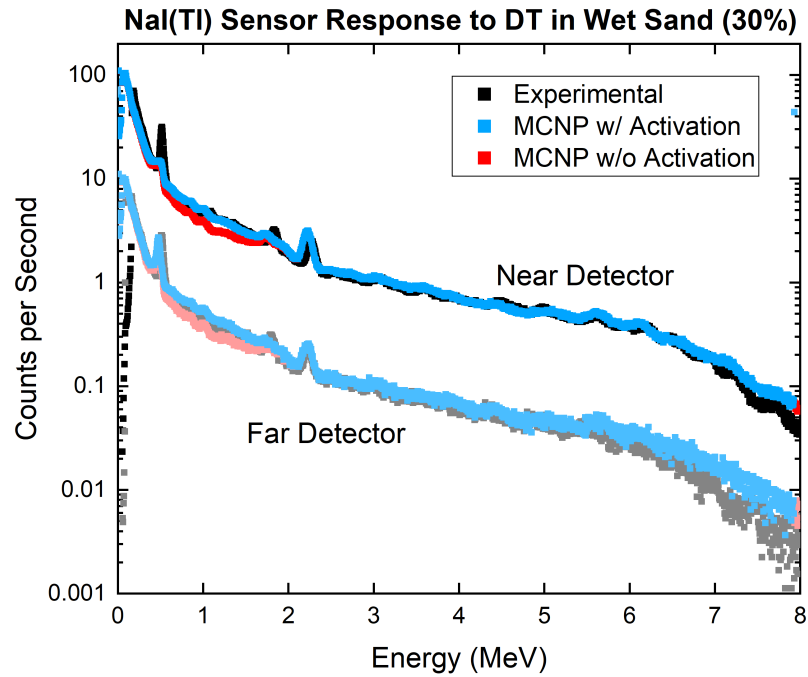


Figure 7.18: MCNP NaI(Tl) wet sand simulation with DT source vs. experimental results

7.4.6 Summary

Overall, simulation results were very consistent among all five experiments. The BF_3 and ^3He simulations did not match experimental measurements perfectly. The neutron sensor measurements had varying degrees of broadening among experiments that were not approximated by the simple, one-parameter, GEB broadening parameters used in simulations. However, the magnitude of the full-energy peaks were well matched. Because proportional counters are not used for their spectroscopic capabilities, approximating the magnitude of the response is most important in simulation.

It was surprising and gratifying to see NaI(Tl) simulations approximate experimental measurements so well. However, there are two sources for discrepancy between simulation and measurements. First, MCNP does not accurately simulate the 511 keV energy peak present in near NaI(Tl) detector measurements. While a 511 keV peak is present in far NaI(Tl) detector simulations, it tends to underestimate measurements. Second, the 1.71 MeV single-escape peak from hydrogen is always underestimated in simulations.

It is possible that these two discrepancies may have a common source. If MCNP is not handling pair production or positron and electron annihilation correctly, due to user or software error, it could explain the missing peaks. As of this date, three publications have shown a similar problem with Monte Carlo simulations. While research continues on this topic, these simulations represent the highest fidelity MCNP[®] models we have been able to produce to date.

Chapter 8

Conclusion

After having presented the journey of this research, this concluding chapter summarizes the findings, how the objectives were met, the context of the research in terms of radioisotope replacement, and a look to the future. The chapter is set up as follows: First, the studies conducted to design and construct an oil well logging benchmarking tool and a testing facility are summarized. Final simulation results are compared with experimental data; the strengths and weaknesses of the MCNP model are discussed. Then, the research objectives are reviewed and the obtained outcomes presented. The context of how this research helps past and current efforts is examined. Finally, possible future work is discussed.

8.1 Summary

An oil well logging benchmarking tool and a test enclosure have been designed for the purpose of acquiring experimental measurements that will be used to benchmark a Monte Carlo-Library Least Squares code, which is currently under development at North Carolina State University. Extensive simulations were conducted to understand the behavior of various design parameters and their effect on the tool's sensitivity to porosity. A test enclosure was designed to mimic an effectively infinite medium in which to take measurements. The test enclosure can be filled with a variety of wet or dry materials. Simulations were conducted

to design shielding of the room that houses the test enclosure. Following is a summary of the oil well logging benchmarking tool and the test enclosure design.

8.1.1 Tool Design

After reviewing literature and learning about common oil well logging tool configurations, the initial tool design included two thermal neutron detectors, two gamma ray detectors, and a neutron source. The neutron and gamma ray detectors were paired as near and far set of detectors. The tool was simulated varying the distance of the far set of detectors from the source. As the spacing between the two sets of detectors increased, the γ -ray response of the far detector became indistinguishable for limestone, sandstone, and water.

A similar phenomenon was observed for the far ^3He detector; after some point of separation from the source the neutron response of the far detector changed little for limestone and sandstone, although not for water. These results indicate that shorter detector spacing is desired for the γ -ray detectors. However, the porosity studies conducted showed that larger spacing of the neutron detectors yielded higher sensitivity to changes in porosity. The tool was also simulated with and without shielding. There were no significant differences or improvements in tool sensitivity between shielding materials and no shielding at all.

The final design of the tool took into consideration the size limitations of the laboratory space. The benchmarking tool constructed consists of an interchangeable neutron source, two ^3He neutron detectors filled to 4 atm (near) and 2 atm (far), and two NaI(Tl) γ -ray detectors. The tool was used to take measurements using AmBe and DT neutron sources.

8.1.2 Testing Enclosure Design

A testing enclosure was designed to be an effectively infinite medium in which to take measurements using the benchmarking tool. Initial studies featured a large cylindrical geometry filled with limestone that was modeled around the tool. The radius of the limestone was varied to determine the size at which the near and far detector responses would saturate, indicating the size of an effectively infinite medium.

Due to concerns over the practicality of building a cylindrical enclosure, the geometry was changed to a rectangular chamber with concrete walls and a pipe suspended horizontally in the middle. The final size of the enclosure is approximately 6.5 ft tall, 6.5 ft wide, and 8 ft deep. The enclosure was built against a wall that separates the room from a hallway. Therefore, shielding was designed and put in place to maintain the ambient dose rate in the hallway below 2 mrem/hr. The test enclosure was built in room 107 of the King Hall Annex at KSU. Many safety features were installed in the laboratory space to prevent unintended exposure of radiation to workers and the public.

8.1.3 Experimental Results vs. MCNP Simulations

Experiments were conducted using the benchmarking tool inside the enclosure. Measurements were collected using an AmBe source while the enclosure was filled with water. Initial simulations showed that the neutron activation of the NaI(Tl) crystals was not being modeled. Separate simulations were conducted to approximate the near and far NaI(Tl) responses due to activation in the crystal. After combining the two results, the MCNP simulation matched experimental results for AmBe and DT experiments reasonably well.

It was shown that there is a small discrepancy between experimental measurements and simulation results. The measured spectra for both near and far detectors have a peak near 511 keV, where the simulated spectra do not. Many attempts were made to understand this discrepancy, including checking the way that shielding was modeled and adding possible materials that are present in PMTs, detector housings, and impurities in water to the simulation model. So far no approach has proven fruitful in determining the cause for the discrepancy. Similar issues with the 511 keV peak discrepancy between experimental and simulated results were observed in other publications. Further research is necessary to determine the source of this error in simulations.

8.2 Objectives

At the beginning of this research, there were several objectives to be met. One major goal was to design an oil well logging tool and a testing enclosure in which to take measurements. The second was to produce an MCNP model that simulates experimental measurements as accurately as possible. Both the experimental measurements and MCNP model are necessary to test and further develop the MCLLS code being developed at NCSU.

The objectives set out for this research have been met as best as possible with the time and resources available. This research has provided experimental measurements and MCNP models with which to test and perfect the MCLLS code. The work presented in Ch. 4 helped define the needs and constraints of an appropriate testing enclosure. The simulations outlined in Chapter 5 resulted in the construction of the KSUMI facility. The MCNP model produced over the course of Chapters 6 and 7 matches experimental measurements reasonably well.

8.3 Contribution to Research Efforts

Past research efforts in AmBe source replacement in oil well logging has provided valuable information about the feasibility of using alternative sources. The large majority of research focused solely on simulation to compare expected sensor responses with varying levels of porosity. Using the current definition of porosity, derived from neutron diffusion length theory, detector responses were less sensitive to changes in porosity when using a DT generator instead of an AmBe neutron source.

A new method of identifying the subsurface environment is under development at NCSU. The MCLLS code works by comparing Monte Carlo generated material libraries that are matched to subsurface measurements using the whole gamma-ray spectrum from a neutron source. The MCLLS code is a promising new technique that can help incentivize the oil well logging industry to replace radioisotopes in their tools with safer machine sources. In order to further develop the code, experimental measurements and a well validated Monte Carlo model of the experiment were needed.

The purpose of this research was to produce data with which to test the MCLLS code. Therefore, a tool and a test enclosure were designed and constructed to collect experimental data. An MCNP model of the experiment was developed and refined to match measured data as accurately as possible. Both experimental measurements and the MCNP model have been provided to NCSU for further development of the MCLLS code. Based on preliminary MCLLS tests, determining the composition of subsurface environments with algorithms such as the MCLLS code is no different whether the source is radionuclide such as AmBe or a machine source such as a DT generator. Such algorithms make the transition in the oil well logging industry from radionuclides to machine sources feasible in the future.

Another contribution of this research is the design and construction of the KSUMI facility. Extensive simulation studies were carried out to design the proper laboratory space. Many people were involved in the physical construction of the enclosure walls, installing shielding, devising safety features, wiring monitoring systems, and ensuring that the laboratory space became operational. The facility is versatile and is beginning to serve as a functional laboratory space for other research projects. The KSUMI facility is now an asset to the research community as it provides a large and safe space for testing materials and radioactive sources.

8.4 Future Work

Due to the discrepancy between simulation and measured NaI(Tl) spectra, specifically in the 511 keV region, further investigation should be aimed at determining the source of the difference. Further inquiry into how MCNP6 treats pair production and tracks 511 keV annihilation photons could also provide a reasoning for the discrepancy. Future investigation should include the use of other Monte Carlo modeling codes to compare our MCNP results. The experiments performed could be modeled and simulated in GEANT4 to determine whether the same 511 keV discrepancy is present.

At NCSU, the MCLLS code will be tested and improved using the experimental measurements taken and the MCNP model developed during the course of this research. The

data provided for the MCLS code should help to refine the algorithm, improve current capabilities, and develop new features. The ability to identify the subsurface environment with the help of high-fidelity material libraries instead of relying on legacy AmBe measurements, will help incentivize the oil well logging industry to replace radioisotope sources with safer machine sources.

Bibliography

- [1] Y. Xiao, S. Xiang, Z. Zhao, and Z. Qian. Design of high reliability nuclear logging probe. *Procedia Engineering*, 7:223–228, 2010.
- [2] R.J. McConn Jr, C.J. Gesh, R.T. Pagh, R.A. Rucker, and R.G. Williams III. *Compendium of Material Composition Data for Radiation Transport Modeling*. Pacific Northwest National Laboratory, 2011.
- [3] National Research Council of the National Academies. *Radiation Source Use and Replacement*. The National Academic Press, 2008.
- [4] C. R. Peeples, M. Michael, and R. P. Gardner. On replacing Am-Be neutron sources in compensated porosity logging tools. *Applied Radiation and Isotopes*, 68:926–931, 2010.
- [5] United States Nuclear Regulatory Commission. PART 20STANDARDS FOR PROTECTION AGAINST RADIATION. URL <https://www.nrc.gov/reading-rm/doc-collections/cfr/part020/>.
- [6] Z. Bassiouni. *Theory, Measurement, and Interpretation of Well Logs*. Society of Petroleum Engineers, 1994.
- [7] D.V. Ellis and J.M. Singer. *Well Logging for Earth Scientists*. Springer, 2nd edition, 2007.
- [8] C. Afonso de Andre, A. Mainieri Vieira da Cunha, P. Boonen, B. Valant-Spaight, S. LeFors, and W. Schultz. A Comparison of Logging-While-Drilling and Wireline Nuclear Porosity Logs in Shales from Wells in Brazil. *Petrophysics*, 46, 2005.
- [9] A. Nikitin and S. Bliven. Needs of well logging industry in new nuclear detectors. *IEEE*, pages 1214–1219, 2010.

- [10] J.R. Hearst. *Well logging for physical properties: A handbook for geophysicists, geologists, and engineers*. Wiley, 2000.
- [11] J. Asfahani and M. Borsaru. Low-activity spectrometric gamma-ray logging technique for delineation of coal/rock interfaces in dry blast holes. *Applied Radiation and Isotopes*, 65, 2007.
- [12] M. Oraby, K. Verghese, and R. P. Gardner. Investigation of an improvised-sensitivity neutron-porosity oil-well logging tool. *Nuclear Instruments and Methods in Physics Research A*, 299:674–681, 1990.
- [13] W. A. Metwally. Porosity calculations using a C/O logging tool with boron-lined NaI detectors. *Applied Radiation and Isotopes*, 69:217–219, 2011.
- [14] M. Rasoulinejad, R. Izadi Najafabadi, and N. Ghal-Eh. A simple well-logging tool using boron-lined sodium iodide scintillators and an ^{241}Am -Be neutron source. *Radiation Protection Dosimetry*, 151:580–585, 2012.
- [15] S. Croft. The use of neutron intensity calibrated $^9\text{Be}(\alpha, n)$ sources as 4438 keV gamma ray reference standards. *Nuclear Instruments and Methods in Research A*, 281, 1989.
- [16] J.C. Vitorelli, A.X. Silva, V.R. Crispim, E.S. da Fonseca, and W.W. Pereira. Monte Carlo simulation of response function for NaI(Tl) detector for gamma rays from ^{241}Am /Be source. *Applied Radiation and Isotopes*, 62, 2005.
- [17] Z. Liu, J. Chen, P. Zhu, Y. Li, and G. Zhang. The 4.438 MeV gamma to neutron ratio for the Am-Be neutron source. *Applied Radiation and Isotopes*, 68, 2007.
- [18] A. X. Chen, A. J. Antolak, and K. N. Leung. Electronic neutron sources for compensated porosity well logging. *Nuclear Instruments and Methods in Physics Research A*, 684: 52–56, 2012.
- [19] C. M. Frankle and G. E. Dale. Unconventional neutron sources for oil well logging. *Nuclear Instruments and Methods in Physics Research A*, 723:24–29, 2013.

- [20] W.L. Dunn and J.K. Shultis. *Exploring Monte Carlo Methods*. Elsevier, 2012.
- [21] J. Bernoulli. *Ars conjectandi. Impensis Thurnissiorum, Fratrum, Basilea*, 1713.
- [22] G.L. Leclerc Buffon. *Essai d'arithmétique morale. Supplément à l'Histoire Naturelle*, 4, 1777.
- [23] R. P. Gardner and A. Sood. On the future of Monte Carlo simulation for nuclear logs. *Applied Radiation and Isotopes*, 68:932–935, 2010.
- [24] X-5 Monte Carlo Team. MCNP-A general Monte Carlo N-Particle Transport Code, version 5. *Los Alamos National Lab*, Vol 1-3, 2003.
- [25] E. Eftekhari Zadeh, S.A.H. Fegghi, E. Bayat, and G.H. Roshani. Gaussian energy broadening function of an HPGe detector in the range of 40 keV to 1.46 MeV.
- [26] C.M. Salgado, L.E.B. Brandao, R. Schirru, C.M.N.A. Pereira, and C.C. Conti. Validation of a NaI(Tl) detector's model developed with MCNP-X code. *Progress in Nuclear Energy*, 59, 2012.
- [27] C. Kim, Y. Kim, M. Moon, and G. Cho. Iterative Monte Carlo simulation with the Compton Kinematics-based GEB in a plastic scintillation detector.
- [28] H.M. Hakimabad, H. Panjeh, and A. Vejdani-Noghreiyani. Evaluation of the nonlinear response function of a 3x3 in NaI scintillator detector for PGNAA applications.
- [29] R.P. Gardner, E. Sayyed, Y. Zheng, S. Hayden, and C.W. Mayo. NaI detector neutron activation spectra for PGNAA applications. *Applied Radiation and Isotopes*, 53, 2000.
- [30] T.E. Booth. Genesis of the Weight Window and the Weight Window Generator in MCNP - A Personal History. *Los Alamos National Laboratory Report LA-UR-06-5807*, 2006.
- [31] H. Yu, J. Sun, J. Wang, and R. P. Gardner. Accuracy and borehole influences in pulsed neutron gamma density logging while drilling. *Applied Radiation and Isotopes*, 69:1313–1317, 2011.

- [32] J. Neal, L. Boatner, Z. Bell, H. Akkurt, and M. McCarthy. Evaluation of neutron and gamma detectors for high-temperature well-logging applications. *IEEE*, 2011.
- [33] A. Mendoza, W.E. Preeg, C. Torres-Verdin, and F.O. Alpak. Monte Carlo modeling of nuclear instruments in vertical and horizontal wells in the presence of mud-filtrate invasion and salt mixing. *Petrophysics*, 48, 2007.
- [34] W. Wu, M. Tong, L. Xiao, and J. Wang. Porosity sensitivity study of the compensated neutron logging tool. *Journal of Petroleum Science and Engineering*, 108:10–13, 2013.
- [35] A. Vijaya and A. Kumar. The neutron spectrum of Am-Be neutron sources. *Nuclear Instruments and Methods*, 111, 1973.
- [36] T.D. Mclean and D.T. Seagraves. ANS 2018 Tutorial on MCNP Applications revision 1. *Los Alamos National Laboratory Report LA-UR-18-28070*, 2018.
- [37] A. Nohtomi and G. Wakabayashi. Accuracy of neutron self-activation method with iodine-containing scintillators for quantifying ^{128}I generation using decay-fitting technique. *Nuclear Instruments and Methods in Physics Research A*, 800, 2015.
- [38] D. Sudac and V. Valkovic. Irradiation of 4" x 4" NaI(Tl) detector by the 14 MeV neutrons. *Applied Radiation and Isotopes*, 68, 2010.
- [39] G. Wakabayashi, A. Nohtomi, E. Yahiro, T. Fujibuchi, J. Fukunaga, Y. Umezu, Y. Nakamura, K. Nakamura, M. Hosono, and T. Itoh. Applicability of self-activation of an NaI scintillator for measurement of photo-neutrons around a high-energy X-ray radiotherapy machine. *Radiological Physics and Technology*, 8, 2015.
- [40] National Bureau of Standards. *Tables for the Analysis of Beta Spectra*. United States Government Printing Office, 1952.
- [41] H.X. Shi, B.X. Chen, T.Z. Li, and D. Yun. Precise Monte Carlo simulation of gamma-ray response functions for an NaI(Tl) detector. *Applied Radiation and Isotopes*, 57, 2002.

- [42] H.D. Tam, H.D. Chuong, T.T. Thanh, and C.V. Tao. A study of the effect of Al_2O_3 reflector on response function of NaI(Tl) detector. *Radiation Physics and Chemistry*, 125, 2016.
- [43] A.W. Drescher. *Characterization of $\text{LaBr}_3:\text{Ce}$ Detectors in a Gamma-Gamma Coincidence Configuration*. Master's thesis, University of Texas at Austin, 2017.
- [44] J. Cubiss. *Modeling of STEFF NaI Detectors Using the MCBEND Monte Carlo Code*. Master's thesis, University of Manchester, School of Physics and Astronomy, 2013.
- [45] M.W. Shaver, A.M. Casella, R.S. Wittman, and B.S. McDonald. Radiation detection computational benchmark scenarios. *Pacific Northwest National Laboratory Report PNNL-22794*, 2013.

Appendix A

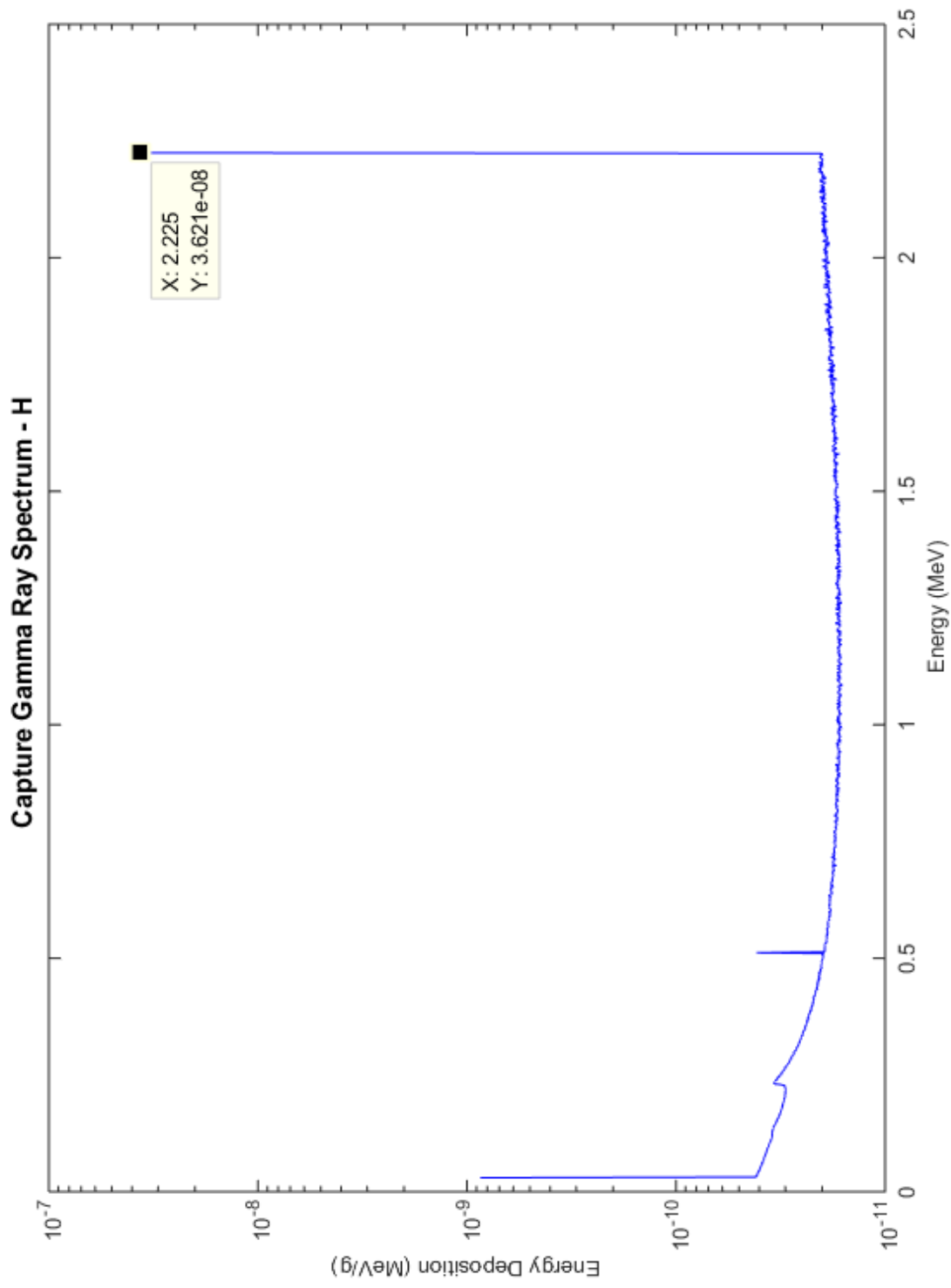
Gamma Ray Database

MCNP5 was used to create a database of neutron capture and inelastic gamma-ray responses for various elements. The MCNP code used to create the database consists of a sphere with a 14.1 MeV neutron source in the middle. The sphere was filled with each element (densities between 0.5 and 1.0 g/cm³) and ran for 10⁶-10⁸ histories. The cross section tables used in these simulations were from the ENDF71x files. Elements included in the study are those typically found in: clay, coal, earth, oil, various rocks (limestone, sandstone, granite, shale, etc.), steel, and aluminum alloys. The density and number of histories for each element were carefully chosen in order to maintain tally errors close to or below 1%. An energy deposition tally (F6) was placed on the surface of the sphere; it creates a histogram of 8,000 channels of the energy deposited by inelastic and capture gamma rays generated from neutron interactions in the medium. Each output was plotted on a semi-log graph and major peaks were identified. The full database containing 21 elements is presented in this appendix.

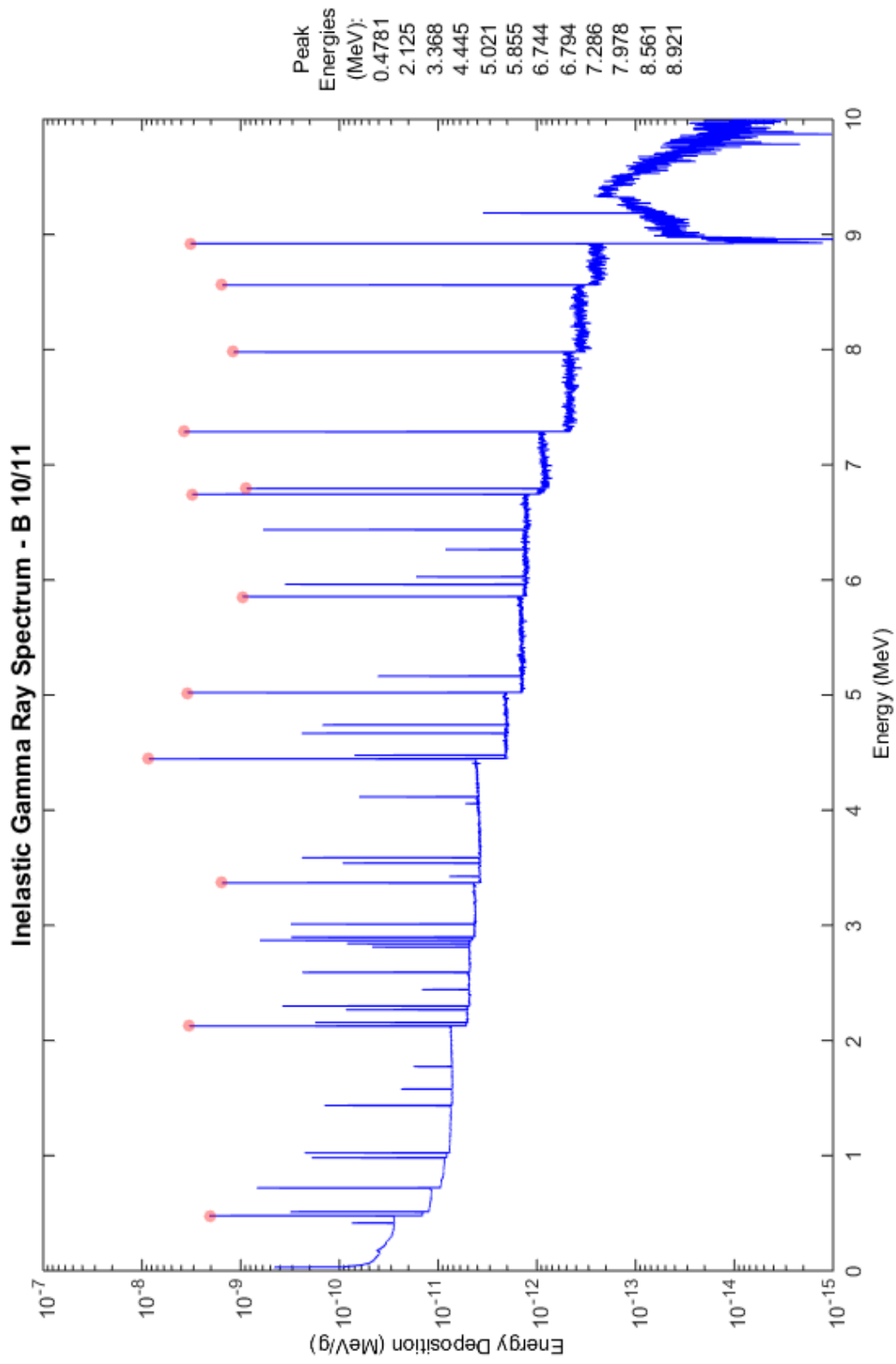
Table of Contents

Introduction.....	2
1 Hydrogen: (material composition: 1001)	3
5 Boron: (material composition: 50% 5010, 50% 5011).....	4
6 Carbon: (material composition: 6000)	6
7 Nitrogen: (material composition: 7014).....	8
8 Oxygen: (material composition: 8016).....	10
11 Sodium: (material composition: 11023).....	12
12 Magnesium: (material composition: 12000)	14
13 Aluminum: (material composition: 13027)	16
14 Silicon: (material composition: 14000).....	18
15 Phosphorus: (material composition: 15031)	20
16 Sulfur: (material composition: 16000).....	22
17 Chlorine: (material composition: 17000).....	24
19 Potassium: (material composition: 19000)	26
20 Calcium: (material composition: 20000)	28
22 Titanium: (material composition: 22000).....	30
25 Manganese: (material composition: 25055).....	32
26 Iron: (material composition: 26000)	34
29 Copper: (material composition: 29000)	36
74 Tungsten: (material composition: 74000)	38
82 Lead: (material composition: 82000)	40
92 Uranium 238: (material composition: 92238)	42
Appendix	44

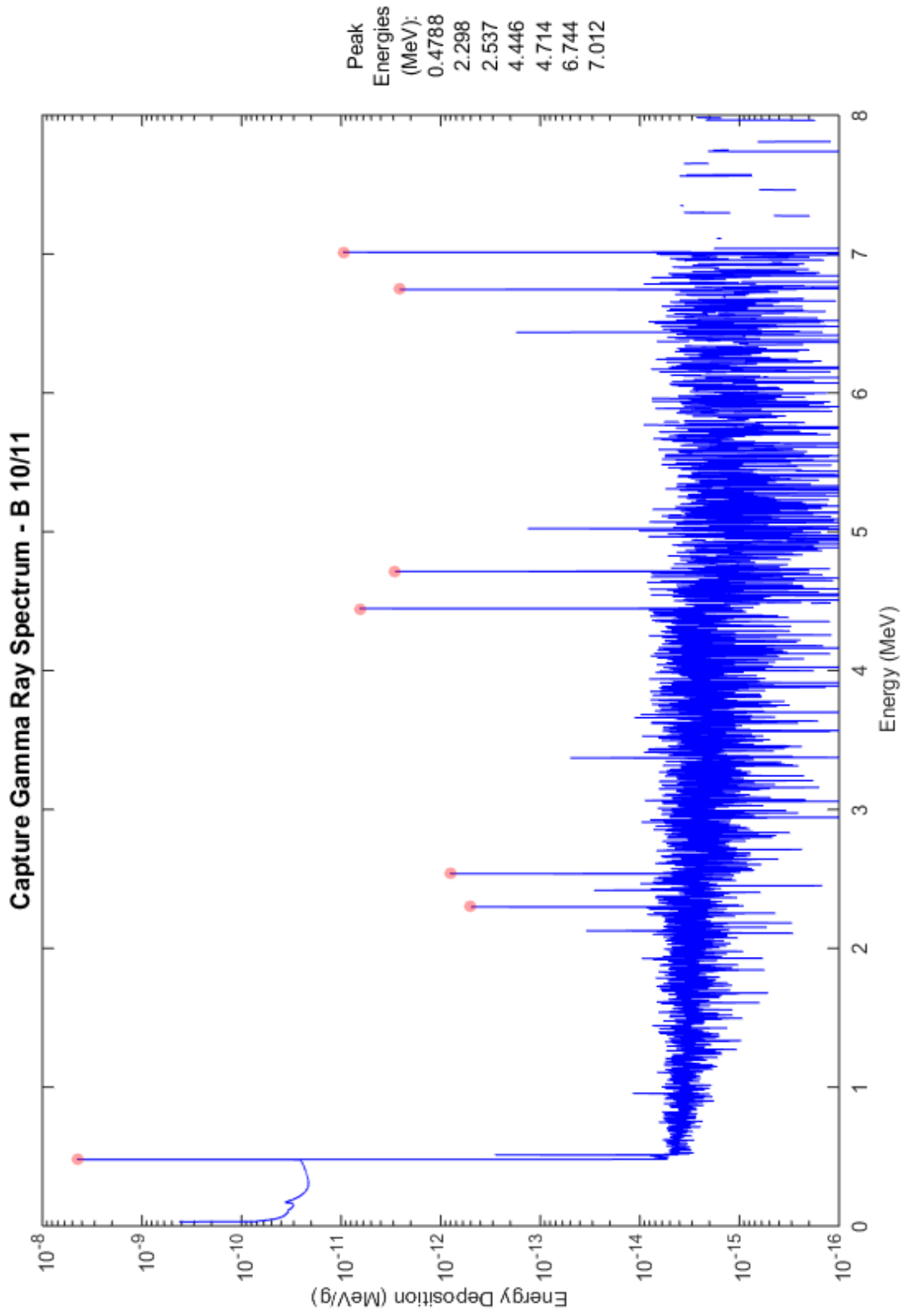
1 Hydrogen: (material composition: 1001)



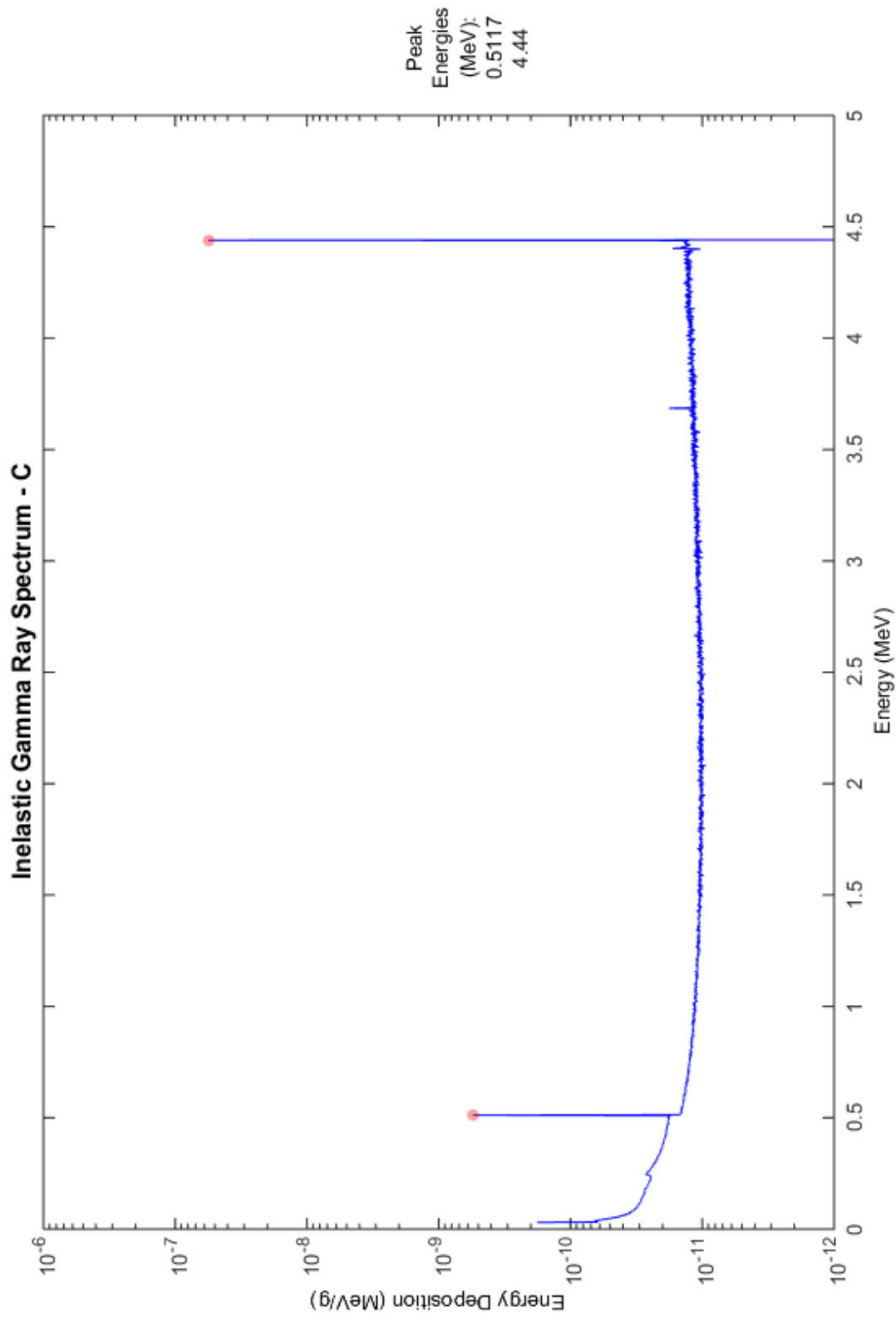
5 Boron: (material composition: 50% 5010, 50% 5011)



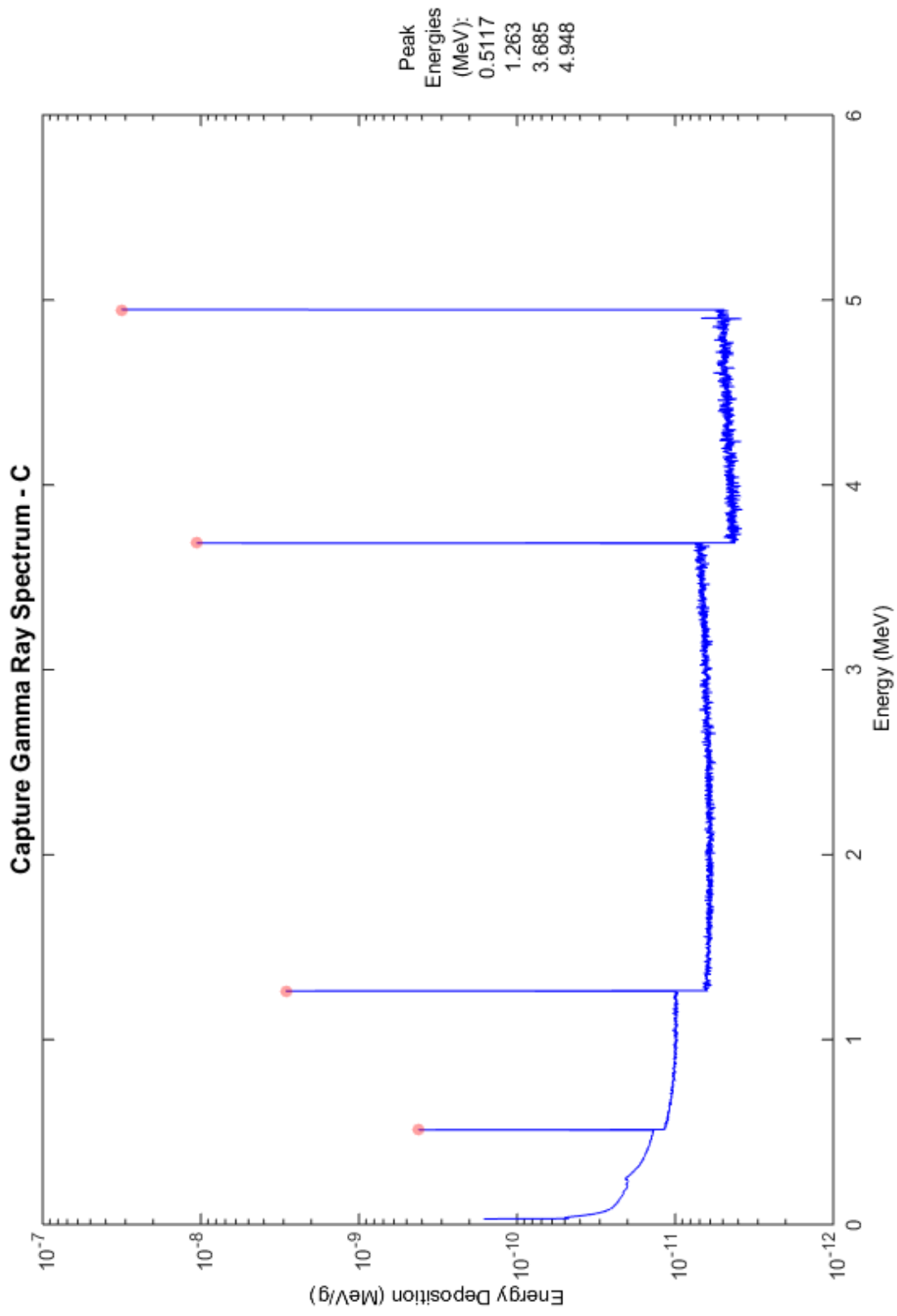
5 Boron: (material composition: 50% 5010, 50% 5011)



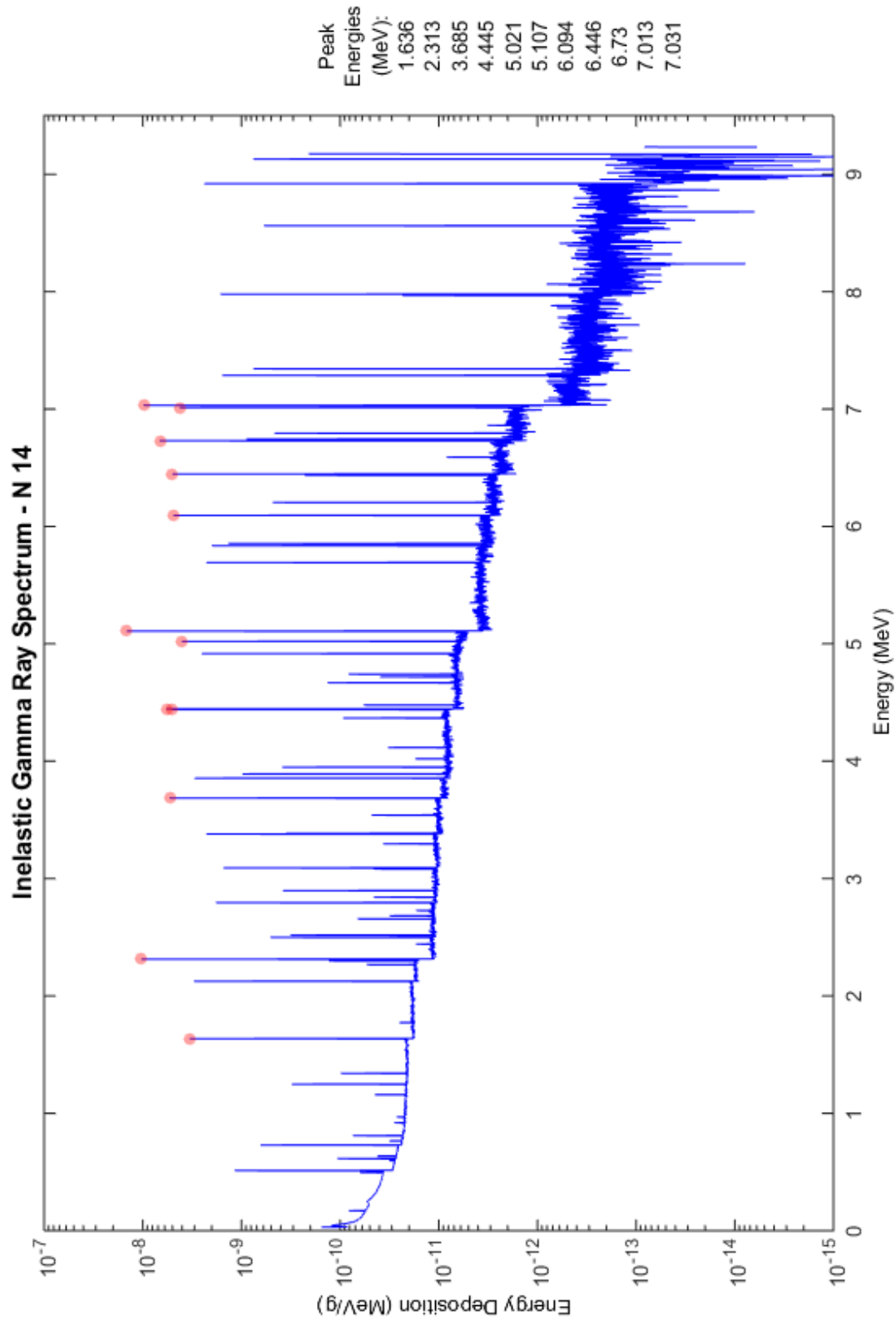
6 Carbon: (material composition: 6000)



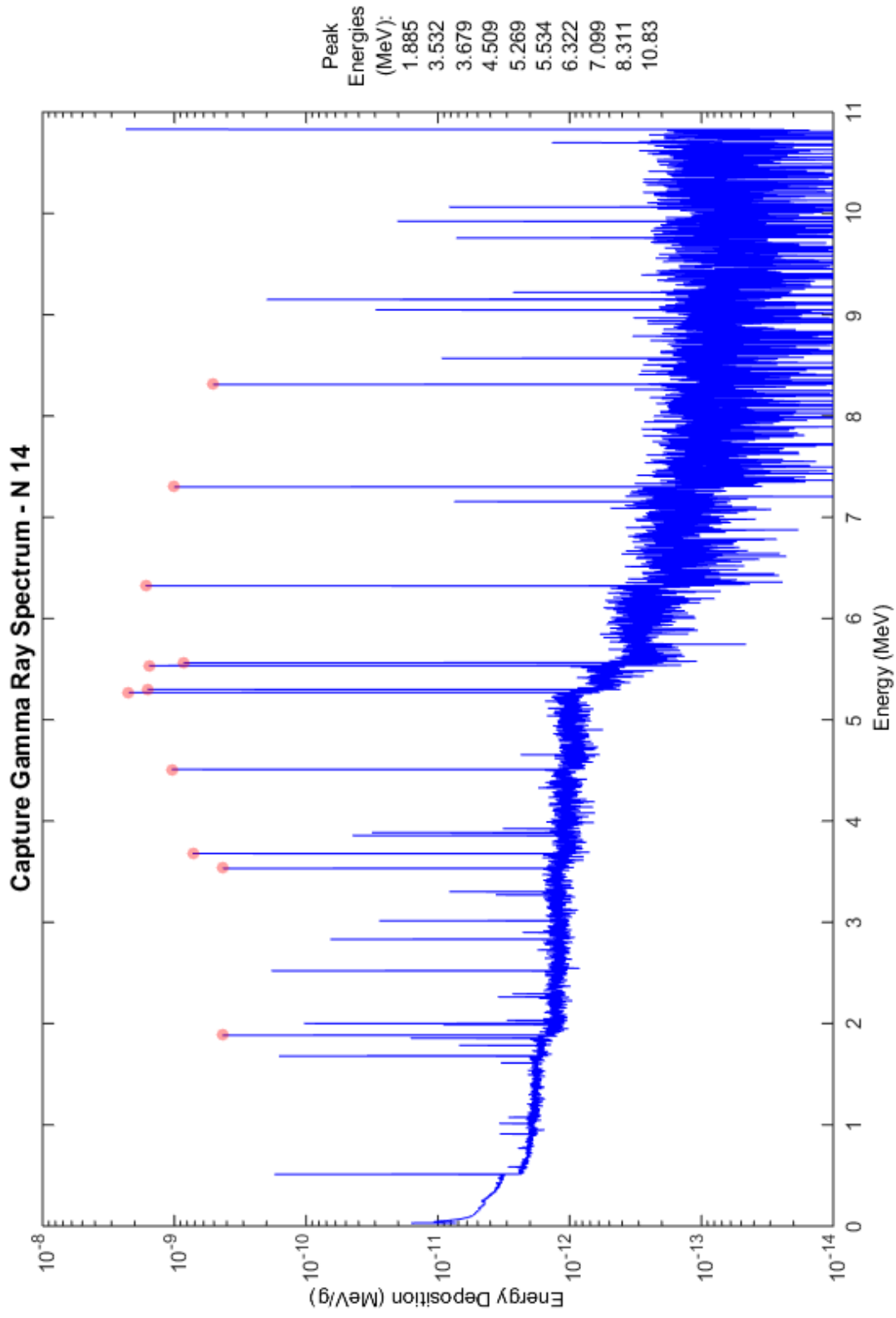
6 Carbon: (material composition: 6000)



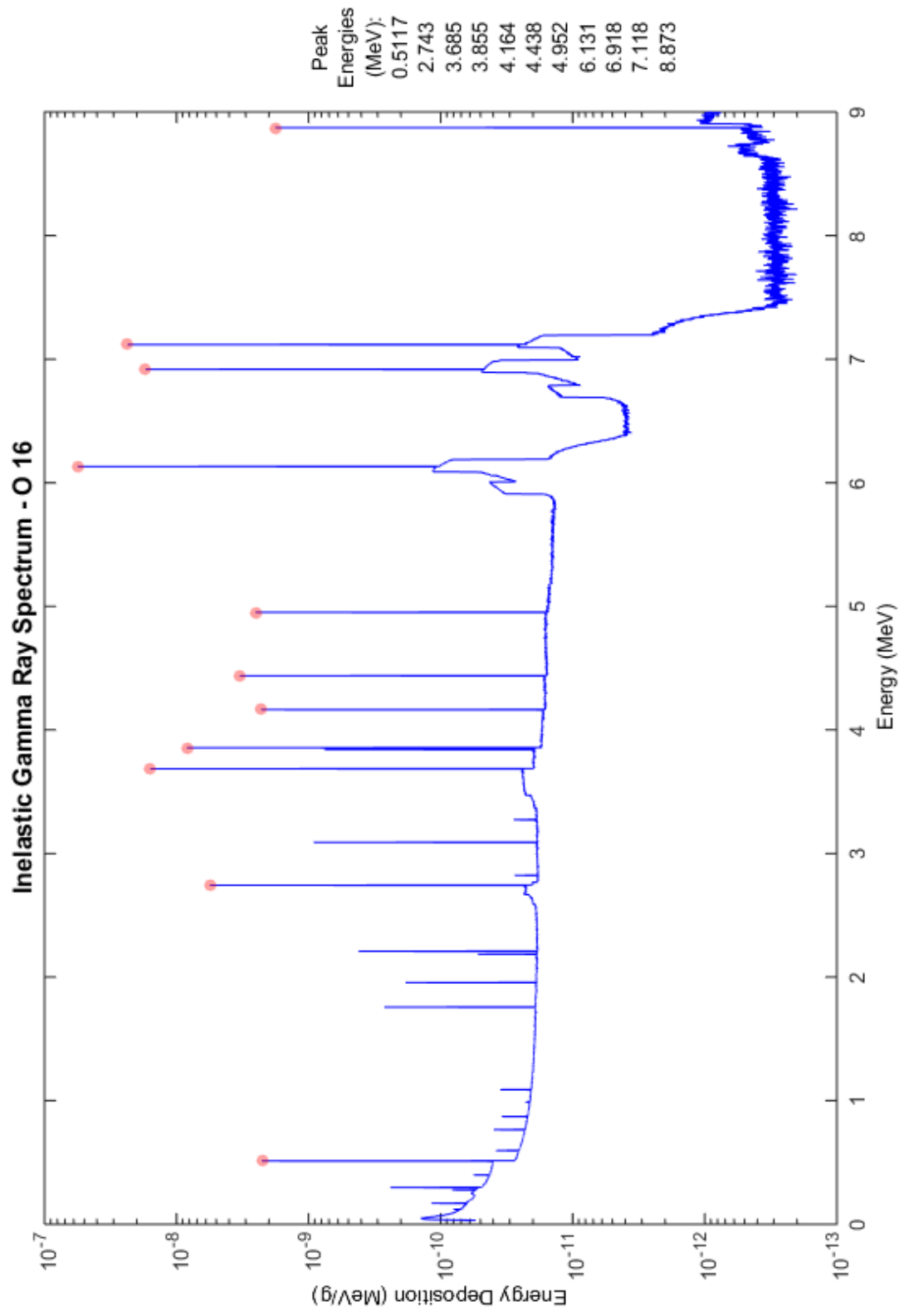
7 Nitrogen: (material composition: 7014)



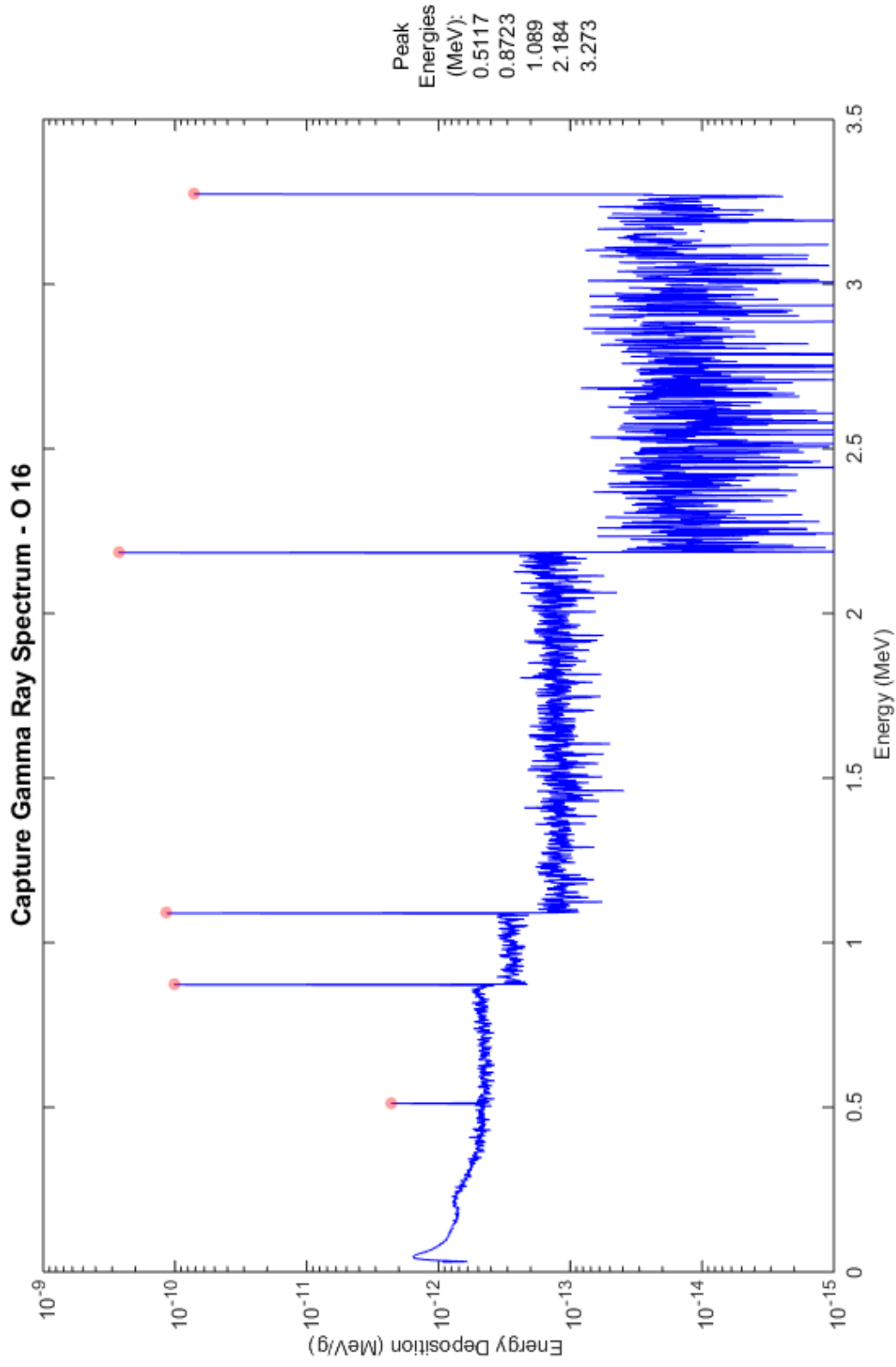
7 Nitrogen: (material composition: 7014)



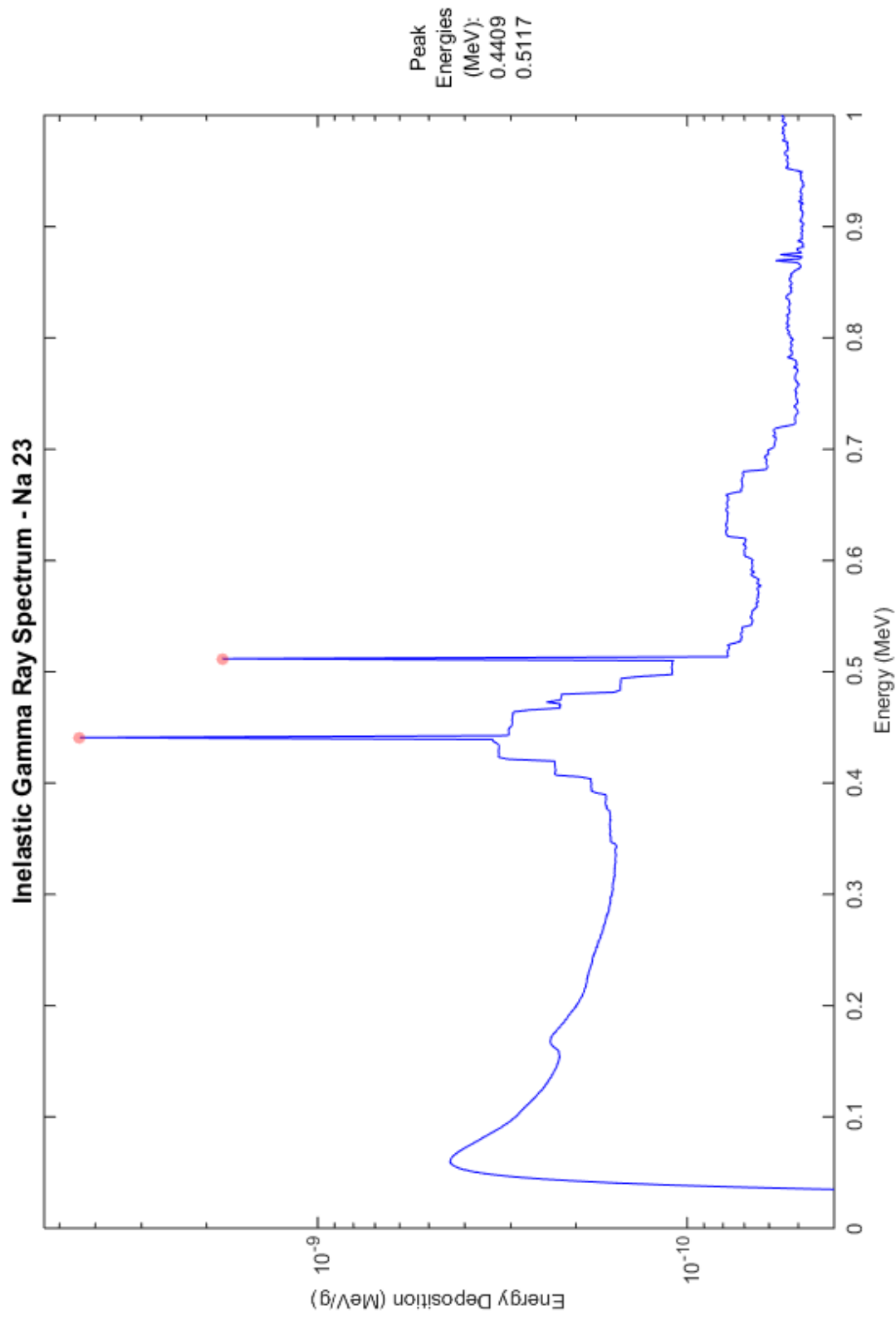
8 Oxygen: (material composition: 8016)



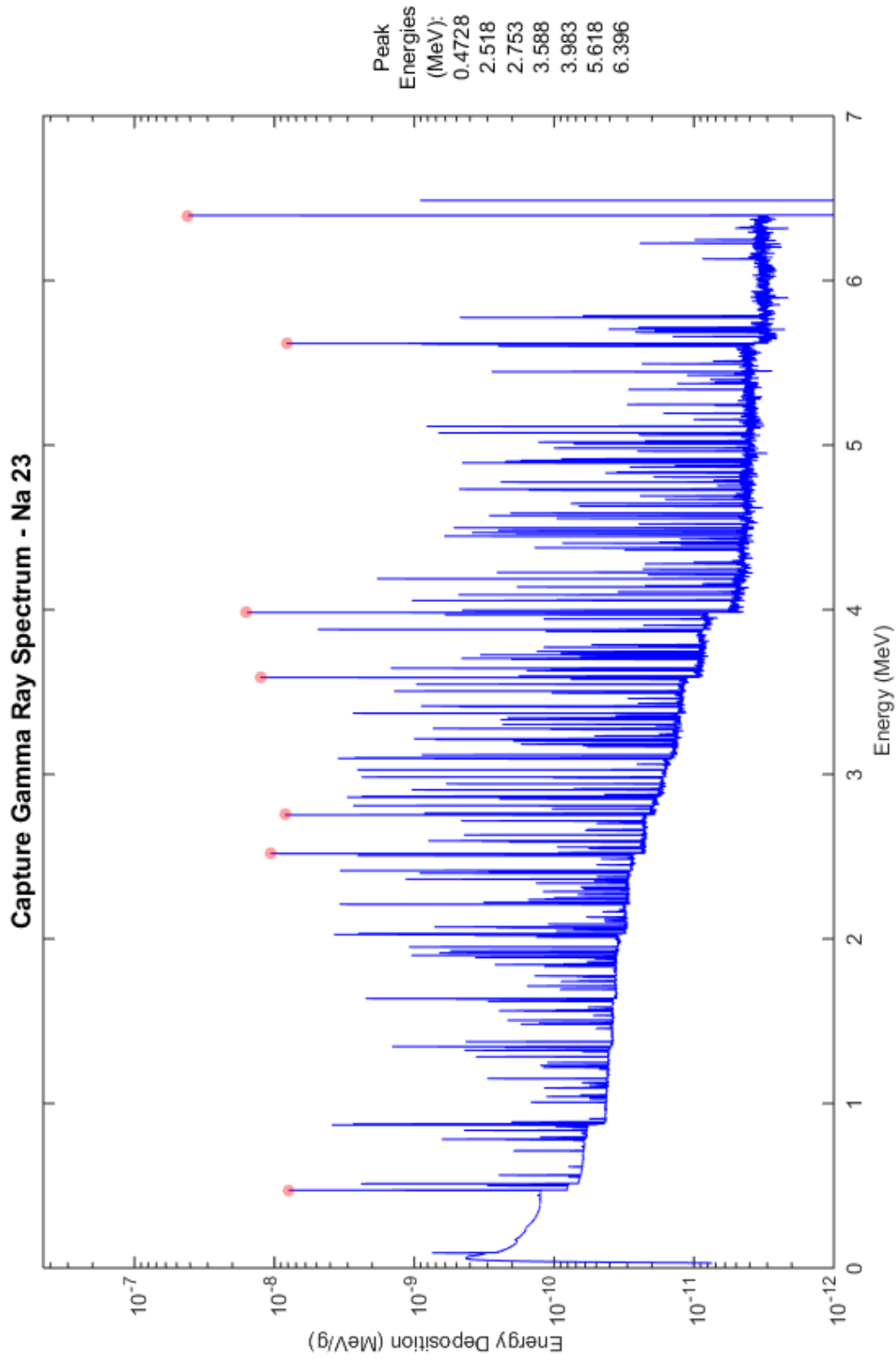
8 Oxygen: (material composition: 8016)



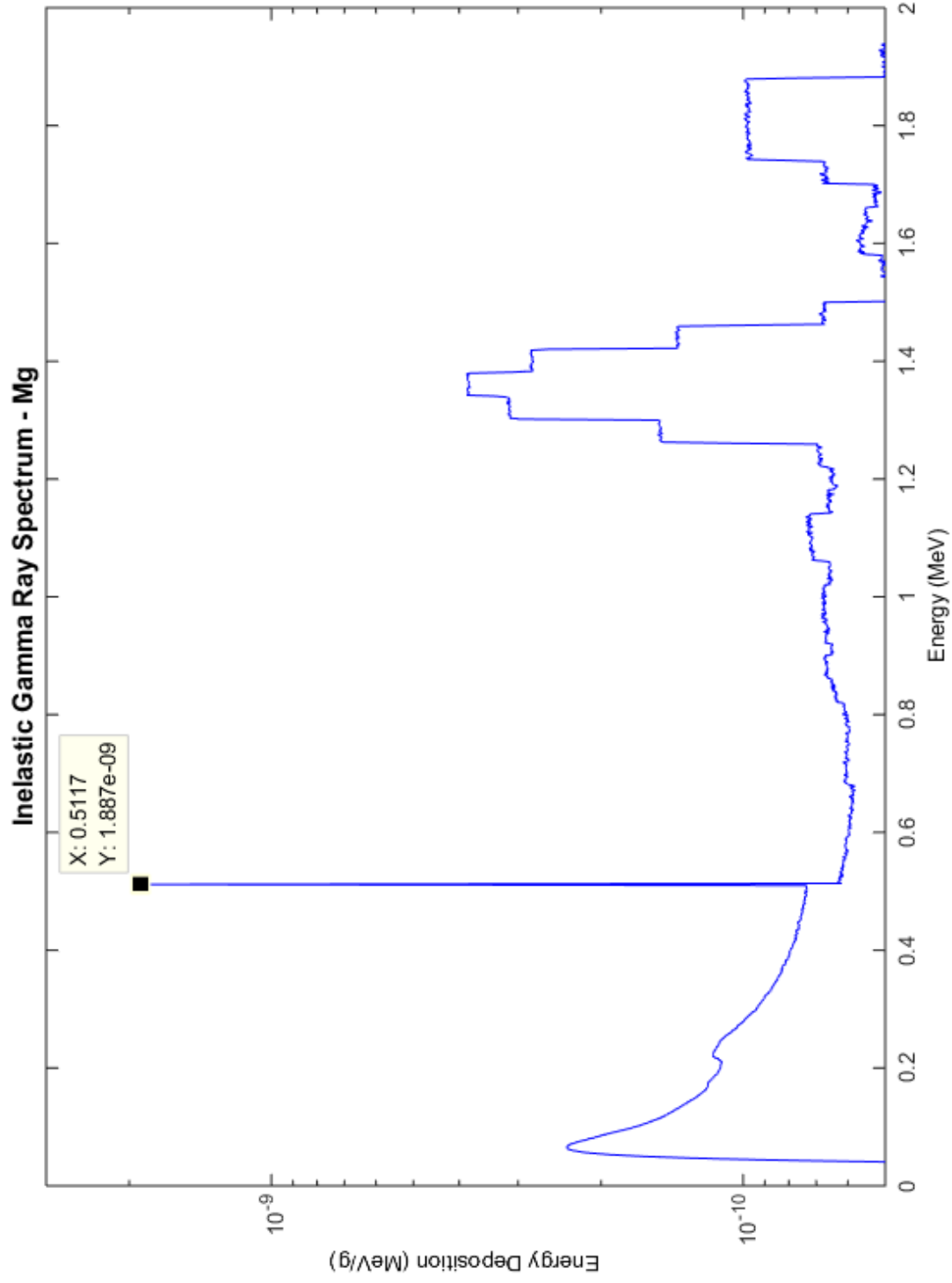
11 Sodium: (material composition: 11023)



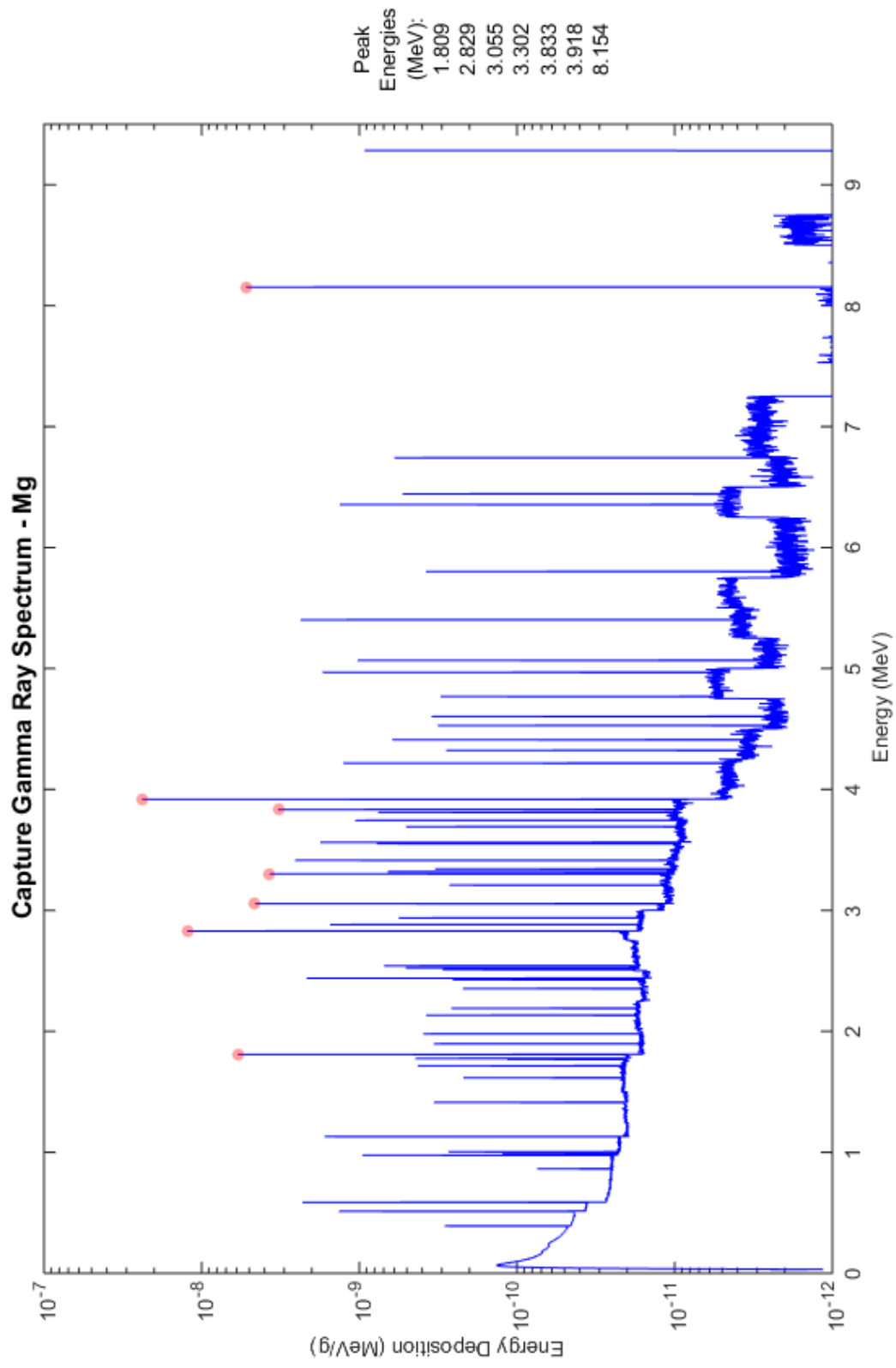
11 Sodium: (material composition: 11023)



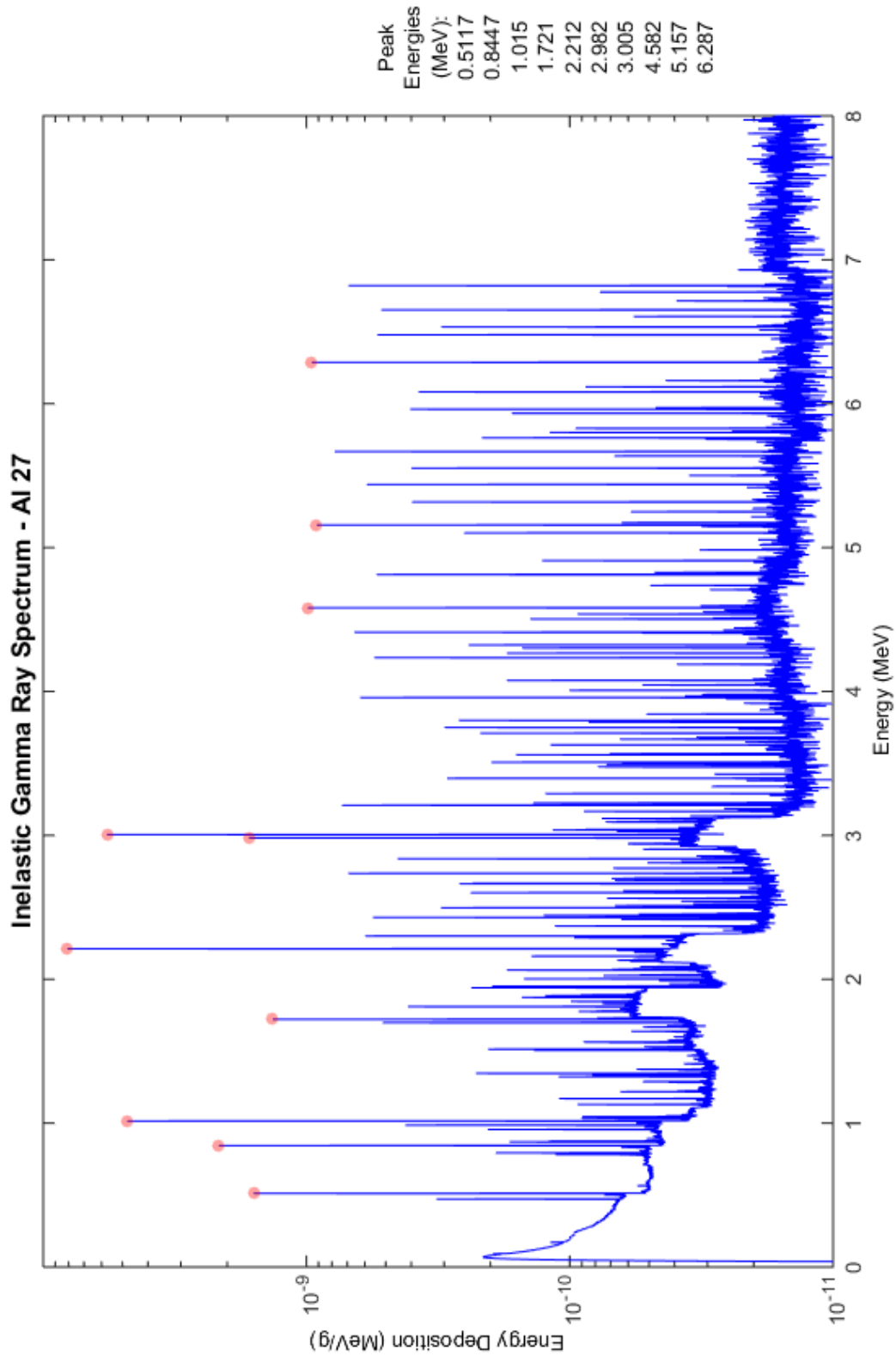
12 Magnesium: (material composition: 12000)



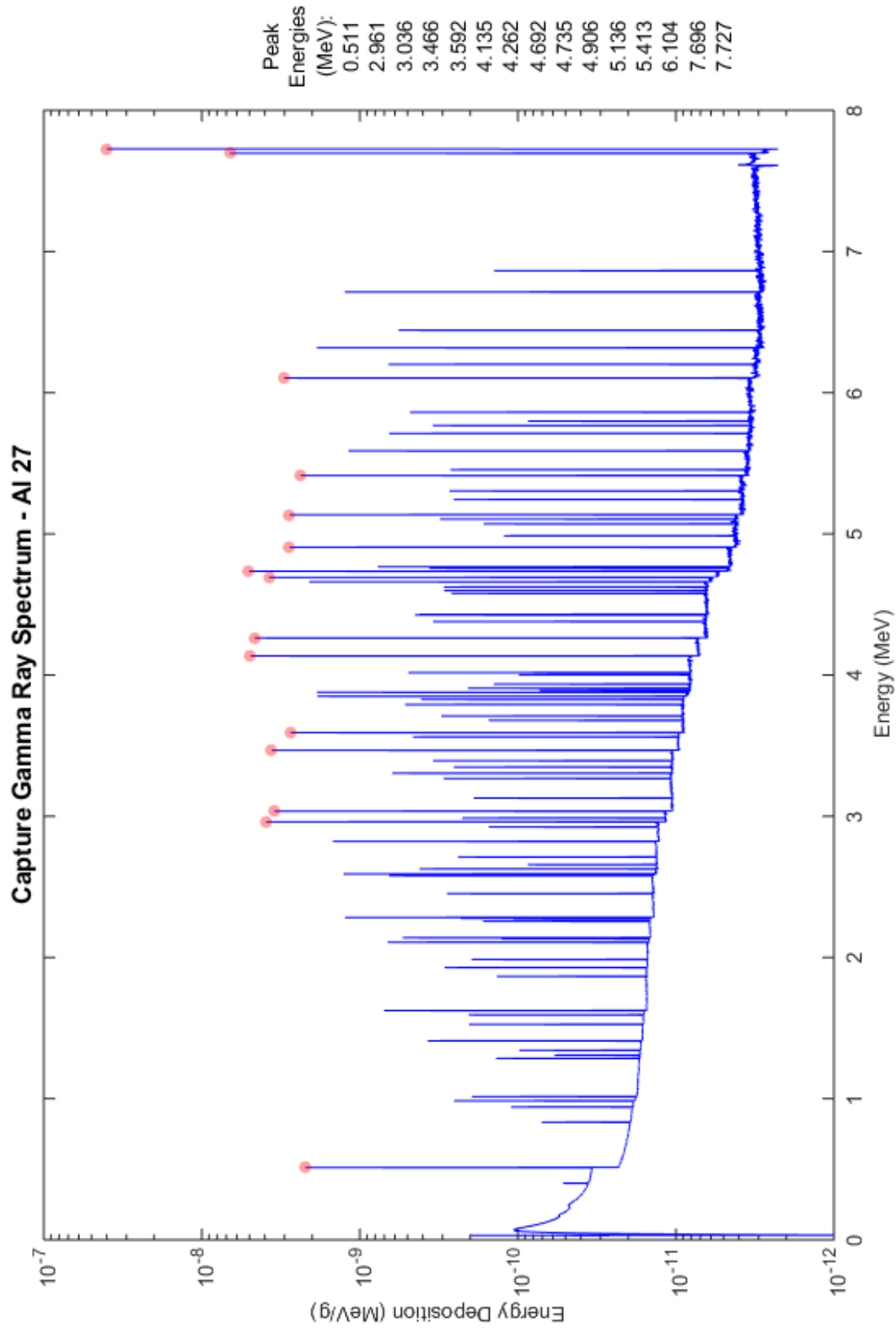
12 Magnesium: (material composition: 12000)



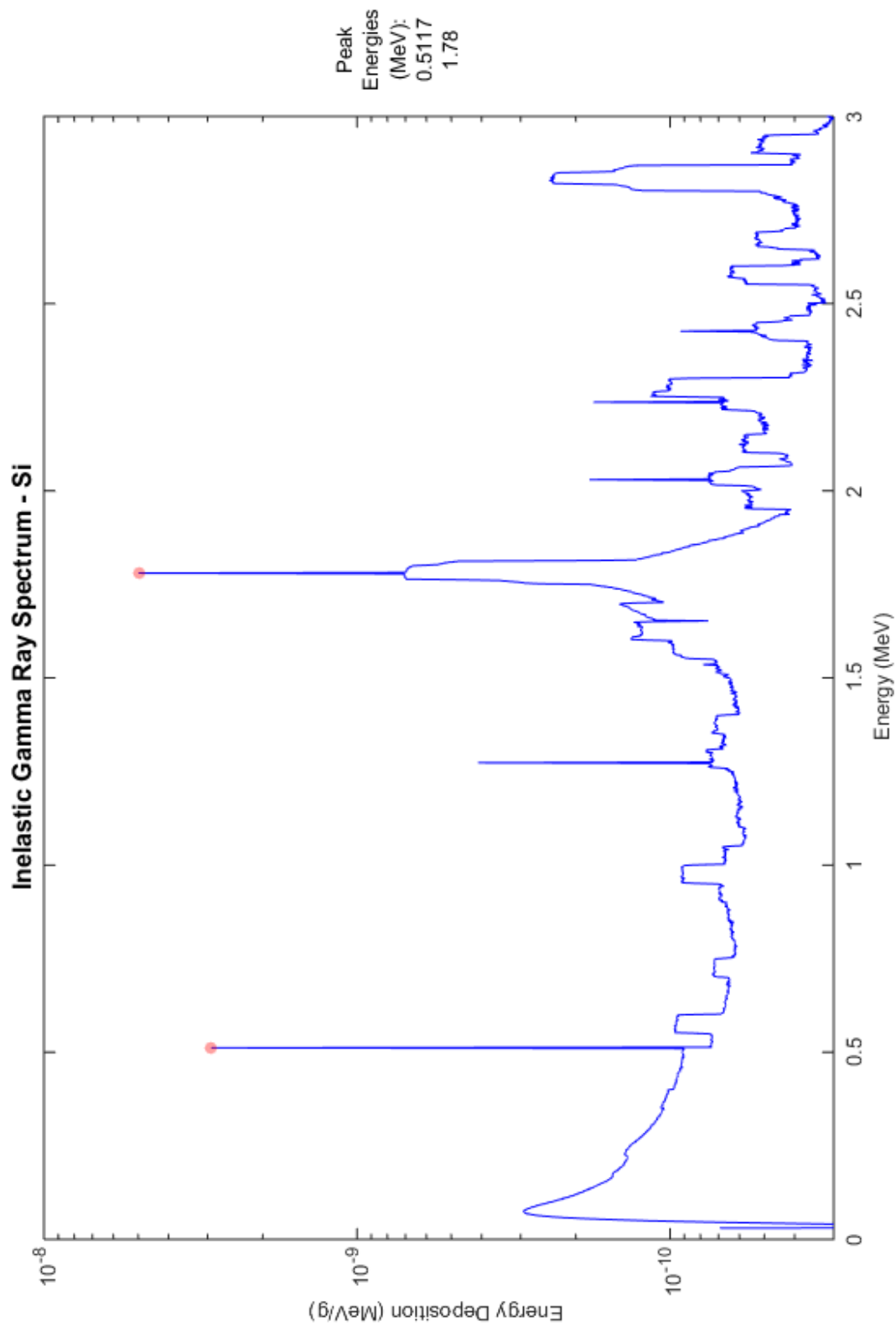
¹³Aluminum: (material composition: 13027)



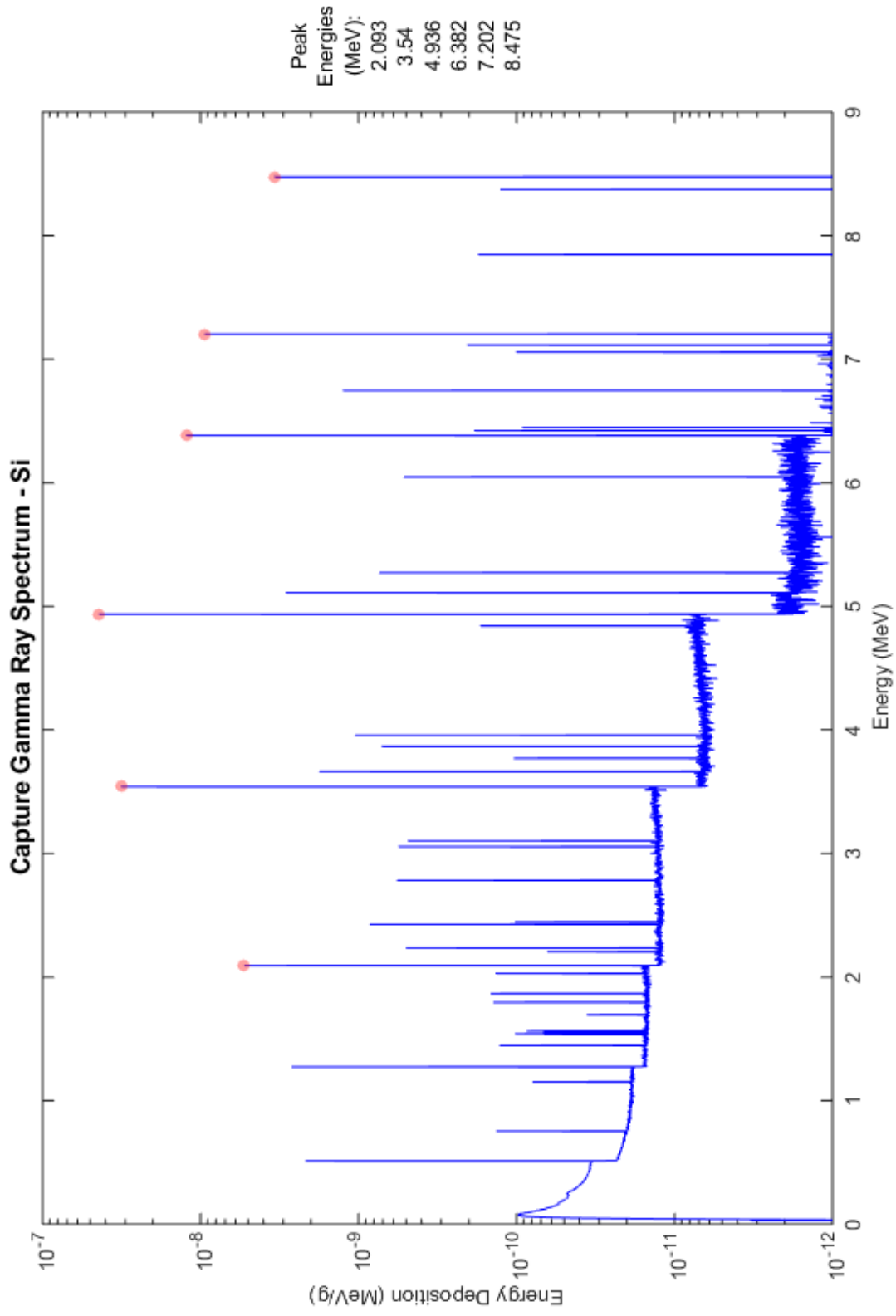
¹³Aluminum: (material composition: 13027)



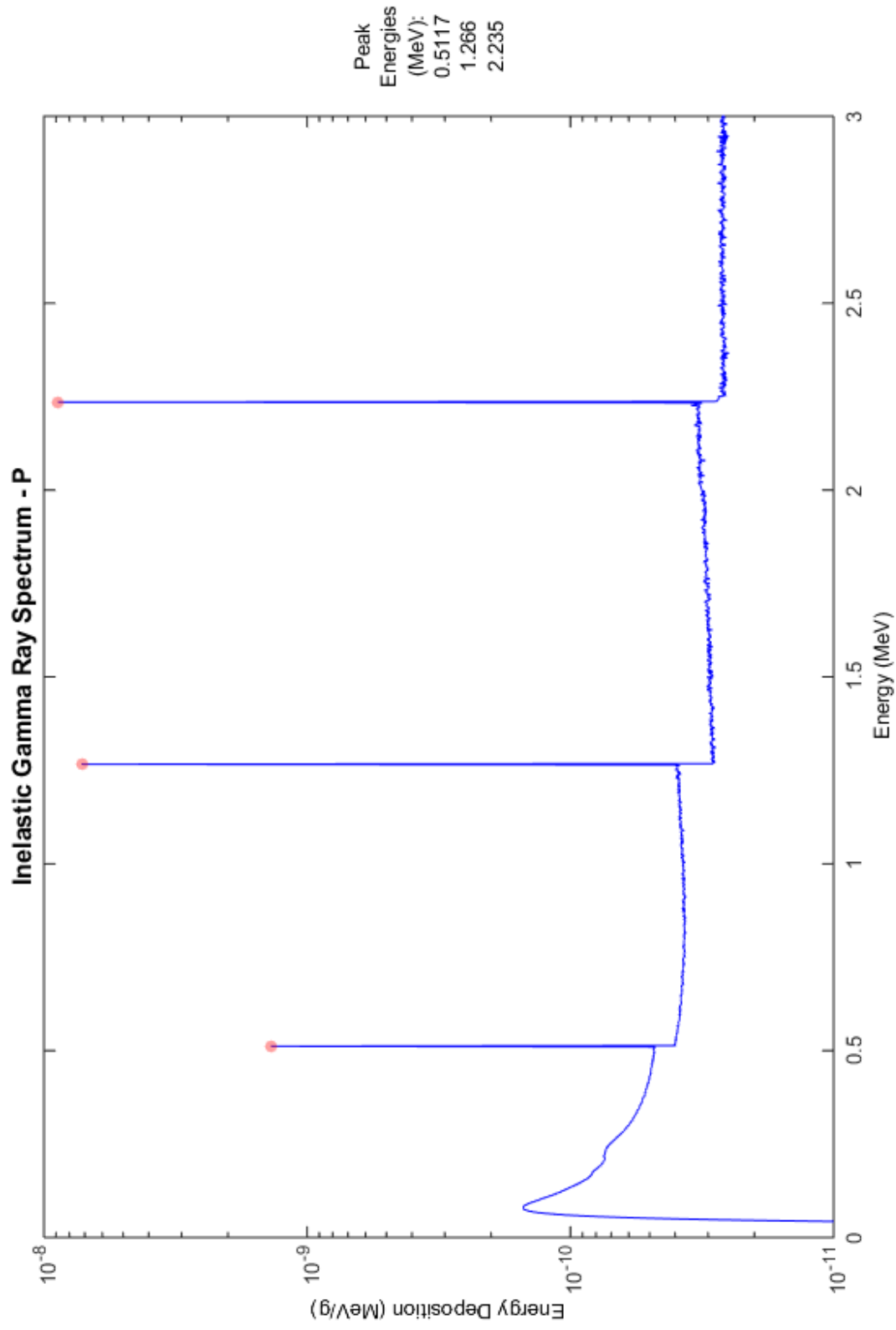
14 Silicon: (material composition: 14000)



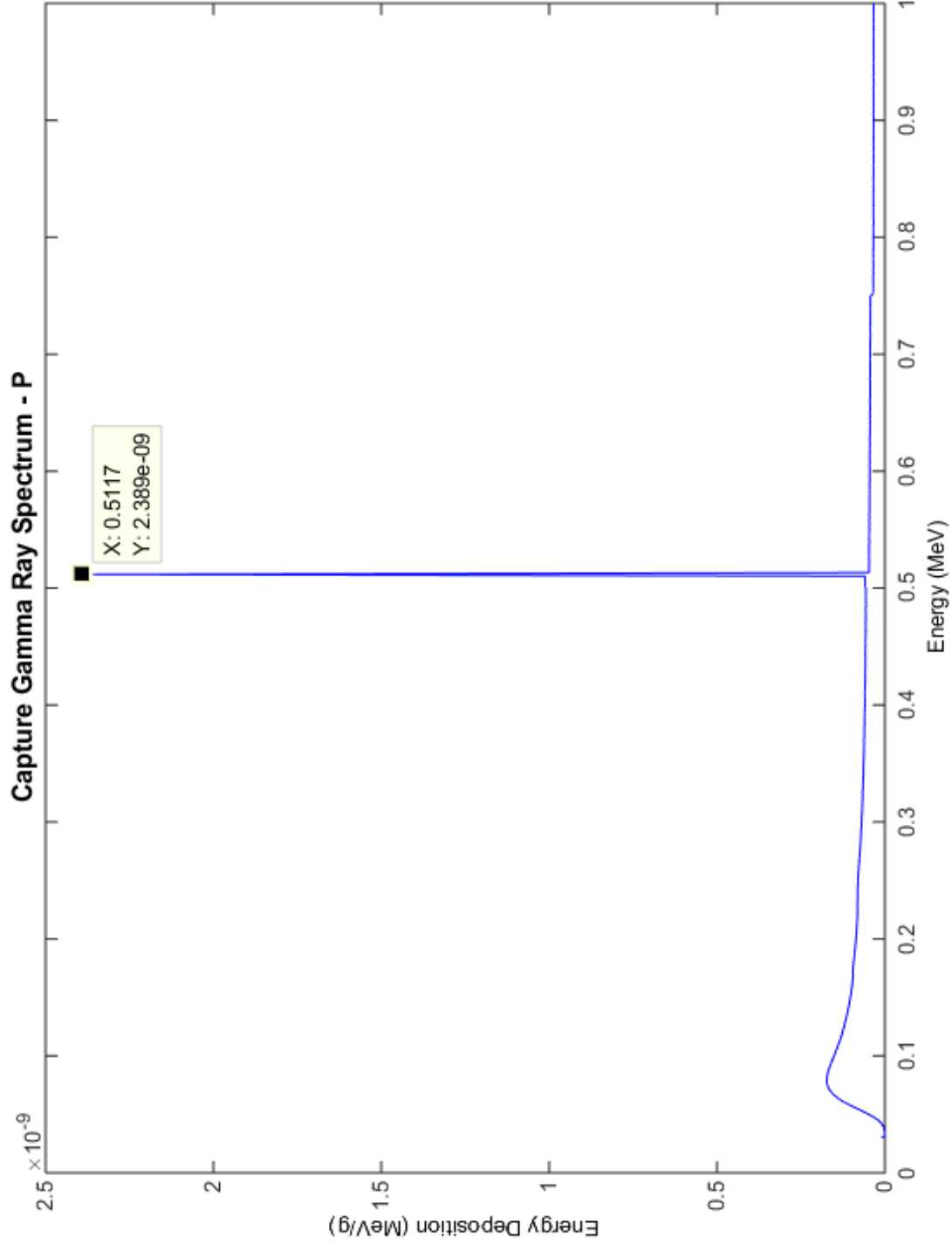
14 Silicon: (material composition: 14000)



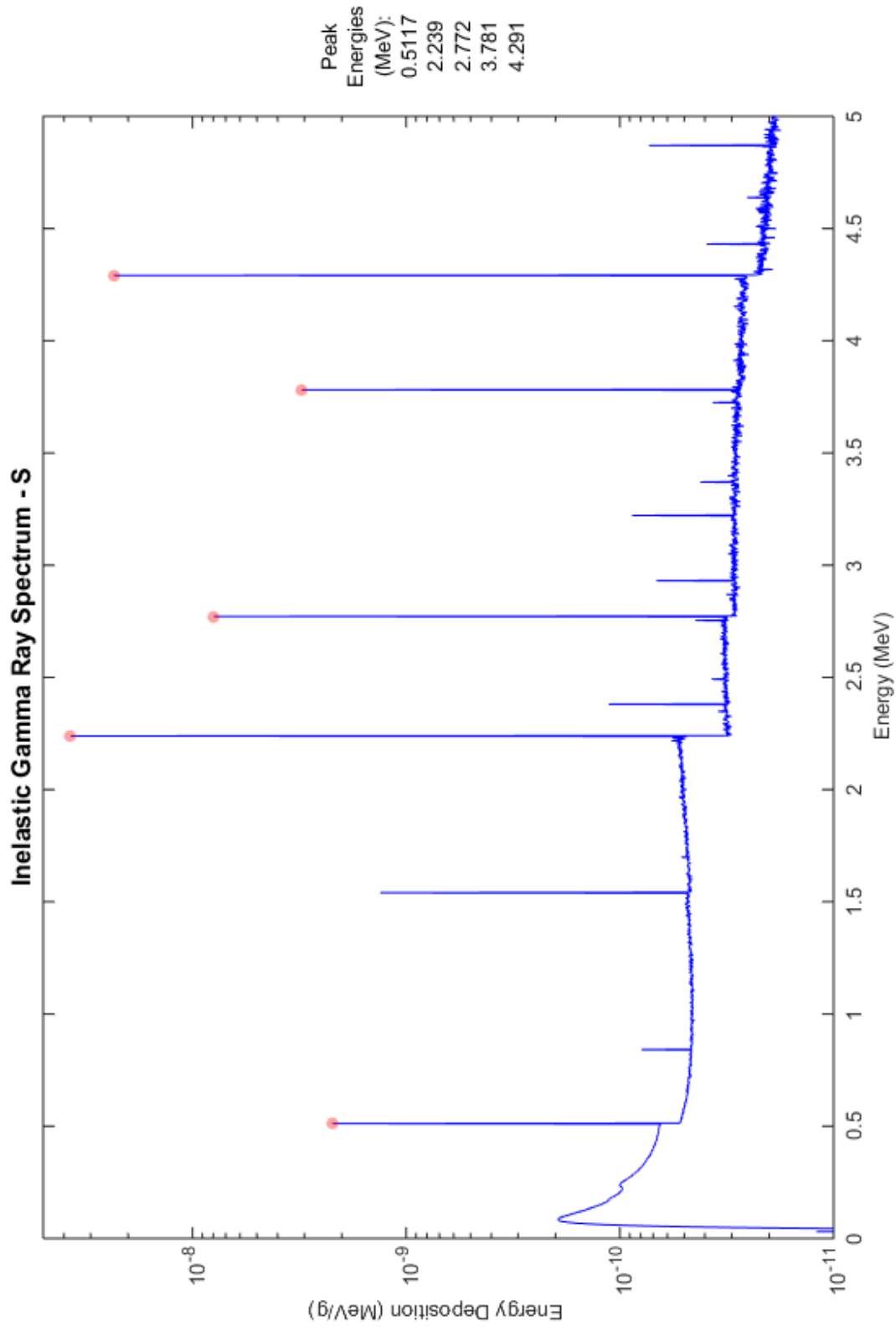
15 Phosphorus: (material composition: 15031)



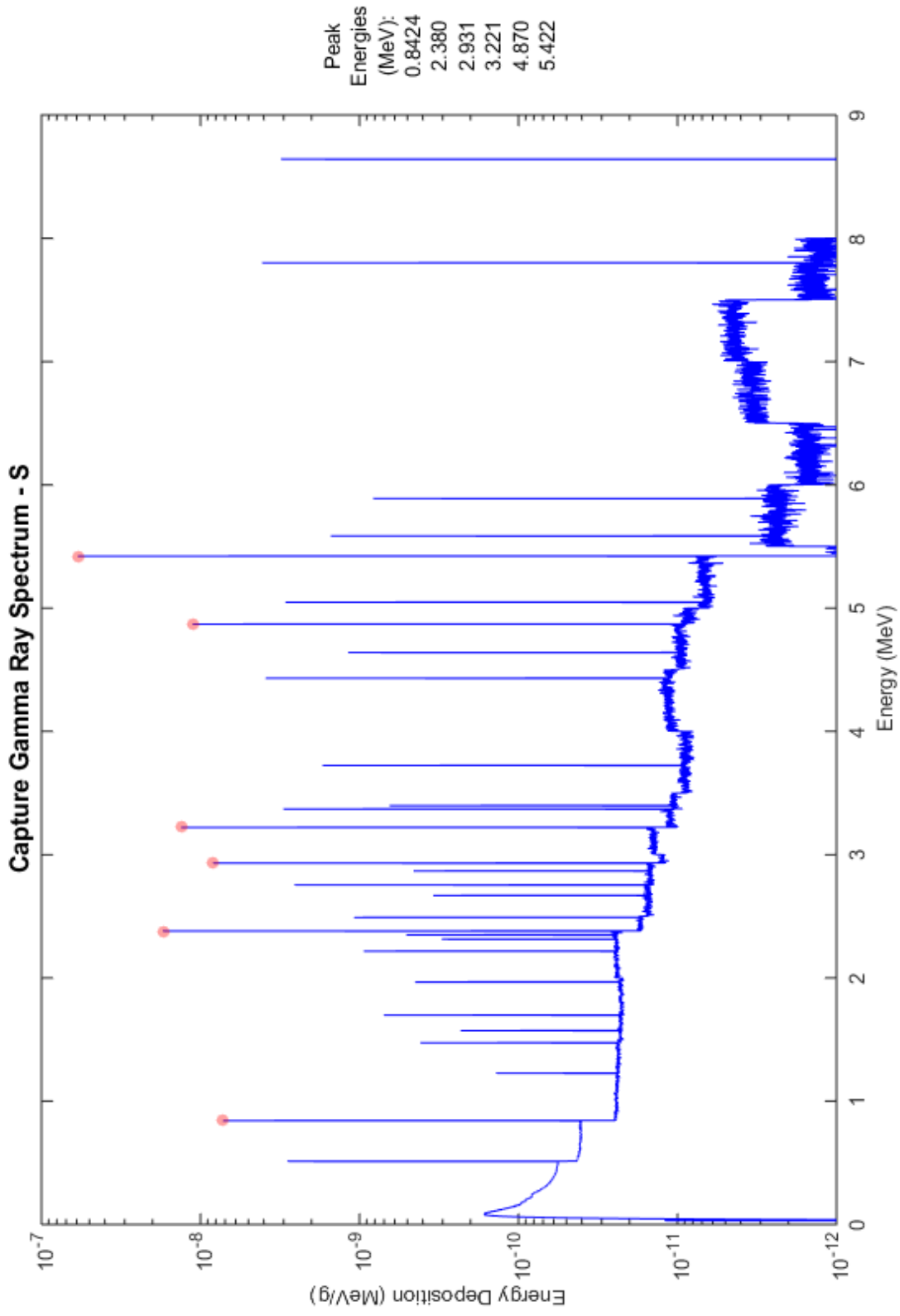
15 Phosphorus: (material composition: 15031)



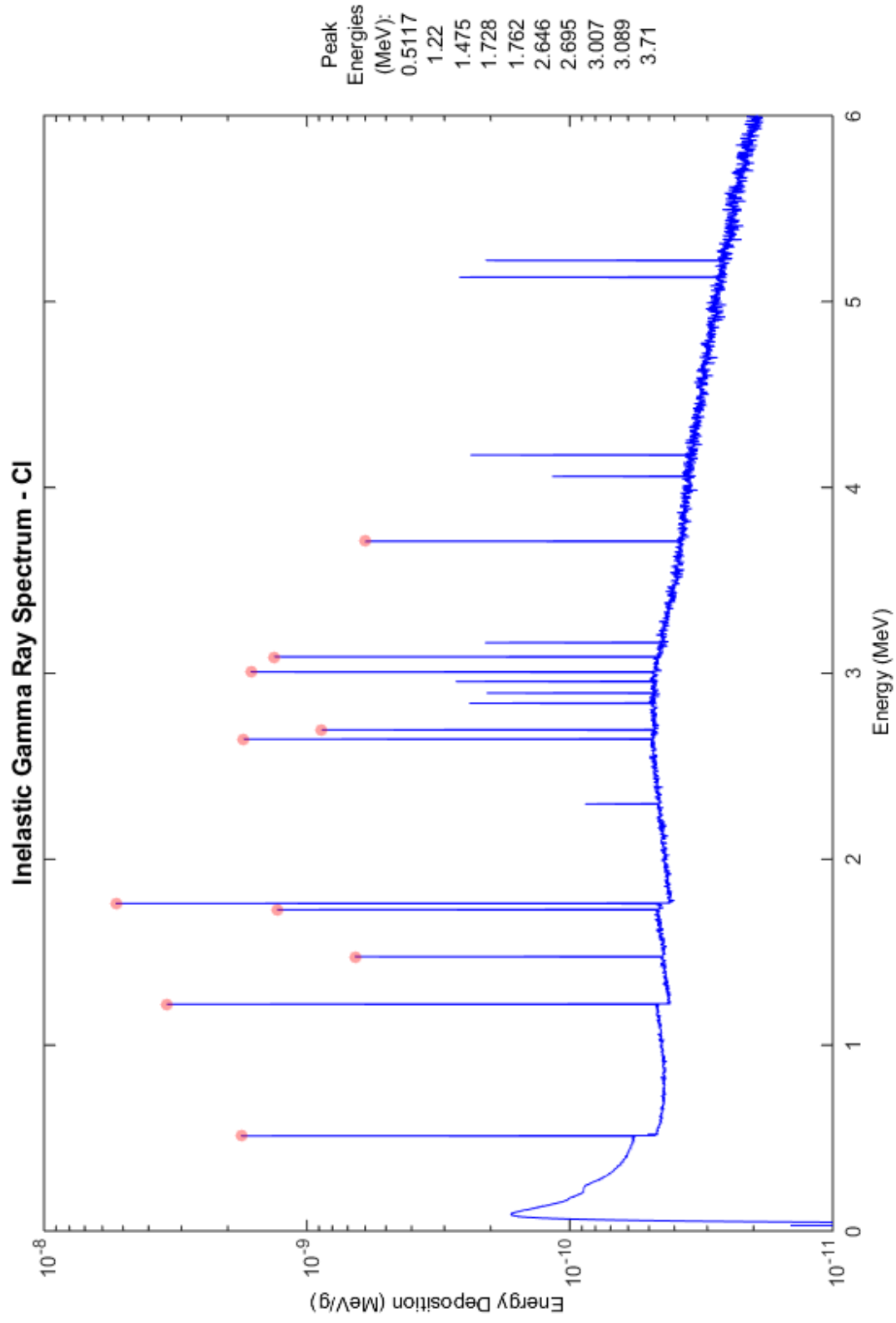
16 Sulfur: (material composition: 16000)



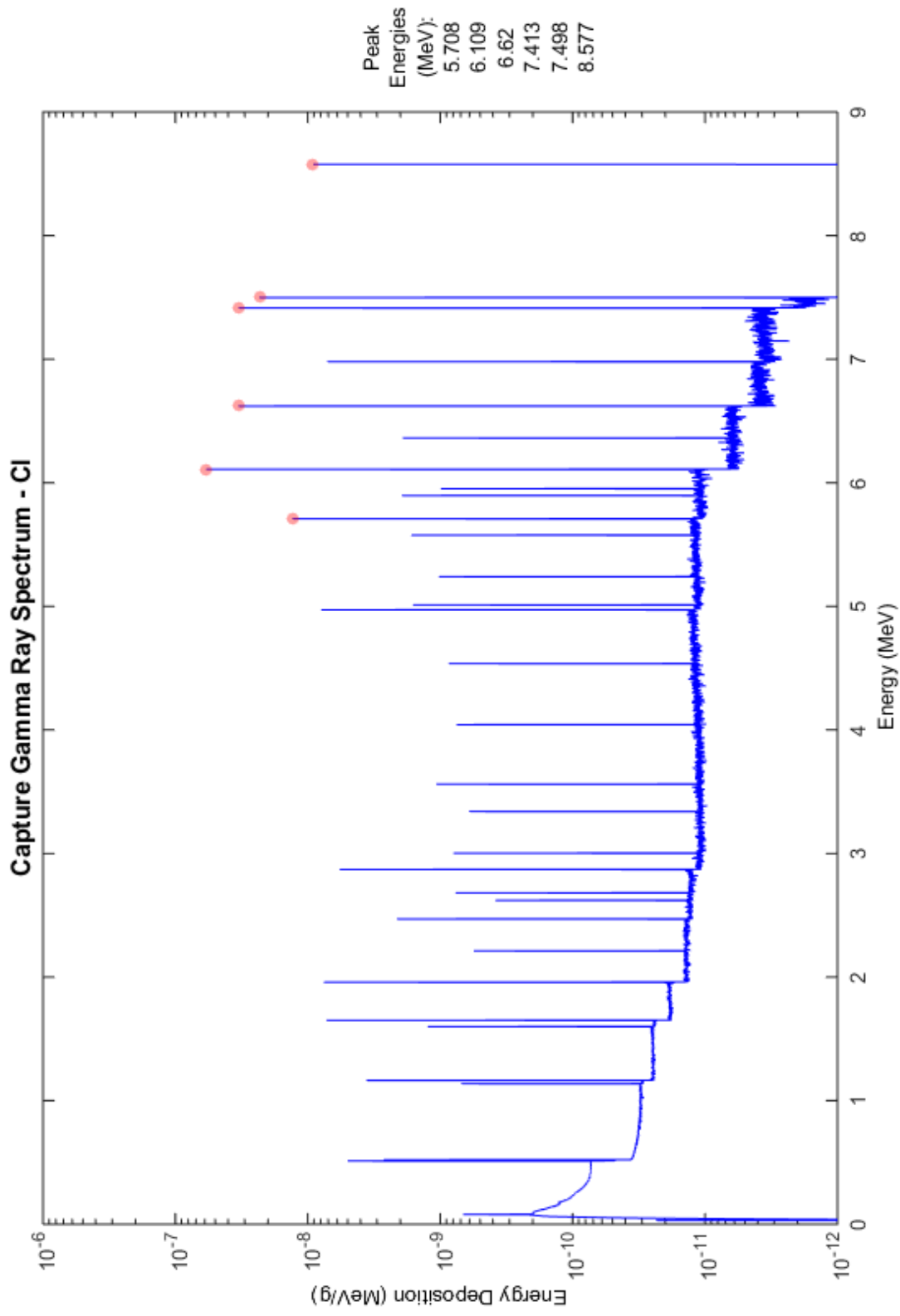
16 Sulfur: (material composition: 16000)



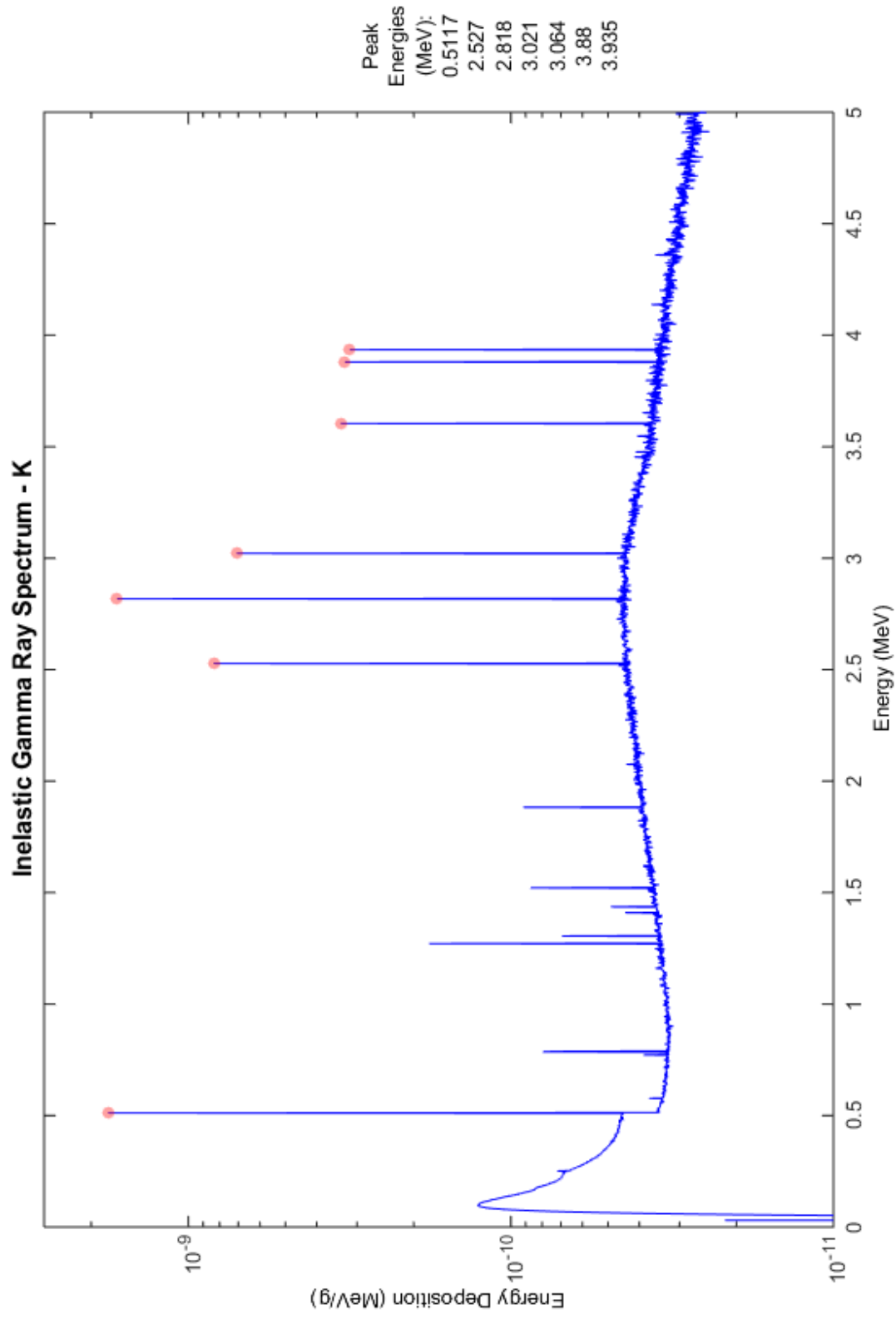
17 Chlorine: (material composition: 17000)



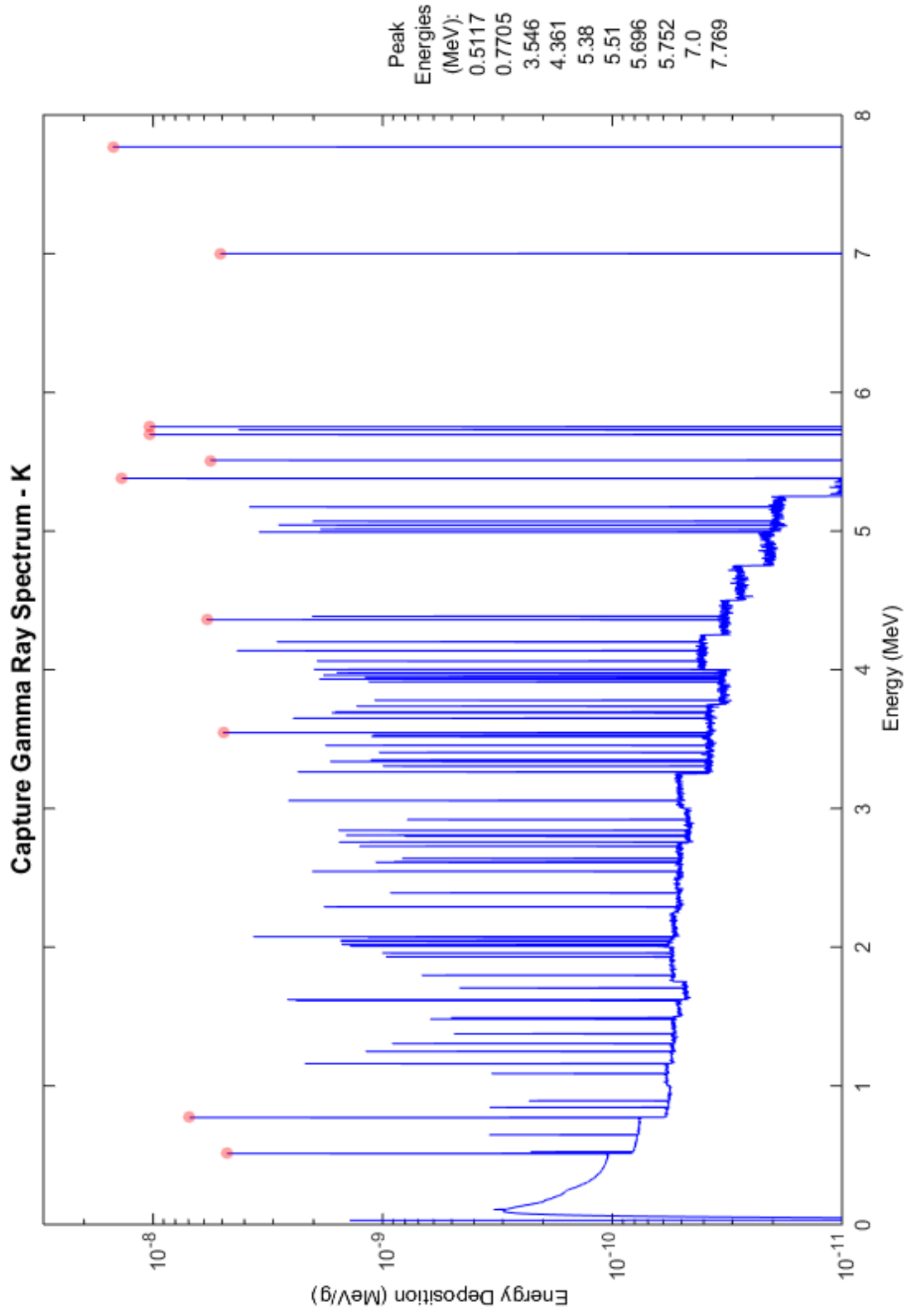
17 Chlorine: (material composition: 17000)



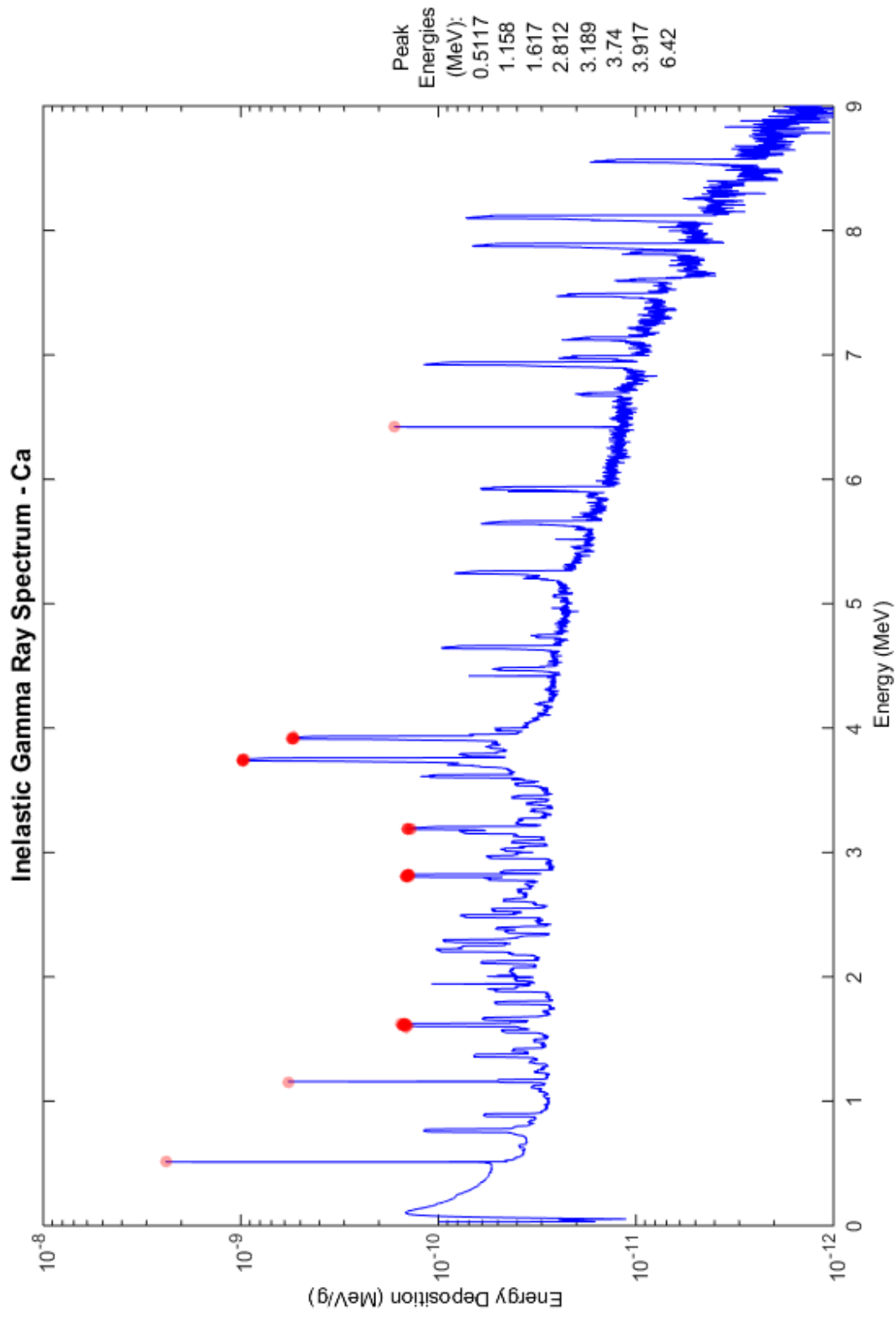
19 Potassium: (material composition: 19000)



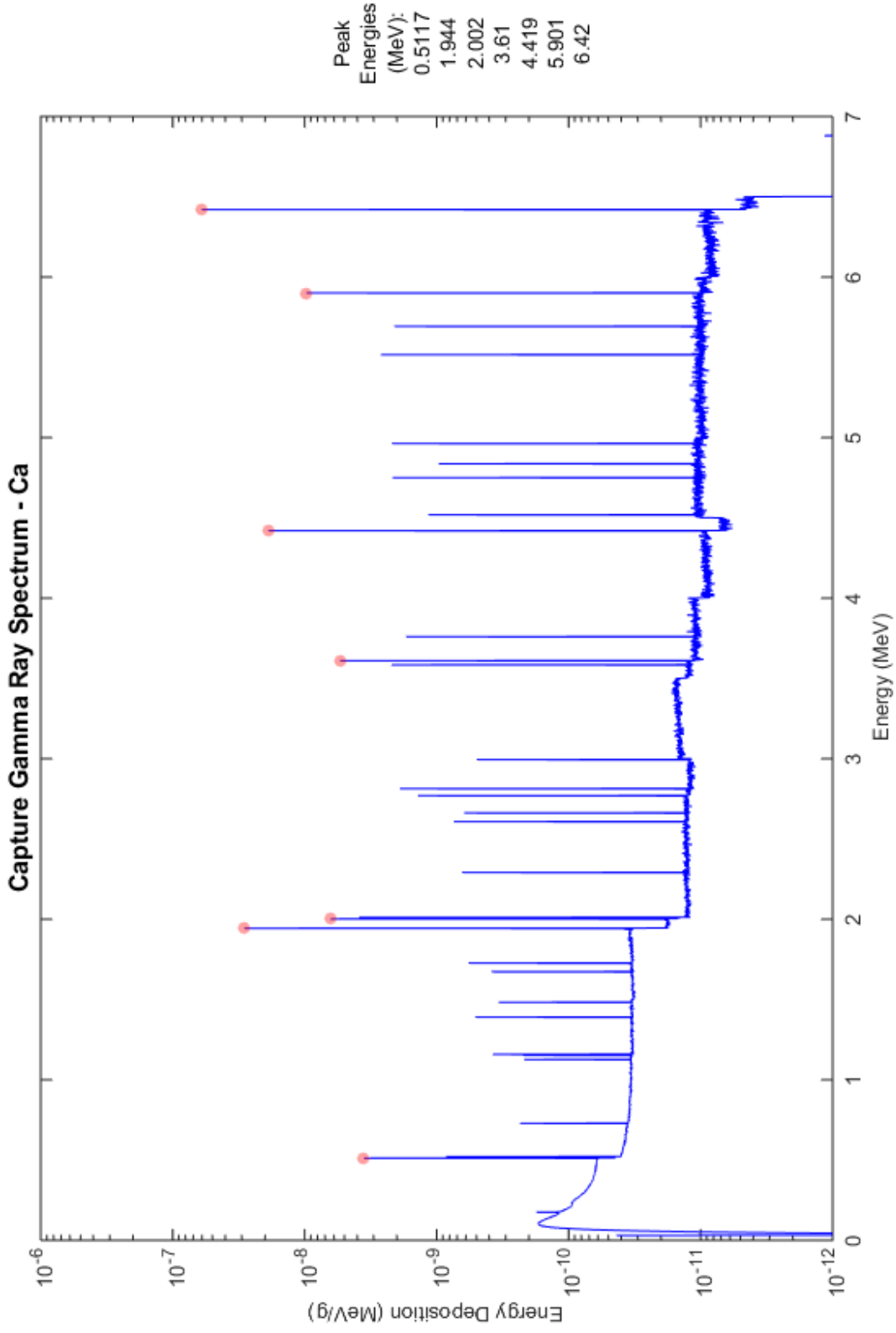
19 Potassium: (material composition: 19000)



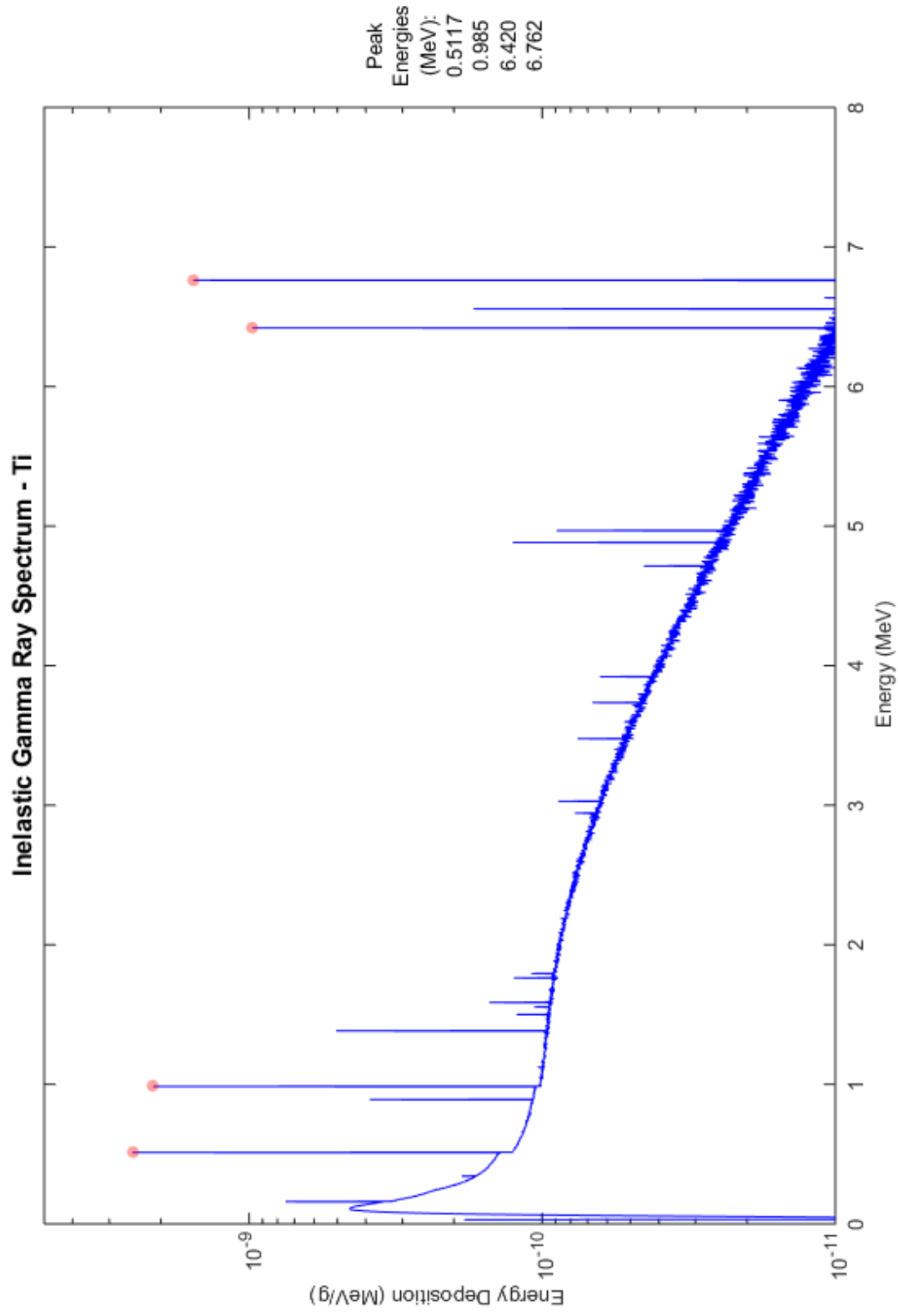
20 Calcium: (material composition: 20000)



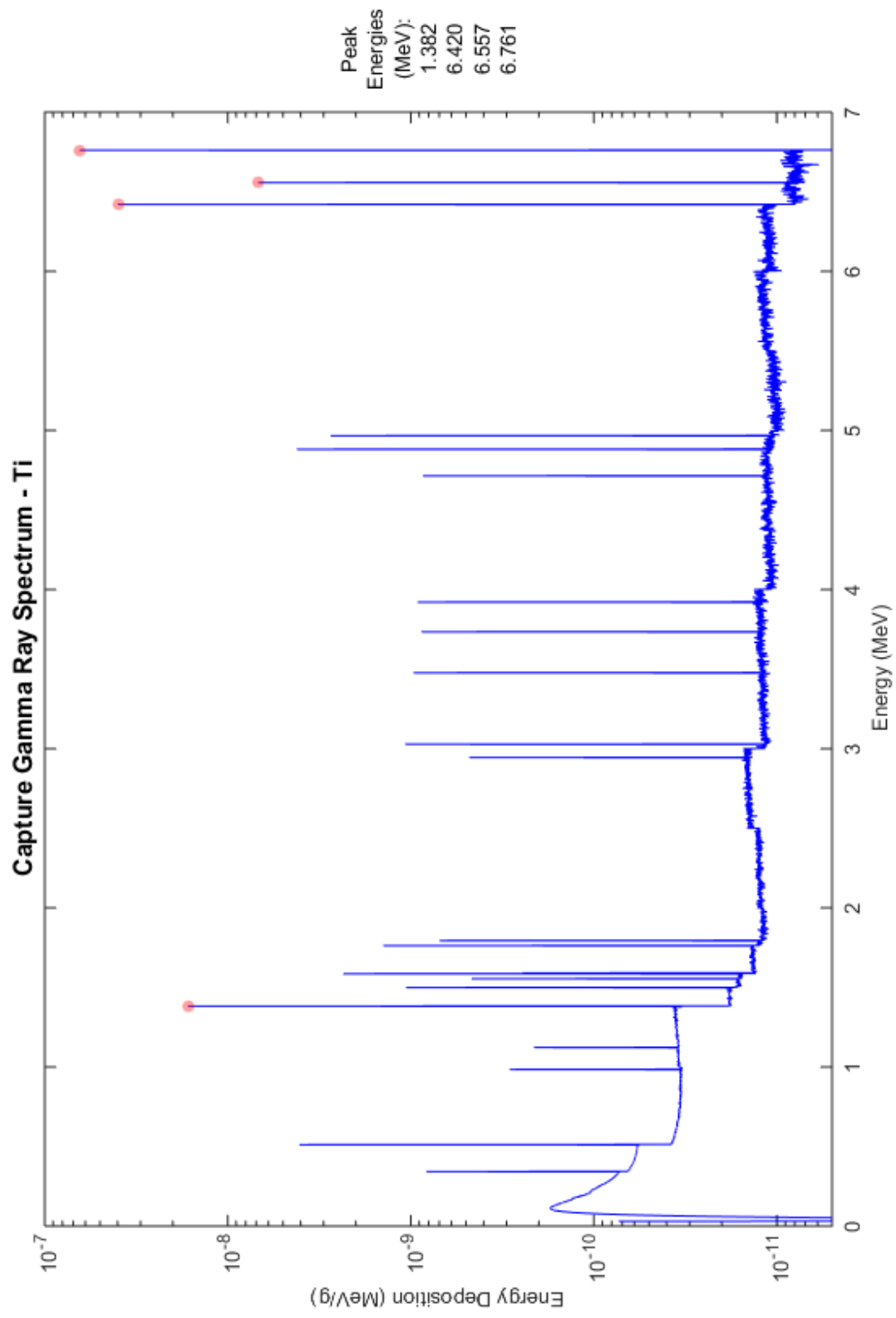
20 Calcium: (material composition: 20000)



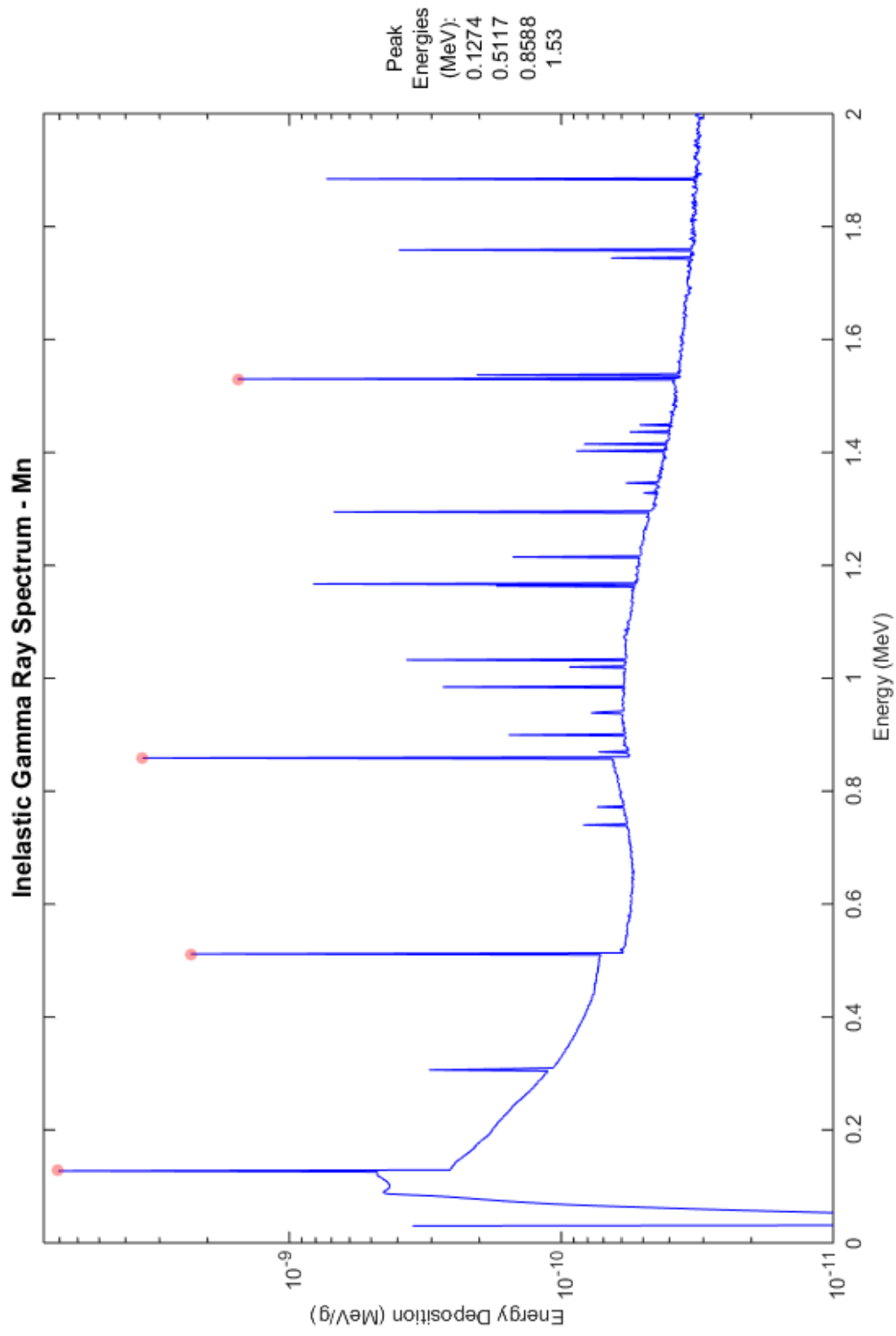
22 Titanium: (material composition: 22000)



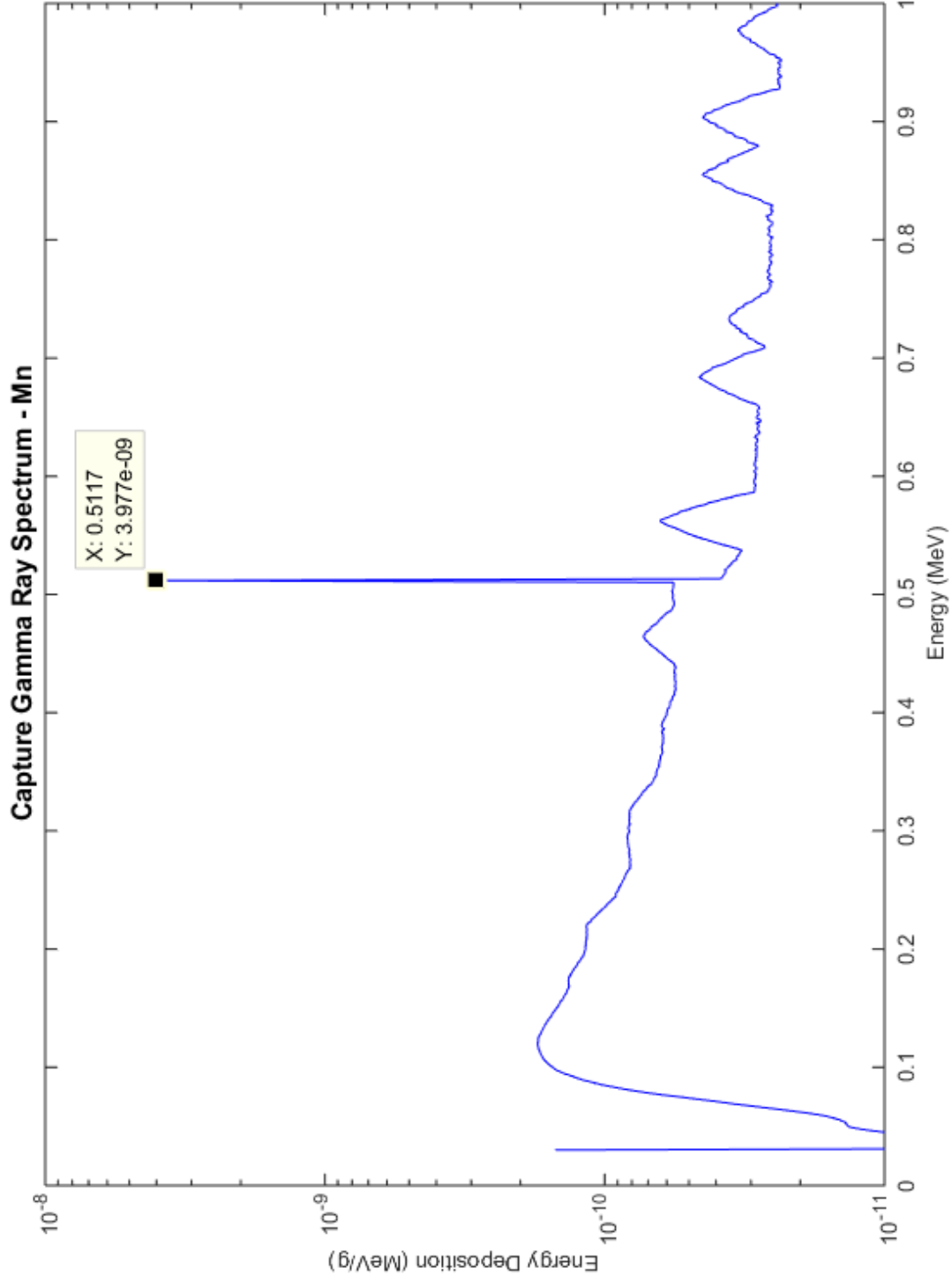
22 Titanium: (material composition: 22000)



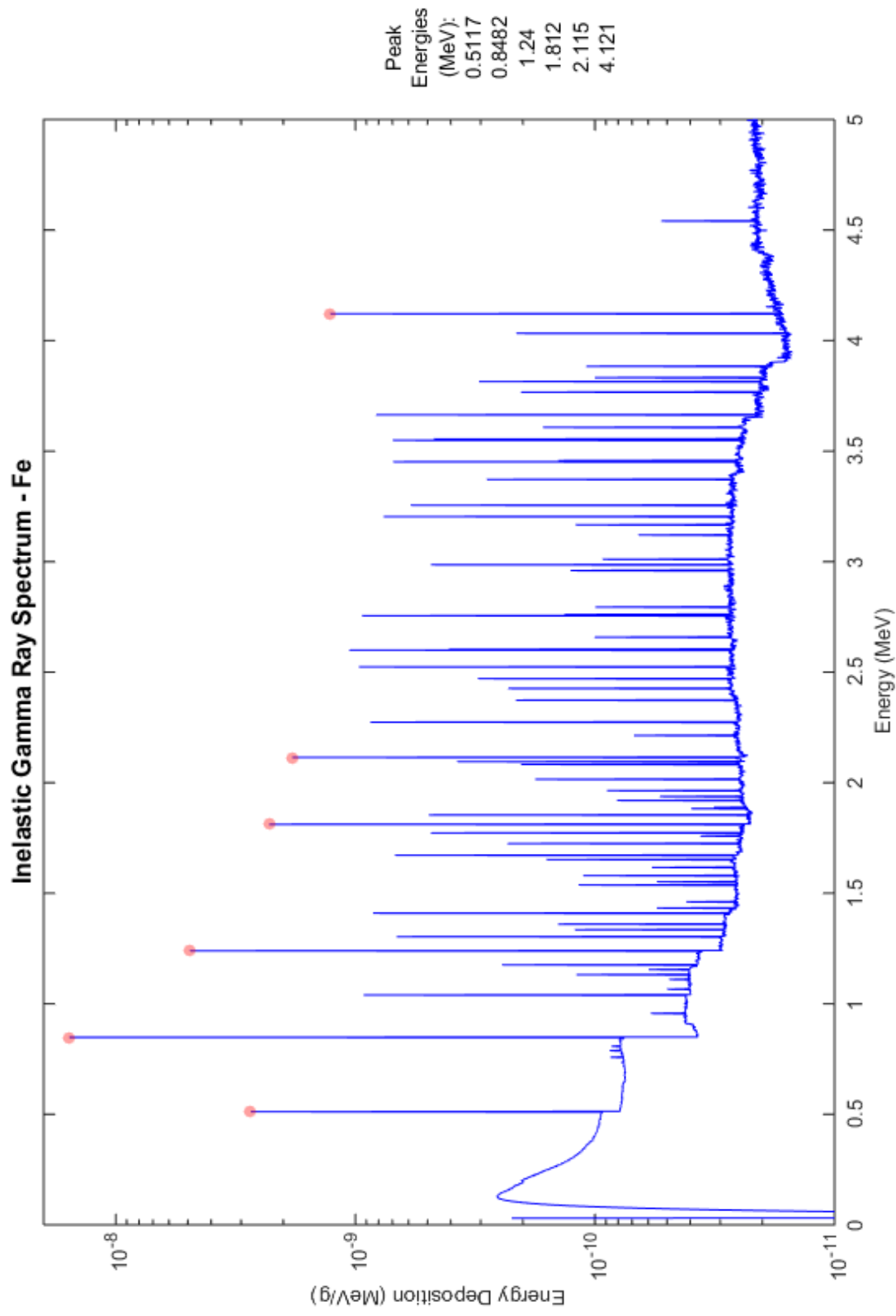
25 Manganese: (material composition: 25055)



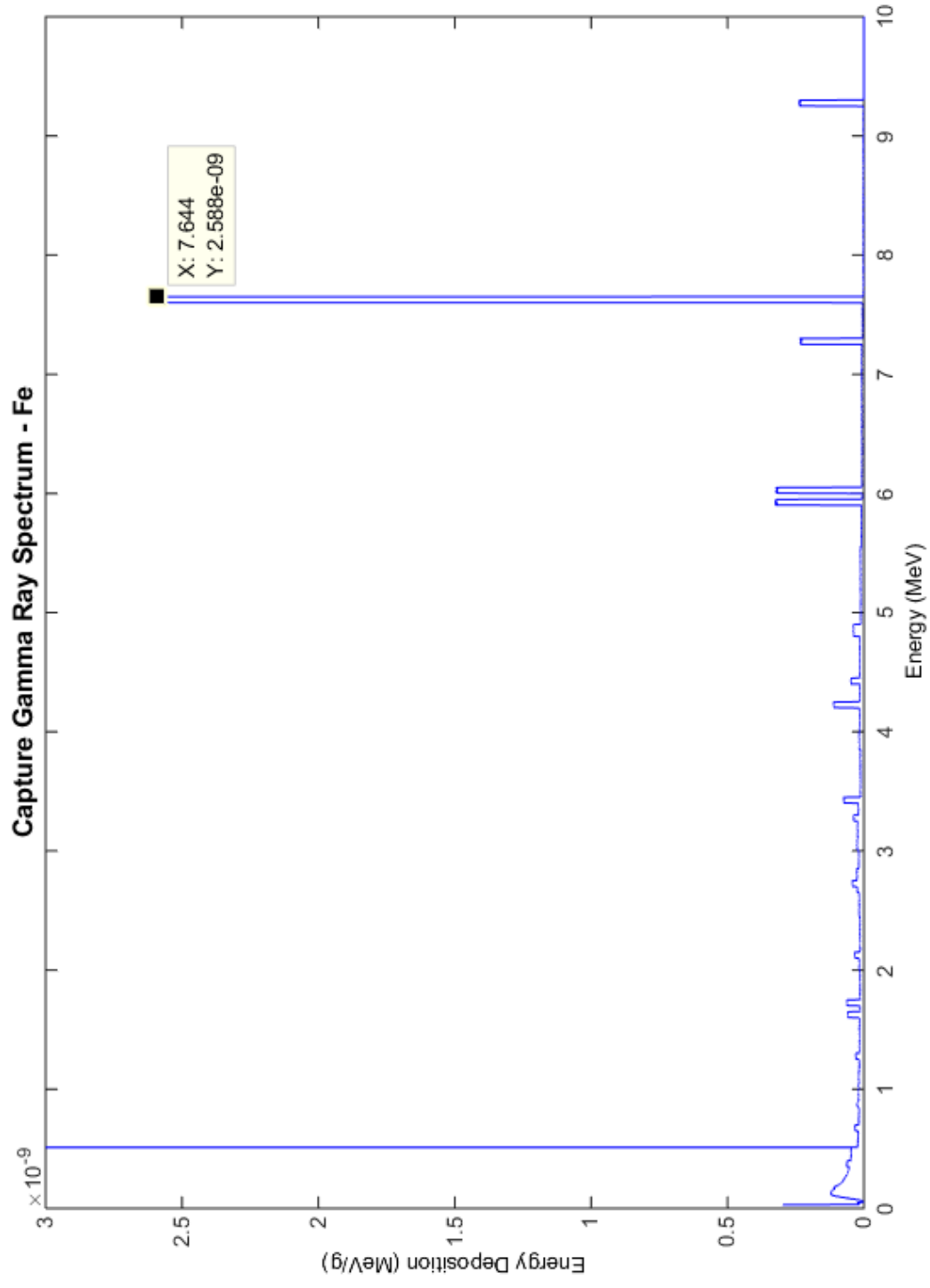
25 Manganese: (material composition: 25055)



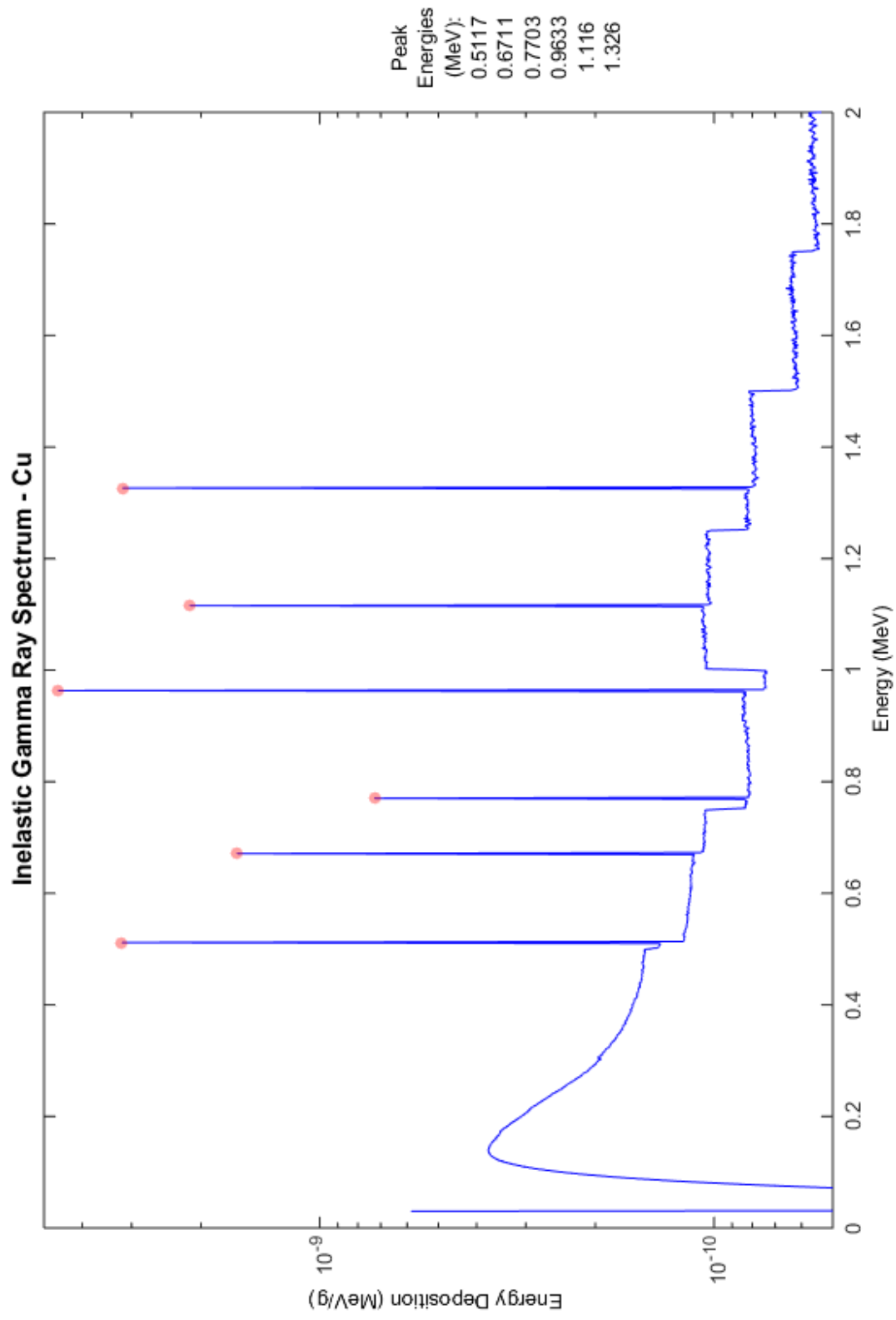
26 Iron: (material composition: 26000)



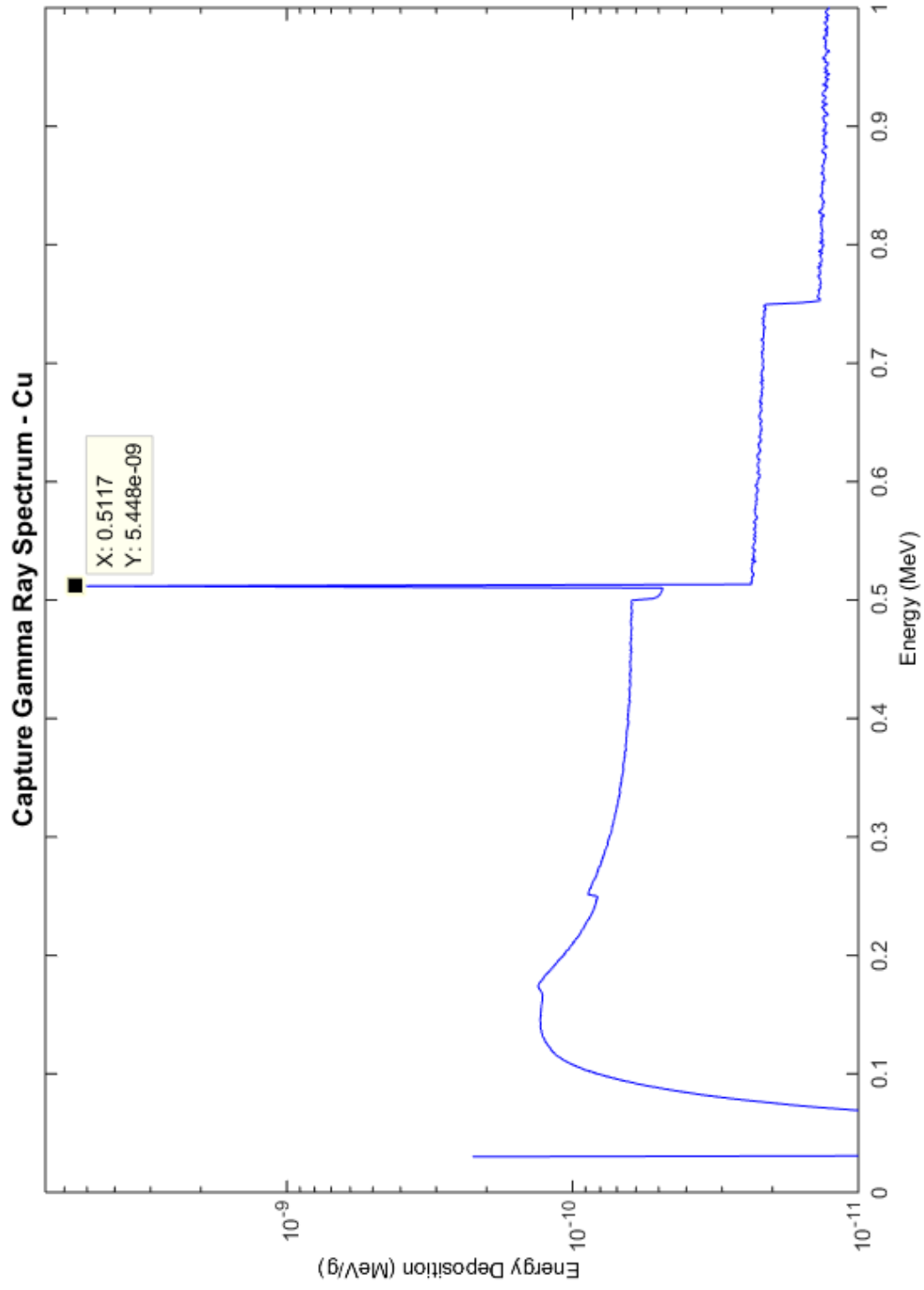
26 Iron: (material composition: 26000)



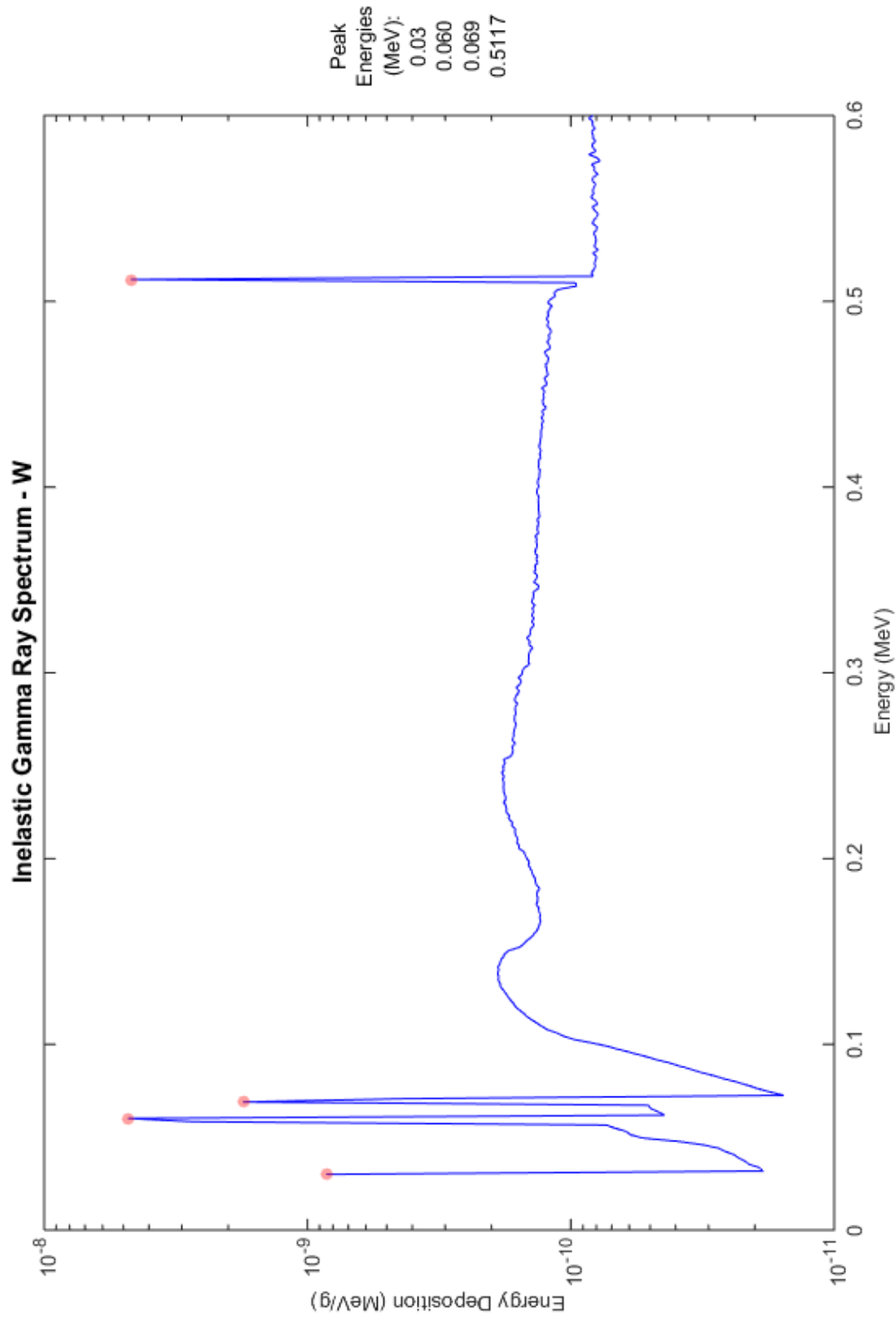
29 Copper: (material composition: 29000)



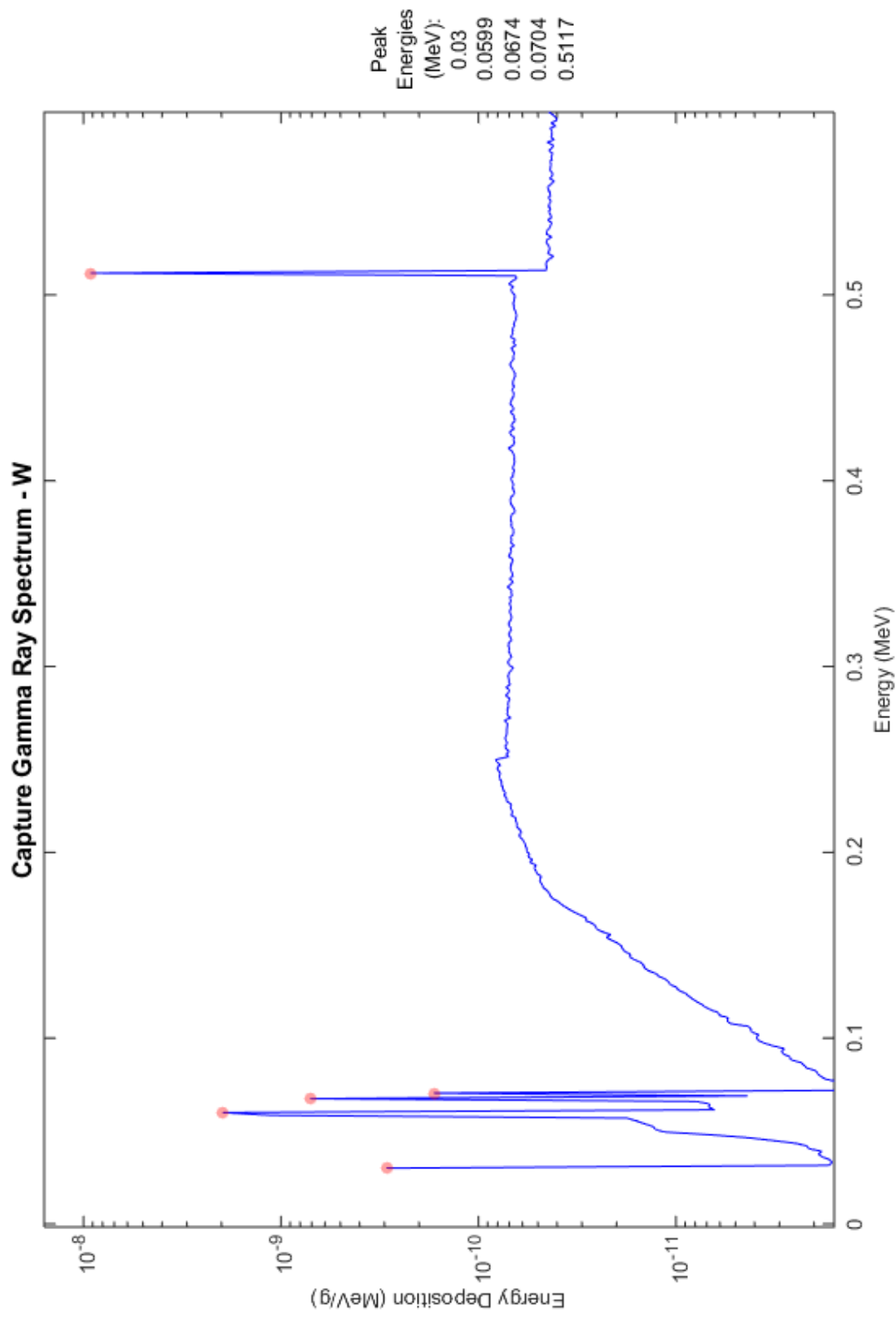
29 Copper: (material composition: 29000)



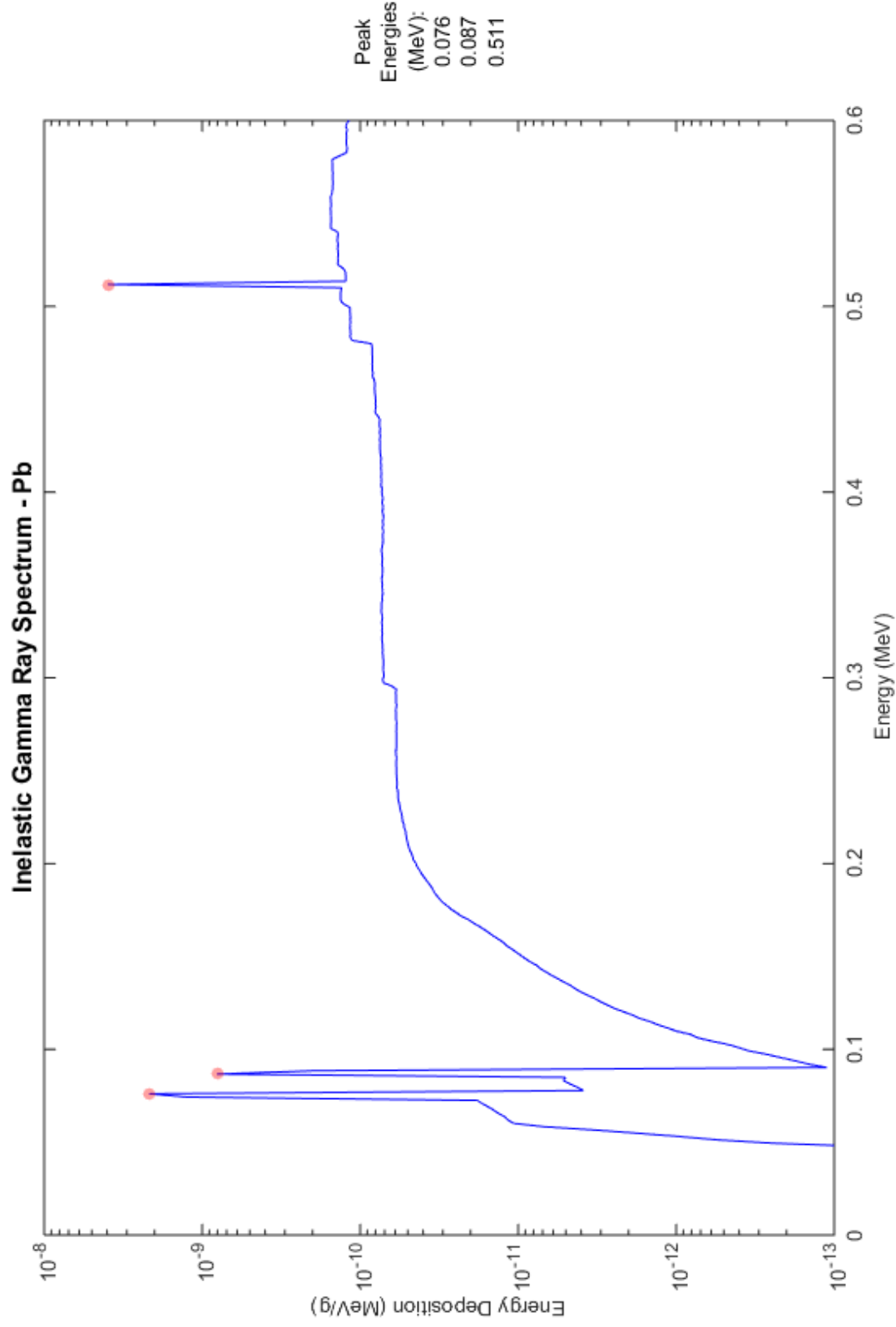
74 Tungsten: (material composition: 74000)



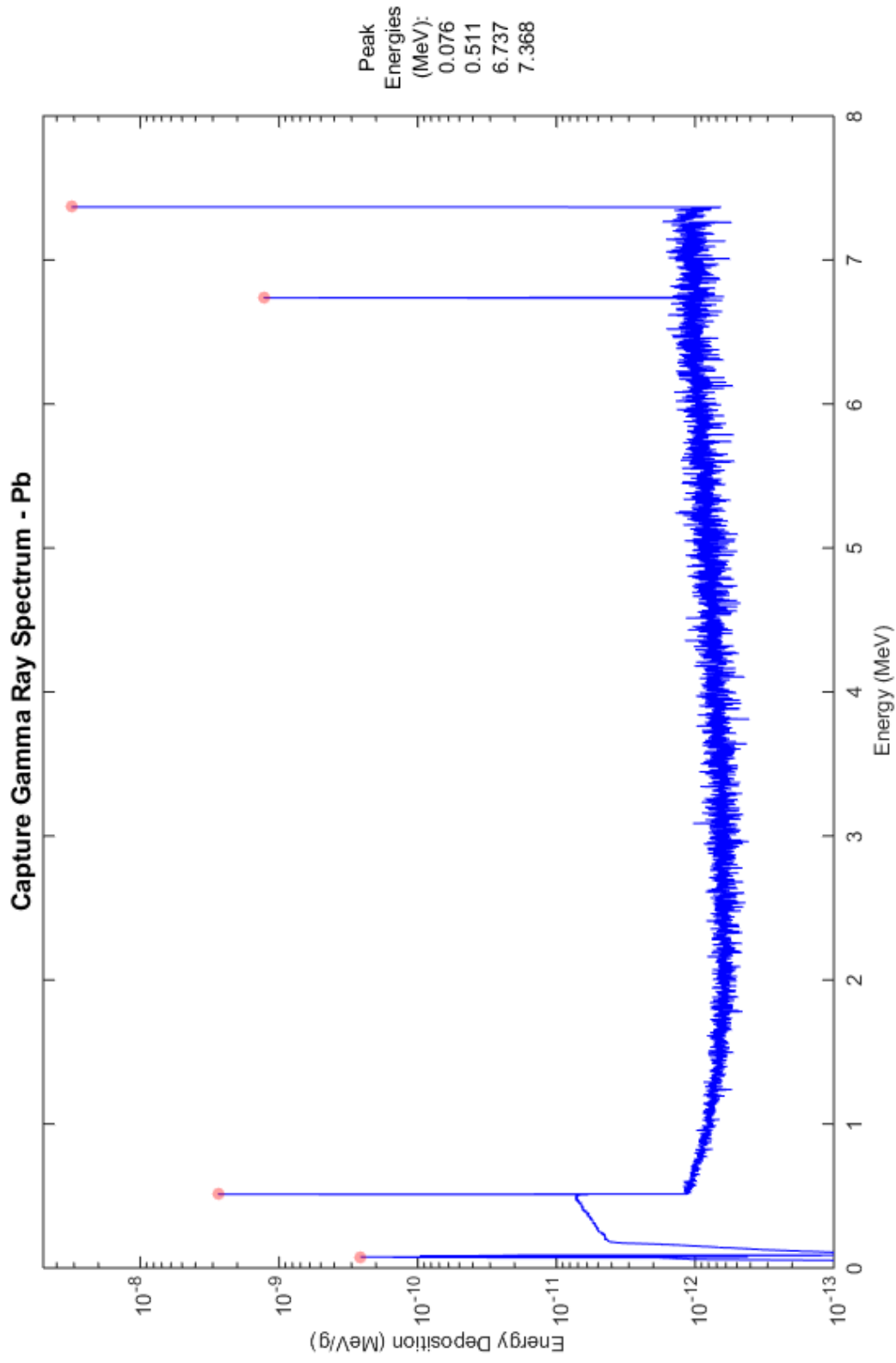
74 Tungsten: (material composition: 74000)



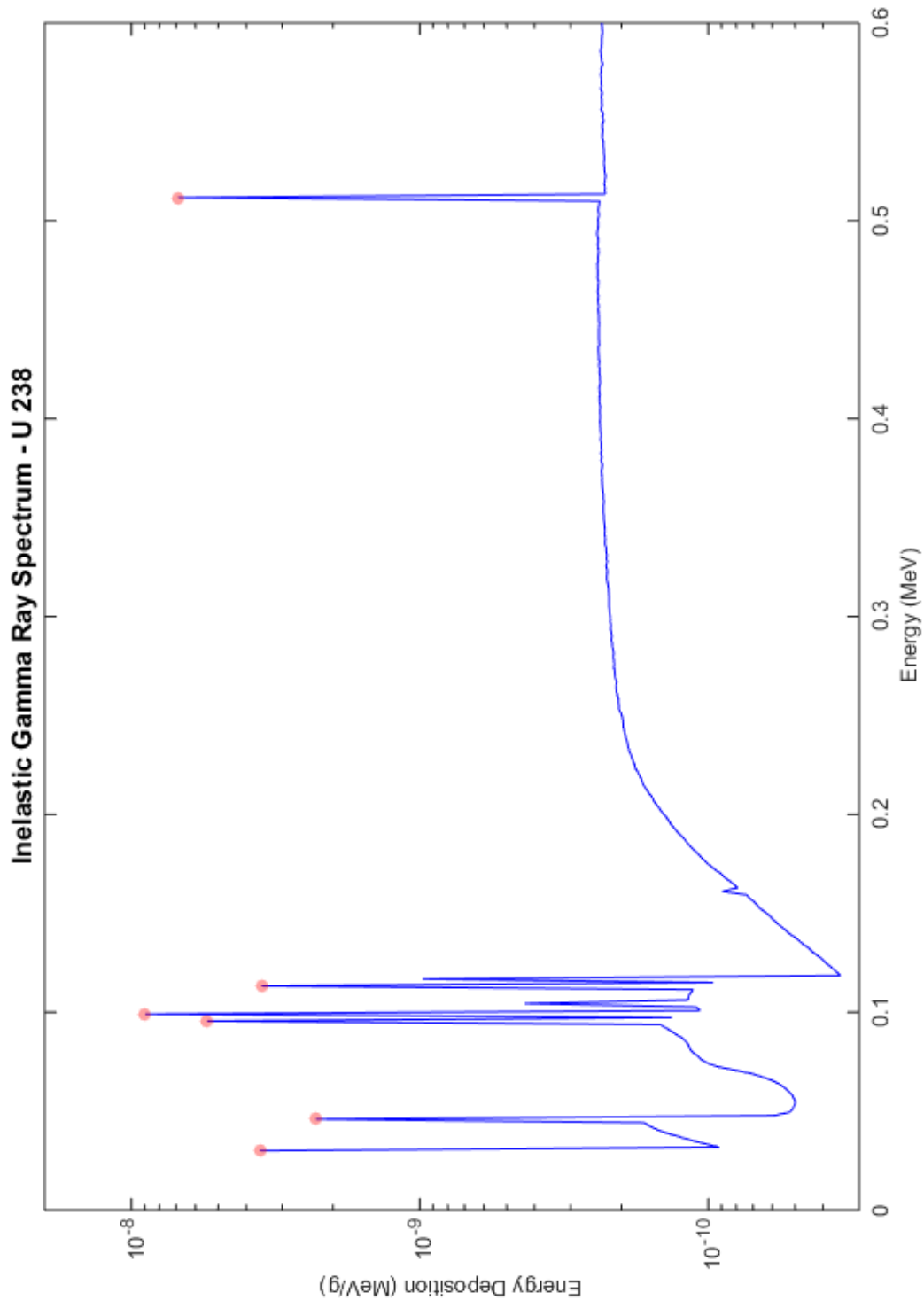
82 Lead: (material composition: 82000)



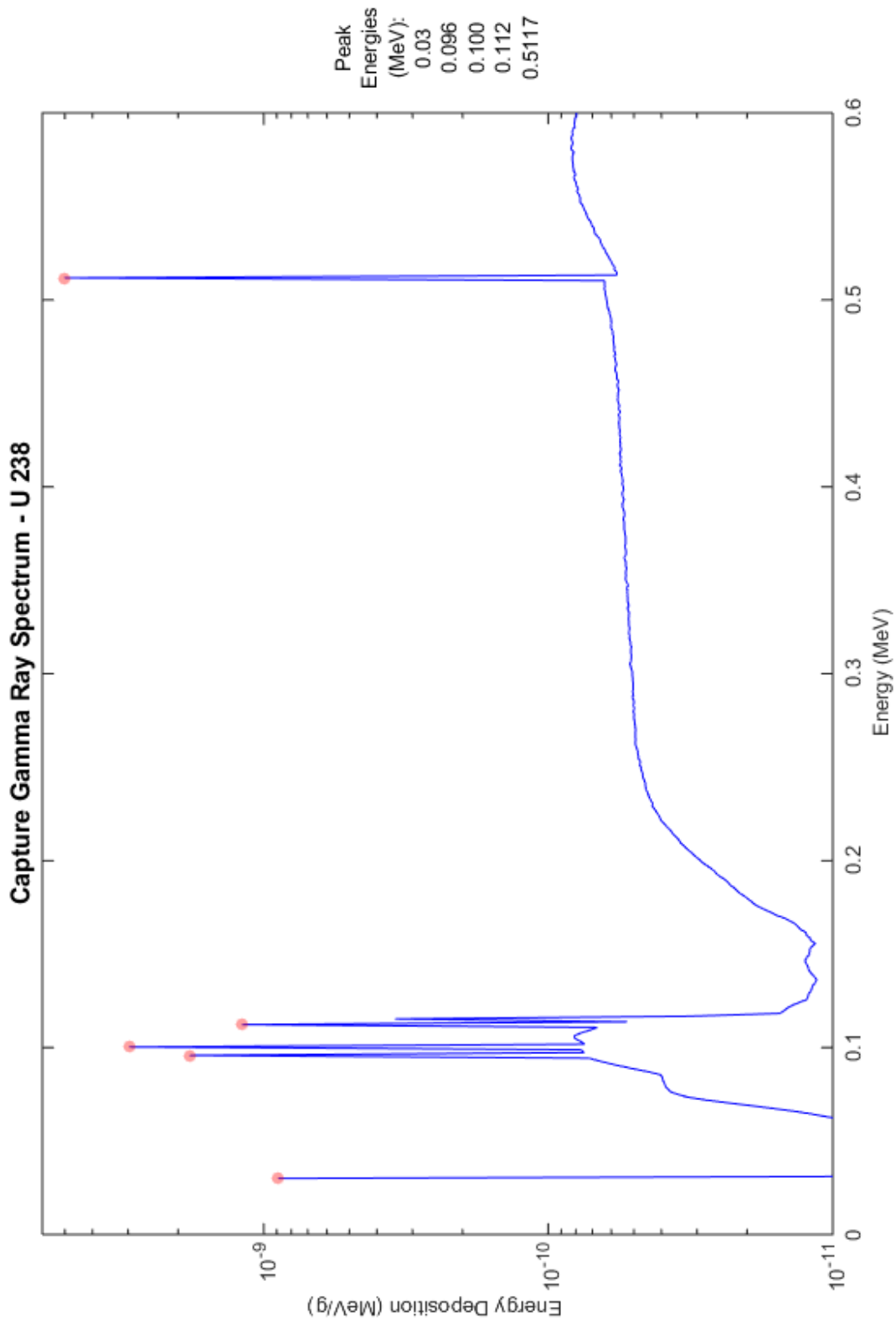
82 Lead: (material composition: 82000)



92 Uranium 238: (material composition: 92238)



92 Uranium 238: (material composition: 92238)



Appendix

Sorted by Element

ENERGY (MEV)	ELEMENT	A	TYPE
2.225	H	1	Capture
2.125	B	5	Inelastic
2.298	B	5	Capture
2.537	B	5	Capture
3.368	B	5	Inelastic
4.445	B	5	Inelastic
4.446	B	5	Capture
4.714	B	5	Capture
5.021	B	5	Inelastic
5.855	B	5	Inelastic
6.744	B	5	Inelastic
6.744	B	5	Capture
6.794	B	5	Inelastic
7.012	B	5	Capture
7.286	B	5	Inelastic
7.978	B	5	Inelastic
8.561	B	5	Inelastic
8.921	B	5	Inelastic
1.263	C	6	Capture
3.685	C	6	Capture
4.440	C	6	Inelastic
4.948	C	6	Capture
1.636	N	7	Inelastic
1.885	N	7	Capture
2.313	N	7	Inelastic
3.532	N	7	Capture

Sorted by Energy

ENERGY (MEV)	ELEMENT	A	TYPE
0.671	Cu	29	Inelastic
0.770	Cu	29	Inelastic
0.771	K	19	Capture
0.845	Al	13	Inelastic
0.848	Fe	26	Inelastic
0.859	Mn	25	Inelastic
0.872	O	8	Capture
0.963	Cu	29	Inelastic
0.985	Ti	22	Inelastic
1.015	Al	13	Inelastic
1.089	O	8	Capture
1.116	Cu	29	Inelastic
1.220	Cl	17	Inelastic
1.240	Fe	26	Inelastic
1.263	C	6	Capture
1.266	P	15	Capture
1.326	Cu	29	Inelastic
1.382	Ti	22	Capture
1.475	Cl	17	Inelastic
1.530	Mn	25	Inelastic
1.580	Ca	20	Inelastic
1.617	Ca	20	Inelastic
1.636	N	7	Inelastic
1.721	Al	13	Inelastic
1.728	Cl	17	Inelastic
1.762	Cl	17	Inelastic

3.679	N	7	Capture	1.780	Si	14	Inelastic
3.685	N	7	Inelastic	1.809	Mg	12	Capture
4.445	N	7	Inelastic	1.812	Fe	26	Inelastic
4.509	N	7	Capture	1.885	N	7	Capture
5.021	N	7	Inelastic	1.944	Ca	20	Capture
5.107	N	7	Inelastic	2.002	Ca	20	Capture
5.269	N	7	Capture	2.093	Si	14	Capture
5.534	N	7	Capture	2.115	Fe	26	Inelastic
6.094	N	7	Inelastic	2.125	B	5	Inelastic
6.322	N	7	Capture	2.184	O	8	Capture
6.446	N	7	Inelastic	2.212	Al	13	Inelastic
6.730	N	7	Inelastic	2.225	H	1	Capture
7.013	N	7	Inelastic	2.235	P	15	Capture
7.031	N	7	Inelastic	2.239	S	16	Inelastic
7.099	N	7	Capture	2.298	B	5	Capture
8.311	N	7	Capture	2.313	N	7	Inelastic
10.83	N	7	Capture	2.380	S	16	Capture
0.872	O	8	Capture	2.518	Na	11	Capture
1.089	O	8	Capture	2.527	K	19	Inelastic
2.184	O	8	Capture	2.537	B	5	Capture
2.743	O	8	Inelastic	2.646	Cl	17	Inelastic
3.273	O	8	Capture	2.695	Cl	17	Inelastic
3.685	O	8	Inelastic	2.743	O	8	Inelastic
3.855	O	8	Inelastic	2.753	Na	11	Capture
4.164	O	8	Inelastic	2.772	S	16	Inelastic
4.438	O	8	Inelastic	2.812	Ca	20	Inelastic
4.952	O	8	Inelastic	2.818	K	19	Inelastic
6.131	O	8	Inelastic	2.829	Mg	12	Capture
6.918	O	8	Inelastic	2.931	S	16	Capture
7.118	O	8	Inelastic	2.961	Al	13	Capture
8.873	O	8	Inelastic	2.982	Al	13	Inelastic

2.518	Na	11	Capture	3.005	Al	13	Inelastic
2.753	Na	11	Capture	3.007	Cl	17	Inelastic
3.588	Na	11	Capture	3.021	K	19	Inelastic
3.983	Na	11	Capture	3.036	Al	13	Capture
5.618	Na	11	Capture	3.055	Mg	12	Capture
6.396	Na	11	Capture	3.089	Cl	17	Inelastic
1.809	Mg	12	Capture	3.189	Ca	20	Inelastic
2.829	Mg	12	Capture	3.221	S	16	Capture
3.055	Mg	12	Capture	3.273	O	8	Capture
3.302	Mg	12	Capture	3.302	Mg	12	Capture
3.833	Mg	12	Capture	3.368	B	5	Inelastic
3.918	Mg	12	Capture	3.466	Al	13	Capture
8.154	Mg	12	Capture	3.532	N	7	Capture
0.845	Al	13	Inelastic	3.540	Si	14	Capture
1.015	Al	13	Inelastic	3.546	K	19	Capture
1.721	Al	13	Inelastic	3.588	Na	11	Capture
2.212	Al	13	Inelastic	3.592	Al	13	Capture
2.961	Al	13	Capture	3.604	K	19	Inelastic
2.982	Al	13	Inelastic	3.610	Ca	20	Capture
3.005	Al	13	Inelastic	3.679	N	7	Capture
3.036	Al	13	Capture	3.685	C	6	Capture
3.466	Al	13	Capture	3.685	N	7	Inelastic
3.592	Al	13	Capture	3.685	O	8	Inelastic
4.135	Al	13	Capture	3.710	Cl	17	Inelastic
4.262	Al	13	Capture	3.740	Ca	20	Inelastic
4.582	Al	13	Inelastic	3.781	S	16	Inelastic
4.692	Al	13	Capture	3.833	Mg	12	Capture
4.735	Al	13	Capture	3.855	O	8	Inelastic
4.906	Al	13	Capture	3.880	K	19	Inelastic
5.136	Al	13	Capture	3.917	Ca	20	Inelastic
5.157	Al	13	Inelastic	3.918	Mg	12	Capture

5.413	Al	13	Capture	Al	19	Inelastic
6.104	Al	13	Capture	Na	11	Capture
6.287	Al	13	Inelastic	Fe	26	Inelastic
7.696	Al	13	Capture	Al	13	Capture
7.727	Al	13	Capture	O	8	Inelastic
1.780	Si	14	Inelastic	Al	13	Capture
2.093	Si	14	Capture	S	16	Inelastic
3.540	Si	14	Capture	K	19	Capture
4.936	Si	14	Capture	Ca	20	Capture
6.382	Si	14	Capture	O	8	Inelastic
7.202	Si	14	Capture	C	6	Inelastic
8.475	Si	14	Capture	B	5	Inelastic
1.266	P	15	Capture	N	7	Inelastic
2.235	P	15	Capture	B	5	Capture
2.239	S	16	Inelastic	N	7	Capture
2.380	S	16	Capture	Al	13	Inelastic
2.772	S	16	Inelastic	Al	13	Capture
2.931	S	16	Capture	B	5	Capture
3.221	S	16	Capture	Al	13	Capture
3.781	S	16	Inelastic	S	16	Capture
4.291	S	16	Inelastic	Al	13	Capture
4.870	S	16	Capture	Si	14	Capture
5.422	S	16	Capture	C	6	Capture
1.220	Cl	17	Inelastic	O	8	Inelastic
1.475	Cl	17	Inelastic	B	5	Inelastic
1.728	Cl	17	Inelastic	N	7	Inelastic
1.762	Cl	17	Inelastic	N	7	Inelastic
2.646	Cl	17	Inelastic	Al	13	Capture
2.695	Cl	17	Inelastic	Al	13	Inelastic
3.007	Cl	17	Inelastic	N	7	Capture
3.089	Cl	17	Inelastic	K	19	Capture
3.935	K	19	Inelastic			
3.983	Na	11	Capture			
4.121	Fe	26	Inelastic			
4.135	Al	13	Capture			
4.164	O	8	Inelastic			
4.262	Al	13	Capture			
4.291	S	16	Inelastic			
4.361	K	19	Capture			
4.419	Ca	20	Capture			
4.438	O	8	Inelastic			
4.440	C	6	Inelastic			
4.445	B	5	Inelastic			
4.445	N	7	Inelastic			
4.446	B	5	Capture			
4.509	N	7	Capture			
4.582	Al	13	Inelastic			
4.692	Al	13	Capture			
4.714	B	5	Capture			
4.735	Al	13	Capture			
4.870	S	16	Capture			
4.906	Al	13	Capture			
4.936	Si	14	Capture			
4.948	C	6	Capture			
4.952	O	8	Inelastic			
5.021	B	5	Inelastic			
5.021	N	7	Inelastic			
5.107	N	7	Inelastic			
5.136	Al	13	Capture			
5.157	Al	13	Inelastic			
5.269	N	7	Capture			
5.380	K	19	Capture			

3.710	Cl	17	Inelastic	5.413	Al	13	Capture
5.708	Cl	17	Capture	5.422	S	16	Capture
6.109	Cl	17	Capture	5.510	K	19	Capture
6.620	Cl	17	Capture	5.516	Ca	20	Capture
7.413	Cl	17	Capture	5.534	N	7	Capture
7.498	Cl	17	Capture	5.618	Na	11	Capture
8.577	Cl	17	Capture	5.696	K	19	Capture
0.771	K	19	Capture	5.708	Cl	17	Capture
2.527	K	19	Inelastic	5.752	K	19	Capture
2.818	K	19	Inelastic	5.855	B	5	Inelastic
3.021	K	19	Inelastic	5.901	Ca	20	Capture
3.546	K	19	Capture	6.094	N	7	Inelastic
3.604	K	19	Inelastic	6.104	Al	13	Capture
3.880	K	19	Inelastic	6.109	Cl	17	Capture
3.935	K	19	Inelastic	6.131	O	8	Inelastic
4.361	K	19	Capture	6.287	Al	13	Inelastic
5.380	K	19	Capture	6.322	N	7	Capture
5.510	K	19	Capture	6.382	Si	14	Capture
5.696	K	19	Capture	6.396	Na	11	Capture
5.752	K	19	Capture	6.420	Ca	20	Inelastic
7.000	K	19	Capture	6.420	Ca	20	Capture
7.769	K	19	Capture	6.420	Ti	22	Inelastic
1.580	Ca	20	Inelastic	6.446	N	7	Inelastic
1.617	Ca	20	Inelastic	6.450	Ti	22	Capture
1.944	Ca	20	Capture	6.557	Ti	22	Capture
2.002	Ca	20	Capture	6.620	Cl	17	Capture
2.812	Ca	20	Inelastic	6.730	N	7	Inelastic
3.189	Ca	20	Inelastic	6.737	Pb	82	Capture
3.610	Ca	20	Capture	6.744	B	5	Inelastic
3.740	Ca	20	Inelastic	6.744	B	5	Capture
3.917	Ca	20	Inelastic	6.761	Ti	22	Capture

4.419	Ca	20	Capture
5.516	Ca	20	Capture
5.901	Ca	20	Capture
6.420	Ca	20	Inelastic
6.420	Ca	20	Capture
0.985	Ti	22	Inelastic
1.382	Ti	22	Capture
6.420	Ti	22	Inelastic
6.450	Ti	22	Capture
6.557	Ti	22	Capture
6.761	Ti	22	Capture
6.762	Ti	22	Inelastic
0.859	Mn	25	Inelastic
1.530	Mn	25	Inelastic
0.848	Fe	26	Inelastic
1.240	Fe	26	Inelastic
1.812	Fe	26	Inelastic
2.115	Fe	26	Inelastic
4.121	Fe	26	Inelastic
7.644	Fe	26	Capture
0.671	Cu	29	Inelastic
0.770	Cu	29	Inelastic
0.963	Cu	29	Inelastic
1.116	Cu	29	Inelastic
1.326	Cu	29	Inelastic
6.737	Pb	82	Capture
7.368	Pb	82	Capture

6.762	Ti	22	Inelastic
6.794	B	5	Inelastic
6.918	O	8	Inelastic
7.000	K	19	Capture
7.012	B	5	Capture
7.013	N	7	Inelastic
7.031	N	7	Inelastic
7.099	N	7	Capture
7.118	O	8	Inelastic
7.202	Si	14	Capture
7.286	B	5	Inelastic
7.368	Pb	82	Capture
7.413	Cl	17	Capture
7.498	Cl	17	Capture
7.644	Fe	26	Capture
7.696	Al	13	Capture
7.727	Al	13	Capture
7.769	K	19	Capture
7.978	B	5	Inelastic
8.154	Mg	12	Capture
8.311	N	7	Capture
8.475	Si	14	Capture
8.561	B	5	Inelastic
8.577	Cl	17	Capture
8.873	O	8	Inelastic
8.921	B	5	Inelastic
10.83	N	7	Capture